Investigations into AFM-Tip Based Vibration-Assisted Nanomachining

Thesis submitted in fulfilment of the requirement for the degree of Doctor of Philosophy

By
Sameeh Baqain

Cardiff School of Engineering

Cardiff University

United Kingdom

January 2022

Publications:

- Baqain S., Borodich, F., and Brousseau, E., 2021. Characterisation of an AFM Tip Bluntness Using Indentation of Soft Materials. In Borodich, F. & Jin, X. (Eds.) *Contact Problems for Soft, Biological and Bioinspired Materials*. Switzerland: Springer Nature Switzerland AG.
- Baqain S., Borodich, F., and Brousseau, E., 2021. "Theoretical Study of Factors Affecting the Effective Rake Angle of AFM Tips for Nanomachining Applications" *The 7th International Conference on Nanomanufacturing (nanoMan2021)*, Xi'an, China, November 2021.

Abstract

The recent global shortage of microchips highlighted the exponential increase in demand in the past three decades. It also showcased the fragile supply chain and its vulnerability to bottlenecking. Hence, it became evident that there is a need to explore additional manufacturing methods for miniature device manufacturing. The use of the atomic force microscope (AFM) has gained traction due to it being more environmentally friendly and its lower cost of operation when compared to other nanofabrication methods. The use of the AFM tip as a cutting tool is well established, especially when silicon workpieces are machined. In addition, the introduction of vibrations to the nanomachining process was found to provide improvements. However, the majority of research looks into silicon, with copper being investigated to a much lesser degree. Hence, this thesis investigates AFM tip-based vibration-assisted nanomachining of single crystal copper theoretically and experimentally.

Following the introduction, a literature review of nanomachining is done, followed by a review regarding Atomic Force Microscopy. After that, conventional and ultraprecision machining are reviewed. Stagnation zones that play an important role at micro and nanoscales are examined. Additionally, vibration-assisted nanomachining and its various methods are explained. Also, the advantages of vibration-assisted nanomachining over conventional nanomachining are discussed. Finally, the analysis necessary for the determination of the one-direction vibration-assisted nanomachining parameter is done. Equations that govern the vibrations are explained in detail, including values extraction necessary for selecting the various frequencies and amplitudes used during experimentation.

Chapter 3, in turn, studies the material deformation mechanisms at different scales and how they differ. Since the motion of dislocations is common among all size scales, it is analysed in addition to slip and the resolved shear stress. Four categories are agreed upon in the research community and are studied: (i) atomic scale, (ii) nanoscale, (iii) microscale (iv) macroscale. A brief discussion of the atomic scale is done with the inverse

Hall-Petch effect on the grain size being mentioned. The nanoscale is studied in most detail due to its close relation to the experimental work of this thesis, with emphasis on nucleation of dislocations and the variations between metals and macroscopically brittle materials like silicon. After that, the microscale is discussed with its most prominent plastic deformation theory, referred to as the strain gradient plasticity (SGP). Also examined is the applicability of SGP at the nanoscale. In addition, the macroscale plastic deformation is studied, including classical theories, which in turn is followed by hardness analysis. Fatigue and specifically low-cycle fatigue are analysed then, with the impact of the size scale on the latter also reviewed. Finally, an analytical study of an experiment similar to one done in this thesis wherein proof is provided regarding the prominence of dislocation nucleation in the nanomachining of copper.

As for Chapter 4, characterisation of the AFM tip shape and condition is performed. Following an introduction to tip characterisation, a review on how the shape of the tip impacts AFM operations, including nanomachining, is carried out. Methods including in-situ and ex-situ used to characterise the tip are then showcased. Later, images using the SEM are taken of the tip and later processed for tip shape extraction. Consequently, a power-law function is used to characterise the tip shape using a non-integer bluntness value. Bluntness values were extracted for both vertical and 12° tilt angle orientation, where the latter is observed in practice. Afterward, a force-displacement experiment of the same tip is done to validate the results obtained from the SEM images, using the Borodich rescaling formula. The bluntness impact of the work of adhesion and pull-off force is analysed using values extracted during experimentation, in addition to other arbitrary but practical non-integer values. In the end, an analytical study is done to investigate the factors affecting the effective rake angle. Such angle plays a vital role in the nanomachining process, including forces exerted and surface quality. However, the tip bluntness, depth of penetration, and tilt angle all impact this angle to varying degrees.

Chapters 5 and 6 cover the vibration-assisted nanomachining experimental work and consequent results. Chapter 5 discusses the test setup and all the necessary equipment to complete the experiment. The cutting conditions and parameters of the tests are discussed, such as the three different amplitudes and frequencies of the vibrations

resulting in nine combinations plus a conventional test used as reference. Parameters also include the cutting velocity and direction in each test and the data acquisition software settings. The chapter then briefly explains the imaging and scanning techniques used to investigate the resultant grooves.

Chapter 6 discusses the outcomes and results of the experiment. The chapter starts by presenting the first test's results with no vibrations induced. Following that, the nine tests with vibrations induced are presented with specific parameters compared to the first test. These include groove depths, pile-up heights, surface roughness, chip formation, and live signal acquired from AFM nanomachining experiment. The results are then discussed, highlighting the cases where the induced vibrations did provide improvements, where they did not, and where no significant changes are noticed. Later, trends observed during testing are presented. Finally, evaluation and comparisons between the results and what is available in the research community, including theoretical and analytical studies with consequent conclusions, are presented.

Finally, Chapter 7 concludes with the knowledge gaps addressed in this thesis, in both the characterisation of AFM tips as well as the optimisation of AFM tip-based vibration-assisted nanomachining and followed by a summary of the work done in this thesis and conclusions encompassing work done across the thesis. Then, suggestions regarding the additional future work that can be done to expand and improve upon what was done throughout this thesis.

Acknowledgments

My sincerest gratitude for my supervisors Feodor Borodich and Emmanuel Brousseau. Their nonstop guidance and support throughout my PhD have been a blessing, especially during such challenging times caused by the pandemic.

My gratitude also extends to my family for always being there for me. I am also thankful for the friendships I made in Cardiff, as I was able to rely on them whenever I needed support.

Last but foremost, I would like to thank the American University of Madaba for sponsoring my PhD, making all of this possible.

List of Acronyms

AFM	Atomic Force Microscope
NEMS	Nanoelectromechanical System
MEMS	Microelectromechanical System
UV	Ultraviolet
CPU	Central Processing Unit
VANM	Vibration-Assisted Nanomachining
SEM	Scanning Electron Microscopy
DAQ	Data Acquisition System
UCT	Uncut Chip Thickness
STM	Scanning Tunnelling Microscope
PSPD	Position-Sensitive Photo Diode
1D	One-Dimensional
2D	Two-Dimensional
3D	Three-Dimensional
NC	Non-Contact
BUE	Built-Up Edge
DSI	Depth-Sensing Indentation
EAM	Embedded-Atom Method
HV	Hardness Value
DMZ	Dead Metal Zone
SLF	Slip Line Field
PMI	Polymethacrylimide
PEI	Polyetherimide

MD	Molecular Dynamics
CNC	Computer Numerical Control
UVAG	Ultrasonic Vibration Assisted Grinding
LVC	Linear Vibrational Cutting
EVC	Elliptical Vibration Cutting
PMMA	Poly (Methyl Methacrylate)
FEM	Finite Element Methods
OVITO	Open Visualization Tool
FCC	Face-Centred Cubic
HPE	Hall-Petch Effect
IHPE	Inverse Hall-Petch Effect
TEM	Tunnelling Electron Microscopy
FIB	Focus Ion Beams
nc	Nano-Twin
SGP	Strain Gradient Plasticity
ISE	Indentation Size Effect
UTS	Ultimate Tensile Stress
HCF	High Cycle Fatigue
LCF	Low Cycle Fatigue
S-N-P	Stress-Cycle-Probability
S-N	Stress – No. Of Cycles
AISI	American Iron and Steel Institute
BTR	Blind Tip Reconstruction
HRTEM	High-Resolution Transmission Electron Microscope
STM or STEM	Scanning Tunnelling Microscopes

JKR	Johnson Kendall Roberts
DMT	Derjaguin Muller Toporov
CMB	Coffin Manson Basquin
LHS	Lefthand Side
RHS	Righthand Side
Typ.	Typical
Max.	Maximum
PC	Personal Computer
USB	Universal Serial Bus
NI	National Instruments
SAM	Signal Access Module
X DET1	X Detector (V)
Y DET1	Y Detector (V)
LFM	Lateral Force Microscopy
DAQ	Data Acquisition
FF	Face Forward
EF	Edge Forward
FF1	Start of Face Forward
FF2	End of Face Forward
EF3	Start of Edge Forward
EF4	End of Edge Forward

Nomenclature

γ_{eff}	Effective rake angle
θ_s	Stagnation angle
E^*	Effective elastic modulus
A	Undeformed chip thickness
D	Degree of bluntness
$B_d(\theta)$	Function of the indenter height at $r=1$
τ_{ath}	Minimum athermal stress
τ_{CRSS}	Critical resolved shear stress
σ_{app}	Applied stress
α	Initial inclination angle
φ	Increase in angle due to maximum load
$\Delta\varphi$	Shift in the inclination
h_{max}	Maximum depth
P_{max}	Maximum normal load applied
L	Length of the cantilever
C	Tip apex centre at working position before indentation
C'	Tip apex centre at the maximum depth
X	Distance between C and C'
h_f	Residual displacement
m	Slope of the unloading part of the load-displacement curve
$(h - h_f)$ or δ	Shift in force-displacement
K	Spring constant

$\mathbf{B}(\alpha, \beta)$	Beta function
$\tilde{P}$	Dimensionless load
$\tilde{\delta}$	Dimensionless displacement
$-\tilde{P}_c$	Pull off force
Λ	Transition parameter
σ_0	Stress (constant)
f	Frequency
$x(t)$	Current position
$x'(t)$	Current velocity
A	Amplitude
ω	Angular frequency
V	Velocity
T	Full cycle
V_{crit}	Critical upfeed velocity
F_{UP}	Upfeed increment
HSR	Horizontal speed ratio
t_2	Time when the tool separates from the machined material
t_1	Time when it enters the uncut material

Table of Contents

List of Figures

List of Tables

Chapter 1

Introduction

1.1 Background and Motivation

Since the invention of the Atomic Force Microscope (AFM) by Binnig et al. (1986), its use expanded from its original purpose, that is, topographical measurements, to other applications, mainly nanoindentation and nanomachining. The demand for miniaturised components increased in the past 20 years, requiring more fabrication methods. Applications for such components include Nanoelectromechanical (NEMS) and Microelectromechanical systems (MEMS) like wearable electronics and smart surfaces, aerospace, telecommunications, and medical such as implants and nanorobots that can be utilised for microsurgeries or to be used to destroy specific dangerous cells and much more.

A report published by BCCResearch's McWilliams (2018) suggested that the global market for nanodevices and nanomachines should grow from $736.1 million in 2018 to $1.3 billion in 2023 and then to $2.7 billion in 2028, at a compound annual growth rate of 11.6% from 2018 to 2023 and 16.0% from 2023 to 2028.

Although tip-based nanomachining is one of many fabrication methods at such scales, this method is one of the most cost-effective and most straightforward. Also known as ultra-precision machining, this method mainly utilises tips made from diamond due to its extreme hardness.

However, the technology most used in nanomanufacturing is lithography-based, especially photolithography. Although this technology impressively can produce features at scales of around 10nm, in addition to being highly demanding in R&D, the equipment used in such technology is from £800,000 for a basic electron beam lithography system and up to £80,000,000 for a high-end extreme UV lithography machine. All these costs, however, do not guarantee a 100% success rate in testing. According to Liddle and Gallatin (2016), the complexity of the coupled illumination-mask diffraction problem is so great that each future generation of chips relies on the computing power made available by the current generation of devices to solve it and, for all but the highest-volume devices, the mask cost is the dominant factor in the cost of ownership.

Dimov et al. (2012) highlighted that lithography-based approaches are limited to fabricating planar (i.e., two-dimensional) features. In addition, Krishnan et al.

(2008) discuss the environmental impact of lithography-based processes, which are inherently limited to materials that react to laser irradiation, and these materials are limited. Materials also need to be reactive to the environmentally harmful chemical etching process. The process is both energy and resource intensive, in addition to producing a significant amount of waste.

In addition, some significant technological challenges remain to be solved, which include the surface preparation and conditioning for the controlled deposition of the atoms, control of impurities and site uniformity, and quality of the reactants. The challenge in the bottom-up assembly of complex structures is to engineer the element-to-element interactions, formation of intermediate structures, and process conditions (e.g., annealing schedule) so that there is a clear path for the components to follow through the potential energy landscape to the global minimum. This problem becomes highly challenging unless the manufactured structure has a clear and simple pattern.

However, different nanomanufacturing approaches that use bottom-up self-assembly do exist. For example, a process includes an organised structure that spontaneously forms from individual components due to specific, local interactions among the components. Such processes, stochastic by nature, are driven by a combination of thermodynamics and kinetics, which then determines the desired structure.

Lastly, nanomachining is considered the most cost-effective and straightforward method compared to other nanofabrication methods. This technology, similar to its traditional macro counterpart, relies on the physical removal of the material via localised high-energy influence such as the focused ion beam method, mechanical scratching grinding, or milling-like processes, as discussed in Gao and Huang (2017).

Mechanical nanomachining appears to be one of the best alternatives to the other existing nanofabrication methods because:

- Its cost-effectiveness
- The fact that it resembles approaches of conventional machining and thus can be applied to a wide range of materials

- The ability to produce three-dimensional features (unlike lithography)
- More environmentally friendly

AFM probes can be suitable nanoscale cutting tools to create sub-100 nm grooves in width and depth. Thus, AFM-based nanomachining can complement ultra-precision machining when the intended groove dimensions reach sub-100 nm. Also, when the intended nanotechnology-based applications require metallic substrates, such as nanofluidic-based sensors, copper can be a material of interest in AFM-based nanomachining. The interest stems from its yield strength and ultimate tensile strength being comparatively low enough to enable the AFM-based nanomachining to be applied, as it is limited in the range of cutting loads generated. In this specific context, vibration-assisted nanomachining is of interest, given that vibration-assisted machining has been proven to provide improvements such as better surface quality and a reduction in cutting tip wear, as discussed in chapter 2.

Understanding the underlying mechanisms of metal deformation occurring during the nanocutting processes is essential, including plastic deformation, chip formation, and adhesion forces. Such understanding allows for more accurate simulation-based studies of such processes. However, metals such as copper are investigated much less than materials such as silicon.

In addition to the importance of more understanding of the underlying deformation mechanism of copper at the nanoscale, practical applications such as magnetic hard disks can be improved by applying such techniques to copper. For instance, such magnetic hard disks involve spacing between the rotating disk and sliding head that does not exceed 10 nm. Any wear and friction improvements can significantly impact the performance and capacity of such hard disks.

Also, chemical-mechanical polishing applied mainly to semiconductor substrates is essential in manufacturing semiconductors. Here, nanomachining can be utilised in the planarisation of multi-level semiconductor wafers (see., Steigerwald et al. 1997 and Ye et al. 2003).

So, in this thesis, the AFM tip-based vibration-assisted nanomachining (VANM) of copper is investigated. As explained later in Chapter 2, introducing vibrations into the conventional nanomachining process provides various benefits, such as improved repeatability and surface quality. Hence, nine different

combinations of vibrations are used to compare VANM against conventional nanomachining. Various combinations allow for understanding the impact of changing both the frequency and amplitude. That is done in addition to analysing the impact of changing cutting direction on the nanomachining process when a three-sided pyramidal AFM tip is used.

Here, the detailed analyses were not limited to the cross-sectional profile of the resultant grooves but extended the surface roughness and the signal generated by the data acquisition system during the nanomachining process.

This is done to optimise the process and better understand the governing framework of the deformation mechanism. This improved understanding could be a source of information for future simulation using a proper framework to yield more accurate models.

1.2 Research Goals and Objectives

The main goal of this thesis is to optimise and better understand the AFM tip-based nanomachining process of copper. The investigation starts with analysing the shape of the tip, followed by an analytical study of the impact the tip shape has on the effective rake angle, which is proven to impact tip-based nanomachining. Following this, conventional AFM tip-based nanomachining is benchmarked against vibration-assisted nanomachining (VANM) with varying frequencies and amplitudes.

Hence, the main objectives of this work are to:

- Provide an analysis of theoretical models describing governing processes that lead to the plastic deformation during the AFM based vibration-assisted nanomachining procedures, and investigate the specific features of these nanoscale processes that distinguish them from meso and macroscale processes

- Develop an experimental methodology for extracting AFM tip bluntness characteristics from SEM images and then validating the results with AFM nanoindentation using Borodich's rescaling formula
- Explore the impact of the variation in tip bluntness on adhesion of the AFM tips and the influence of the rake angle on nanomachining operations
- Develop an experimental methodology for effective studies of AFM tip-based vibration-assisted nanomachining of copper supported by extensive experimental data related to various combinations of frequencies and amplitudes of the vibrations
- Investigate the impact of select combinations of frequencies and amplitudes on the VANM process as well as the impact of changing the cutting direction when a non-axisymmetric tip is used, all in order to provide optimal cutting conditions

1.3 Thesis Layout

The second chapter of this thesis starts by reviewing what nanomachining is, followed by explaining what Atomic Force Microscopy is and what are its main components and working modes. Afterwards, cutting and chip formation at the macroscale and nanoscale are discussed, including nanoindentation. Stagnation zones which research emphasises their importance at smaller scales, are discussed at both macro and nanoscales in indentation and cutting. Vibration-assisted nanomachining is also reviewed to discuss its benefits over conventional nanomachining.

Chapter 3 discusses the theory behind plasticity at the atomic, nano, micro, and macro scales, with particular emphasis on the nanoscale. Dislocations which play an essential role during the plastic deformation of materials are also discussed. Fatigue and specifically low-cycle fatigue are also studied. Finally, an analysis of a practical experiment similar to the one done in this thesis which was also done in the same lab is used to prove the physical phenomena mainly used to explain plasticity at the nanoscale.

In Chapter 4, the apexes of AFM tips were characterised using SEM images of the tip. The degree of bluntness was calculated for both vertical and 12° tilt angle orientations. Afterwards, nanoindentation experiments were conducted on polycarbonate, a soft and elastic material. The unloading curve was also used to extract the degree of bluntness. Using Borodich's rescaling formula, it was possible to compare the results of the two mentioned techniques. The DSI results were used to validate bluntness values extracted using SEM images in this case. The impact of the tip's degree of bluntness on the pull-off force and the importance of not using integer values only to characterise the tip bluntness. Finally, an analytical study of the impact of tip bluntness on the effective rake angle was conducted. The effective rake angle plays a vital role in experimental and analytical studies of tip-based nanomachining.

Chapter 5 discusses the experimental setup for vibration-assisted nanomachining after analysing the equations that govern such operation. Cutting conditions and parameters used during testing are laid out. The first test conducted used conventional nanoscratching without induced vibrations. Then, nine vibration-assisted tests consisted of three different frequencies and amplitudes. Every test includes creating two grooves, each in opposite directions. Finally, the grooves' SEM imaging and AFM scanning techniques are presented, including limitations faced during operation.

In the end, in Chapter 6, the results of the ten conducted tests are presented and analysed. The conventional nanoscratching tests are benchmarked against the following nine tests utilising vibrations. The benchmarking is done to find the optimal frequency and amplitude, depending on the application. Parameters such as groove depth and its pile-up height, roughness, and the data obtained from the DAQ signal are used to make the comparisons. Towards the end, analyses are done to explain the difference the cutting direction has on the grooves created.

Chapter 2

Literature Review

2.1 Introduction

Micromachining is a term that encompasses a machining application smaller than 1 mm and larger than 1 μm that enables the manufacturing of miniaturised devices with micrometre features. The most practical difference between micromachining and macromachining consists of two specific features which are of great importance for the process and its simulations: (i) the uncut chip thickness (UCT) is comparable and even smaller than the material grain size; (ii) the cutting tool edge in macromachining is traditionally modelled as infinitely sharp, i.e., the cutting tool edge radius of curvature is zero. In other words, the cutting tool roundness is ignored (see, e.g., Masuzawa 2000).

Similarly, nanomachining is used to describe nanoscale processes with nanometric accuracy. The uncut chip thickness here can be even smaller than the smallest average grain size, and the consideration of the cutting tool edge is even more crucial.

In this chapter, the atomic force microscope is discussed, including its components and modes of operation. After that, conventional (macroscale) cutting is analysed, including some theoretical background. Then, material deformation during nanoindentation as well as nanomachining is reviewed. Following that, in-depth analysis of stagnation zones (dead zones) that form at the front face of a cutting tool, firstly at the macroscale, including both indentation and cutting, followed by stagnation zone occurring at nanoscale operations.

2.2 Atomic Force Microscope

The invention of the Atomic Force Microscope by Binnig et al. (1986) filled a gap in the microscopy field as it enabled researchers to scan non-conductive materials as well, which was not possible with the group's first Microscope, the Scanning Tunnelling Microscope (STM) in 1981 which was such a significant breakthrough that Gerd Binning and Heinrich Rohrer won the Nobel Prize in 1986. The STM enabled for the first time researchers to obtain atomic resolution three-dimensional images of material surfaces. Unlike the STM, where a bias

voltage is needed between the tip and the conductive scanned surface that allows electrons to move freely through the vacuum, the AFM is able to scan surfaces without the need for a vacuum or a conductive surface. In fact, in addition to its original medium set up, which is air, it was used in vacuum by Meyer and Amer (1990) and in liquids by Hansma et al. (1988). Over the life span of the AFM, its applications expanded from three-dimensional surface imaging to force-displacement applications such as nanoindentation that can be used to measure nanoscale material characteristics such as Young's modulus, nanotribology, as well as surface modification applications such as nanomachining.

2.2.1 AFM Components

An AFM consists of a probe with a sharp tip supported by a piezoelectric element that descends towards the workpiece, during which a laser beam reflects off the top of the cantilever and on a position-sensitive photodiode (PSPD). Figure 2.1 demonstrates the main components of an AFM. As the probe descends, no interactive force between the probe and workpiece is noticed. However, as it progresses, a gradual increase in the attractive force (e.g., Van der Waals and electrostatic forces) starts to dominate, reaching a maximum point after which an instant increase in the repulsive force is seen that causes the cantilever to bend upwards away from the workpiece, as Figure 2.2 shows.

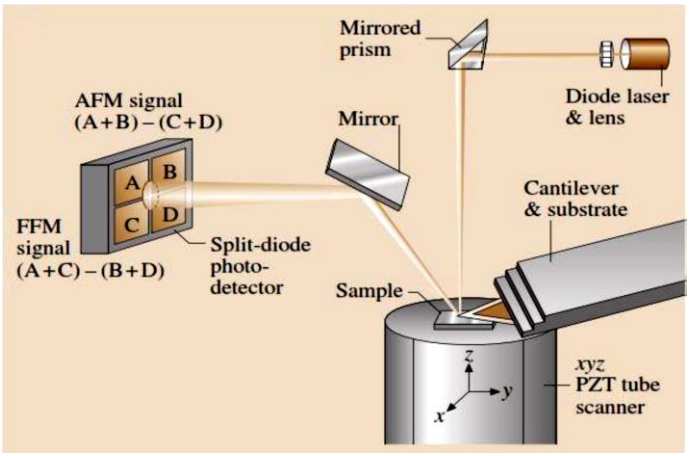

Figure 2.1 Components of an AFM system (Bhushan 2011)

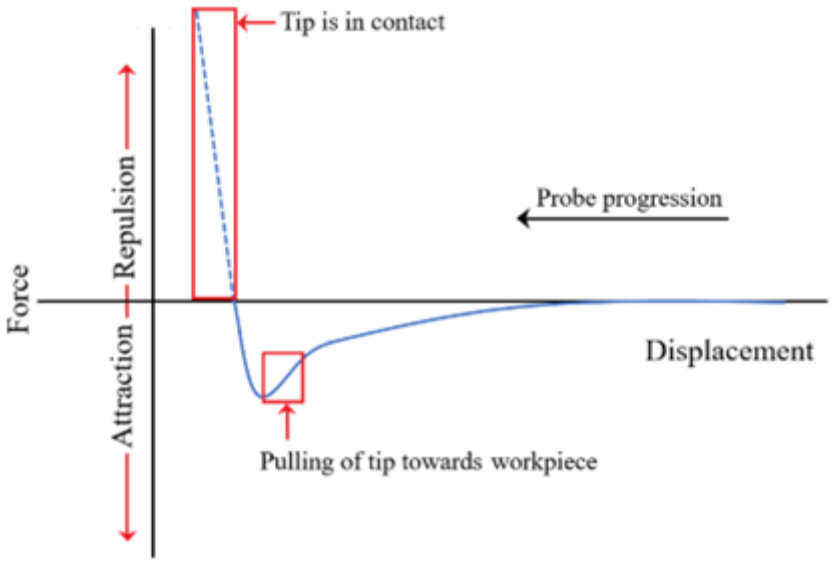

Figure 2.2 Interatomic force as the AFM probe nears the surface

Phenomena observed in Figure 2.2 plays an important role in explaining the behaviour of the probe and the resulting Force-Displacement graphs during nanoindentation experiments, as discussed in detail in Chapter 4 of this thesis.

2.2.2.1 Piezoelectric actuators

Piezoelectric actuators contain both Z-scanners and XY-scanners. The former is what supports and holds in place the probe and is usually made of piezoelectric ceramics. And the latter has two XY piezoelectric actuators, one that is built into the AFM system and is responsible for the in-plane motion of the workpiece in relation to the probe, in addition to a custom-made piezoelectric stack that is responsible for the one-direction vibrations. Piezoelectric materials have the unique ability to elongate or retract when undergoing an applied external voltage. They also can generate voltage due to externally applied forces.

2.2.2.2 Cantilever deflection sensing elements

Consisting of the probe (see Figure 2.3), the laser generator, and the PSPD, these components are essential for detecting any deflections during operation, be it lateral (normal) or torsional, with the use of the optical lever method. With this method, a laser beam is pointed towards the free end of the reflective surface of the AFM probe's cantilever. This laser reflects onto a position-sensitive photodiode that converts the change in the deviation of the laser from the centre point into an electrical signal (i.e., voltage). The strength of the signal is proportional to the amount of defection occurring.

PSPDs are divided into four quadrants wherein if the laser is only going up and down, there is only vertical deflection, and pure sideways motion means torsion. However, a combination of both cases occurs often, and the laser pointer moves with a particular quadrant. The operation of the PSPD is discussed in detail in Chapter 5.

As for AFM probes, this integral component has many variations in size and material build, both changing depending on the application. For example, a diamond tip would be used for machining, whereas silicon would be used for topographical applications. The stiffness of the cantilever of probes is application dependent as well. However, all AFM probes have three components, a tip, a cantilever, and a chip. As mentioned earlier, tips can vary in build material but also vary in size as well.

In contrast, small tips can provide higher resolution scans when used in topography and finer grooves and when used in ultraprecision machining. Where for the cantilever portion, they usually have a rectangular shape with a varying degree of chamfering of the filleting of the edges, in addition to a thin layer of coating added to the upper surface of the probe to improve laser reflectivity. Finally, the chip which is the part the is used to hold the probe in place to be mounted inside the AFM head.

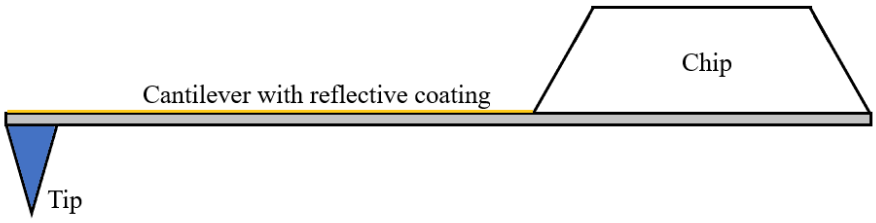

Figure 2.3 AFM probe consisting of a tip, a coated cantilever, and a chip

2.2.2.3 Feedback loop

To ensure continuously but at the same time non-destructive contact between the tip and the workpiece, a non-stopping corrective feedback loop is utilised. The optical lever method relies on the feedback loop where the AFM operator sets a maximum force which the system is not allowed to surpass. During operation, the controller within the AFM system analyses the input signal received from PSPD that corresponds to the deflection of the cantilever, then this controller compares the signal received and benchmarks it to the reference signal corresponding to the values put by the operator. Finally, the Z-scanner adapts to the signal to minimise the difference in values by contracting or expanding as it tries to maintain a constant force or distance between the tip and workpiece.

Linearity between the surface change in elevation (i.e., topography) and the strength of the voltage signal obtained from the PSPD is assumed. However, although this is a safe assumption to most heights, some exceeding certain limits lose this linearity, as discussed by Gozen and Ozdoganlar (2010), leading to some errors at such limits. Hysteresis and creep are additional sources of error when the voltage applied is used to present topography using the Z-scanner. A strain gauge fixed below the XY-scanner stage can be an additional source of vertical motion and as a reference when there is doubt.

2.2.2 Contact, non-contact, and tapping modes

The three modes of operation that are used for scanning the topography of surfaces using an AFM are contact mode, non-contact mode, and tapping mode with each having their own advantages over the others.

Contact Mode

Contact mode is the original scanning mode used when the AFM was invented. This mode works within the repulsive regime wherein the tip comes in close proximity with the surface of the workpiece. When this mode is used, the operator has the choice between two sub-modes: Constant force and constant height.

- Constant Force: Constant force mode was used before the constant height one. In this mode, the Z-scanner moves the probe vertically changing the height, adapting to the topography of the workpiece, and relying on the data it receives from the feedback loop as the cantilever deflects during operation. Higher resolution scans are achievable when the vertical deflection signal is kept constant. Hence, this mode can more accurately convert the outgoing signal of the Z-detector into topographical information. However, this accuracy comes at the cost of speed be it scanning or machining, caused by the inherent lag in the feedback loop within the AFM.
- Constant Height: As the name suggests, the height of the Z-scanner does not change in this mode, consequently not relying on the feedback loop features of the system. This lack of feedback increases the chance of damage occurring to the tip as the force interaction between the workpiece and tip is continuously changing. In this feedforward system the surface topography is created using the movement of the laser beam reflected over the photo-sensitive photodiode.

Non-Contact mode (NC)

This mode has a clear advantage over the prior when soft specimens are to be investigated. This advantage arises from the lack of the repulsive interactive forces during operation that has the ability to damage surfaces especially softer ones. Unlike the contact mode where repulsive force is what is needed to create

the topographical data, the non-contact mode utilises the attractive forces between the tip and the specimen using what is referred to as the amplitude modulation principle. Martin et al. (1987), which were the first to suggest this mode of operation in which the distance separating the tip from the surface ranges between 30 and 150 Å that in turn creates a light attractive force (i.e., Van der Waals) inducing a change in the phase and amplitude of the probe's vibrations. These changes then are recorded and are fed to the feedback of the system where it counteracts these changes by creating Z-scanner movements that negate any changes in the amplitude.

Tapping mode

This mode was created to negate an issue occurring in both aforementioned modes which is the tip sticking on the workpiece surface during operation. This occurs when the system's feedback loop tries to compensate for the slow lateral motion provided by the Z-scanner and tries to overcome the impact of the interactive forces, causing a noticeable drop in the lateral resolution. Zhong et al. (1993) suggested this mode to overcome the "stickiness" caused by adhesive and electrostatic forces by inducing lateral (tapping) vibrations strong enough to insure uninterrupted motion. As the vibration-induced probe approaches the surface, energy dissipation commences as the tip gets closer to the surface causing a decrease in the vibrations. This deduction is the amplitude of oscillations is then utilised to characterise the surface and create and topographical map of the surface. This mode is applicable in both air and fluids. Figure 2.4 demonstrates how this mode works as per the manufacturer Bruker.

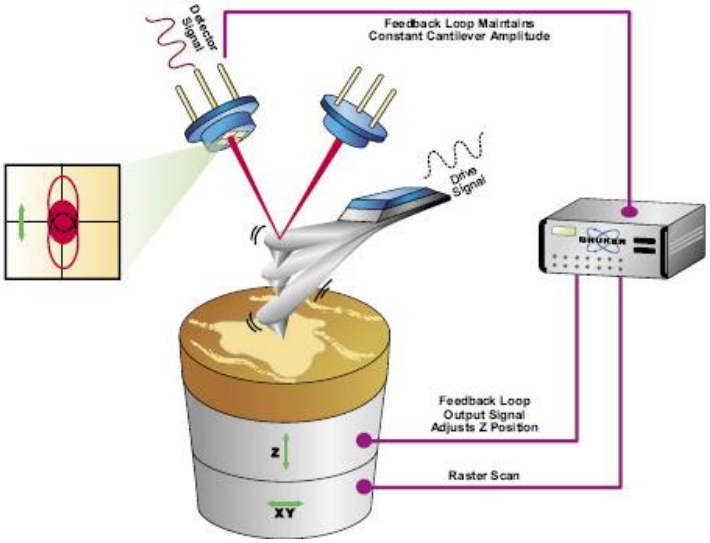

Figure 2.4 Tapping mode (Bruker)

2.3 Cutting and chip formation

Chips formed during machining can give great clues on how the deformation occurs during operation. For instance, by examining the metal chips forming, if the outcome is a continuous chip, this gives a good indication that the material is relatively ductile. On the other hand, a discontinuous chip can indicate brittle behaviour. It is important to remember that how brittle or ductile the material is, impacts how the chips are formed. Other factors such as cutting speeds and the rake angle also impact how chips form. Generally, larger rake angles, high cutting speeds, low cutting friction and small cut depths are all factors that increase the likelihood of continuous chips forming. On the other hand, combining low feed rates with small rake angles, high cutting speeds, high cutting friction, and an increased depth of cut elevates the possibility of discontinuous chips forming.

Chips form from scooping ice cream (see Figure 2.5), and a continuous chip is formed, as explained below gives a perfect example of a continuous chip formed when a ductile material is cut.

Figure 2.5 Ice cream scooping representing continuous chip forming

Although wood is not considered ductile, when other factors mentioned earlier such as the cutting angle and cutting speeds satisfy the continuous chip formation conditions, they form. As, Figure 2.6 demonstrates.

Figure 2.6 Continuous chip formation of wood (Stock Image)

Chip forming in metals is highly dependent on the factors mentioned before and affect the quality of the surface finish, power consumed during machining, tool life and amount of waste material generated so great deal of attention is focused on how chips formed. Figure 2.7 is an example of chip formation in steel.

Figure 2.7 Chip formation in steel (JJ Harrison 2008)

2.3.1 Conventional cutting

Piispanen (1937) created what is known as the Card Model to illustrate how the cutting process occurs. In this model, the material is depicted as a stack of cards with a certain angle with the material that corresponds to the shear angle as Figure 2.8 shows.

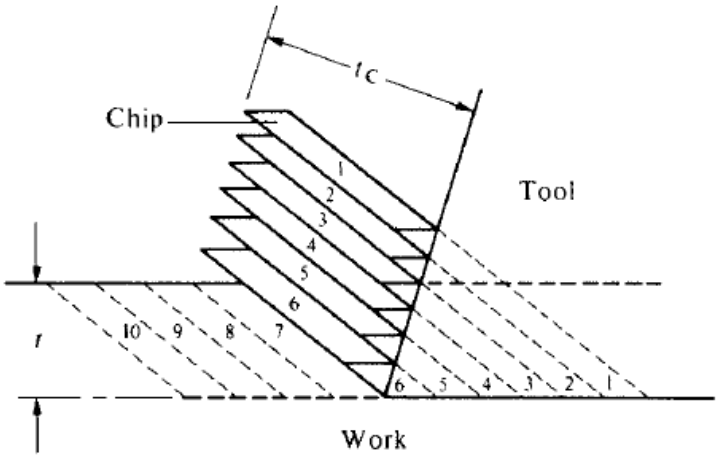

Figure 2.8 The Card Model (Piispanen 1937)

However, this model suffers from many inaccuracies, such as ignoring built-up edge (BUE) formation, the shear angle being assumed arbitrarily and assumes the shearing of a perfectly planar surface. Nevertheless, the model gained

attraction due to its simplicity and the incorporation of the steady state chip formation process.

On the other hand, one of the earliest to study the mechanisms describing the material removal during cutting was Merchant (see, e.g., Ernst and Merchant 1941, Merchant 1945)), which modelled the chip formation process relying on the concentration of shear. As Figure 2.9 shows.

Though, multiple subsequent publications suggested that steady state chips (i.e., continuous chips) do not follow Merchant's model in certain cases. For example, a pie-shaped triangular deformation zone will develop if the material is soft and does not experience prior strain hardening. Also, in the case of more blunt cutting tool tips, wherein the tip's radius is large compared to the undeformed chip thickness, the shear zone extends even more. The latter, however, is more prevalent at micro and nanoscales.

Shaw (2005) discussed an ideal orthogonal cutting process (Figure 2.9) that assumes a complete homogeneous behaviour of the material, disregarding any variations of strain within the material.

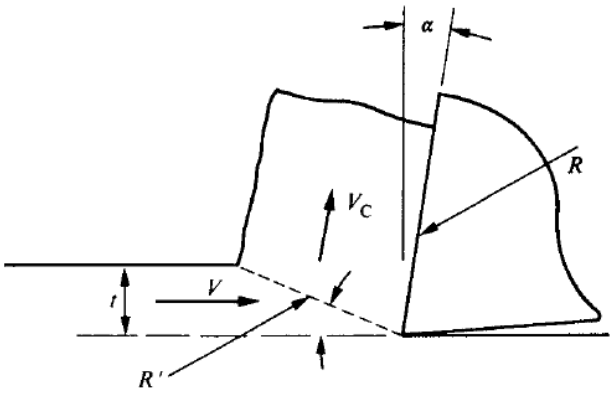

Figure 2.9 Resultant forces R and R′ (orthogonal cutting)

This two-dimensional model assumes a completely sharp tool, a planar shear surface that flows upwards, and no sideway flow. The model also assumed uniform cutting velocity and a constant depth of cut, in addition to other assumptions made to simplify the application of this model.

The author also analysed the forces acting on the chip during cutting. Two forces in particular were considered, R which is the force acting in the interface between the chip and tool face, in addition to R' the force between the worked material and the chip along the shear plane.

2.3.2 Nanoindentation and ultraprecision cutting

Given that it is established within the scientific community that the material at the nanoscale deforms differently from the macroscale, investigations of the material behaviour during nanocutting is necessary. But before that, studies regarding material deformation during nanoindentation are reviewed as DSI studies give great insight into material behaviour and characteristics in addition to being researched more in depth.

The term "dislocation nucleation" is mentioned throughout this section. However, more details regarding it and its significance in the nanoscale will be discussed in chapter 3. In addition, materials investigated will not be restricted to metals but also to conventionally brittle materials such as silicon. This is done because such materials exhibit a brittle-to-ductile transition at very small scales including the nanoscale. In addition to the significant availability of research for both DSI and nanomachining applications for such materials.

2.3.2.1 Nanoindentation (DSI)

More significant strengths are observed during nanoindentation compared to the macroscale indentation. At the former, dislocations multiply via double cross-slip, which increases dislocation density and leads to Taylor-type hardening. On the other hand, at the nanoscale, dislocations travel small distances before vanishing at free surfaces; thus, no multiplication of any dislocations that weaken the material.

Zhang and Tanaka (1999) simulated nanoindentation of single crystal silicon. They found that octahedral shear stress was the crucial factor in phase

transformation to an amorphous state from previously a diamond structure when the hydrostatic stress changed the threshold of the phase transformation. They also discovered that plastic deformation initiated at different thresholds depending on the orientation explained by the anisotropic nature of this material decreasing from 7.6 GPa for [110] orientation to 4.6 GPa for [100] orientation.

As for polycrystalline copper, Li et al. (2016) did MD simulations from which they concluded that the temperature, hardness, and elastic recovery rely on crystal structure and the twin-lamellae-thickness. In addition, they realised that initial dislocation constantly nucleated just beneath the indenter and annihilated during the indentation process. Also, the polycrystalline copper plastic deformation depended on the dislocation–grain boundary interactions.

Another study on amorphous materials was done by Qiu et al. (2014), in which Cu50Zr50 was analysed and found that the migration and growth of shear transformation zones were consistently observed during nanoindentation. The deeper the indentation and the bigger the descending velocity and tip radius led to more considerable loading forces. An increase in the loading speed also changed the material's properties by increasing the elastic modulus and hardness. However, tip size variation did not have any noticeable impact.

Rester et al. (2007) investigated how the microstructure below the indentation in copper is affected. Their work suggests that for large indentations, dislocation piles up and the Nix and Gao models sufficiently describe the indentation (~1.75 µm contact depth), as for the shallow indentations (0.25 µm and below contact depth), they lead to a "decrease in the number of activatable dislocation sources" suggesting that mechanisms other than what is discussed in the Strain Gradient Plasticity theory are responsible for the plastic deformation.

Possible mechanisms include heterogeneous dislocation generation caused by superficial defects, including fractured oxide layers and random dislocation nucleation. The newly generated dislocations push older ones inside the bulk of the material. Dislocation loops are nucleated in the vicinity below the surface and propagate to undeformed spots with the increase of loading.

Tschopp and McDowell (2008) investigated how a single crystal copper's homogenous dislocation nucleation process is affected by uniaxial loading using

EAM under 10 K and 300 K temperatures. They concluded that not only Schmid factors are essential but also non-Schmid parameters to characterise dislocation nucleation for monocrystals undergoing tension and compression.

Schmid factors are represented through the resolved shear stress within the slip direction, whereas the resolved tensile stress normal to the slip plane is exemplified via the non-Schmid normal factor.

2.3.2.2 Nanomachining

Two studies by Zhang and Tanaka (1997, 1998) highlighted four regimes of deformation during the nanoscratching process with gradually increasing applied force, which was emphasized later on (see, e.g., Elkaseer and Brousseau 2013) and Geng et al. 2018). The first regime was the no-wear regime that had no defects. The second was the adhering regime, where surface atoms of the two interacting surfaces swapped over. The third was ploughing, described by a triangular atom-cluster motion. The final regime was the cutting regime, in which chip formation was evident due to complete material removal. Increasing the indentation force and consequently, the tip depth inside the material gradually shifts from the no wear regime to the cutting one.

In the first two regimes, no considerable fracture occurs to the material. However, modes I and II are dominant in the ploughing regime modes, as Figure 2.10 (a), (b) show. The resultant shape will be similar to a triangle.

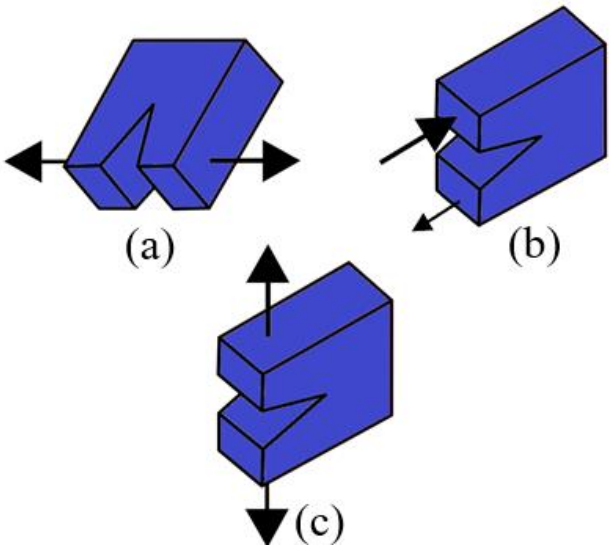

Figure 2.10 Dominant fracture modes: (a) Ploughing mode I horizontal opening (b) Ploughing mode II vertical in-plane shearing (c) cutting with chip formation Mode I vertical opening

As for the cutting regime, Mode I vertical opening is the dominant proved by the chip creation due to material separation with the two modes mentioned above still in action but less prevalent (see., Broek 1982) as shown in Figure 2.10 (c).

During an analytical study, Hosseini and Vahdati (2012) noticed that when a certain edge radius to minimum uncut chip thickness ratio threshold is surpassed, the dead zone acts as an additional cutting edge in the cutting process, shifting the shearing point towards it. In turn, when the edge radius to minimum uncut chip thickness ratio is equal to or less than the minimum value, the stagnation region is weak. It cannot act as a cutting edge and just slides on the surface during the cutting operation.

The upper layer of atoms is cut via extrusion in this case. The uncut chip thickness threshold upon which chip formation occurs or not plays an essential role in cutting at smaller size scales.

Elkaseer and Brousseau (2013) investigated machining the surface of a CuZn39Pb3 brass alloy that has two phases, with the first having a hardness value of around 125 HV and the second an approximate 203 HV. In this experiment, eight grooves were made (four for each phase), all starting from zero force and then increasing it linearly, but each groove had a different final applied force.

Three regimes were observed; one had a complete elastic recovery, the second ploughing was observed, and the third cutting with chip formation was observed. These observations suggest that a transition from elastic to plastic deformation happens with the increase of force and hence indentation depth. Also, in the plastic region, a transition from ploughing to cutting is observed with the same elevation in force and depth.

Using a diamond (~25 nm tip radius) AFM tip to nanomachine relatively ductile single crystal Aluminium, Komanduri et al. (2010) observed how the machined material reacts to applied forces. The applied force was ~6.5 mN with a 1 µm/s velocity with a groove depth of 30 nm and length of 0.6 µm.

As Figure 2.11 shows, no chips were formed during operation, and only ploughing is apparent. In addition, Figure 2.11 (b) shows that the amount of material ploughed is roughly the same amount of material removed. Hills' areas were ~250 nm, and the valleys were ~200 nm.

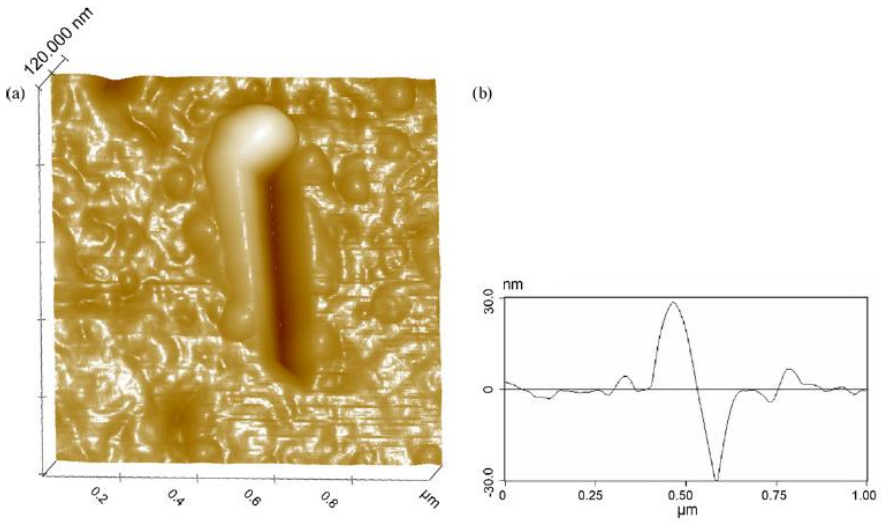

Figure 2.2 Nanoscale machining (a) 3D surface topography (b) cross-sectional profile Komanduri et al. (2010)

Another observation in this study was the discontinuity in the ploughing outcome with increased length, specifically after 0.75 µm.

The impact of cutting speed in the process of nanomachining single crystal copper was investigated by Ye et al. (2003) and found that lower cutting speeds deliver smoother surfaces with dislocations within the worked material. On the other hand, higher speeds yielded more rough surfaces, but the machined material was defect-free. It was also found that higher speeds cause chip size growth.

Liu et al. (2007) found that hydrostatic pressure causes an increase in the critical uncut chip thickness of brittle materials. They also observed that the increase in the cutting tool radius exacerbates this stress causing brittle materials to behave similarly to ductile ones during cutting.

2.4 Stagnation zones

The dead zone, dead metal zone (DMZ) or what is as also known as the stagnation region is where the material being cut acts as a new cutting edge. Due to the importance of understanding the stagnation region, which plays an important role during nanoscale operations, a general review of such phenomena is done in this section.

2.4.1 Stagnation zones during indentation

Murthy et al. (2012) Studied the deformation field during indentation of a model granular material by taking images continuously of the entire process. Their experiment included an ensemble of spherical sand particles averaging a 0.4 mm size using a flat ended punch to perform the indentation. What they found was that while the indenter goes into the material a “dead zone” formed on the face of the flat punch as Figure 2.12 shows.

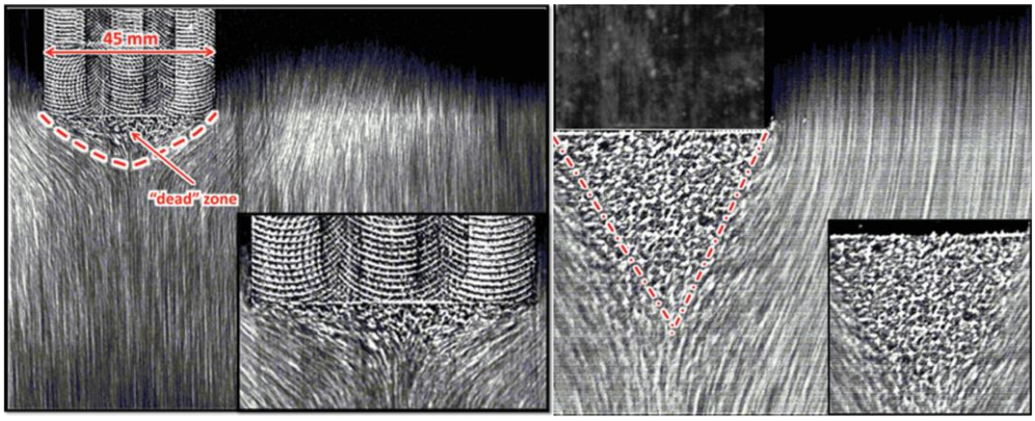

(a) (b)

Figure 2.3 The indentation field with the dead zone (a) sand (b) lead (Murthy et al. (2012)

This region appears as a curved triangle sandwiched between two vertices at the flat punch's bottom fringes, where the mentioned region's material stayed fixed in place as a rigid body of material during indentation and acted as a curved extension of the indenter without any slips forming in front of the indenter's face.

The indenter's shape and the friction between its surface and the penetrated material are the two major factors affecting how the dead zone forms and how it looks in metals. Regarding granular media, microscale structure plays a less critical role in creating such a zone, as discussed in Amarouchene et al. (2001).

It is also worth noting that force-displacement curves are not considered a reliable tool to predict the characteristics of the dead zone formed due to the insensitivity of the load regardless of whether the zone is present or not, applicable to both metals and granular materials. Changing the tip's shape by adding an artificial dead zone at the top only changes the behaviour at the beginning of the indentation. After that, usual behaviour persists, creating a new dead zone with a constant size. Also observed was the minimal influence of the loading rate; hence it is predicted that such a zone can be seen even with fast loadings such as impact loadings. On the other hand, the deformation is highly dependent on the shape of the dead zone.

Meanwhile, Yadav et al. (2016) studied the impact of both the porosity of the material (in this case soft brittle rock) and the geometry of the indenter in terms

of the deformation field. Characteristics such as local material displacement and localisation features were studied. It was found that high porosity specimens had sharper deformation zones, unlike the diffuse nature of less porous ones. Moreover, as expected, low porosity samples were able to carry bigger loads, as Figure 2.13 below shows.

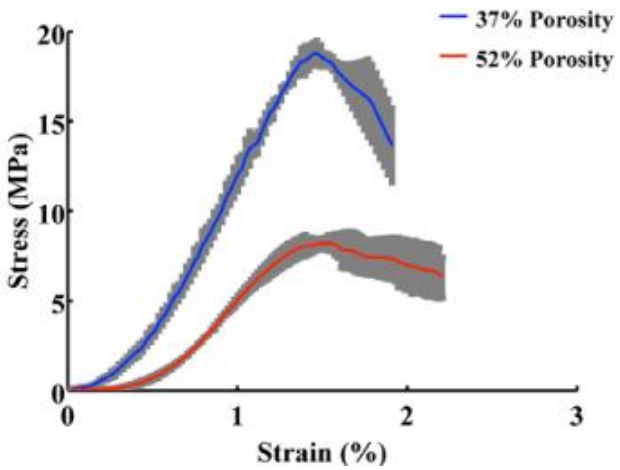

Figure 2.4 Stress-strain curves for different porosities (Yadav et al.(2016)

Also, Flores-Johnson and Li (2010) studied the impact of the tip shape of indenters during the indentation of polymeric foams, namely polymethacrylimide (PMI) and polyetherimide (PEI). The two main factors influencing the indentation were the indenter shape and the density of the foam. This study utilised multiple indenter shapes, including conical, flat, truncated, and hemispherical. Two indentation regimes were, in turn, realised, an immersing regime and a plateau-like one. The authors of this study developed an analytical model to predict the forces exerted during indentation that generally had good agreement with the experimental data.

2.4.2 Stagnation zones during cutting

Regarding cutting, Yadav et al. (2018) expanded their previous work to include how porous; soft rocks deform during cutting. A significant conclusion

of this experimental study was the difference between cutting under positive and negative rake angles. For the positive rake angle cutting, the cutting mechanism was mainly represented by fracture and crack initiation at the cutting interface. Fractures, in this case, initiate at the tool's tip, propagating towards the free surface. In addition, the cutting tool scratches the material until it reengages with the material forming chips. During such process, the forces exerted during cutting reach minimum values as chips are removed and maximum values when the tool reengages cutting into the workpiece. Also noticed was the change between ductile and brittle deformations depending on the rake angle.

Also, it was observed that the cutting force was decreasing and increasing cyclically, which can be attributed to the interaction of the tool with crack propagations (when decreasing) and with the rest of the material (when increasing). Results also suggested that shear was responsible for the removal of the material, as suggested by Nishimatsu (1972).

On the other hand, the negative rake angles produced a dead zone shaped like a triangle at the cutting interface. The size of this dead zone (similar to a 'built-up edge' in metal cutting) varied cyclically as the cutting tool moved through the material. In addition, machining at a negative angle made the depth of the cut a more significant factor in the cutting forces exerted. The depth of cut also influenced and increased the length of cracks formed, which in turn was also influenced by decreasing the rake angle.

The dead zone's size decreases as the chip is removed during cutting because part of this zone leaves the material alongside the removed chips. However, as the tool re-enters the material and starts engaging more workpiece, the dead zone increases in size once again with the accumulation of material. The extent of the dead zone was found to rely on the angle and the strain it imposes during cutting.

2.4.3 Stagnation zones and their prevalence at the nanoscale

In the case wherein the uncut chip thickness (UCT) is significantly larger than the minimum UCT material removal is done through shearing, as in larger size

scales. However, when the UCT is in the range or smaller than the minimum UCT, the material in this case is removed via extrusion (see., Xu et al. 2017b) and material separation is categorised into two approaches; separation due to a stagnation point or due to a stagnation region (see., Denkena and Biermann (2014).

In the stagnation point approach, the material above this point separates from the material as chips, and below it is the newly formed surface of the material, as discussed in Lai et al. (2012).

The effective rake angle can be estimated sing the stagnation angle θ_s seen in Figure 2.14 (a) using $\gamma_{eff} = \pi/2 - \theta_s$. The importance of the effective rake angle and what it impacts during nanomachining are discussed in detail in chapter 4.

The other approach used to explain material separation is the stagnation region, seen in Figure 2.14 (b). This region is likened to a stable dead metal zone or a built-up edge. Factors affecting this region were studied by Kountanya and Endres (2001) including the shape of the cutting tool, cutting speeds, workpiece material, and the coefficient of friction play an important role in the stagnation region.

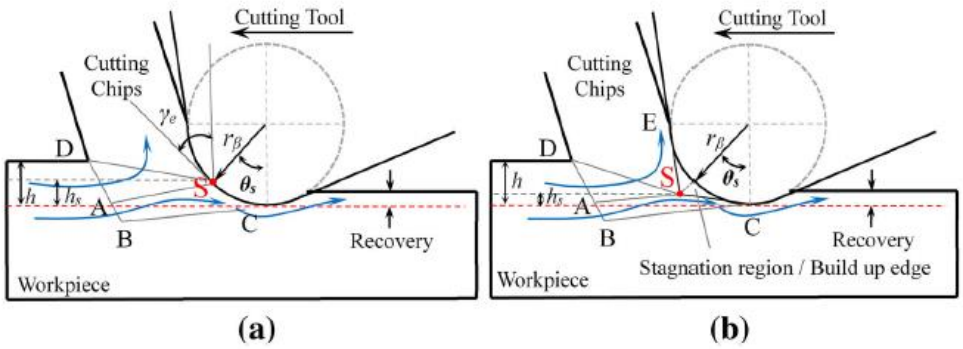

Figure 2.5 Nanometric cutting with (a) stagnation point (b) stagnation region (Fang and Xu 2018)

Regarding the nanomachining of metals, Xu et al. (2017a) studied its impacts on aluminium using molecular dynamics. The authors noticed the creation of a

stagnation zone when the tool edge was cutting with a negative rake angle. No such region was observed when a sharper tool with a positive rake angle was used.

The existence of such a region was confirmed when Chen et al. (2006) found that a portion of the material by the cutting tool had a non-changing relative velocity, confirming the presence of such a region. Meanwhile, Kümmel et al. (2014), during a microcutting of steel experiment, concluded that the hardness of the stagnation region (referred to as the build-up edge in the paper) is two to three times larger than what is seen in other regions of the machined material. In addition, the authors found that under specific conditions, the stagnation zone can protect the tip from wear. Another advantage the stagnation region provides is a reduction in the applied force. For example, Uhlmann et al. (2015) stated that this region provides an additional, less blunt cutting edge with a higher effective rake angle. On the other hand, Fang et al. (2010), when analysing the vibrations induced during machining, found that the continuous change in the size of this region has a negative impact on the condition of the resultant surface.

A study by Wang et al. (2018) analysed the material removal mechanism during nano-scratching. They incorporated a blunt tip and not an infinitely sharp tip; hence factors like adhesion play that vital role. In addition, the two main mechanisms responsible for the material removal stated were shear and extrusion, with the latter being the dominant one when the tool edge radius to the uncut chip thickness ratio (ratio known as R) is above zero. Shear, on the other hand, was dominant when the ratio R was zero (i.e., infinitely sharp tool). Figure 2.15 explains.

This simulation included machining silicon in which they discovered the creation of a buffer region between the tip and the undeformed material, referred to as the stagnation region, is a feature of the extrusion process. In the case of silicon, this region consists of phase transition that explains the ductile behaviour during the nano-scratching of monocrystalline silicon. In the extrusion, the material is removed due to the plastic deformation of contact-induced amorphisation above the stagnation region. As for the shear process, strain-induced amorphisation is responsible for creating shear bands and shear-caused

material removal. Ultimately, in a typical process, extrusion, and shear both contribute to the material removal evident in the polycrystalline chip structure. However, how much each contributes depends on the ratio of the tool edge radius to the undeformed chip thickness, and as the latter increases, the shear effect diminishes, followed by an increase in cutting energy and less material removed.

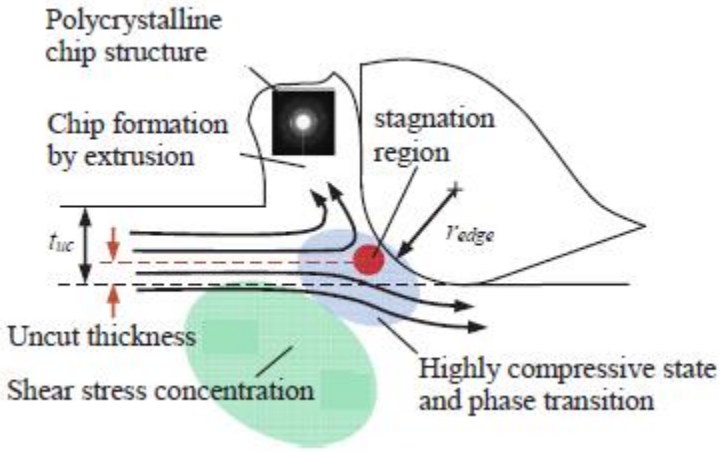

Figure 2.6 Stagnation region during nanomachining Wang et al. (2018)

Although discussed on the microscale, De Oliveira et al. (2015) refer to a critical value known as the minimum uncut chip thickness which if not reached no chips are formed and only ploughing occurs. On the other hand, if it is reached chip formation occurs.

The simulation confirmed the existence of a stagnation or as referred to as the dead metal zone (DMZ) that increases in size whenever the cutting speed decreases as well as any increase in the cutting distance. Multiple factors were used to characterise the location including the ploughing thickness and separation height. The latter impacts the location of the stagnation point in addition to the minimum uncut chip thickness. The effective rake angle in turn varied between -42° and -51°.

2.5 Vibration-assisted nanomachining

Vibration-assisted machining has several advantages over conventional machining including:

- Reduction of machining forces
- Formulation of thinner chips
- Better surface finishing
- Improved accuracy
- Reducing burr formation
- Enhanced tool life expectancy

VAM was also found to improve the depth of cut for ductile regime cutting is achievable, which enables the creation of complex shapes that do not require further finishing processes.

AFM tip-based nanomachining can be categorised into two types, depending on the axes of motion: one-dimensional (1D) and two-dimensional (2D). The former is also referred to as linear VANM, and the latter as elliptical VANM, wherein combining two motions usually produces an elliptical motion path. Vibrations are produced by either the motion of the AFM probe or the workpiece material.

Regarding the 1D VANM, the most common and used in this thesis is where the vibration direction is parallel to the cutting direction. Other modes include lateral, which is similar to tapping mode scanning (Figure 2.16 (a)) and flexural (Figure 2.16 (b)).

Two-dimensional VANMs are produced by combining motions. Such techniques were developed to machine difficult-to-cut materials (see., Shamoto and Moriwaki 1999). In-plane motion (Figure 2.17 (a)) and out-of-plane motion (Figure 2.17 (b)) modes of nanomachining are the most common in the field of ultra-precision machining. However, additional modes are used, such as Figure 2.16 (c).

Also, Voigt et al. (2009) explored the possibility of using the AFM's cantilever chip system in nanomachining while it is vibrating in resonance mode.

The cantilever in this study moves in flexural and torsional manners. They found an intermedia and e stripe-like region between the cantilever and the chip, enhancing the system's vibrational motion.

Shown below, Figure 2.16 shows the three vibrational modes investigated, where (a) is lateral due to torsional vibrations of the frame. Whereas (b) is flexural caused by the piezo excitation effect and (c) is a mixture of both mentioned modes (a) and (b), resulting in a two-dimensional elliptical shape of the movement. The periodic contact with the material due to the elliptical movement leads to improved material removal. The authors compared this process to material ablation processes similar to excavators and the elliptical motion to the shovel of an excavator.

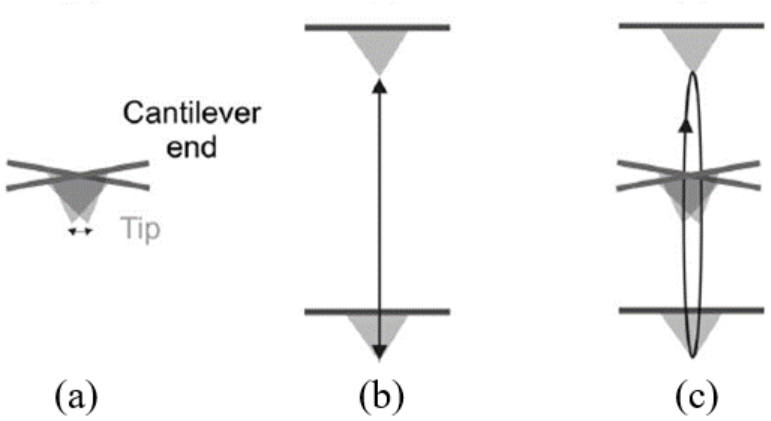

Figure 2.7 Cantilever moving in (a) lateral, (b) flexural, and (c) combined modes (Voigt et al. 2009)

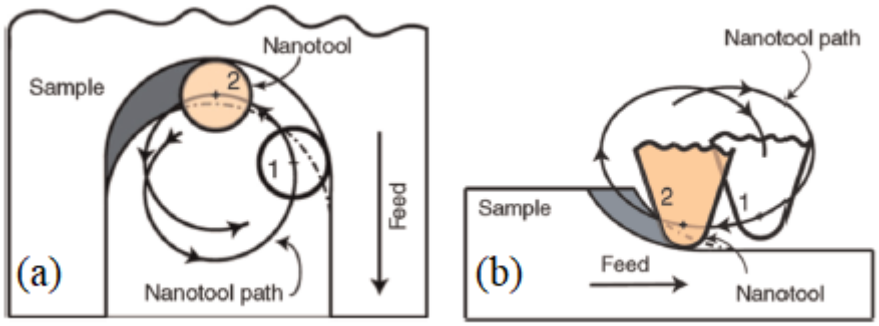

Figure 2.8 (a) in-plane motion (b) out-of-plane motion (Gozen and Ozdoganlar(2010)

2.5.1 Advantages of VANM over conventional nanomachining

To better understand the impact of the vibrations' amplitudes and frequencies on the process of VANM on single crystal copper, Zhu et al. (2016) conducted a molecular dynamics (MD) study of such a process. Where the authors concluded that the higher the frequency of the vibrations is, the smoother the surface is. This observation was explained due to the increased number of instances where the tip presses the material, causing less waviness within the groove. Consequently, higher vibrational frequencies were found to create more dislocations, making it easier to deform the copper specimen. Authors also concluded that using higher frequency vibrations resulted in reduced tangential forces on average and hence less energy, prolonging the tip's life.

Yan et al. (2007a) attempted to address some of the issues that face conventional AFM-based nanomachining issues, such as low repeatability of positioning and nonlinearity, by utilising a CNC machine tool-like system but at the nanoscale by using a setup that relied on the motion of the stage rather than the tip itself. A diamond tip was used to nanomachine a 1 um thick copper film positioned above a silicon substrate. The nanomachining never exceeded 200 nm; hence the effects of the silicon material were safely ignored.

For instance, Figure 2.18 below demonstrates the difference in grooves created due to changes in directions. Both the width and depth of grooves changed with the change in the direction, although the applied normal load of 30 nN was applied equally to all.

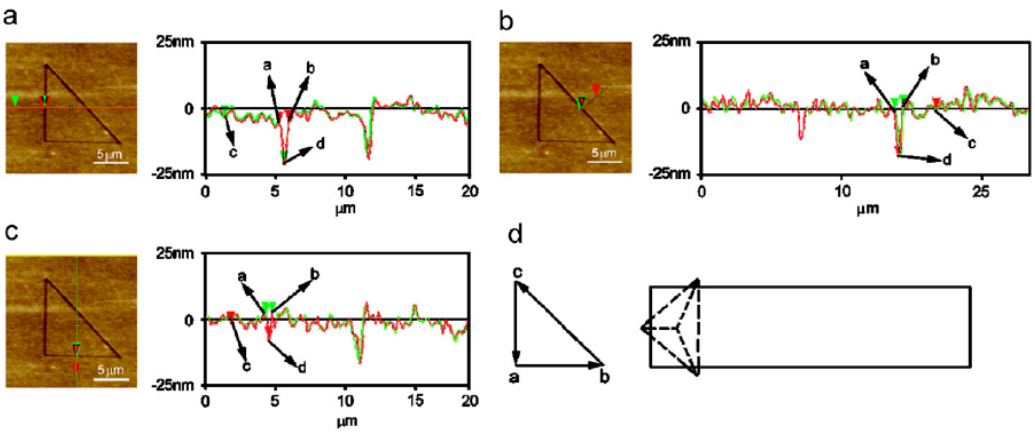

Figure 2.9 Impact of machining direction with (a) vertical (b) diagonal (c) horizontal motions and (d) the probe layout Yan et al. (2007a)

Authors attribute these changes to two main factors; the fact the tip is not axisymmetric in addition to the normal load decreases along the long axis of the cantilever compared to its perpendicular for example. The change in forces due to changes in direction was also analysed and proven in Al-Musawi et al. (2016).

Meanwhile, Figure 2.19 (a) shows a positive correlation between the load and depth as to be expected. As for the material. Finally, increasing the feed as Figure 2.19 (c) shows decreases the depth during nanomachining.

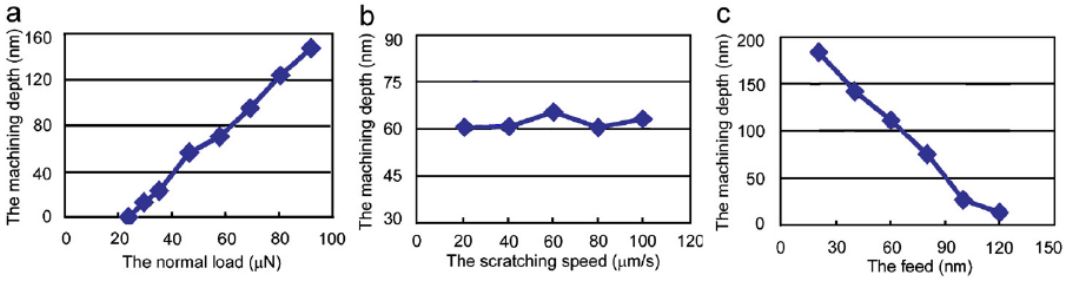

Figure 2.10 How the machining depth is affected by (a) the normal load, (b) scratching speed as well as (c) the feed Yan et al. (2007a)

In addition to improving repeatability and reducing the nonlinearity, the range of the machining was also improved for both 2D and 3D structures.

Additionally, Li et al. (2017) compared conventional grinding (CG) with ultrasonic vibration-assisted grinding (UVAG) for the nanomachining of SiC ceramics. The authors identified multiple stages of material removal, starting with chip-less plastic deformation, then ductile removal, followed by brittle-to-ductile transition, and then finally brittle removal. These stages progress with the increment of force applied. The elastic-plastic transition was also identified using the Hertzian contact theory. Comparing the CG and UVAG, it was proven that using UVAG resulted in better surface quality and less deep subsurface damage. Surface morphology scanned using an SEM was the criterion to differentiate whether the deformation was ductile or brittle.

Similarly, Zhang et al. (2016) reviewed several vibration-assisted micro and nanomachining methods. In the mentioned paper, the authors discuss both linear vibrational cutting (LVC) as well as elliptical vibration cutting (EVC) while also discussing cases of when to and when not to resonance vibrations in the latter.

Improvements achievable when utilising vibrations during machining include allowing for additional lubrication. Reduction in rake face's friction allows for an enhanced shear deformation and a reduction in the chemical interactions, diffusion and adhesion between the cutting tool and the machined material. They also reference studies that proved that using such technology reduces the cutting forces required, tool life longevity, a more stable cutting process in general and a much better surface finish. The burr generation is also reduced when utilising vibrating tools.

The authors emphasise that when using LVC, special care should be taken so as not to allow the cutting edge to interfere with the cut surface as it retreats backwards; hence the design must consider and precisely adjust the motion of the tool as it vibrates. Discarding such detail causes the sharp and brittle tool to be chipped, caused by the generation of tensile stress over the flank face.

Explaining why vibrating the cutting tool is beneficial, the authors mention the fact that due to the cyclic nature of the movement of the tool, its tip will contact a finished surface that was cut in the earlier stroke and, at the same time, push away chips as it moves to cause the chips to be smaller when compared to conventional methods. Hence, the real depth of the cut is quite narrow when

compared to the nominal one. This, in turn, results in an achievable depth of cut smaller than the critical ductile machining threshold causing an improved nominal critical depth of cut in the ductile machining mode of brittle material.

Deng et al. (2016) used ultrasonic vibration-assisted nanomachining relying on AFM tips to create 3D patterns in polymethyl methacrylate (PMMA). The motion the AFM tip followed was circular in the XY-plane as well as ultrasonic motion on the z-axis (perpendicular to the plane of the sample). The authors concluded that the XY vibrations dictated how the width of the machine features came to be, whereas the vertical vibrations, feed rate and setpoint force influenced the depth.

Kong et al. (2016) used a similar set-up as Deng et al. (2016) and had the same conclusion regarding what influences both the width and depth. However, the authors expanded by creating a semi-empirical model to predict the depth during the machining of PMMA.

They explain that the scratch force is on feature dimension where is the setpoint force and is threshold contact force that depends on the characteristics of the machined material as well as the dimensions of the AFM tip and is the least amount of force required to machine certain materials, is a feature dimension, and is the efficiency of the tip's ability to machine a certain material.

Kong et al. (2017) expanded their work by using a discrete voxel method (Figure 2.20) to approximate the material removal rate. However, this study still relied on empirical models to analyse the forces. An AFM tip with a 30 nm radius semi-sphere was used in the study, and machining features inherent in nanomachining, such as the tip bluntness and the negative rake angle, were considered. The depth of cut, meanwhile, was small than the 30 nm tip radius during the circular vibration process. However, given how complex using 3D voxels is, the study used a model with 60 x 60 x 60 voxels with 1 voxel = 1 x 1 x 1 nm.

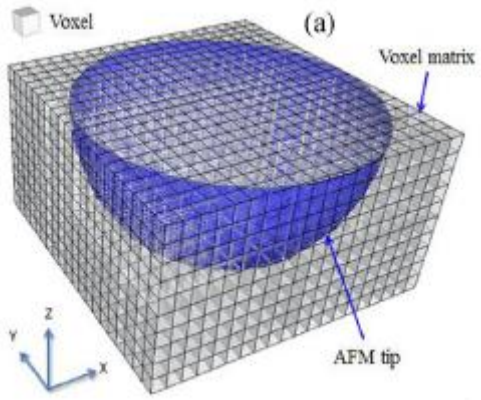

Figure 2.20 Voxel matrix of AFM tip within the PMMA substrate. The overlapping of volumes indicates material removal Kong et al. (2017)

Their model accurately predicted the material removal rate when the machined depth and width were given. Their previous study relied on the setpoint force and the planar vibration amplitudes. They also used a machining force model that correlates forces applied with the feed rate, and like previous models, this one also needed calibration from experimental studies.

Moreover, Kong et al. (2020) studied the effect of the parameters mentioned in their previous works on the wear of the AFM tip during vibration-assisted nanomachining. The condition of the tip was inspected using both SEM images as well as an analysis of the pull-off force, which was found to correlate significantly with the tip shape (see, e.g., Borodich and Galanov 2004 and Carpick et al. 1996), allowing for in-situ estimation of the tip wear without interrupting the process.

The rate at which the tip changed shape was mainly affected by setpoint force and feed rate. In addition, three stages of tip wear were highlighted, the initial tip wear region, the transition region, and finally, the tip failure region.

During testing, a brand-new tip produced channels with uniform depths. However, as the process continued, the radius of the tip kept increasing as it kept wearing, causing the depth of the channels to be shallower caused by the reduced applicable stress induced by the tip, mainly because the force applied is constant. Eventually, when the tip was severely worn, no material removal was observed.

The wear rate at the initial tip region was the lowest and increased until it reached its maximum value at the failure region. Figure 2.20 shows the relationship between the tip condition region and the depth of features.

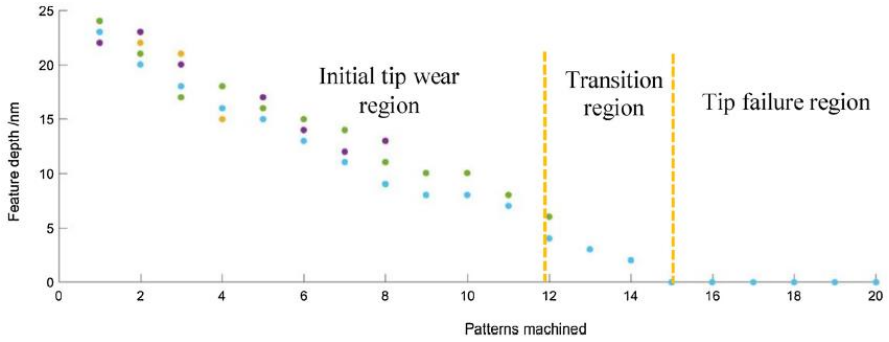

Figure 2.11 The three regions observed during nanomachining depending on the tip's condition Kong et al. (2020)

On the other hand, Figure 2.22 below shows how the pull off force and tip radius correlate.

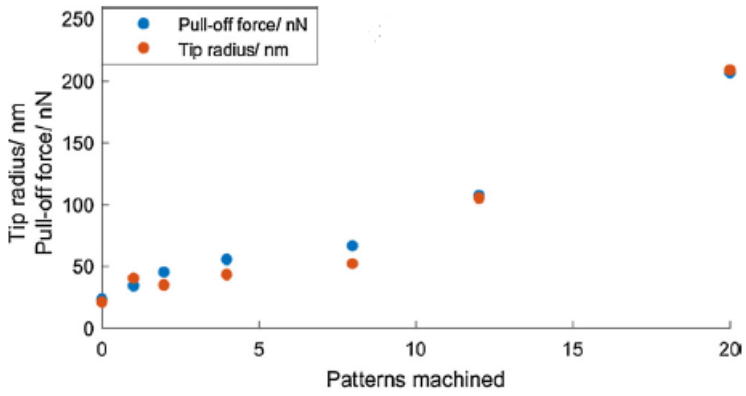

Figure 2.12 Relationship between tip radius and pull-off force Kong et al. (2020)

2.5.2 One-dimensional Vibration Assisted Machining Analysis

This section explains and analyses equations that govern the one-direction vibrations utilised later on (Chapter 5). Isaev (1961) is reportedly the first to

incorporate ultrasonic vibrations in metal cutting. Later, Moriwaki and Shamoto (1991) expanded the work to include 2D elliptical vibrations. Brehl and Dow (2008) studied both one direction (1D VAM) and elliptical (2D VAM) vibration-assisted machining in detail. Figure 2.23 highlights the assumed coordinate system in which the X-axis is the primary cutting direction, Y-axis is the crossfeed direction, and the Z-axis is the normal to the uncut surface of the workpiece.

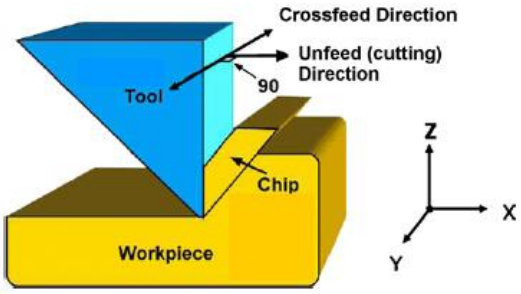

Figure 2.13 One-direction vibration assisted machining (Brehl and Dow 2008)

The cutting tool has a harmonic motion that follows a linear path that is superimposed on the upfeed movement of the machined material. Assuming a value f for vibration frequency follows a critical upfeed velocity lower than which the tool's rake face will continuously break contact with the uncut portion of the workpiece surface, as Figure 2.24 demonstrates.

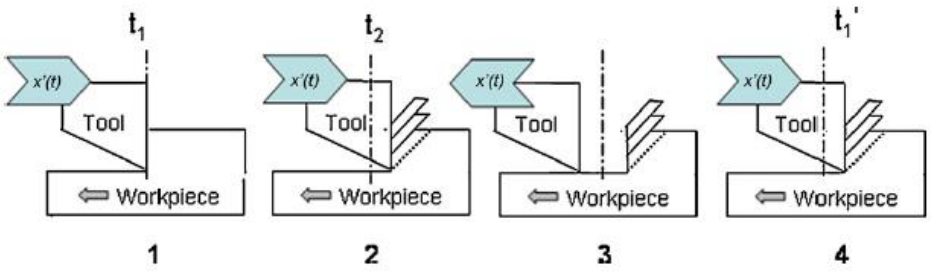

Figure 2.14 Ideal 1D VAM (Brehl and Dow 2008)

Denoting V to be the upfeed velocity, the following equations describe the tool's position and velocity respectively:

$$x(t) = A\ sin(\omega t) + V_t \tag{2.1}$$

$$x'(t) = A\omega\ cos(\omega t) + V \tag{2.2}$$

where, $x(t)$ is the current position and $x'(t)$ is the current velocity. Also, A is the amplitude of the vibration and ω is the angular frequency ($\omega = 2\pi f$). In the two equations above, velocity V has a positive sense in spite of it showing to be moving in the negative direction. Reason for this is that V is the relative velocity between the cutting tool and the machined material (i.e., fixing the workpiece and allowing for the motion of the cutting tool only at a certain velocity v in the X poisitive direction gives the exact relative tool displacement).

The first part of Figure 2.24 shows the cutting tool's velocity $x'(t)$ relative to the work is more than zero. During this, the contact between the tool's rake face and uncut material starts and the cutting process is initiated at time t_1. In part 2, the limit of the one direction vibrations is shown with zero velocity where just after that point the cutting tool will move backwards and t_2 is the time the tool finishes its contact with the worked material. As for part 3, the tool is retracting and $x'(t)$ is on the opposite direction. Finally, part 4 shows the second cycle at which the tool is again moving in the positive direction and is advancing in the workpiece material and t'_1 is the time of the initial contact in the new location. A full cycle is denoted by T, which is equal to $1/f$. The part of the cycle where the tool is cutting is $t_2 - t_1$.

The second equation (2.2) can be useful for calculating the critical upfeed velocity at which the rake face of the tool will never separate from the machined material's surface:

$$V_{crit} = 2\pi f A \tag{2.3}$$

Here, if $V < V_{crit}$ then cyclic interruptions (i.e., detachment from material) of cutting occur at frequency f. On the other hand, if $V \geq V_{crit}$ then cutting is continuous despite the harmonic variation of relative velocity between the cutting tool and working piece. Generally, it is preferable to work under the first regime

(i.e., $V < V_{crit}$) because the VAM advantages mentioned earlier are gained due to the periodic separation between the cutting tool and the worked material.

The intermittent contact the cutting tool and formed chips have can be characterized using two time variables: t_2 is when the tool separates from the machined material and t_1 is when it enters the uncut material.

$$A\sin(2\pi f t_1) = A\sin(\arccos\left(\frac{-V}{2\pi fA}\right) - V\left(t_1 - \frac{\arccos\left(-\frac{V}{2\pi fA}\right)}{2\pi f}\right) \quad (2.4)$$

$$t_2 = \frac{\arccos(-\frac{V}{2\pi fA})}{2\pi f} \quad (2.5)$$

The upfeed increment F_{UP} and horizontal speed ratio HSR can be found from solving equation (2.4):

$$F_{UP} = \frac{V}{f} \quad (2.6)$$

$$HSR = \frac{V}{2\pi fA} \quad (2.7)$$

Where equation (2.6) is used to calculate the distance separating equivalent points on the tool's path during 1D vibrations for successive cycles and is equal to the distance travelled in a single vibration cycle in relation to the workpiece. As for equation (2.7), the HSR represents the ratio between the upfeed velocity of the workpiece and the peak horizontal vibrational speed of the tool. When the HSR ratio is equal or above unity then cutting is continuous as does not detach.

2.6 Use of analytical simulations for nanoscale applications

Given how difficult it is to observe the physical phenomena occurring during nanomachining (i.e., in-situ) due to limitations in microscopy, numerical methods such as Finite Element Methods (FEM) and Molecular Dynamics (MD) can be powerful tools for understanding how the material behaves. However, these methods have caveats due to their computationally demanding nature; they tend to have physical inaccuracies.

Larger scale applications that can do without showing the detailed microstructural changes during plastic deformation use FEM. On the other hand, much smaller and more specific cases, especially the nanoscale using molecular dynamics.

The finite element method solves partial differential equations using up to three space variables. To resolve problems, the method divides complex systems into smaller, simpler ones; each called finite elements. Arrazola et al. (2013) list parameters such as thermo-physical and mechanical as essential for an accurate FEM model to produce valuable results. For anisotropic single crystal materials, a theory for crystal plasticity was created to understand the impact of crystallographic orientation and the activated slip systems in Roters et al. (2010). Meshing plays an essential role in FEM studies, where Niesłony et al. (2015) studied the effect of accurate tool edge representation and emphasized its impact on the simulation outcome.

Regards for Molecular Dynamics (MD), which was first utilised by Osaka University and the Lawrence Livermore National Laboratory according to Shaw (2005). In addition, Shimada et al. (1993) conducted one of the earliest nanocutting studies of single crystals using molecular dynamics.

For example, Honeycutt and Andersen (1987) analysed the dislocation evolution and microstructural changes of tested materials using what is known as common neighbour analysis. Also, Stukowski et al. (2012) used a dislocation extraction algorithm and the displacement vectors module in the Open Visualization Tool OVITO.

When using molecular dynamics, one of the most important aspects that dictate the simulation's accuracy is the potential function used. To address this issue, Oluwajobi and Chen (2011) used three of the most commonly used potentials: Lennard-Jones potential, Morse potential as well as the embedded atom method. This study simulated nanoscale cutting of copper using a diamond tool. They found that due to its enhanced metallic bonding description, as well as exhibiting the least variation in cutting forces, the embedded atom method was seen as the best alternative. As for the interaction between a diamond tip and

silicon, the analytical bond order potential proposed by Erhart and Albe (2005) is commonly used.

Given that the FEM models are more suitable for relatively ‘larger scale phenomena such as temperature in the cutting region and cutting forces, and MD models are for more ‘smaller scale’ phenomena such as defect evolution, several multiscale simulations were conducted to deal with the gap present between the two models such as the work done by Sun et al. (2006) and later by Pen et al. (2011) for nanocutting of single crystal copper.

In this thesis, studies that use molecular dynamics, finite element methods or both at the same time are used as a valuable source of information for understanding phenomena that state-of-the-art microscopy does not have the capabilities to investigate thoroughly.

2.7 Summary

This chapter discussed the history, original use, advantages over other microscopy techniques, and the various applications of the atomic force microscope. In addition, the components of the AFM and how it works, including operation modes, were also analysed.

Following that, the cutting and chip formation process are studied—factors impacting whether continuous or discontinuous chips are mentioned. Then, a few renowned conventional macroscale theories that explain the cutting process are discussed, each with its advantages and shortcomings.

Nanoscale indentation and machining are afterwards discussed. In the nanoindentation section, both amorphous and crystalline materials were mentioned, and the impact of crystalline orientation on the plastic deformation. Also emphasised was the importance of dislocation nucleation in applications at such shallow indentation depths. Schmid and non-Schmid factors, on the other hand, were found to be significant when varying temperatures were considered.

As for nanomachining, the four regimes observed during nanomachining with gradually increasing applied force were discussed. The effect that the minimum uncut chip thickness on the process and especially on dead zones were emphasised. The length of the cut, wherein increased lengths were reported to cause discontinuous chips and the cutting speeds inverse impact surface quality with higher speeds.

Next, stagnation zones or dead zones, which play a critical role in the nanoscale cutting processes by acting as an additional cutting edge, were studied. The subsection starts with the macroscale indentation of various materials. It was found that dead zones act as additional tip reducing the impact of the original tip's shape as indentation proceeds. Also reported was the inability of force-displacement curves to predict the dead zone's behaviour. As for stagnation zones during macroscale cutting, it was reported that negative rake angles are responsible for creating such zones; the same did not apply to positive rake angles. Also reported was the inverse relationship between the dead zone's size and chip formation, wherein the dead zone shrinks as more material detaches the workpiece.

Due to the uncut chip thickness (UCT) being in the range of the minimum UCT at the nanoscale, dead zones play a significant part in the nanomachining processes. However, shearing and ploughing are dominant when the UCT is significantly smaller. Stagnation in front of the cutting tool occurs due to either a stagnation point or a stagnation region. The latter is discussed more in research with its behaviour affected by tool shape, cutting speeds and others. This stagnation region had a stable relative velocity and helped protect tips from wear. Stagnation regions during nanocutting of silicon consisted of phase transition, which explains the ductile behaviour of silicon at such a scale.

Depending on the motion, vibration-assisted nanomachining (VANM) can be one- or two- dimensional (i.e., one direction or elliptical). The cyclic motion provided enhanced surface quality with reduced force requirements. Also, due to the UCT effect and non-axisymmetric tips, such a process is highly affected by the cutting direction. Another improvement was in the enhanced repeatability and linearity. However, it was reported that care should be taken when one direction

vibrational cutting is used, ensuring detachment is guaranteed during each cycle. Otherwise, the advantages of VANM would not be ensured. The impact of tip shapes and wear on this process were discussed.

Following that, values necessary for choosing VANM parameters during testing were analysed. Critical upfeed velocity, for instance, is necessary to assure material detachment during each cycle, requiring a minimum frequency and amplitude for the vibrations utilised. Upfeed increment and horizontal speed ratio are also crucial for parameter determination and analysis after the testing is done.

Analytical models give great insights that complement theoretical and experimental work at the nanoscale; hence Finite Element Methods (FEM) and Molecular Dynamics (MD) are analysed. The difference between each, the advantages, and the limitations were discussed.

The theoretical framework under which material behaves at the nanoscale, specifically the significance of dislocation nucleation that was discussed in this chapter, is explained in detail in the next chapter.

The advantages of vibration-assisted nanomachining of copper over conventional nanomachining are well established; however, the impact of varying only the frequency or amplitude is not well established yet. When discussing vibration-assisted nanomachining, most research mainly focuses on changing the frequency alone, with fewer studies considering amplitude by itself. Consequently, the impact of changing vibrations on two different cutting directions is yet to be fully investigated, especially when a non-axisymmetric three-sided pyramidal AFM tip is used.

Chapter 3

Theoretical Background

This chapter investigates the theoretical framework that explains material deformation at the nanoscale. The main section of this chapter categorises the material into four size scales: atomic, nano, micro and macroscales. Each of these size scales has its defining characteristics. Given that the DSI and nanomachining depths in this thesis's experiments range between 30 nm and 200 nm, the research evidence stresses the framework for the nanoscale and that it differs from other size scales. Strain gradient plasticity, widely used to explain plasticity at miniature scales, is discussed in detail. It does not apply to the nanoscale of this thesis's experimental work but to the larger microscale. Moreover, the concept of dislocation nucleation, mentioned in chapter 2, is explained due to its significance in the nanoscale. The thermal effects on plasticity follow this.

Also, a review of some classical theories that explain material deformation is laid out. Moreover, hardness is essential in indentation, cutting, and scratching surfaces.

In addition, analyses towards the end of the chapter are used to confirm the proposed theory within the nanoscale section, specifically the dislocation nucleation part. This is based upon an experiment similar to the one done in chapters 5 and 6 as both were done using the same equipment under the same cutting conditions (albeit without induced vibrations).

3.1 Size-scales categorisation

The concept of Nanotechnology was first mentioned in 1974 by Taniguchi during the international conference on production engineering. Now, this concept is the basis for what is referred to as ultra-precision engineering. In addition, according to the British Standard, a nanomaterial is a material with at least one dimension not exceeding 100 nm. So, this section includes a review not only limited to the external dimensions of a particular material but also the internal structure of a given material.

Considering the material's size scale is important when evaluating its characteristics, such as strength. For example, Polonsky and Keer (1996a)

analysed the scale effect theoretically and by simulation and concluded that the asperities at scales as small as the material's characteristic microstructural lengths could withstand loads higher than the classical macro-asperities contact theory predicts.

Also, it was assumed that the size of the indenter did not affect how the material reacts (deforms) and that classical continuum mechanics sufficed to explain phenomena at the bulk, macro, micro and nanoscales. However, since the models of the classical continuum theory do not contain length scale parameters, they cannot predict how the material behaves at smaller scales giving significant deviation between theoretical and experimental values up to three times difference. The improved material characteristics (i.e., hardness) can be explained by the decreased probability of facing defects as the material volume decreases (Bhushan and Nosonovsky 2003).

Material size-scale (spatial domain) can be categorised into four groups each reacting differently to applied loads and hence deforming plastically in different manners as in the work of Horstemeyer et al. (2001) which used the embedded atom method (EAM) on nickel single crystal sized between 102 to 108 atoms:

1. Nanoscale up to 20 nm
2. Submicron scale (or sub-micron) 20 nm to 2 μm
3. Microscale 2 μm to 300 μm
4. Macroscale above 300 μm

The authors emphasise that the nucleation of dislocations dominates the first two regions. Meanwhile, the authors refer to strain gradient plasticity (Fleck et al. 1994) as being dominant in length scale 3. Figure 3.1 below shows the stress and strain response, and it is apparent that the yield stress elevates as size scales shrink.

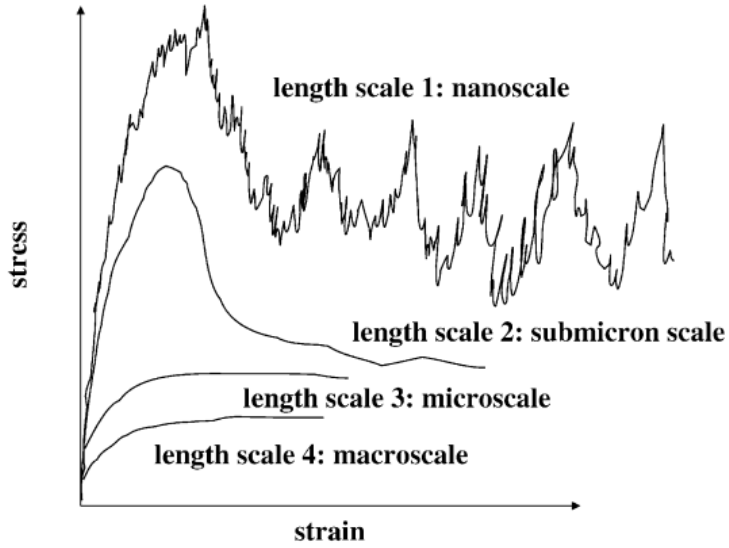

Figure 3.1 Stress-strain curves for multiple length scales Horstemeyer et al. (2001)

Borodich and Savencu (2017) in turn categorised the material in a similar matter but with different ranges when applying their B-S model on multiscales that have different physical-chemical mechanisms, with each range reflecting phenomena specific to the corresponding characteristic length l, as follows:

1. **Atomic-scale** with characteristic length less than $1\,nm$, concerning chemical interactions between surfaces.
2. **Nanoscale** with its characteristic length ranging $1\,nm \leq l \leq 1\,\mu m$ encompassing van der Waals surface interactions.
3. **Microscale** concerning lengths ranging between $1\,\mu m \leq l \leq 1\,mm$ covering asperities' mechanical interlocking.
4. **Macroscale** applicable to lengths exceeding 1 mm that includes the material's bulk behaviour coupling micro-asperities together

However, most research uses the latter categorisation by Borodich and Savencu (2017) rather than the one used by Horstemeyer et al. (2001) for the first two size scales. Though, any categorisation is arguable –in terms of naming and size range- given the disparity in the research community.

Most researchers agree that discrete dislocation mechanics are most suitable for nanoscale plasticity analysis—strain gradient plasticity for the microscale and classical continuum mechanics for the macroscale.

The machining process proposed in this thesis will include depths not exceeding 200 nm; hence very localised. For example, a study by Yan et al. (2007b) that analysed a copper film with 1 μm thickness deposited on a silicon surface neglected the effect of the silicon substrate due to the machining depth not exceeding 200 nm. This assumption can be corroborated by Zhang et al. (2015) with a nanoindentation study that concluded that regardless of the indentation depth or the crystal orientation, the plastically deformed area was around four times larger than the indenter contact area.

Given that the main objective of this thesis is to understand the deformation mechanism occurring during the nanomachining of a bulk-sized single crystal of copper, a broader understanding of what impacts the deformation process is needed and is explained in this section. Grain size (for atomic and nanoscales), workpiece material (mostly silicon and FCC metals), and workpiece dimensions (nanopillars, thin films, and bulk-sized materials), in addition to thermal effects, are considered.

Some researchers use the terms ‘nanoindentation’ and ‘nanoscale’ to refer to applications on the larger microscale. So, caution was taken when reviewing research containing such terms as what size and length scales are used.

3.1.1 Atomic Scale

The atomic scale is the most challenging scale of the four mentioned to investigate. Mainly because of limitations in the state-of-the-art microscopy’s resolution. Hence, research at this scale is limited to grain size effect rather than materials with external dimensions or most machining features at such scale.

While investigating the grain size and its effect on how a material deforms, Greer and De Hosson (2011) argue that grains sized less than 40 nm engage plastic deformation mechanisms, including grain boundary sliding, absorption at

grain boundaries and partial dislocation emission, as they cannot accommodate multiple lattice dislocations. At 20 nm or less sized grains, an Inverse Hall-Petch Effect (IHPE) occurs where the material softens with decreased grain size. The activation of grain boundary causes this assisted deformation, as Figure 3.2 shows.

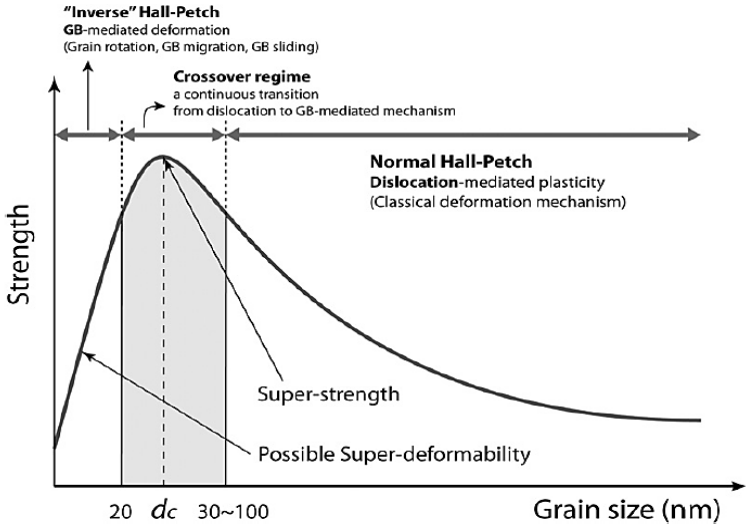

Figure 3.2 Changes in polycrystalline material strength with change in grain size (Greer and De Hosson 2011)

Also, Carlton and Ferreira (2007) attempted to explain this size scale where the material becomes highly deformable due to the IHPE. Their study discussed a 'critical grain size' below the material is super soft and above the Hall-Petch effect slope transitions to its usual behaviour. Multiple studies such as Nieh and Wadsworth (1991) and Eckert et al. (1992) designated 10 nm as the critical grain size at which transition to IHPE occurs. To explain the IHPE, Carlton and Ferreira categorized the models proposed to explain it into four groups: dislocation-based, diffusion-based, grain-boundary-shearing, and two-phase-based models.

Beyond the grain size considerations, applications at this scale are still limited (see. Fang et al., 2019). Nonetheless, prominent semiconductor manufacturers are already making CPUs with 5nm Fin Field-Effect Transistor (FinFET) technology. However, fabrication methods in such applications are unsuitable for explaining plasticity at such a size scale. Hence, plasticity analyses at this scale are limited

and are still confined to analytical studies that are difficult to complement with experimental work due to limitations mentioned earlier.

3.1.2 Nanoscale

As for the nanoscale, Koch (1999) referred to nanocrystals with grain sizes smaller than 100 nm as ‘ultrasmall’ and argued that they have dramatically improved properties than grains sized 1 μm and above, which he referred to as conventional sized grains.

Nevertheless, Koch does, later on, discuss hardness measurements and highlights a change in behaviour in nanocrystal grains smaller than 20 nm, where he discusses a change in the Hall-Petch slope similar to what is in Figure 3.2 and around the 20 nm from positive (Hall-Petch) to flat (no dependence) to a negative slope (Inverse Hall-Petch).

On the other hand, regarding indentation depths, Huang et al. (2006) developed a model that characterizes the indentation hardness-depth relationship that considered the limitation of the groups’ previous model (Nix and Gao 1998); the details of both studies discussed in the microscale section. However, in the former study, the authors emphasize that their model, which relies on the strain gradient plasticity, should not be used if the indentation is in the smaller nanometre order (around 100 nm) as discrete dislocation occurrences dominate scattering the results of the hardness tests that rely on for their model (i.e., their model is less reliable at the smaller mentioned scale).

3.1.2.1 Deformation Mechanism

This sub-section discusses the mechanisms responsible for the plastic deformation at the nanoscale. Due to deformation localisation, it is argued that what applies to nanostructured materials also applies to nanomachining of bulk-

sized ones. This argument is supported by the research reviewed in the previous chapter and the analyses at the end of this chapter.

Berghezan and Fourdeux (1959) used the TEM to understand the deformation of an aluminium specimen better. This study was aimed at a better understanding of the deformation mechanism, and in which they were able to visually observe dislocation nucleation, slip propagation, and then accumulation until rupture of the thin specimen. However, due to the use of microscale specimens, they could also understand the role of grain boundaries. They discovered that they act as donors and acceptors of dislocations.

Although referring to it as ‘Microcontacts’, Polonsky and Keer (1996a) were one of the earliest to analyse integrating a scale factor in elastic-plastic contacts and, at the same time, discuss the nucleation and the movement of discrete dislocations. They also emphasise its applicability on a scale too big for atomic simulations and too small for classical continuum mechanics.

Extrinsic size effects on nanoscale plasticity

Referring to the material at this scale as "ultra-strength materials", Zhu and Li (2010) published a review that explains why nanostructured materials (e.g., nanoparticles, nanowires, thin films…) have great strength reaching up to a significant fraction of the ideal strength (zero temperature and defect-free materials). They emphasized that strengths at this scale transcend "high-pressure physics" effects as nanoscale materials can sustain stresses much higher than conventional materials.

According to Sieradzki et al. (2006), yield strength at such small scales is highly dependent on the probabilistic nature of dislocations nucleate. Given the limited number of atoms existing at the nanoscale, this also limits the dislocation sources possible so that when a source comes up when yielding develops, it can be measured as demonstrated in the strain bursts in Figure 3.3. When estimating a sample's yield strength, the statistical dispersion of source strengths leads to the problem of yield strength variation depending on the location.

It was found that material strength has an inverse relationship with sample dimensions, referred to as extrinsic size effects by Greer and De Hosson (2011). For example, in an experiment on a single crystal, Au nanopillars had around 50 times higher strength than the bulk form when uniaxially compressed (see., Greer et al. 2005). An additional size effect has also been reported, external geometric size in single crystals, wherein the strength of the material decreases with the sample size increase. In the work of Greer et al. (2005), experimentation on single crystal nanopillars had intermittent discrete strain bursts in the stress-strain response shown in Figure 3.3 below. This suggests that dislocation starvation occurs where mobile dislocations are annihilated to the free surface, forcing the creation (nucleation) of new dislocations to sustain the new increasing loads.

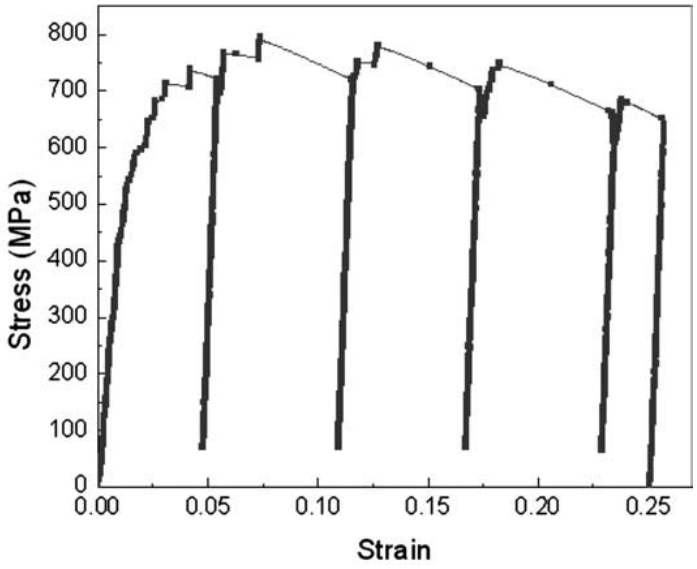

Figure 3.3 Stress-strain diagram of the compression of Au nanopillars (Greer et al. 2005)

A group of researchers (Kiener et al. 2008) reported the ability of nanowires to sustain almost theoretical fracture strength (Brenner 1958) with values surpassing ones stated for microwires. The tests displayed stresses ranging from 1-7 GPa at which the nanowires fractured perpendicular to the loading axes, and due to the lack of dislocations, the fracture was completely brittle. This, in turn, indicated that there are fewer dislocations; hence the stronger material is present.

Also, Rinaldi et al. (2008) studied nano-sized-crystals in Ni pillar-sized samples impact on the yield strength based on pop-in events. When a case of compressing nanopillars is considered, a series of events are to be expected; a dislocation nucleating at the weakest link; this dislocation will annihilate to a free surface or a nearby grain boundary (at this scale, it is difficult for a dislocation to multiply), given that no changes happen to the geometric configuration it is most probable that the same source will keep on nucleating dislocations. This cyclic process of nucleation and then annihilation of dislocations is the reason for the strain bursts highlighted in Figure 3.3.

Moreover, Jennings et al. (2010) compared two cases of copper nanopillars, one manufactured using focus ion beams (FIB) and the other without FIB. They found that both have a similar initial dislocation density.

To explain the increase in strength with the decrease in size, two theories that explain the deformation mechanism were introduced: single-arm source theory and dislocation starvation followed by surface nucleation. The former applies to pillars of micron sizes (above 500 nm), which is more appropriate to be discussed later in the microscale section. On the other hand, the latter proposed by Greer et al. (2005) and Greer and Nix (2006) applies to what is described as ‘deep in the sub-micron regime.

Figure 3.4 compares three specimens having varying diameters and highlights the inverse relationship between extrinsic size and maximum stress.

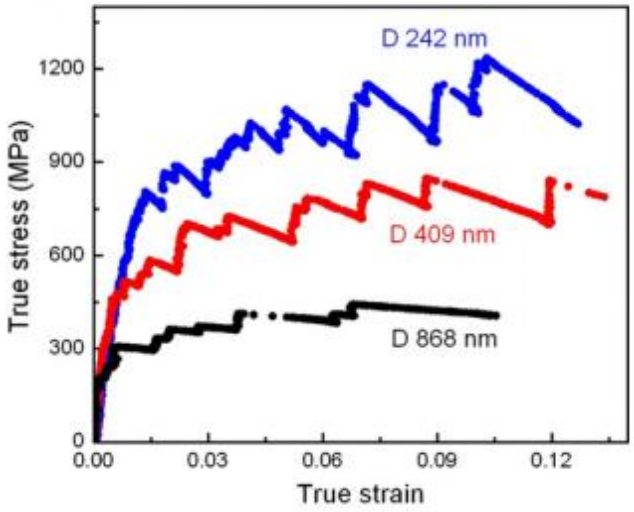

Figure 3.4 compression accompanied by compressive stress versus strain (Greer et al. (2005)

3.1.2.2 Nucleation of dislocations

Considering dislocation nucleation, Li (2007) did extensive analyses on defect nucleation mechanisms at the sub-micron scale. At the most basic level, Li describes the nucleation of defects as a result of 'bond breaking and reformation events' and are 'driven typically by mechanical strain and electronegativity differences' according to the author.

Li also compared the ideal bulk shear strength at zero pressure (using density functional theory in Ogata et al. 2004) to maximum shear stresses extracted using nanoindentation experiments with copper attaining 272% higher experimental values than the ideal ones 6 GPa (see., Wang and Lu (2006) and 2.2 GPa (see., Ogata et al. (2002). Copper and all other materials mentioned by Lu have similar magnitudes between ideal and experimental. Using Li's arguments and the experimental work of Elkaseer and Brousseau (2013) a proof will be provided that this applies also to nanomachining using AFM tips towards the end of this chapter.

Dislocation nucleation and mobility dictate how defects behave. However, contrasting the two is not a straightforward process so considering them as a

continuum between the two can useful. Defect nucleation is when a defect forms its 'individual, independent identity' while mobility the translation of it while keeping the same identity.

Frank-Read dislocation generation demonstrates the nucleation because dislocation loops that are free and separate form with every source operation. In order for those loops to exist there must be a minimum athermal stress equal to $\tau_{ath} = G\mathbf{b}/d$ where G: Shear elastic modulus, $\boldsymbol{b}$: Burgers vector, d: distance separating two pinning point (i.e., length scale).

Lu et al. (2004) investigated highly pure Cu with nanoscale growth twins made using pulsed electrodeposition with -as apparent in Figure 3.5 below- tensile stress exceeding 1 GPa which is close to the material's ideal strength.

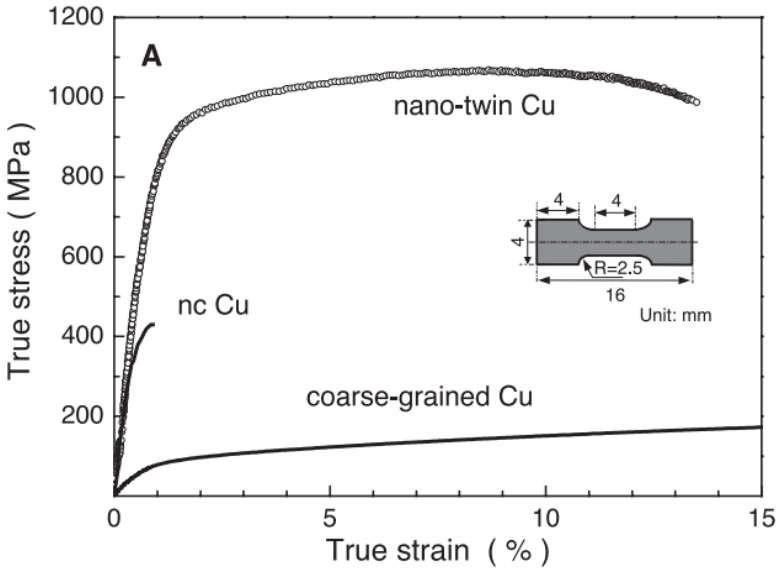

Figure 3.5 Stress-strain curve of nano-twin Cu compared to nc Cu and coarse Cu (Lu et al. 2004)

To explain this great increase, when observing Figure 3.6 it possible to notice a zigzag shape which suggests that the plastic deformation occurring in that zigzag manner due to the need for the active slip system to jump from one lamella to the other. As proof for the claim made earlier, measuring strain rate sensitivity the activation volume was found to be $12b^3$ to $22b^3$ which indicate that interface mediated slip motion reactions to be the rate-limiting process. Another

explanation can be given simply stating that new dislocations have to be nucleated at each twin interface for it to satisfy the Burgers vector conservation.

However, for this study nc Cu gives more representative strength values. Nevertheless, the nano-twin Cu enables for a better understanding of the dislocation nucleation process.

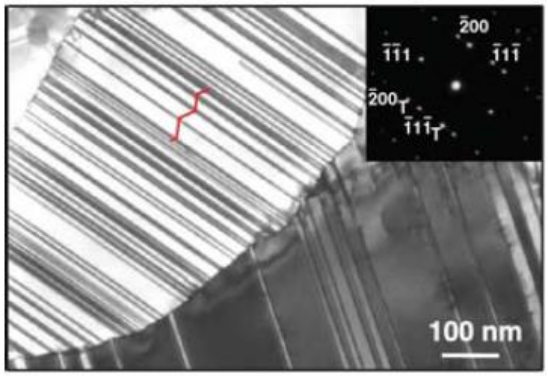

Figure 3.6 Transmission electron microscope images of the nano-twin Cu (Lu et al. 2004)

Types of nucleated dislocations

With regards to the types of dislocations that nucleate, two types are known, either homogeneous dislocations or heterogeneous dislocations. According to Bei et al. (2008a), homogeneous dislocations occur as full loops within the bulk of the material whereas heterogenous ones occur as a half or even a quarter of a loop and nucleate surfaces and edges. In the study, the authors were able to distinguish the difference between the two types based on the experimental theoretical strengths. It was found that the critical stress needed for a full dislocation (i.e., homogenous) is higher than its partial counterpart (i.e., heterogeneous).

During nanoindentation, dislocation nucleation is expected to happen within the solid because of the nonuniform nature of the stress where the maximum resolved shear stress occurs below the contact.

In addition, Nawaz et al. (2017) investigated the elastic-plastic deformation mechanisms of single crystal 6H-SiC using DSI techniques. The authors utilised

a Berkovich indenter with a 160 nm radius at depths less than 30 nm, and 96 a nm radius one when the depth is between 30 nm and 60 nm. The study analysed the impacts of loading rates on the maximum shear stress as well as the critical pop-in loads and displacements and concluded that phase transformations are improbable. They also used the Nix-Gao models to study the important size effects and the depth independent hardness. In addition, Johnson's cavity model was used to estimate the indentation size during plastic deformation.

Elastic-plastic regions were realised using both Hertzian contact models in addition to Johnson's cavity model. A 13 GPa tensile strength and a 31 GPa cleavage strength were estimated using an indentation load of 540 μN, and they proved that the elastic-plastic deformation was not caused due to tensile stresses but rather due to pop-in events. Finally, the critical resolved shear stress was found to be near theoretical levels, with 22 GPa and 25 GPa, respectively. By comparing the shear results to other research works, it can be confirmed with confidence that homogenous dislocation nucleation is the reason for the plastic deformation rather than already present dislocations.

Zhu et al. (2004) developed a model that predicts defect nucleation or more specifically homogenous dislocation nucleation occurring in the nanoindentation of copper described as strain localization caused by elastic instability of a perfect crystal. Their model relied on hyperelastic constitutive relation with the Cauchy–Born hypothesis that enabled them to study dislocation nucleation at length scales larger than atomic dimensions. The model incorporated anisotropy and the effects of nonlinear elasticity of crystals. A slow variation in the deformation field was imposed by a tip with 50 nm radius.

However, this simulation can be considered as a 'mechanical threshold' because it incorporates an atomically flat surface allowing for a homogenous dislocation nucleation inside the crystal and moves towards the free surface in contrast to heterogenous dislocation creation from surface steps that requires much less energy to break bonds.

Another estimate made in this study that idealizes the material above what it really is would be the 0 K temperature approximation hence no thermal effects considerations. Nonetheless, a study by Xu and Argon (2001) played down the

effect of thermal motion when compared to energy barriers in ideal crystals of Au, Cu, Al and Si.

For an ideal case of perfect crystal to deform, dislocations have to nucleate in either the surface and/or the bulk of the material subject to the crystal's geometry and how it is loaded (see., Zhu and Li 2010). Several atomistic studies Li et al. (2002) and Gouldstone et al. (2007) realized that homogeneous dislocations nucleate within the bulk of perfect crystalline materials.

When only athermal factors are considered, dislocation nucleation is caused by elastic instability of the lattice when enduring huge shear stresses (i.e., when nucleations' energy barriers are broken). The criterion or threshold used to characterize instantaneous nucleation, or the movement of dislocations is the critical resolved shear stress (CRSS).

However, because CRSS values depend on the stress state rather than shear when homogeneous dislocation nucleation, it is preferable to consider single valued CRSS in order of magnitudes only (see., Tschopp and McDowell 2007 Zhu et al. 2004).

To solve this limitation, the theory of non-linear hyperelastic instability theory is used to determine the threshold of the case mentioned earlier. These analyses can take account of the impact of various stress components, elastic softening when large deformations occur and crystal anisotropy.

The criterion (atomistic based) used in the hyperelastic instability is known as λ-criterion. According to Li et al. (2002), this criterion balances the enormous stress within large shears with the modulus of elastically softening tangent. The determination of this criterion help with the prediction of critical nucleation conditions at 0 K temperature (see., Van Vliet et al. 2003 and Zhu et al. 2004). However, this criterion has its own limitations such as location-dependency (see., Miller and Rodney 2008 and Delph et al. 2009).

Pre-existing dislocations

Considering pre-existing dislocations, Shan et al. (2008) experimented nickel pillars that had high density of initial defects and can -using only mechanical stress- be made defect free. This process is referred to as mechanical annealing that cause the exhaustion of dislocation before they have the chance to multiply creating what is known as dislocation starvation.

In addition, there is evidence by Bei et al. (2008b) and Lee et al. (2009) that unlike plasticity at the macroscale where introducing dislocations to the material helps its multiplication which in turn leads to work hardening, at the nanoscale introducing dislocations (e.g. by pre-straining) will only make the material weaker.

Impact of cyclic loading on dislocation density

Wang et al. (2015) experimentally utilized the notion that dislocations in nanopillars tend to annihilate, hence not affecting the strength of the material by applying cyclic loading on aluminium single crystals.

Referring to the process as “cyclic healing” and then later on as controlled mechanical annealing this group of researchers applied low amplitude cyclic deformation loads at room temperatures and the outcome as Figure 3.7 below shows was a great decrease in dislocation density with no observable changes in geometry. The set-up included a tensile stress test of a nano-sized specimen while being observed using a transmission electron microscope where they concluded that the amplitude, number of and sequence of cycles was what dictated how dislocation motion (annihilation) occurred.

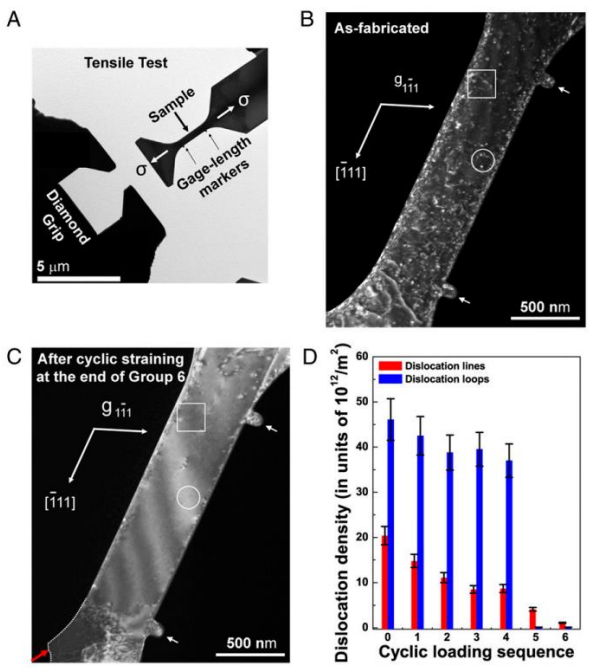

Figure 3.7 Mechanical healing of an Aluminium monocrystal: (A) the experimental setup (B) TEM image before loading (C) TEM image after loading (D) dislocation density changes (Wang et al. 2015)

3.1.3 Microscale

One of the prominent theories used to explain plasticity at smaller size scales is the Strain Gradient Plasticity (SGP). However, it was proven in multiple studies that such a theory becomes less applicable as the size scale shrinks. So, in this sub-section, a review of this theory and proof of its inapplicability for the experimental work of this thesis, which does not exceed 200 nm, are presented.

3.1.3.1 Strain Gradient Plasticity (SGP)

To explain why the material behaves differently at the micro/nano scales, many scientists relied on dislocation movement as the core for their proposed theories. Strain Gradient Plasticity (Fleck and Hutchinson 1993) is a widely accepted theory that explains the size dependence or what is known as the

indentation size effect (ISE). This theory assumes that contact between the indenter and the tested material during indentation is limited to infinitesimal volume. This small volume is the main reason for strain gradients because of the non-uniform stress (and hence strain) created by the indentation (Nix and Gao 1998). Hence, strain gradients are, in turn, responsible for the indentation size effects. So, they developed a theory based on that observation which predicts a "linear relationship between the square of the indentation hardness and the reciprocal of the indentation depth". For the deformation resistance, they used Taylor's relation to calculate the shear strength.

According to the theory, hardening occurs because of:

- Statically stored dislocations associated with plastic strains
- Geometrically necessary dislocations associated with a plastic strain gradient

Meanwhile, dislocations are stored for two reasons:

- Single crystals strain uniformly and do not store dislocations however they accumulate by random trapping i.e., statistically stored dislocations (or geometrically redundant dislocations)
- A gradient plastic strain affecting a crystal causes the storing of geometrically necessary dislocations. Plastic strain gradient is observed due to material geometry (high stress concentration point) or plastic inhomogeneity of the material

Meanwhile, Nix and Gao (1998) also derived an expression the models the indentation size effect in crystalline materials relying on the strain gradient plasticity work (see., Fleck et al. 1994) and using the concept of geometrically necessary dislocations (See., Figure 3.8). Equation below expresses their take on depth dependence of hardness:

$$\frac{H}{H_0} = \sqrt{1 + \frac{h^*}{h}} \tag{3.1}$$

where, H is the hardness at a certain depth h, H_0 is the infinite depth hardness and h^* is the indenter shape dependent length. In the mentioned paper, the authors

stress that the impact of strain gradients becomes more significant when smaller volumes are deformed (i.e., below micron sized indentations). However, they do mention that other factors do play on when the scale is even smaller, and those factors are not related to strain gradients such as thermal expansion mismatch.

Many studies, including Lim and Chaudhri (1999), Kim et al. (2005), Liu and Ngan (2001), Swadener et al. (2002), and Elmustafa et al. (2004), had outcomes that did not agree with the 1998 Nix and Gao equation in the sense that although the hardness does increase with decreasing depth, it does not follow a straight line like predicted by the study as mentioned earlier.

So, Huang et al. (2006) developed an analytical model that overcomes the mentioned limitation based on the maximum allowable geometrically necessary dislocations density. This, in turn, is based on the Taylor dislocation model. The new model degenerates the original Gao and Nix model but at the same time accurately predicts work done by papers that refuted the mentioned original paper. It is mentioned in this study that their model should not be used if the indentation is in nanometres order.

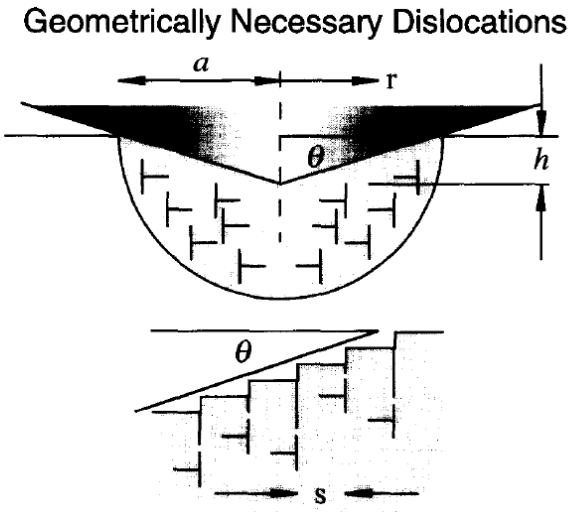

Figure 3.8 Indentation creating geometrically necessary dislocations using a conical indenter (Nix and Gao 1998)

3.1.3.2 Applicability of SGP

With regards to the suitability of where to apply the SGP, Greer and Nix (2005) argue that the Strain Gradient Plasticity theory, although valid, does not apply to all sizes and especially to indentation depths below 100nm. They reasoned that the Nix-The Gao model is continuum based and cannot represent the discrete displacements nucleating in the elastic-plastic transition in mentioned indentation depths. The limitation of the Nix-Gao model can be overcome by relating the plastic deformation with the nucleation of dislocations to explain the discrete displacement bursts when the nanoindentation process starts in single crystal materials.

During nanoindentation, greater strengths are observed. This can be explained by comparing plastic indentation at the nano and macro scales. At the macroscale, dislocations multiply via double cross-slip, as an example which leads to an increase in dislocation density which eventually leads to Taylor-type hardening. On the other hand, at the nanoscale, dislocations travel small distances before vanishing at free surfaces; thus, no multiplication of any dislocations that weaken the material.

The strain gradient plasticity theory authors mention other factors that come into play when smaller scales are considered, as discussed in the previous section. Fleck et al. (1994), for example, in their experimental work used to verify their theory on strain gradient plasticity, used wires of diameters ranging from 20 μm to 170 μm.

Moreover, Borodich (2014), in a review of the relationship between Hertz-type contact problems and DSI of various materials, discussed the applicability of the SGP. Borodich argued that this model is valid only for crystalline materials. He also argued that the bluntness of the indenter might cause opposite relation (see, e.g., Borodich et al. 2003a), i.e., the apparent hardness is increasing.

The Polonsky-Keer effect in which the asperities at the nanoscale do not deform plastically (see., Polonsky and Keer 1996b and 1996c) are necessary to consider. Hence, Borodich and Savencu (2017) suggested approximating the force-displacement diagram from the Lennard-Jones potential as linear and rigid.

In addition, Hutchinson (2000) discussed applying the strain gradient plasticity on experimental data obtained from copper wires with diameters between 12 μm and 170 μm with length parameters ranging from 0.25 to 5 μm. In addition, he also argued that the classical theory could not analyse small sizes due to the lack of a length scale component.

Furthermore, a “large number of dislocations” is discussed in the size scale studied. Hutchinson argued that although microscale analyses are very small for the classical continuum theory, they are too large to be analysed using discrete dislocation theories.

Additionally, Horstemeyer et al. (2001) stressed that for the size scales at atomic and sub-micron levels (i.e., nanoscale), the dislocation nucleation dominates in almost dislocation-free single crystal materials (regardless of strain gradients).

3.1.4 Macroscale

When considering larger size scales such as macroscale, unlike the nanoscale, a significant difference between the theoretical and experimental strengths which are mainly attributed to defects (see., Cottrell 1953). Even in annealed crystals where initial defects are limited, once a deformation initiates, factors such as double cross slip and Frank-Read dislocation sources dominate, making the material considerably weaker.

Hence, in this sub-section, a general review of the classical theories explaining material deformation is done and followed by one regarding hardness due to its significance in indentation and scratching tests.

3.1.4.2 Material deformation

How and what causes the material to deform? One of the earliest to try to explain was Timoshenko, who aggregated his works in the strength of materials into a textbook in 1911 (see. Timoshenko 1911).

Another pioneer was Griffith (1924), who suggested that microcracks and other imperfections existed in all practical materials and are a source of stress concentration. Such microcracks will grow gradually as tensile strains increase until an elastic energy threshold reaches the crack's tip. This energy is enough to satisfy the surface energy required to generate a new surface area following crack growth. By then, crack growth proceeds randomly.

He estimated that the crack-tip stress concentration factor was roughly $2c/w$ (From Figure 3.9). Meanwhile, the elastic energy (per width) at the tip shown in Figure 3.9 (b) is $\pi c^2\sigma^2/E$ in addition to the surface energy of the two areas of the crack $4cT$ (T is the surface energy), which gives a change of energy equivalent to:

$$\Delta U = \left(4cT - \frac{\pi c^2\sigma^2}{E}\right) \tag{3.2}$$

And when allowing for crack growth (as per Griffith's thesis) the plane stress is:

$$\sigma = \sqrt{\frac{2TE}{\pi c}} \tag{3.3}$$

Figure 3.9 below demonstrates how Griffith depicted microcracks as elliptical cracks both inside the material and on the surface.

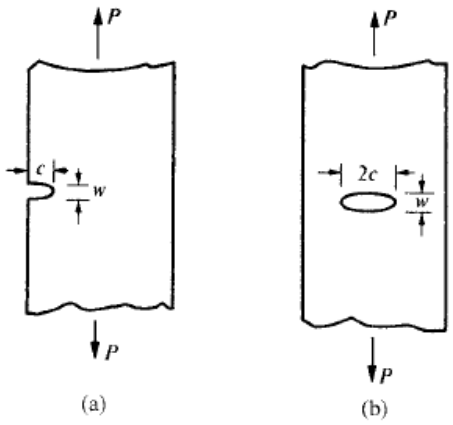

Figure 3.9 Griffith's microcracks: (a) surface crack (b) internal crack (Griffiths 1924)

However, according to Orowan (1950) for quasi-brittle materials, plastic deformation must be considered making the energy responsible for crack growth T_p much larger than surface energy T (i.e., $T_p \gg T$):

$$\sigma = \sqrt{\frac{2T_pE}{\pi c}} \tag{3.4}$$

On the other hand, Irwin (1957) developed what was later known as linear elastic fracture mechanics (LEFM) in which the stress intensity factor (K) was introduced and was experimentally established. This intensity factor highlights the impact of defects present as viewed from a brittle crack growth perspective. And it is defined as:

$$K = \sigma\sqrt{\pi c} \tag{3.5}$$

where σ is the stress of fracture and c is the half length of an internal flaw. Substituting gives:

$$K = \sqrt{2T_pE} \tag{3.6}$$

And K became standardised and is referred to as the 'stress intensity factor' which needs to be calculated using the slopes of the load-deflection graphs of multiple values of crack half lengths (c).

There are three types of stress intensity factors: K_I, K_{II}, K_{III} as Figure 3.10 shows. Where the first represents the crack opening mode, the second perpendicular shear to the crack front and the third parallel shear to the crack front.

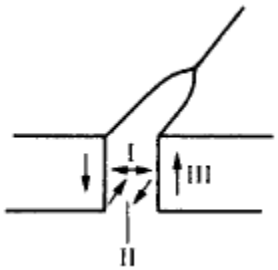

Figure 3.10 Loading modes for the three stress intensity factors (Irwin 1957)

During the cutting of metals, strains accumulated during the formation of steady-state chips are very high, with much experimental evidence that supports the creation of microcracks within the shear plane at stress concentration points and are the main reason for the size effect (i.e., decrease in specific energy when the volume deformed as chips are formed is increased). Also, both microcracks and normal stresses on the shear plane cause the migration of microcracks all over the shear plane when they are formed, welded, reformed, and then rewelded again. This migration of microcracks goes along with the migration of dislocations as the leading cause of the very high strains occurring during the formation of steady-state chips.

3.1.4.1 Hardness

Hardness can refer to multiple things in engineering as it can indicate resistance to flow stress, penetration, wear, scratching or cutting. However, the two dominant ones are the static indentation test (e.g., Brinell, Vickers, Rockwell and Knoop), which includes extracting the load per unit area, and the scratch test (e.g., Mohs hardness test), which in turn tests the capability of one material to scratch the other. The latter compares the scratch resistance of a certain material

versus a standard series of materials, each assigned values ranging from 1 for the softest to 10, which is the hardest (i.e., diamond).

Indentation hardness tests represent the material's resistance to plastic deformation during indentation. The quantity such a test gives is the flow stress at tiny strain values and slow strain rate without frictional considerations.

The most prominent theoretical explanation for what occurs during hardness indentation tests is the slip lone field theory (SLF). This theory suggests that the material below the indenter flows plastically over a region consistent with how much material is moved during the indentation. Beyond this region, the material is assumed to be fully rigid. SLF is a network of maximum shear stress curves. For a flow pattern to be acceptable, it only needs to be consistent when velocities are considered; if this criterion is met, the solution is then considered kinematically admissible.

Figure 3.11 (a) below shows the solution Prandtl (1920), which, due to friction, predicts that a dead zone is created at the punch-material interface at which the friction is maximum. However, when friction is neglected, the interface will be as in Figure 3.11 (b) suggested by Hill (1950).

A more straightforward solution that does not take equilibrium into account is known as an upper bound solution and is considered to give more approximate solutions than SLF.

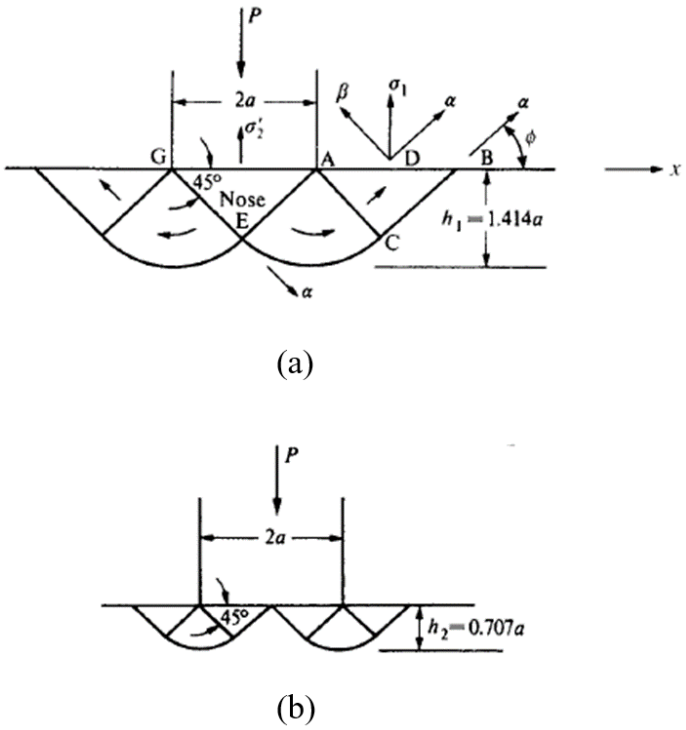

Figure 3.1 (a) Prandtl (1920) slip line field solution for a punch face with considerable friction and (b) Hill (1950) frictionless interface

An important aspect to consider for indentation tests is the flow patterns that occur around the indentation area. Considering a spherical indenter penetrating a sizable portion of a material a flow pattern as in Figure 3.12 is to be expected.

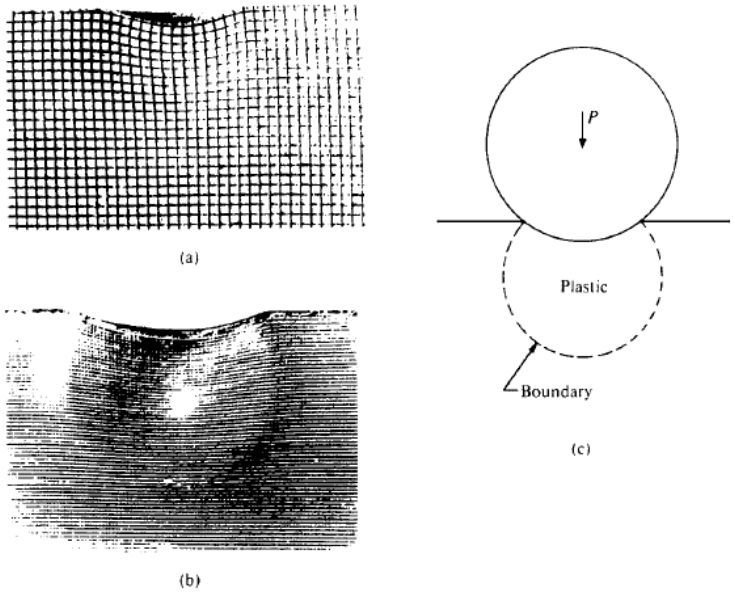

Figure 3.2 Flow pattern in (a) Plasticene (b) Mild Steel during Brinell test and (c) demonstrates the plastic boundary (Shaw 1984)

Figure 3.12 (c) shows a share that resembles a line constant ultimate shear stress below a sphere indenting a flat surface. Hertz (1895) suggested that the contact stress followed a hemispherical pattern over the surface and constant ultimate shear stress lines.

Meanwhile, Shaw and DeSalvo (1970) used a different approach by assuming the material not to be plastic-rigid but plastic-elastic alternatively. This approach suggests that the displaced material can be accounted for entirely by the elastic decrease in volume via compressive forces during indentation. This approach contrasts the slip line field theory by assuming no upward flow.

However, no upward flow requires indenters to have a high degree of bluntness as in such a case, and the friction will hinder any upward flow and, at the same time, increase the likelihood of strain hardening. Hardness measurement is done at the initial yield point during indentation if such conditions are met.

Two flows are essential to consider during the indentation process, an initial plastic flow while loading the indenter into the material (discussed in detail earlier) and a second one during unloading. As the indenter ascends, the load is

removed gradually. It can be approximated to a Hertz solution of a force going up on the sphere equivalent to the original loading force during the hardness test.

The importance of considering the secondary flow of unloading stems from its practical implications. One of such is when calculating indentation hardness, where the plastic flow zone is usually analysed after the unloading and is related to the force applied. Hence, it is important to keep in mind the difference between the shape of the free surface when the load is relaxed versus when it is still applied.

3.2 Thermal effects on plasticity

It was discussed in previous sub-sections that the impact of athermal strength parameters, which are based on zero-temperature elastic limit regardless of any thermal fluctuations. Discussed here are the thermal effects such as activation energy and activation volume. The probabilistic essence of transformation is when the athermal limit is not reached.

With regards to nanoscale plasticity, Zhu et al. (2008) and later Zhu and Li (2010) studied the temperature dependence of surface dislocation nucleation. Where, it was found that the transformation (nucleation) rate for a specific temperature and stress:

$$\nu = N\nu_0 e^{\left(-\frac{Q(\tau,T)}{k_B T}\right)} \tag{3.7}$$

where v_0*:* partial trial frequency, N: number of site transformation, k_BT: thermal energy, Q: activation free energy (value dictated by τ).

Experimental examples of the values in the above equation v_0 can be 10^{11}/s controlled by atomic vibrations, v order of 10^{-2}/s so the activation energy would be ~30k_BT Cahn and Nabarro (2001). A 0.7 eV process barrier is typical for a room temperature laboratory experiment.

For two competing processes with similar activation energies the operating mechanism can be found using activation volume (i.e., rate sensitivity). The transformation rate to stress sensitivity is calculated using the true activation volume Ω:

$$\Omega(\tau, T) \equiv -\frac{\partial Q}{\partial \tau}\Big|_T \approx k_B T \frac{\partial \ln(\nu)}{\partial \tau} \tag{3.8}$$

Activation volume is related to the thermally activated process atoms. While thermal activation is in process, stress assists the activation volume to transition as it reduces the effective energy barriers. Lattice diffusion for example have activation volumes of $\Omega \approx 0.1b^3$ versus $\Omega \approx 1000b^3$ in dislocation Orowan looping in coarse metals. This example highlights the utility of these values to be used to characterise defamation mechanisms.

An empirical power-law equation exists that relates stress and strain rate which can be used to find the activation volume for uniaxial tension of polycrystalline materials:

$$\frac{\sigma}{\sigma_0} = \left(\frac{\dot{\epsilon}}{\dot{\epsilon_0}}\right)^m \tag{3.9}$$

Where the nought denotes reference values and m is a unitless rate sensitivity index ranging from 0 to 1 where 0 give the limit which is rate independent and 1 resembles to the linear Newtonian flow.

Apparent activation volume is estimated to be:

$$\Omega^* = \sqrt{3} k_B T \frac{\partial ln\dot{\epsilon}}{\partial \sigma} \tag{3.10}$$

Combining the two last equations, we can relate m to Ω^*:

$$m = \sqrt{3} \frac{k_B T}{\sigma \Omega^*} \tag{3.11}$$

The $\sqrt{3}$ comes from von Mises yield criterion used to convert the normal stress to effective shear stress ($\tau = \sigma^*/\sqrt{3}$). In addition, it was concluded that stress nucleation can be express using:

$$\sigma = \frac{Q^*}{\hat{\Omega}} - \frac{k_B T}{\hat{\Omega}} ln \frac{k_B T N \nu_0}{E \dot{\epsilon} \hat{\Omega}} \tag{3.12}$$

wherein $\frac{Q^*}{\hat{\Omega}}$ represents athermal nucleation stress offset by thermal fluctuations. Hence, thermal activation plays an important role as well as evident in the equation above with temperature *T* appearing twice.

With regards to classical theories, Kocks (1975) using the kinetic rate theory analysed the kinetics and thermodynamics of slips and observed that higher temperatures decrease the strength due to thermal fluctuations that lead to the activation of stress relaxation mechanisms.

3.3 Impact of dislocation nucleation in nanomachining

The main argument supporting the fact that dislocation nucleation is the main factor causing the deformation when deformation occurs at the nanoscale. However, for this to be the case, near theoretical stresses need to be reached. Ye et al. (2017) indicate that critical shear stress needs to reach theoretical strengths for the deformation process to initiate, which in turn proves that dislocation nucleation is the main cause of the deformation. Otherwise, given that the length of the grooves machined is in the magnitude of several micrometres, the strain gradient plasticity (SGP) can dominate the deformation process.

For example, Li (2007) calculated the maximum shear stress reached during the nanoindentation of Cu to be around 6 GPa (using the equation used later on) compared to the ideal value (at zero pressure) of 2.2 GPa. Hence, when evaluating the Maximum Shear Stress for nanoscratching of copper, we can expect close values (at least at the order of magnitude level). However, suppose such shear stress values are not reached. In that case, the mechanism suggested by Li (2007) becomes inapplicable and further investigations into the applicability of other mechanisms, mainly the SGP, need to be considered.

To achieve this, the work of Elkaseer and Brousseau (2013) was analysed and used as quantitative proof to the case mentioned above. A tip of a DNISP probe from Bruker and a $CuZn_{39}Pb_3$ brass alloy sample were used. In addition, the AFM probe was utilized to induce cuts in the two-phase sample (named α and β) and four different force ranges [0-10] μN, [0-20] μN, [0-30] μN and [0-40] μN resulting in a total of eight different grooves, as Figure 3.13 below shows.

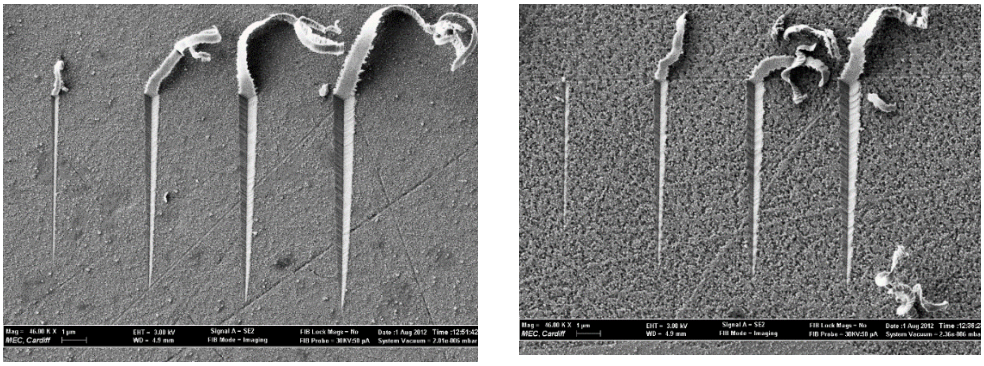

(a) (b)

Figure 3.3 Nanoscratching of brass alloy (a) α phase (b) β phase (Elkaseer and Brousseau (2013)

The groove created in the α phase with forces ranging between [0-20] µN is analysed to determine the three main process regimes namely full elastic recovery, ploughing, and cutting regimes. Figure 3.14 demonstrates the regimes.

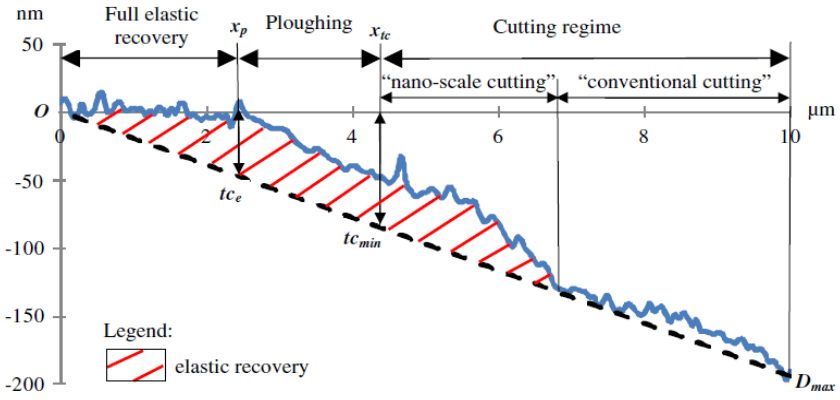

Figure 3.4 Elastic recovery, ploughing, and cutting regimes for the [0-20] µN α phase groove (Elkaseer and Brousseau 2013)

The maximum elastic force (ending at point x_p in Figure 3.14) can be estimated using the maximum applied force of 20 µN and with the aid of the similar right-triangles method wherein hypotenuses of the larger triangle ends at point D_{max} with the applied force equalling 20 µN and the smaller triangle with tc_e end with the required maximum elastic force. Which gives:

$$\frac{10}{2.4} = \frac{F_E}{20} \tag{3.13}$$

In which F_E is the maximum elastic force and is equal to 4.87 μN after solving the equation. The linear increment of the applied force is what enabled the use of the similar right-triangles method.

Then, using the maximum shear stress inferred from linear elasticity Li (2007):

$$\tau_{max} \approx 0.31 \sqrt[3]{\left(\frac{6PE^{*2}}{\pi^3 R^3}\right)} \tag{3.14}$$

where:

P is indentation load

R is radius of curvature of the indenter tip $R = \left(\frac{1}{R_1} + \frac{1}{R_2}\right)^{-1}$

*E** is the effective elastic modulus $E^* = \left(\frac{1-\nu_1^2}{E_1} + \frac{1-\nu_2^2}{E_2}\right)^{-1}$

And:

i = 1 denotes the Copper specimen (Brass 58A)

i = 2 denotes the Diamond Indenter

E_1 = 97 GPa

ν_1 = 0.33

E_2 = 1050 GPa

ν_2 = 0.1

With the above values obtained from each materials' respective manufacturer. Calculating the effective elastic modulus gives $E^* = 96.9\ GPa$.

As for the values of R_1 and R_2 are as shown next, followed by the assumption made for each case:

$R_1 = \infty$ (assuming the Brass 58A specimen has a flat surface)

$R_2 = 70\ nm$ (impact of tip bluntness and the 12° inclination of the AFM probe are not considered due to limited impact on final result)

Based on the previously mentioned assumptions we get $\frac{1}{R_1} = \frac{1}{\infty} = 0$ then $R = R_2 = 70$ *nm.*

Finally, substituting all values in this equation $\tau_{max} \approx 0.31\sqrt[3]{(\frac{6PE^{*2}}{\pi^3 R^3})}$ gives (3.77 GPa). This value is less that the highest value achieved (6 GPa) but more than the ideal (2.2 GPa) hence supporting the notion that defect nucleation is mechanism responsible for deformation.

3.4 Summary

The theoretical framework under which material deforms when considering the size scale that the experimental work of this thesis falls under was established. In addition, theoretical validation of some of the assumptions and hypotheses made in the previous chapter, with particular emphasis on dislocation nucleation, was provided.

Starting by comparing the features dimensions of the experimental work done in the thesis, which is more than 30 nm but does not exceed 200 nm, falls clearly under the 'nanoscale' category, which has the governing theories that set it apart from both the micro and macroscales.

The chapter started with the categorisation of how the material behaves based on its size scale was done. Emphasis was done on the deformation locality, which was essential to consider as the experimental work done in this thesis utilised bulk-sized workpieces. Supporting material, including a review of dislocations which play the primary role when explaining plasticity, slips that depend on dislocations, and the critical resolved shear stress used towards the end of the chapter, are found in the appendix.

The first category included the atomic scale; however, this size scale research is mainly confined to atomic grain-sized materials rather than materials with extrinsic atomic size scale. Grain size was also discussed for the nanoscale, though analysis expanded to include nanosized materials such as nanopillars and

thin films and to nanoscale features in bulk-sized materials. Nucleation of dislocations, which play an integral role in nanoscale plasticity, were analysed. The main characteristic of deformation due to dislocation nucleation is the near to theoretical stress values explained by dislocation starvation, and annihilation to the free surface. In addition, homogeneous dislocations or heterogeneous dislocations, which are the two types of nucleated dislocations, were discussed. Also, it was discussed that pre-straining of nanoscale materials only weakens them, opposite to the work hardening that occurs at the macroscale. Cyclic loading of nanopillars, on the other hand, was found to not affect its strengths due to dislocation annihilation.

Microscale was analysed afterwards, emphasising the strain gradient plasticity theory and its importance in explaining the indentation size effect. It was explained later that several papers did not agree with the original paper, so the authors had to improve and overcome the limitations of their original work. After that, the applicability of the strain gradient plasticity was analysed. Furthermore, it was concluded that although valid for the microscale, which is continuum based, it does not apply to the nanoscale due discrete nature of dislocation nucleations.

The macroscale and the classical theoretical framework that explains plasticity were discussed. The existence of defects explained the gap between theoretical and experimental strengths. Griffith's work on microcracks, their effect on stress concentration, and consequently on crack growth was discussed. In addition, Irwin's work on linear elastic fracture mechanics (LEFM) and the stress intensity factor (K) was discussed. Their corresponding loading modes are the basis of some of the analyses done in chapter 2 regarding ploughing and chip formation.

Hardness, in turn was discussed and its significance in indentation tests with classical theories such as the slip line field theory that explain behaviour at the macroscale. This was followed by an analysis of the thermal effects on plasticity, including factors not included in earlier discussions.

Given that no agreed-upon theoretical framework is used to describe the deformation mechanism in the discussed case, where a groove's cross-sectional

dimensions do not exceed 200 nm but extend several micrometres in length, this study provides necessary answers. Because, as discussed previously in this chapter, at such scales, two mechanisms need to be taken into account, strain gradient plasticity (SGP) as well as discrete mechanics (dominated by dislocation nucleation).

Hence, the analyses at the end of this chapter that is based on the work of Elkaseer and Brousseau (2013) -which in turn used a similar set-up to the one in this thesis- prove the significance of dislocation nucleation in the AFM tip-based nanomachining process and provides a reference to future simulations based on similar cases, where the critical resolved shear stress was calculated and was found to be near theoretical values corroborating the assumption, as was developed by Li (2007).

Distinguishing between strain gradient plasticity and discrete mechanics-based theories plays a crucial role in simulation-based nanomachining studies. Because choosing a suitable framework, impacts the accuracy of the model used.

Therefore, this chapter presented the theoretical framework vital for understanding deformation mechanisms at multiple scales, especially at the nanoscale. This framework is later used to explain the phenomena observed in the vibration-assisted AFM tip-based nanomachining of copper tests, such as changes in surface roughness and cutting modes (i.e., ploughing or chip formation).

Chapter 4

Characterisation of AFM Tip Bluntness

4.1 Preliminaries

It is known that the rake angle of a cutting tool impacts the outcomes of the machining processes, such as the cutting forces, the produced surface roughness, and the residual stress. While in conventional macroscale machining, the edge radius of cutting tools may be approximated as infinitely sharp, this is not the case for nanoscale machining operations with an AFM probe. Because the undeformed chip thickness may be of the same order of magnitude to that of the tip radius, the bluntness of AFM probes directly affects the effective rake angle during the nanoscale machining operations.

The precision of AFM applications is highly dependent on the conditions of the AFM probe tip. Due to forces of contact interactions between the tip and the scanned material, the initial shape of the tip may change. In turn, the bluntness of the tip may cause significant errors in the resulting output and interpretation of the output data, see, e.g., Borodich et al. (2003), Yan et al. (2016), and Ramirez-Aguilar and Rowlen (1998).

Thus, there arises a natural question: How can one characterise quantitatively the tip bluntness? Kindrachuk et al. (2006) suggested to use the difference in depth between the ideal and simulated tips as main parameter of the tip bluntness. Alraziqi et al. (2017) presented two possible quantitative characteristics (metrics) of the tip bluntness: (i) the ratio of the tip volume for a given height to the volume of the imaginary cylinder of the same height in which contains the tip; (ii) the degree d of the power-law approximation of the indenter tip.

The latter metric suggested by Alraziqi et al. (2017) arose from the following theoretical arguments. It is known that the shape of non-ideal indenter near the tip can be well approximated by power-law functions of radius of degree d (see, e.g., Borodich et al. (2003a)). For many materials, contact problems for such indenters are self-similar (see, e.g. Galanov 1981a, 1981b and Borodich 1983, 1989, 2014). In turn, for the self-similar contact problems, the load-displacement curves satisfy the scaling relations and may be presented as special power-law functions (see., Borodich 1989, 1993, 2014). It was suggested to extract degree d of a blunt tip power-law approximation from the

experimental load-displacement curves of elastic indentation of a soft-material samples by the AFM tip under consideration (see, e.g., Alraziqi et al. 2016).

Various methods for characterisation of AFM tip bluntness are discussed in this chapter. The results of experimental studies of AFM probe tips are presented. Both tips are considered; (i) the intact tips as received from factory and (ii) worn tips. The tip bluntness is studied in both vertical position of the probes and in working position when the AFM cantilever is inclined by 12° to the horizontal plane. It is suggested to describe the tips as power-law functions, whose exponent d is used as a characteristic of tip bluntness. It is also argued that the load displacement curve of an experimental depth-sensing indentation (DSI) test may be used to extract the quantitative measure of the AFM tip bluntness. The experimental results showed that one has to be careful in selecting proper soft material (polymer) for bluntness estimations because it was observed rather often practically linear load displacement curves. This was explained by existence of a stagnation zone of polymer macromolecules in front of the AFM tip that moves downward together with the indenter.

Afterwards, the impact of the tip bluntness on the work of adhesion is studied. Borodich et al. (2014b) showed that the frictionless JKR model can be expanded beyond contact between spheres and flat-ended punches to arbitrary convex and blunt axisymmetric bodies. Here, it is argued that the work of adhesion varies considerably at lower degrees of bluntness (i.e., sharp tips) hence emphasising the need to use real numbers and not only integers to characterise the tip bluntness. The error in pull-off force estimation caused by using integer values only will be demonstrated when such values are compared to real numbers. The real numbers used, which represent tip bluntness, are the ones extracted during the experimental part of this chapter. Also used are arbitrary non-integer values that represent a wider range for a better understanding of the sensitivity of the work of adhesion to an approximation of tip bluntness values.

Zheng and Yu (2007) developed a pull-off force – displacement relationship that is dimensionless and only requires the bluntness values for the pull-off force estimation. The authors developed both JKR-n and DMT-n models (wherein the n denotes the bluntness values). However, the former is used only as it is more appropriate for softer polycarbonate material used in the DSI tests conducted for this

chapter. The authors base their expansion to arbitrary shapes values to the work of Borodich and Galanov (2004).

Following that, an analytical study of various factors affecting the effective rake angle of AFM tips for nanomachining applications is done. The shape of an AFM probe tip approximated by the same power law function employed earlier. The analysis conducted has confirmed that the shallower the penetration depth for a given tip shape, the more negative the rake angle is, and that blunter tips result in more negative rake angles for the same penetration depth. Regarding the lesser-known impact of the tilt angle, it was found that the tilted orientation provided less negative rake angles for all tip bluntness and depth values when machining is conducted in a direction parallel to and towards the long axis of the AFM probe. However, for a given penetration depth, the tip bluntness developed due to tip's wear affects the effective rake angle of tilted tips more significantly than vertically orientated ones. Thus, all above mentioned factors should be taken into account by practitioners when implementing AFM-based nanomachining operations.

4.2 Impact of tool shape on ultra-precision machining

The shape of the cutting tool impacts not only the effective rake angle but also the stagnation zone in front of the cutting edge, the material flow as well as how the chips are formed hence controlling the quality of the generated surface.

According to Denkena and Biermann (2014), the cutting edge shape is described using the transition between a rake face and a flank face of a tool's edge. However, unlike macroscale cutting tools which have their own internationally recognised standards, microscale and nanoscale tool edges do not have an international standard and it is up to each researcher to characterise the tool edge as they see best. This in turn, causes inconsistencies in tool edge shape descriptions.

To solve this discrepancy, multiple studies tried to create repeatable and standardised characterisation methods. Wyen et al. (2012) for example created a method in which the fitting area choice is user independent, as Figure 4.1 shows.

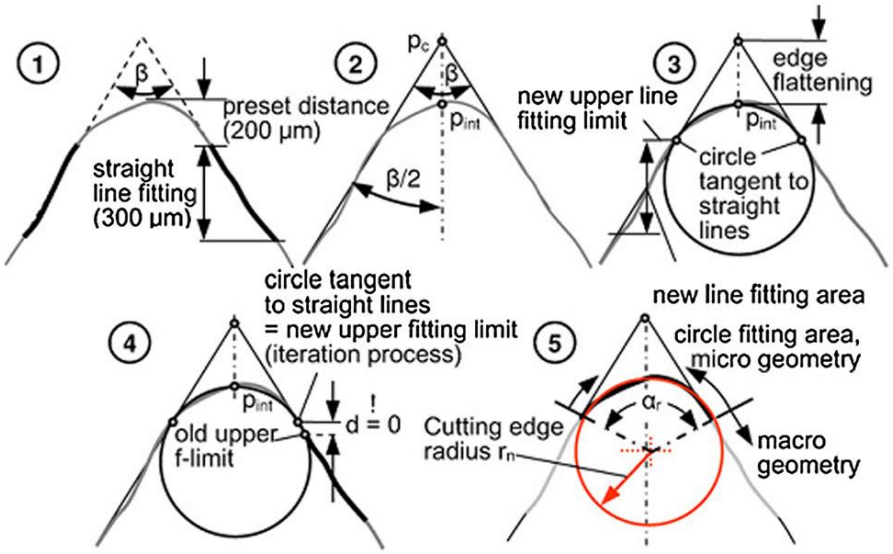

Figure 4.1 rounded edges characterisation method proposed by Wyen et al. (2012)

As Figure 4.1 demonstrates, this method comprises five steps starting with a least square straight line fitting done over the flank and face of the tip, followed by a present distance estimation between such lines and the nose tip, as shown in Figure 4.1 (1) shows. After that, the fitted lines are connected at point P_C that create an angle referred to as β and is connected to point P_{int} via the bisector, as in Figure 4.1 (2). The third step (Figure 4.1 (3)) consists of drawing a circle that tangents the straight lines and goes through point P_{int}. A new upper limit is created where the circle intersects with the fitting lines. The fourth step consists mainly of repetition of the previous two steps until the circle tangent to the straight lines approximately equals the upper fitting limit (see Figure 4.1 (4) when $d = 0$). Completing the fourth steps concludes the transition from macro to micro geometry. Finally, a least squares reference circle (red circle in Figure 4.1 (5)) is created which intersects with the micro geometry limit. Moreover, according to the authors this circle does not need to intersect with the fitting lines nor need to have wedge angle bisector as its centre.

However, although the authors expanded this work to include asymmetric cutting edges, as seen in the steps discussed, the complexity of the methodology could act as a barrier for other researchers to implement and repeat where a significant amount of fitting and approximation has to be done. In addition, the number of iterations needed to complete the fourth step is subjective, making this method less practical.

Meanwhile, Denkena et al. (2005) suggested what is known as the K-factor method, also known as the form-factor method. This method relies on four parameters (seen in Figure 4.2) which in turn are used to extract the form factor K in addition to an average cutting edge rounding parameter. When $K = 1$ then the cutting edge is symmetrically rounded ($\bar{S}$), whereas when $K < 1$ is in waterfall style and in trumpet style when $K > 1$.

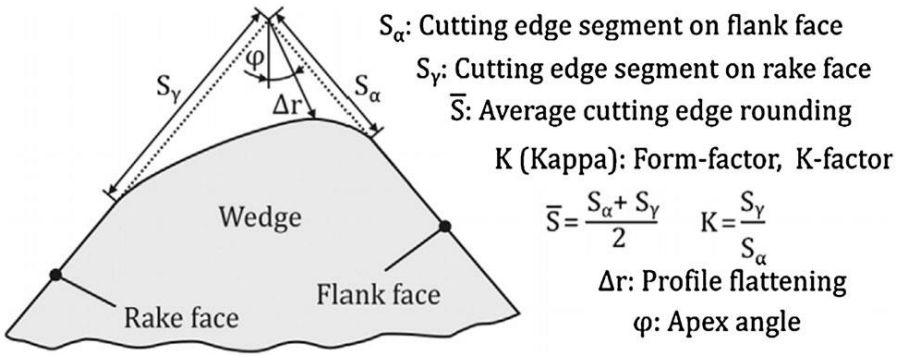

Figure 4.2 K-Factor Method by Denkena et al. (2005)

Nevertheless, this method as the previous one suffers from the increased number of parameters making its application in practice more difficult, especially at nanoscale applications.

The authors Denkena et al. (2012) later on tried to simplify the characterisation process by utilising less parameters and relying on one, named the normalised ploughing zone. This parameter represents the ratio of A_α that is the in between area of the cutting edge profile, the material bordering the stagnation point and the contact point of the side of the flank face, over I_α is the contact length of the cutting edge between the mentioned points given as $A'_\alpha = A_\alpha / I_\alpha$. Authors also analysed the impact of such parameter on burr formation, wearing as well as residual stresses. It was found that the surface integrity is highly affected by the profile of the cutting edge under the stagnation point. Figure 4.3 demonstrates three gradually increasing A'_α values. In the study, the authors concluded that higher the A'_α values correspond to higher cutting forces.

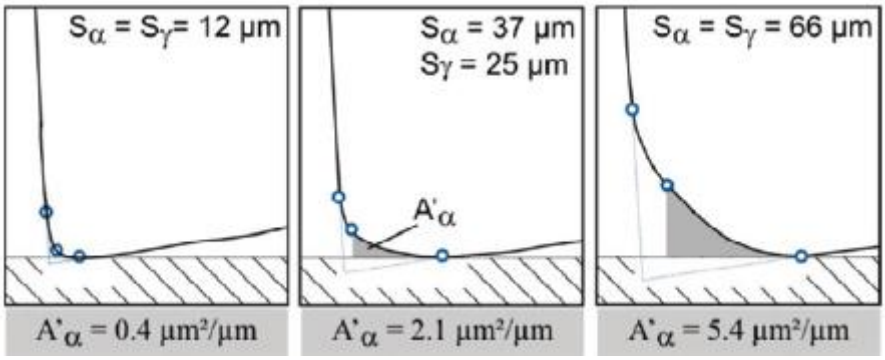

Figure 4.3 Three normalised ploughing zone cases (Denkena et al. 2012)

Xu et al. (2017c) expanded on the work of Denkena et al. by using a tool edge radius r_β that can only be fitted using the profile of the cutting edge connecting the stagnation point and the contact point mentioned in Denkena et al. (2012). It was found that this new parameter has an impact on stagnation area, cutting forces, chip formation and subsurface damage.

Moreover, as discussed previously in chapter 2, Kong et al. (2020) analysed tip ear during vibration-assisted nanomachining and confirmed that wear causes increase in bluntness that directly affects the pull-off force (refer to Figure 2.21). They also found that increased bluntness to the point where the tip is severely worn results in no material being removed during cutting operations.

In metal cutting, the rake angle is defined as the angle between the rake face of a cutting tool and the normal to the work surface at the nominal cutting edge at which chips are formed (Shaw 2005). The rake angle can be positive, negative, or neutral with each configuration associated with advantages and disadvantages. However, a positive rake angle is generally preferred because this results in reduced cutting forces and consequently lower power consumption. In a similar way to well-known observations in microscale machining, the effective rake angle during nanoscale AFM probe-based cutting can be much more negative than the angle evaluated when considering the orientation of the tip face alone. Figure 4.4 illustrates this effect by showing the effective rake angle typical of nanoscale operations which results from the undeformed chip thickness (a) being comparable to the radius of the tip. The shape of the AFM tip shown in this figure is not symmetrical about a vertical axis going

through its apex. This is due to the fact that the figure illustrates the configuration whereby an AFM probe is conventionally mounted at an angle on an AFM instrument.

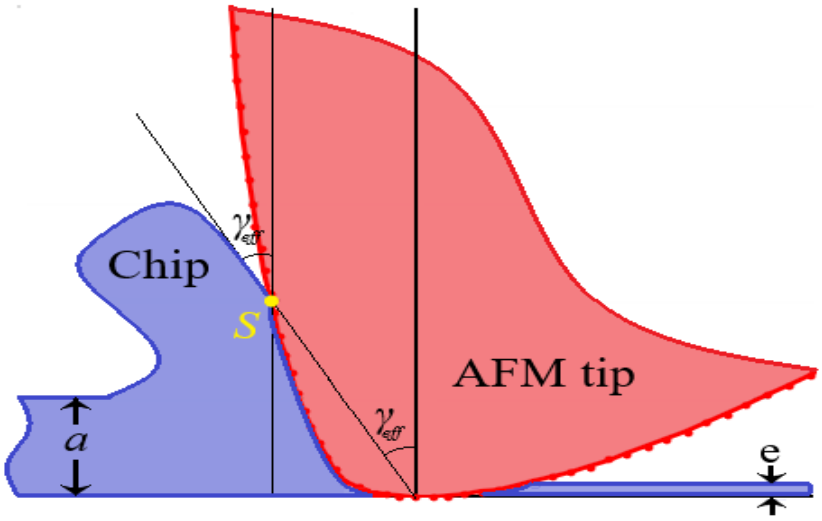

Figure 4.4 Effective rake angle during AFM tip-based nanoscale cutting.

It is important to note that the effective rake angle during AFM probe-based nanomachining does not only depend on the bluntness of an AFM tip but also, it could be affected by two other factors: 1) the depth of penetration of the tip into the processed material and 2) the tilt of probes mounted on AFM instruments. In this context, and through the application of a quantitative method to model the condition of an AFM tip, this section investigates the influence of these factors on the effective rake angle during AFM probe-based nanomachining operations.

4.2.1 Impact of the rake angle in cutting processes

Shaw (2005) reported that a reduction in rake angle tends to result in cutting with discontinuous and plastically deformed chips as well as an increased subsurface damage depth. During the nanometric cutting of silicon, Fang and Venkatesh (1998) experimentally demonstrated that diamond tools with 0° rake angle resulted in improved surface finish compared to diamond tools with -25° rake angle.

To understand the impact of the rake angle on machining outcomes, such as the mechanism of chip formation and generated machining forces, a number of studies relied on molecular dynamics (MD) simulations. For example, Komanduri et al. (1999) used MD simulations to analyse the effect of a range of rake angle values between +10° and -75° during nanoscale cutting of copper. These authors found that, as the rake angle becomes more negative, it causes a decrease in chip length and an increase in the ploughing region ahead of the tool as well as in the deformation occurring below the surface of the machined area. The study also highlighted that a decrease in the rake angle resulted in an increase in the specific cutting energy.

Another study from Pei et al. (2006) also analysed the chip formation process during nanometric cutting of copper using MD simulations. These authors concluded that smaller chips formed with a more negative rake angle due to increased plastic deformation in the worked material. A further MD study from Han et al. (2002) found that the hydrostatic pressure of the negative rake angle was the cause of the plastic deformation in front of the cutting tip. The effect of variable rake angles was also simulated with MD to analyse the process of dry polishing of single crystal aluminium by Han (2006). This author found that with a more negative rake angle, there was an increase in the horizontal force concurrent with a decrease in the thrust force during cutting and an increase in residual compressive stress.

When reviewing the literature on MD simulation studies of ultra-precision machining of silicon, Goel et al. (2015) reported that the rake angle governs the friction coefficient when material removal is occurring at shallow depths. A highly negative rake angle is associated with increased edge roundness. In turn, this causes uniform hydrostatic stress fields and a decrease in the stress concentration in the cutting region, thus promoting the favourable brittle to ductile transition when cutting brittle materials, in addition to the creation of a compressive stress state as the material is pushed downward in front of the tip. Similar conclusions were also reported by Woon et al. (2008) in the context of microscale machining of AISI 4340 steel using finite element simulation.

It was reported by Lucca et al. (1994) that the tip shape also substantially impacts the thrust forces at low uncut chip thicknesses for 105 nm radius tools in the case of this particular study. A negative rake angle causes a shear angle that is lower than

assumed, an increase in the cutting forces, a thrust force larger than the tangential cutting forces, all leading to an unpredicted increase in energy consumption.

The ductile machining mode of brittle material discussed in Yan et al. (2001), Blake and Scattergood (1990), and Shibata et al. (1996) all supported the notion that a rake angle ranging between -20° and -50° is an ideal range for nanomachining. Meanwhile, others such as Fang and Zhang (2003) and Yan (1999) suggest the range of -60° to -80° to be hindering the ductile mode.

The reported literature highlights the important effect of the rake angle on the nanometric cutting mechanism. When implementing nanoscale cutting with AFM instruments, the effective rake angle is affected not only by the bluntness of the AFM tip but also by the depth of penetration of the tip into the material and by the angle at which the probe is mounted on an AFM instrument. In this context, the focus of this section is to examine, from a theoretical point of view, the effect these three factors have on the effective rake angle of tips used in AFM-based nanomachining operations.

4.3 Methods for AFM tip characterization

The importance of having an accurate tip shape description was discussed in many papers. For example, the direct impact of the tip's geometry on the results of piezoresponse force microscopy was discussed by Kalinin and Bonnell (2002). They used piezoresponse imaging in the electrostatic regime in which the capacitive and Coulombic interactions of the surfaces caused an attractive force that occurred during indentation. These interactions were, in some instances, approximated to a plane-plane capacitor which is incorrect because the capacitive force in a plane-plane geometry cannot cause a tip deflection. The authors concluded that an accurate tip shape is necessary for a correct interaction description. Borodich (1990, 1993) and Borodich et al. (2014a, 2014b) also emphasised the importance of tip bluntness for evaluating mechanical and adhesive properties of materials from nanoindentation experiments.

Further on, this concern also rises when one intends to describe the bluntness of new AFM probes because the information based on data provided by manufacturers can be misleading. Indeed, as proven in several studies, see, e.g., Sedin and Rowlen (2001)

and Jacobs et al. (2016), the actual tip radius values can deviate significantly from their nominal values stated by manufacturers. In addition, the shape of the tip may not be spherical.

AFM tips are designed to scan up to thousands of metres during their life spans depending on the application and build materials. However, with continuous use, the tips are eventually prone to degradation that negatively impact the tips' ability to do their intended tasks accurately, especially during scanning of surfaces (see, e.g., Yan et al. 2016), in addition to the negative impact on the tips ability to cut through surfaces (see, e.g., Kong et al. 2020). Hence, the need for assessing the tips' condition became more prominent when the factors responsible for the deterioration were analysed (see, e.g., Miller et al. 1995). This gave rise to multiple techniques dedicated to the assessment of the tip's apex condition with such techniques varying from in-situ, wherein the probe is kept in place within the AFM where further analysis is done, to ex-situ techniques in which the probe investigated is relocated to another setting to be investigated using different microscopy techniques, mostly using electron microscopes.

4.3.1 In-situ

Multiple sub-techniques can be used to investigate AFM tips in-situ, including a technique commonly known as blind tip estimation or reconstruction, in which the scanned data is processed using the mathematical method of dilation and erosion. Another method includes assessing various wear metrics. A third technique relies on using an ultra-sharp tip with a smaller tip radius to characterise the tip in question. A fourth includes using a tip characteriser tool that incorporates a range of asperities or sharp pins. While a fifth technique also uses tip characterising sample, the features are not only sharp but can still extract tip features.

4.3.1.1 Blind Tip Reconstruction

This technique is also referred to as BTR and was first suggested by Villarrubia (1994) allows for the construction of a 3D model of the tip regardless of the scanned surface's geometry. In this method, an outer shell of the tip that is similar to the section of the tip apex that is in contact during operation is created. Villarrubia joined another experimental study by Dongmo et al. (2000), where the BTS method was also employed to characterise two diamond profiler tips where they scanned a commercial roughness calibration sample. The resulting tip shape produced using BTS was comparable to the profile of the SEM image of the same tip up to 600nm from the apex, as shown in Figure 4.5, where this method is demonstrated.

In Figure 4.5 (a), the thick line represents the profile as obtained as an image, whereas the thin line is the actual shape of the surface. The thick line was created using the dilation process with a tip with a broken apex. The numbering from 1 to 3 refers to the apexes of the surface, where Figures 4.5 (b) and (c) are examples of the blind tip reconstruction. Starting with Figure 4.5 (b), an overlap is observed and highlighted in the darker shade with apex 1 with the thin line and apex 2 with the thick cross. This is then followed by another step in Figure 4.5 (c), in which the area highlighted in (b) is shown in the thin line in addition to extra improvement of the estimation of the tip represented by the shaded area that includes data from apex 3 in the thick line, with a dotted white line in (c) showing the completed blind tip reconstruction procedure. Finally, Figure 4.5 (d) compares the real profile of the tip with the thin line and the reconstructed profile using this method with the thick line.

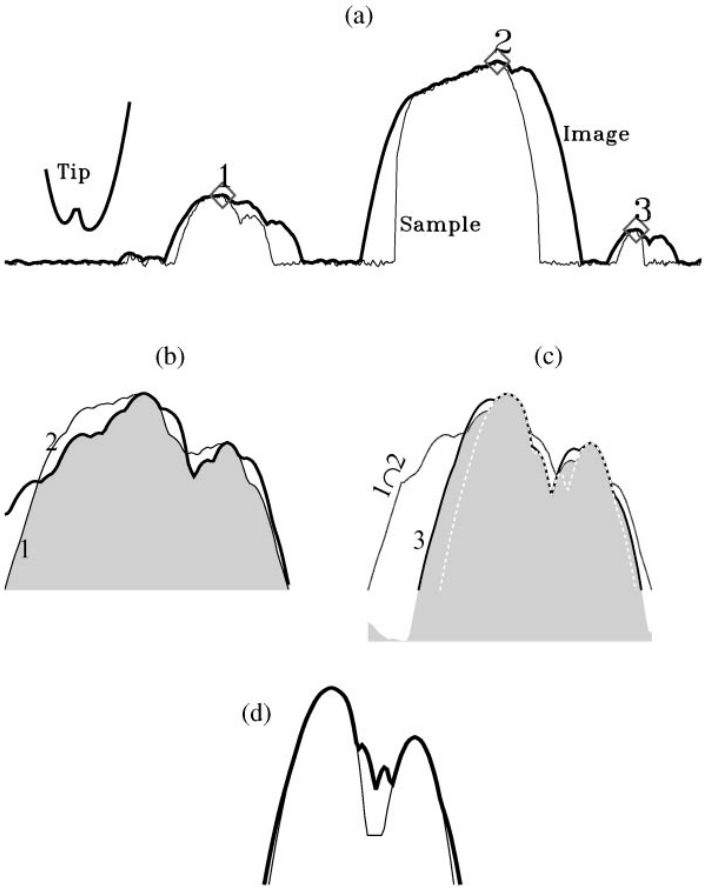

Figure 4.5 Blind Tip Reconstruction illustration (Dongmo et al. 2000)

When the blind tip reconstruction method was compared to the data obtained using a scanning electron microscope good agreement was found when the distance from the tip's apex was less than 600 nm, and in cases where values were larger than 600 nm this method tended to overestimate the size of the tip in question. Wang et al. (2010) concluded that the caveat of using the BTS method is its sensitivity to noises during AFM operations.

Liu et al. (2010) did a study that included using the BTR method in addition to other techniques in which four different probes were analysed and the profiles extracted were compared to the ones resulting from a scan using a tunnelling electron microscope, as seen in Figure 4.6. Similar to Dongmo et al. (2000), the closer the apex the profile was, the more accurate it was.

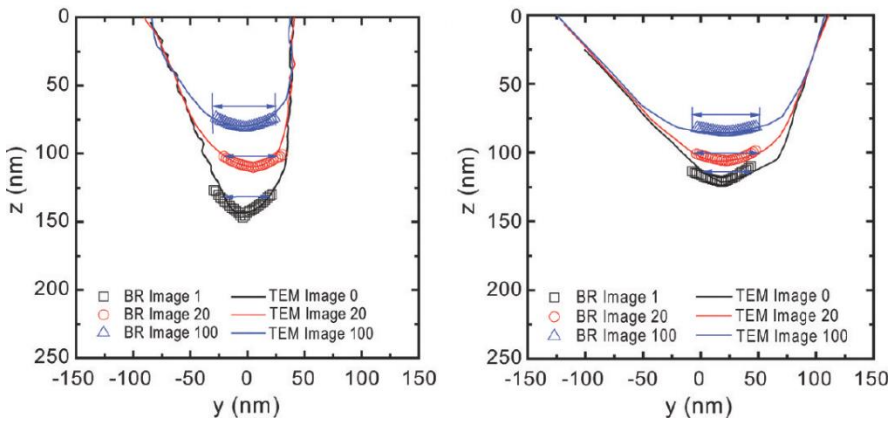

Figure 4.6 Comparing the tip profile extracted using the BTR (BR) and TEM images (Liu et al. 2010)

4.3.1.2 Wear metrics

Wear metrics-dependent approaches vary in setups and methods; however, they are not designed to directly produce geometrical information about the tips. Conversely, such approaches extract wear metrics that impact the shape and bluntness of AFM's tip.

Gotsmann and Lantz (2008) used AFM probes with silicon tips and were tested on polymer samples with applied forces ranging between 5 – 100 nN at total distances exceeding 700 m. Work of adhesion between the tip and sample surface was tested at varying stages of the test. Given that the blunter the tip is, the more surface contact there is, which is a clear indication that higher pull-off forces required means a blunter tip is mainly caused by wear of the tip's apex. A similar approach to this is made in this chapter, wherein the impact of the bluntness on the pull-off force is analysed.

A technique that is able to measure the change in mass by studying the shift in the resonance frequency of the probe's cantilever was introduced by Schmutz et al. (2010). In this study, the authors attached a sphere to the tip of the probe, making what is known as colloid probes. Changes in mass with the pico-scale resolution was achieved using this technique. However, due to the attachment of the spherical mass to the apex, the visual changes in shape of the apex could not be extracted in this method.

An acoustic transducer fixed on the top of the AFM tip was utilised by Cheng et al. (2011). This transducer, in turn transmits acoustic waves along the tip. Figure 4.7 below shows.

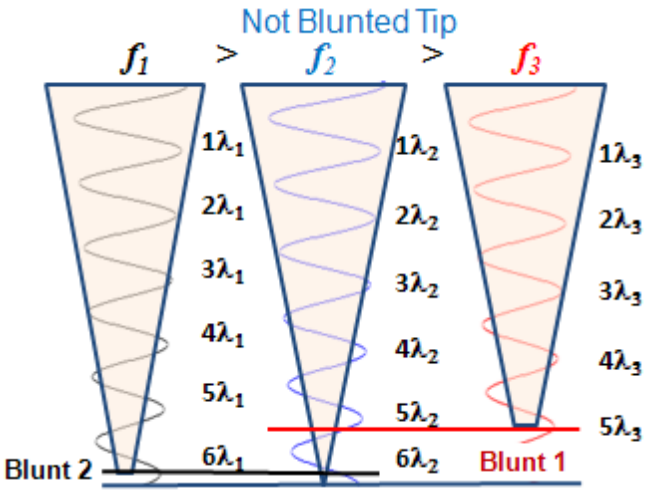

Figure 4.7 Method proposed by Cheng et al. (2011) in which a change in apex shape corresponds to a change in frequency

This method primarily relies on comparing the frequency of tips that are intact with worn ones with blunter apexes. Although this method is able to detect minuscule changes in the tip geometry both in-situ and without need for contact, this technique requires custom-made probes made with a thin film piezoelectric material that has the ability to convert the motion to an electrical signal making applying this technique on a larger scale much more difficult.

4.3.1.3 Ultra-sharp tips

Although this technique requires the removal of the probe and placing it upside down, it is still considered an in-situ technique as the operation is still done within the AFM. With the probe's tip facing now, a sharper tip with a smaller radius is used to scan it where the characterising tip becomes the characterised workpiece. Khurshudov and Kato (1995) used one tip to investigate the other when they analysed the wear of an AFM with a Si3N4 tip with tip radii ranging between 10 – 20 nm with loads not exceeding 10 nN. This study proved that similar build material and size probes could

be used to assess one another, especially in wear metrics. However, Khurshudov and Kato (1997) later on did a study that more fits the utilisation of an ultra-sharp tip narrative by using a Si3N4 tip to characterise a diamond tip which the latter had a 65nm tip radius making it more than three times larger in size.

Zhao et al. (2001) used a similar set-up in which a Si3N4 tip was used to scan a similarly three times larger diamond one. However, the aim of this study was to analyse how the tip degrades with use and how wear metrics would be affected. This study analysed the impact of nanomachining of a polished single crystal silicon sample at the various steps of the machining process. Gozen and Ozdoganlar (2014) also employed this method for a nanomilling process analysis in which a diamond tip was investigated via non-contact scans with conical ultra-sharp tips and was used to follow the progression of the volumetric removal rate on the tip's surfaces as more material is machined.

4.3.2 Ex-situ

Techniques in this section mainly include the placement of the investigated probe in an electron microscope, including scanning electron microscopes (SEM), transmission electron microscopes (TEM), scanning tunnelling microscopes (STM or STEM), in addition to the high-resolution transmission electron microscope (HRTEM). For example, Lantz et al. (1998) investigated several AFM probes, especially the reliability of ones coated with metal and semiconductor materials. During analysis, the authors used STM to check for any tip wear to validate their understanding of the conductivity data obtained after AFM experiments.

For example, Chung and Kim (2003) conducted a comparative study in which they compared the condition of Si3N4 and Si AFM tips before and after use on multiple types of materials and a range of loads between 10 - 800 nN. Two years later, the authors Chung et al. (2005) used HRTEM as they investigated tips made of silicon to scratch silicon and diamond-like carbon surfaces with forces applied ranging between 10 – 100 nN.

Bhaskaran et al. (2010) studied tips made of diamond-like carbon and how scratching would impact such tips. The authors utilised both an SEM and TEM to scan for any changes in the geometry of the tips. Hence, creating a direct relationship between the distance accumulated during scratching and how much wear occurs (volumetric) every applied load causes.

Meanwhile, to overcome the issues occurring during the mounting of the probes, especially the difficulty of realigning the probe at the same position every time, Jacobs et al. (2016) proposed using a fixture that enables a straightforward and precise positioning of AFM probes for TEM imaging. This fixture uses a spring-loaded clip that can hold up to three probes at the same time.

The authors explained how such fixtures could be designed, fabricated, and used. After applying their method on 17 different probes, they concluded that their method reduced contamination risks during the relocation of probes and reduced the risk of tip damage caused by practitioners. However, this fixture suffers from limited applicability and can be used for certain TEMs, namely JEOL 2010, JEOL 2010F, and JEOL 2100 TEM systems.

4.4 Power-law approximations of the indenter shapes

In this section, an approximation of the AFM probe's tip shape is made, which is extracted from SEM images to a non-axisymmetric power-law function of degree d.

The adhesive contact problems solved in the framework of JKR theory are not self-similar. However, if the shape of the indenter is described by the axisymmetric power-law function, one can extend the JKR theory to such indenters (see e.g., Galanov 1993, Carpick et al. 1996, Borodich and Galanov 2004). The difference between Galanov's solution and Carpick's is that the values of d for former solutions are arbitrary real positive numbers $d \geq 1$, while for the latter are integer numbers only.

The values of d will have real positive numbers and only not integers as used in Grierson et al. (2013). Then, the exponent d will be used to describe the degree of the bluntness of the tip quantitatively. Because it corresponds to a cone or a sphere, the higher the value d, the flatter (blunter) the tip is.

For the sake of simplicity, it will be assumed that the results obtained from vertically indenting materials by a probe applied to AFM probe indentation as lateral displacements during the nanoindentation are considered negligible, as will be proven in the following section. Indenters following power-law shapes have self-similar contact problems. Hence, the Borodich scaling approach can be applied, and the 3Dcontact applicable formulae within Borodich (1989, 1993, 2011, 2014), the monomial function in polar coordinates can be expressed as follows:

$$z = B_d(\theta) r^d \tag{4.1}$$

where, $x_1 = r \cos\theta$, $x_2 = r \sin\theta$ and $B_d(\theta)$ is a function of the indenter height's at *r=1*. Applying this law to the approximately 30 nm (part of tip that penetrates) is done. The relationship between the power-law functions and homogeneous functions can be understood from the definition of homogeneous functions that:

$$h_d(x_1, x_2) = \lambda^{-d} h_d(\lambda_{x_1}, \lambda_{x_2}) = \lambda^{-d} h_d(\lambda r\cos\theta, \lambda r\sin\theta) \tag{4.2}$$

Assuming $\lambda = r^{-1}$ then

$$h_d(x_1, x_2) = \lambda^d h_d(\lambda r\cos\theta, \lambda r\sin\theta) = r^d B_d(\theta) \tag{4.3}$$

where,

$$B_d(\theta) = h_d(\cos\theta, \sin\theta) \tag{4.4}$$

Therefore, it is valid to assume that the indenter shape is presented as a power-law function of power d or the shape of the indenter is expressed by a degree d homogeneous function.

Graph below (Figure 4.8) shows the shape of the parabola z = *f(r)*= r^d where d increases 1, 1.5, 2, 2.5 up to 3 with 1 being the straight line and 3 being the rightmost and most curved one. The previous equation has a $B_d(\theta)$ part that is not constant

where $B_d(\theta)$ describes the height of the indenter at some point (θ, r) on a circle of a unity radius $r = 1$.

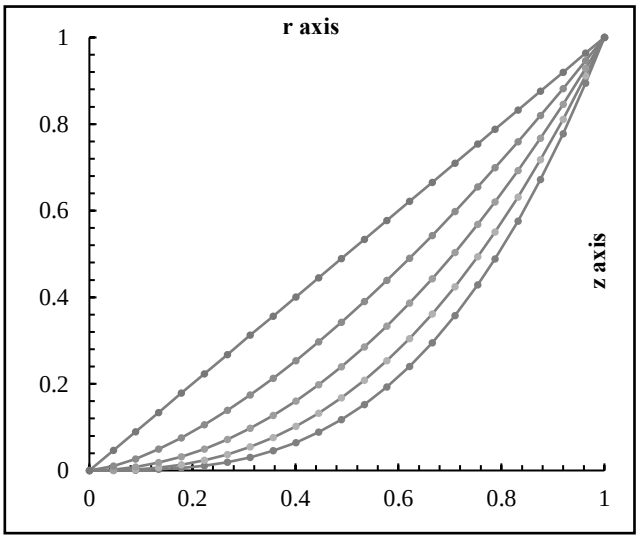

Figure 4.8 *d* values of 1,1.5, 2, 2.5, 3

One has to take into account that the AFM cantilever in its working position is not horizontal (see, e.g., Heim et al. 2004, Hutter 2005 and Al-Musawi et al. 2016). In fact, it is inclined by a 12°, as it is shown in Figure 4.8. Initially the inclination angle of the cantilever in its mounted position is α, while under the maximum load the angle increases by φ. The total inclined angle of the AFM cantilever is φ+α.

If the indentation is considered shallow, then one can safely assume that the cantilever inclination angle φ+$\alpha \cong \alpha$ during the nanoindentation test. This means that the first point of the probe that may touch the material sample is not at the geometrical tip apex of the probe in its vertical position C' but rather the point C (see the exaggerated version of the AFM probe in Figure 4.9). During nanoindentation, the tip's point C will have not only vertical displacements but also some shift in the horizontal direction. If one neglects the elastic deflection of the cantilever, it will cause reduction of the angle φ.

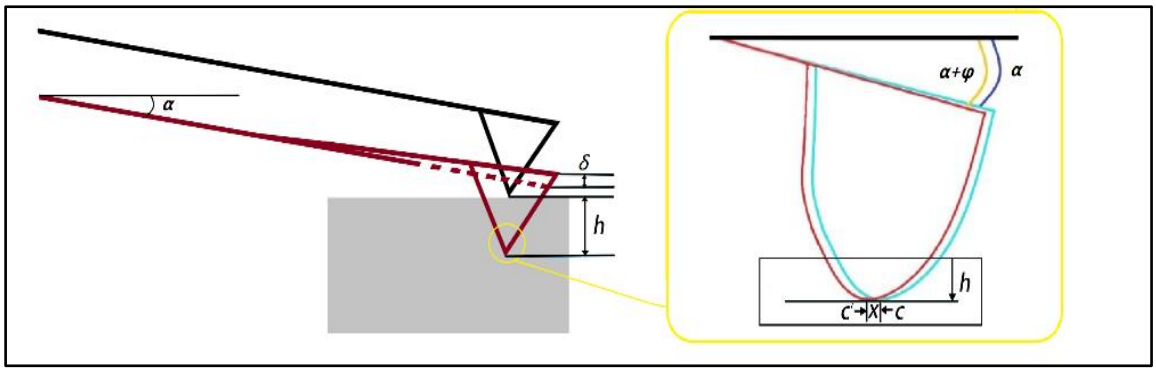

Figure 4.9 AFM probe in its working orientation

Hence, for a good estimate of the value of $\Delta\varphi$ the equations below are used:

$$\Delta\varphi = \frac{P_{max}L^2}{2EI} \tag{4.5}$$

$$h_{max} = \frac{P_{max}L^3}{2EI} \tag{4.6}$$

where, $\Delta\varphi$ is the shift in the inclination from the initial value φ, P_{max} is the maximum normal load applied, L is length of the cantilever, E is the elastic contact modulus of the cantilever's material, I is the moment of inertia of the cantilever cross section and h_{max} is the maximum depth.

If the indentation is assumed to be shallow, then the maximum nanoindentation depth h_{max} inside the indented material's surface $h_{max} \approx 50\,nm$. So, using (5) and (6) it is found that:

$$\Delta\varphi = \frac{3\,h_{max}}{2\,L} \tag{4.7}$$

Assuming $L \approx 100\,\mu m$ (manufacturer provided) then the value of $\Delta\varphi$ = 0.00075° (i.e., $rad = 0.043$) which can be considered as infinitesimal. Then, in this case to find the needed shifting distance X between C and C' using the following equation:

$$X = h_t \sin \Delta\varphi \tag{4.8}$$

Assuming $h_t \approx$ 10 μm then the estimated value of the shifting distance X=7.5 nm. Thus, this shift is considerably small, the rescaling formulae developed for the case of regular indenter to the AFM probe tips indenting soft elastic materials is applicable.

The tip shape can be described by a monomial function of radius $z=(\theta)r^d$ when it is in tis vertical position (i.e., α=0). Here, it is argued that the probe tip apex at the

working position (i.e., α=12°) could also be describe as this equation $z_1 = B_d(\theta)r^{d_1}$. For non-axisymmetric shaped tip, it is obvious that d_1 (approximation of the tip bluntness at the maximum depth) is not equal to *d* of the same tip at the vertical position and will be proven experimentally later.

It is important to remember that representing the AFM's tip shape is not a trivial task that can be solved by simply approximating it to a sphere as figure below highlights. As Figure 4.10 demonstrates, three possible spheres with three different radii can be applied to the same non-ideal shape and all having a certain amount of accuracies. Hence, to get more reliable tip shape representation, the non-ideal nature of the tip shape must be taken into consideration as discussed in Borodich et al. (2003a) in addition to Borodich and Galanov (2004).

The axisymmetric assumption used when profiling AFM tips is also erroneous as the following Figure 4.10 demonstrates.

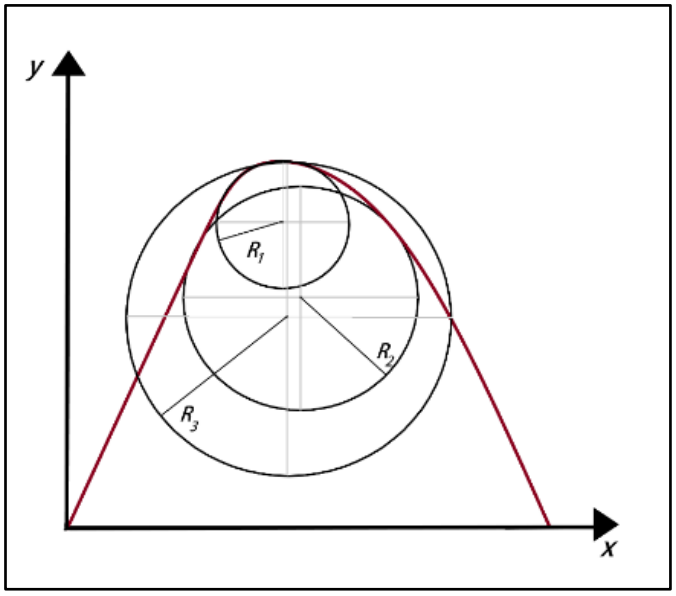

Figure 4.10 Non-ideal tip shape with 3 plausible spherical approximations to the real shape in the dark red colour

As 3D tip reconstruction Figure 4.11 (a) and (b) below suggests, the tip appears not axisymmetric and follows an arbitrarily changing profile due to manufacturing limitations at such small sizes. In particular, it can be observed that the slope on the RHS is steeper than on the LHS; this is corroborated with the top view of the same

image showing a clearer edge on the RHS than on the LHS, which is more gradient. In addition, looking at the 3D profile from a top view in Figure 4.11 (c), it can be dissected into 8 sections at 0°, 45°, 90°, 135°, 180°, 225°, 270° and 315° angles. Such consideration will allow in-depth analysis of the tip's non-axisymmetric nature. In Figure 4.11, the horizontal red line is always along the (0°-180°) axis, and the green lines represent the other 3 profiles.

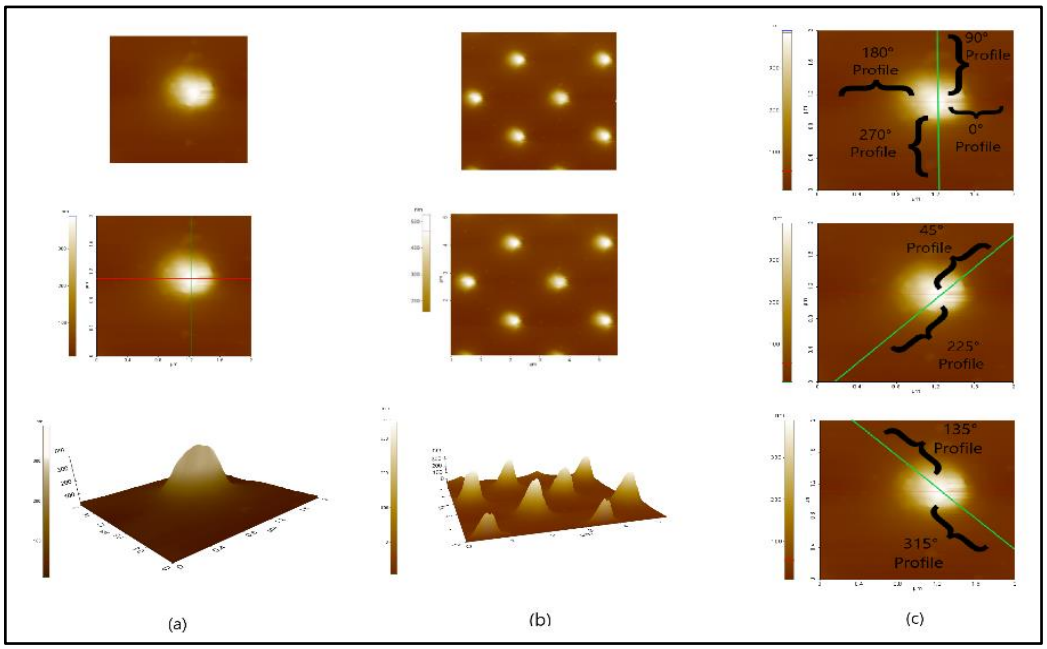

Figure 4.2 AFM images of the TGT01 tip characteriser scanned by one of the tested tips. Points (a) a single asperity, (b) are of multiple asperities and (c) Illustration of the selection of the (0°-180°), (90°-270°), (45°-225°), (135°-315°) profile cross sections for Tip

4.5 AFM nanoindentation: Load-displacement data

Here analysis of the load-displacement curves, extracting values from their respective slopes. Then, the values are used to calculate the bluntness values using the Borodich rescaling formula. Finally, the new values are used to evaluate the values obtained from the SEM images. From Borodich (1993) and also Galanov (1981b), assuming that the material is nonlinearly elastic then the depth of indentation $\alpha(c, P)$ under loadings P and P_1 is:

$$\alpha(c,P) = c^{(2-\mu)/[2+\mu(d-1)]}(P/P_1)^{d/[2+\mu(d-1)]}\alpha(1,P_1) \quad (4.9)$$

where c, is the ratio of slopes and is equal to 1 in our case. Whereas μ, is also equal to one because of linearity resulting in what Borodich et al. (2003a) explained that the load-displacement curve can be used to approximate the tip shape directly using the following relation:

$$d = 1/(m-1) \quad (4.10)$$

where d, is the tip shape and m come from the following equation:

$$LogP \sim \log (h-h_f)^m = mlog(h-h_f) \quad (4.11)$$

where, P is the Load, h is the displacement, h_f is the residual displacement, and m is the slope of the unloading part of the load-displacement curve.

And equation (4.9) was the product of comparing a modified version of equation (4.1) and equation (4.11):

$$logP = m\, log\big(h-h_f\big) \quad (4.12)$$

$$log\, z = log\ B_d(\theta) + d \log r \quad (4.11)`$$

Further on, the term $\big(h-h_f\big)$ will be referred to as δ Force-displacement curve as in the following figure. In Figure 4.12 (a) below, the dark red curve is the raw data obtained with an AFM instrument. The black curve shows the required data after removing the cantilever deflection. However, as Figure 4.12 (b) demonstrates, the process of shifting the data (i.e., using δ) is not a trivial task as any issues with the calibration (sensitivity analysis) will result in an incorrect shift in the data. In the same

figure, the red data set is the original curve, and the grey is the one made after calibrating the probe and finding that k was 14.1 N/m. However, clearly such value is incorrect and a 20 N/m (yellow) or 30 N/m (blue) are more likely to be the correct value for the spring constant of the probe.

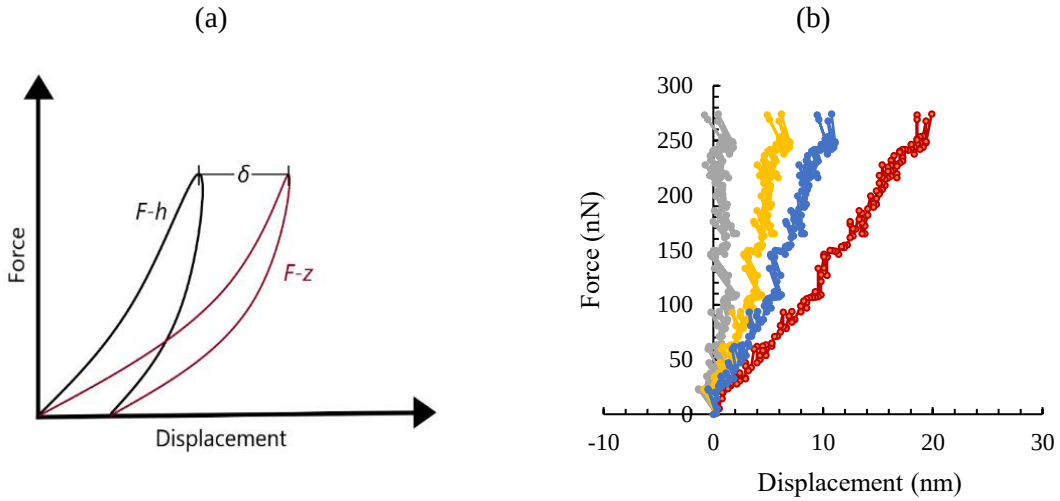

Figure 4.3 (a) Ideal Force-Displacement curve before and after considering the initial tilt of the AFM probe. (b) Practical unloading curve cases were the calibrated K value of 14.1 N/m produces incorrect curve (Grey) compared to 20 N/m (Yellow) and 30 N/m (Blue) in addition to the original data (Red)

4.6 Work of adhesion

A load-displacement relation was derived by Zheng and Yu (2007) which is based on an extended JKR theory for an arbitrary *d>0* and is based mainly on tip bluntness *(n≡d)*:

$$\tilde{\delta} \equiv \tilde{\delta}_H + \tilde{\delta}_a = \frac{1}{2}\mathrm{B}\left(\frac{n}{2},\frac{1}{2}\right)\tilde{a}^n - \sqrt{2\pi\tilde{a}} \tag{4.13}$$

$$\tilde{P} \equiv \tilde{P}_H + \tilde{P}_a = \frac{1}{\pi}\mathbf{B}\left(\frac{n}{2}+1,\frac{1}{2}\right)\tilde{a}^{n+1} - \frac{2}{\pi}\sqrt{2\pi\tilde{a}^3} \tag{4.14}$$

And the pull-off force is:

$$-\tilde{P}_c^{JKR-n} = \frac{2(2n-1)}{(n+1)\sqrt{2\pi}}\left(\frac{3\sqrt{2\pi}}{n\mathbf{B}\left(\frac{n}{2},\frac{1}{2}\right)}\right)^{3/(2n-1)} \tag{4.15}$$

where the function within the equations above **B**(α, β) is the beta function (Euler); subscripts "H" and "a" refer to the impact of the function of surface shape and the adhesive interaction of the surface. The beta function meanwhile can be expressed as $\boldsymbol{B}(\alpha,\beta) = \int_0^1 x^{\alpha-1}\,(1-x)^{\beta-1}\,dx$.

Several assumptions were made for the above equations including a sufficiently high load (i.e., adhesive component is negligible) as well as a large transition (transitioning from DMT-n to JKR-n) parameter Λ value.

The same study introduced a dimensionless load-displacement for the revised DMT model with a small Λ value:

$$\tilde{\delta} \equiv \tilde{\delta}_H + \tilde{\delta}_a = \frac{1}{2}\mathrm{B}\left(\frac{n}{2},\frac{1}{2}\right)\tilde{a}^n - 2n\Lambda^{(n-1)/n} \tag{4.16}$$

$$\tilde{P} \equiv \tilde{P}_H + \tilde{P}_a = \frac{1}{\pi}\mathbf{B}\left(\frac{n}{2}+1,\frac{1}{2}\right)\tilde{a}^{n+1} - n^{2/n}\Lambda^{(n-2)/n} \tag{4.17}$$

The pull-off force at zero contact radius:

$$-\tilde{P}_c^{DMT-n} = n^{2/n}\Lambda^{(n-2)/n} \tag{4.18}$$

where:

$\tilde{a} \equiv a/(Q^2\Delta\gamma E^{*-1})^{1/(2n-1)}$

$\tilde{\delta} \equiv \delta/(Q\,\Delta\gamma^n E^{*-n})^{1/(2n-1)}$

$\tilde{P} \equiv P/\pi(Q^3\Delta\gamma^{n+1}E^{*n-2})^{1/(2n-1)}$

$\Lambda \equiv \sigma_0(Q\,\Delta\gamma^{1-n}E^{*-n})^{1/(2n-1)}$

σ_0 is stress (constant)

4.7 AFM tip in working position

In this section, the steps taken from extracting the image to fitting the tip shape to the power law will be demonstrated.

4.7.1 SEM image analysis

Using a scanning electron microscope, 2D images of the tips of Bruker's RTESPA probes. Those images were taken with a magnitude of magnification of 5 x 10^5. Figure 4.13 shows the raw 2D image extracted from the SEM with .tiff extension. As this figure shows, the tip shape is differentiable from the background.

Also, two sets of probes of model RTESPA-300-125 and RTESPA-150-125 with 125 nm tip radii were analysed. RTESPA-300-125 probes have pre-calibrated probes with certified stiffness of $k = 40\ N/m$ whereas RTESPA-150-125 are similar but with $k = 6\ N/m$. An SEM system by Carl Zeiss of model 1540xB and a dual-focused ion beam was used to capture the images Figure 4.13 (a) shows the stiffer RTESPA-300-125 probe and Figure 4.13 (b) shows the softer RTESPA-150-125. Given that our analysis is based on comparing the tip's geometry to a monomial function, the image and specifically the tip's surface edge will be converted into a line on a plane so it can be superimposed on the graph mentioned earlier and extract d values by comparison. The RTESPA-300-125 probe will be used to explain the procedure used to extract the bluntness d value.

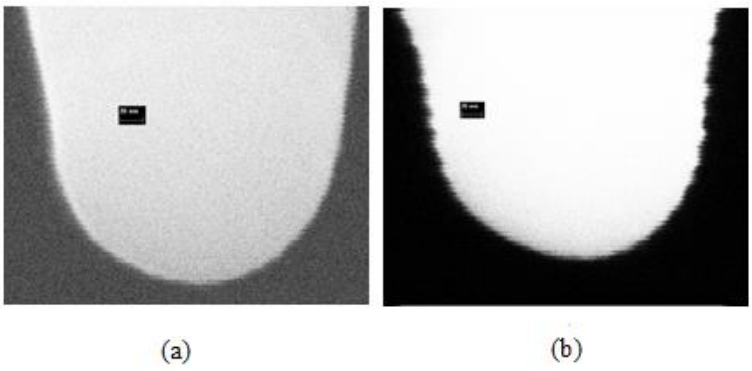

Figure 4.4 The SEM images of the two probes analysed with 5 x 105 magnification (a) RTESPA-300-125 probe tip (b) RTESPA-150-125 probe tip (scale of 20 nm is used)

Firstly, an increase to the contrast of the image is done to the point where a clearly defined line separates the tip and background without any grayscale gradient, as in Figure 4.14 (a). A photo processing software was used to edit the raw SEM image Figure 4.14 (a) resulting in the image obtained in Figure 4.14 (b).

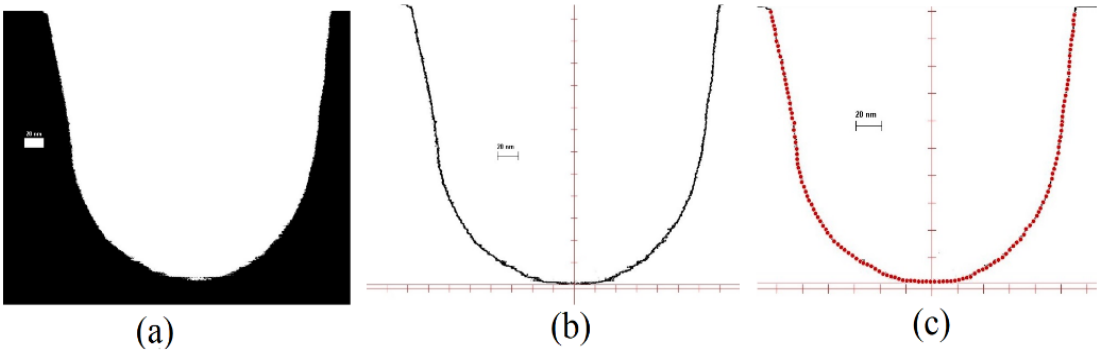

Figure 4.5 (a) Highly contrasted version of the SEM image (b) Adding the two major axes then the scale onto the added axes (c) Detection of data points (scale of 20 nm is used)

An important point to consider when contrasting the image is to make sure the overall size and shape of the tip do not change. Because, simply increasing the contrast using any photo editing software will increase the tip's size, making it blunter and yielding inaccurate values. The point of contrasting the image is to create a well-defined edge that can be detected using a software tool. The software imports images as matrices, with each pixel of the matrix having a different value corresponding to its colour. So, having a defined edge with no grey pixels (i.e., only black or white pixels) makes edge detection more robust.

The process starts by keeping the original image unchanged while an exact duplicate is edited to ensure the size does not change during the contrasting process. The duplicate is used as a 'layer' above the original, such layering functionality is available in most photo edits software. Then, the contrasting process begins by manually adjusting parameters such as levels, brightness, contrast, and exposure. While doing so, one must keep referring back to the original image. This is done by adjusting the opacity of the duplicate layer to allow seeing both the original and

duplicate. Hence, enabling a clear comparison between the edges of both layers, ensuring that the duplicate's edge does not shift away from the original's edge.

Once contrasting is complete and a clear edge is obtained. An edge detection software is then used to produce a continuous line of data points representing the tip's edge. After that, this continuous line's lowest point is determined and assigned a (0,0) value for two axes: horizontal representing the radius and vertical representing the tip's height. From this origin point, two curves will branch out: left-hand side and right-hand side curves. The two mentioned curves will be used later for further analysis and compared to the power law function. When the origin point is determined, a horizontal and vertical axis is added to the image where they intersect at the origin point. After that, cloning is done to the dimensions of the image scale (60 pixels ≡ 20 nm or 3 pixels ≡ 1 nm) located on the bottom-left corner of the two axes added as Figure 4.14 (b) shows. The two curves are then transformed into coordinate points, with the right-hand side having both positive horizontal and vertical values.

In contrast, the left-hand side has positive vertical values but negative horizontal ones. Figure 4.14 (c) shows the detected points. Using this method, the software scans the selected area of interest and the tip profile, and if any noise data is detected, those points can be removed manually. The software is programmed to detect black pixels inside the designated scanning area (excludes the scale). It scans every pixel, detects black ones and then calculates the distance from the reference origin. Two points on the vertical axis and two on the horizontal are determined manually, and from those four points, the software automatically interpolates and extrapolates the remaining points. To avoid detecting excessive points, a spacing of 7 pixels between each detected point is imposed on the horizontal axis while 6.5 on the vertical one. After locating the data points on the curve, the software generates a data sheet containing the coordinates of each point detected in an (X, Y) format. As mentioned before, this study focuses on nanoindentation and nanomachining. So, only the first 30 nm of the tip will be analysed as the part is in contact with the machined material.

The method used here consists primarily of the following steps for the right-hand side:

1. Converting the first 30 nm values into dimensionless values and creating a graph of the resulting values

2. Creating r vs r^d graphs were d = 1, 1.5, 2, 2.5 and 3
3. Superimposing each graph obtained in point 2 on the graph in point

Meanwhile for the left-hand side:

1. Mirroring the graph to the right-hand side to get positive values on the horizontal axis in addition to the already positive vertical axis
2. After that, the same three steps are done as in the right-hand side

Figure 4.15 represents plotting the extracted points as a verification to the work done earlier.

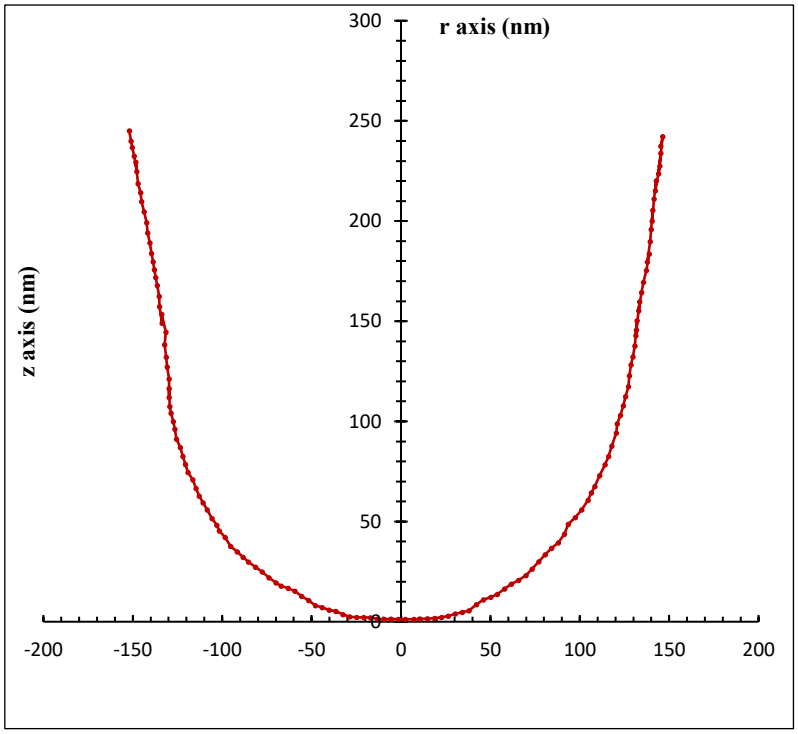

Figure 4.6 Data points extracted re-graphed

Now the first 30 nm of the tip are converted into dimensionless values (ratios) ranging between 0 and 1 and superimpose them on d values shown in Figure 4.16 (a) for the left-hand side and Figure 4.16 (b) for the right-hand side. It should be noted that all tip figures from now on will be presented in their respective dimensionless forms.

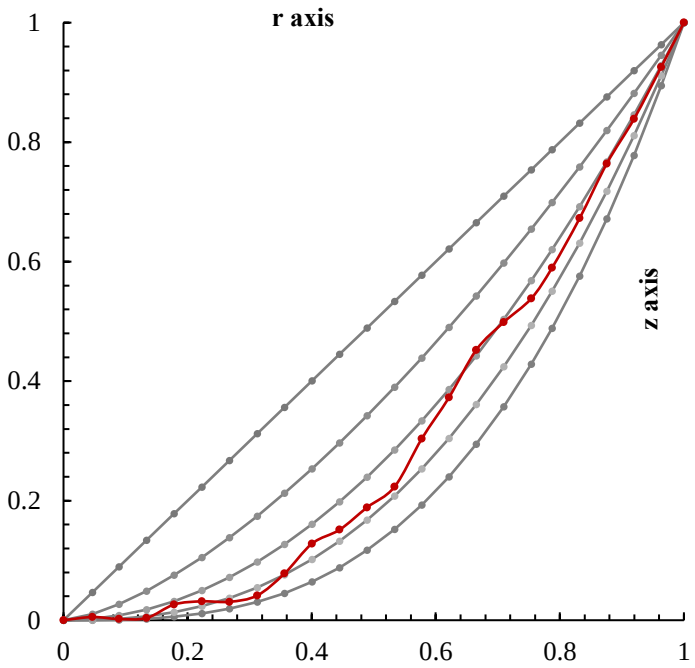

(a)

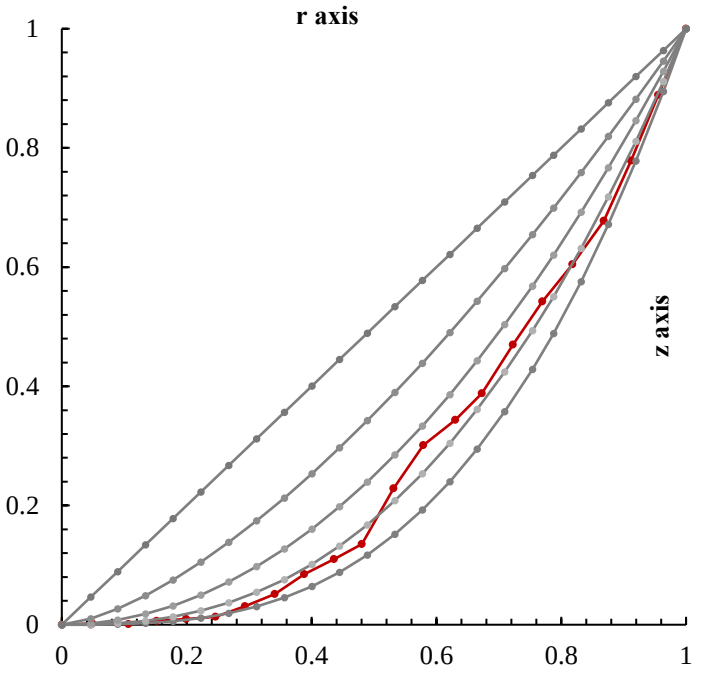

(b)

Figure 4.7 LHS (a) and RHS (b) of actual vertical tip shape (red) over d values 1 to 3 with 0.5 intervals

4.7.1.1 Rotating the tip 12° clockwise

It is important to remember that the tips operate at 12° clockwise rotated orientation and not vertical as the image shows. So, applying the rotation matrix to the values obtained earlier.

The rotation matrix for a clockwise rotation is as in the equation below:

$$R(-\theta) = \begin{bmatrix} \cos\theta & \sin\theta \\ -sin\,\theta & \cos\theta \end{bmatrix}$$

where $\theta = 12°$

As Figure 4.17 (a) shows, rotating about the lowest point created a new lowest point. And for the method to work the graph must always be in the positive vertical axis. So, locating the new lowest point is done and a shifting of the graph in a way that allows this point to be the new origin or (0, 0), as the Figure 4.17 (b) demonstrates. In addition, the rotation of the tip will expose a different portion of the surface to contact the machined material; hence a different value of d are to be expected, as Figure 4.17 (b) highlights.

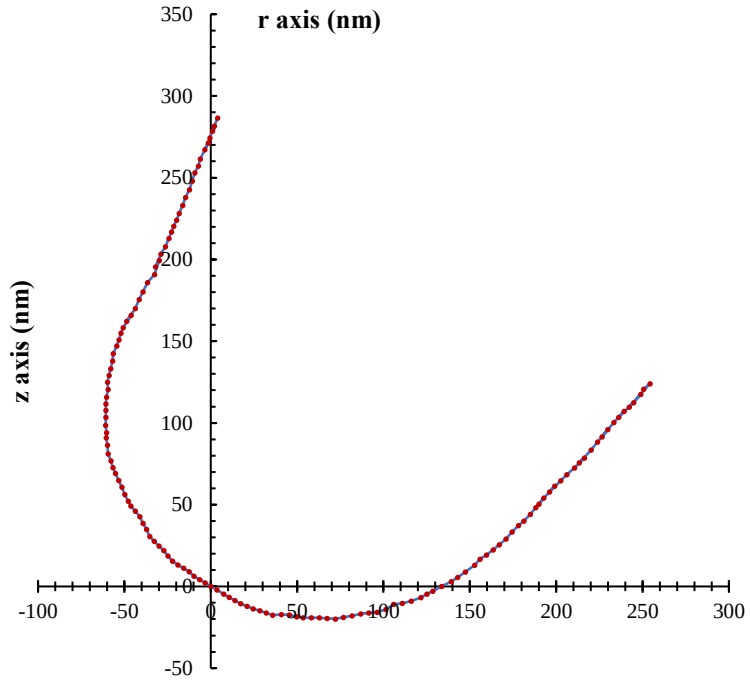

(a)

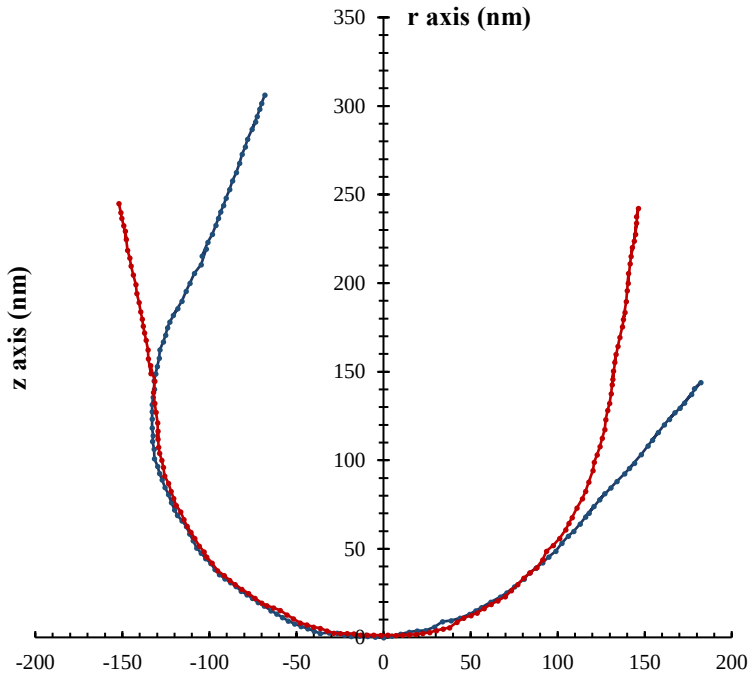

(b)

Figure 4.8 (a) Tip data points after applying the 12^{O} clockwise rotation matrix (b) repositioning of the rotated tip shape with a new origin point and no values below zero

Figure 4.18 shows the tip in its new orientation both left- hand (a) and right-hand (b) sides compared to different d values.

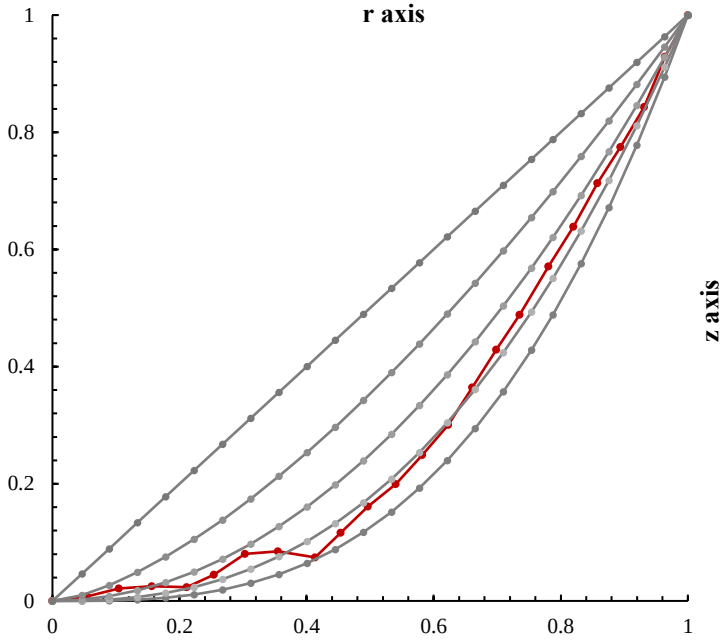

(a)

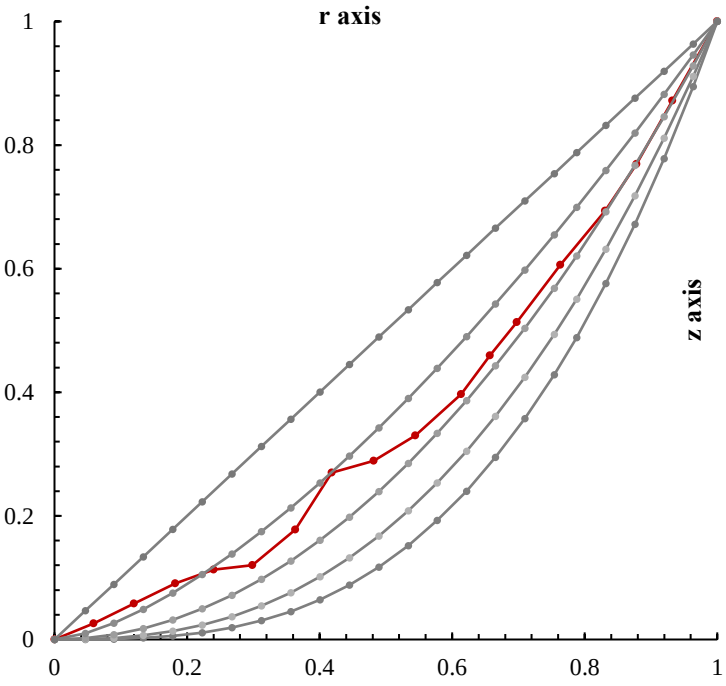

(b)

Figure 4.9 LHS (a) and RHS (b) actual rotated tip shape (red) over d values 1 to 3 with 0.5 intervals

4.7.2 AFM nanoindentation: force-displacement analysis

The Atomic Force Microscope used in this experiment is the XE-100 model from Park Systems positioned over a TS 150 anti-vibration table from Table Stable dampening vibrations using three individual piezoelectric actuators. Bruker's RTESPA probes were used in this experiment as they are pre-calibrated and have certified spring constant values allowing for more robust experimental outcomes. Multiple trials of the same test and probe were conducted due to the nature of polycarbonate, where different indentation locations can produce different indentation behaviour hence the need to deal with average values rather than exact instances as discussed Bouchonville and Nicolas (2019). High bluntness values were not considered because physically they indicate that the contact was completely flat due to unattended reasons such as contamination. The fifth and sixth sets of testing, for example, resulted in around 200 load-displacement graphs each (consequently the same number for m and d values) to have better confidence in the results.

The first set of nanoindentations consisted of using probe 5 $k = 40\ N/m$ to indent a polycarbonate sample. After the first set, probe 5 $k = 40\ N/m$ underwent a series of scratching processes to increase its bluntness and investigate whether it is reflected with a new nanoindentation test represented in the second set. Again, tested on a polycarbonate sample. The third and fourth sets of testing included the use of the softer probe 5 $k5$ on polycarbonate and copper, respectively. As for the fifth and sixth sets, probe 4 $k40$ was used on copper and polycarbonate, also respectively. All sets had pre-set values of depth starting from 10 nm up to 100 nm with 10 nm intervals, all at different locations within the PC sample. Starting from set four, instead of doing one indentation for each depth, six were done all averaged into one value. Test number 8 (depth of 80 nm) of the second set will be used to present how the data imported from the AFM software is analysed and d value is extracted from it.

Figure 4.19 (a) does not consider the inherent deflection of the probe when mounted in the AFM hence the need to consider $(h - h_f)$ arises which is also known as δ all discussed earlier which in turn is considered in Figure 4.19 (b). Finally, the log

values of both force and displacement are taken and the slope of the new curve is taken which is value m that is used to find bluntness value d.

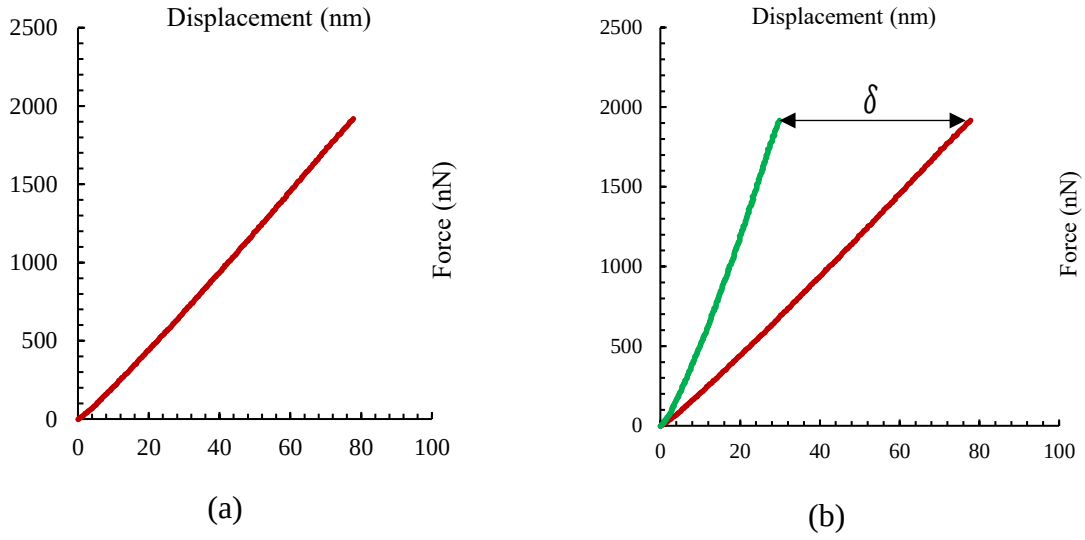

Figure 4.10 (a) Raw unloading data extracted from AFM software Mirroring and removal of extra unnecessary points Raw unloading data extracted from AFM software (b) taking δ into account (Red line old, Green line new)

4.8 Results and Discussions

Results obtained in the experimental work are explained and discussed in this section.

4.8.1 SEM vertical orientation

Examining Figures 4.20 it is clear that the left-hand side (LHS) curves upwards at a further distance from the centre than the right-hand side (RHS) i.e., blunter. Hence, d values must be higher in the LHS and indeed the LHS as Figure 4.20 (a) shows almost perfectly follows the $d=3$ line with a small deviation towards $d=2.5$ where the RHS in Figure 4.20 (b) varies between $1.5<d<2$.

Discussing the changes of d value quantitatively rather than qualitatively and taking the LHS portion for analysis, it should be expected that a value near but less than 3 as

discussed earlier to be present. Figure 4.20 (a) has a best-fit curve over the tip's actual shape. The grey continuous line represents a monomial power law function $z(r)=r^{2.2}$ where $B_d(\theta) = 1$.

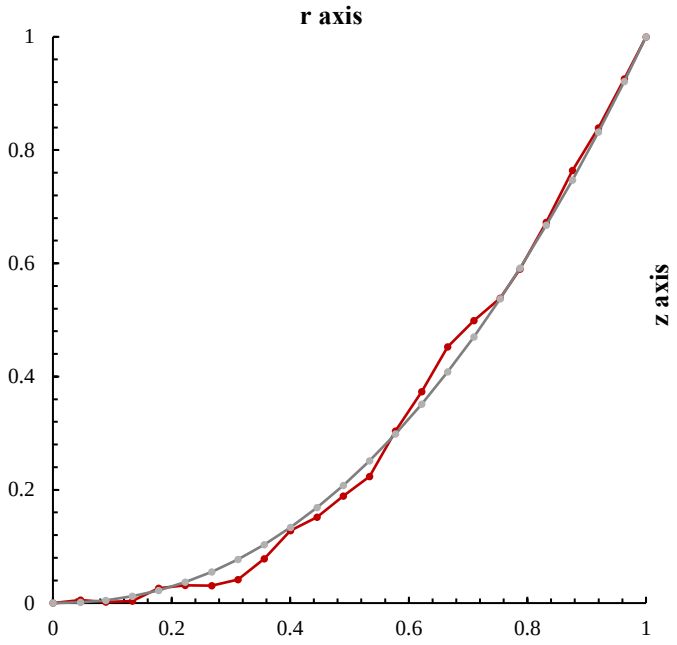

(a)

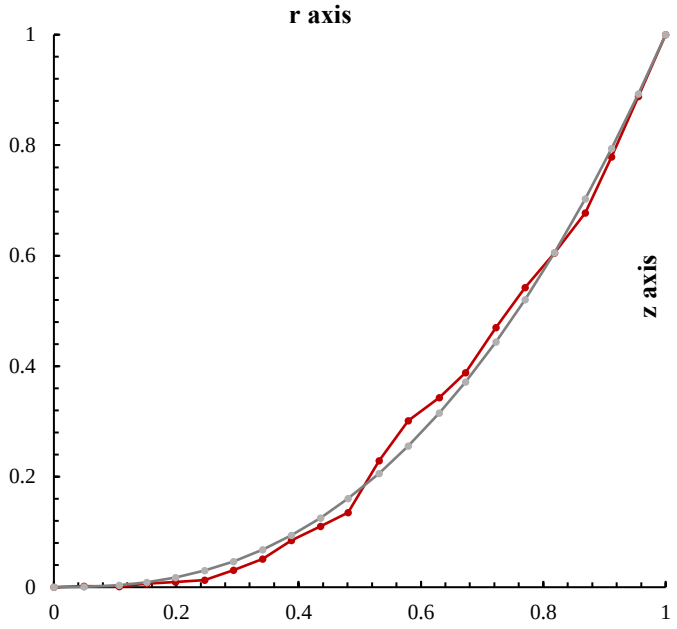

(b)

Figure 4.20 Actual tip shape (Red) and curve fit of power law function (grey) (Dimensionless) for (a) LHS (Vertical) and (b) RHS (Vertical)

As for Figure 4.20 (b), it also has a best-fit curve over the tip's actual shape. The grey continuous line represents a monomial power law function $z(r)=r^{2.5}$ where $B_d(\theta) = 1$. Regarding the RTESPA-150-125 probe, the left-hand side had a d value of 1.8 whereas the right-hand side had a 2.1 d value.

4.8.2 SEM 12° clockwise rotation

On the other hand, rotating the tip creates a new lowest point with different d values which refutes any assumption that suggests that the probe's tip is a circle although some parts have d values close to 2.

Figure 4.21 (a) and (b) show the new LHS and RHS tip shapes respectively compared to their best fit curve with monomial power law functions $z(r)=r^{2.4}$ and $z(r)=r^{1.7}$ where $B_d(\theta) = 1$ for both.

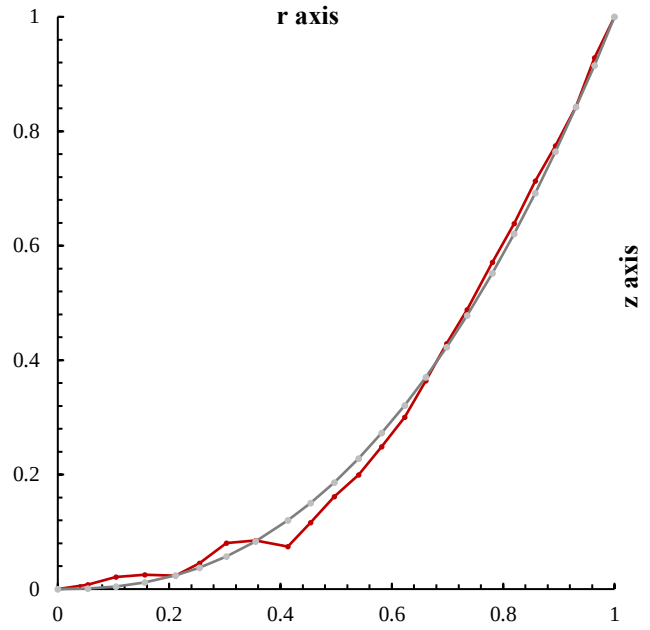

(a)

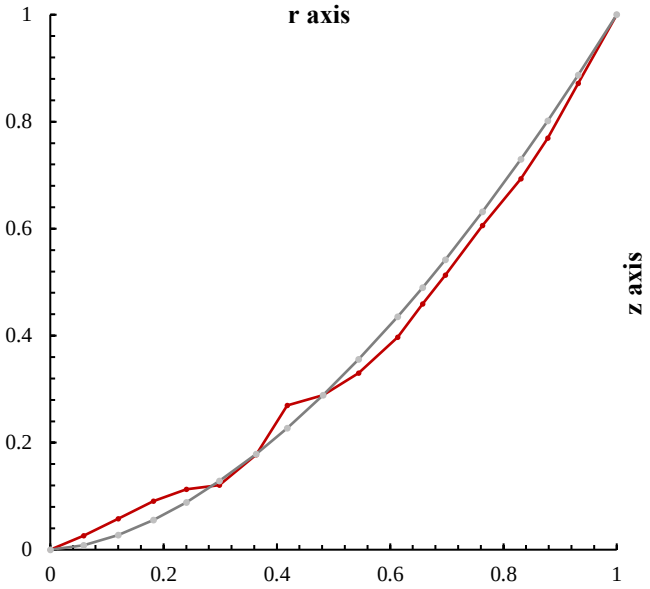

(b)

Figure 4.11 Actual tip shape (Red) and curve fit of power law function (grey) (Dimensionless) for (a) LHS (Tilted) (b) RHS (Tilted)

Concerning the RTESPA-150-125 probe, the left-hand side had a d value of 2.2 while the right-hand side had a 2.4 d value.

4.8.3 AFM nanoindentation

As mentioned earlier, there were six sets of tests. Both m (slope of log curves) values and d values (bluntness values) as well as their average and standard deviations were recorded. Points of the first half of the unloading curve were considered only due the distortion in the other 50%. The m values were considered due to the inverse relationship between it and d causing m values near unity to be unproportionally high.

4.8.3.1 First set

RTESPA-300-150 probe no. 5 was used in this test with pre-calibrated $k = 40\ N/m$ and 125 nm tip radius (spherical as stated by the manufacturer). The test sample was polycarbonate. For this set the average m value was 1.41 with 0.14 standard deviation as for the bluntness d value it was 2.73 with 1.07 standard deviation.

4.8.3.2 Second set

Same probe as in the first set but blunted by scratching it over a harder material. Here, the average m value was 1.27 with 0.07 standard deviation. As for the d value, the average was 3.79 having 0.74 standard deviation.

4.8.3.3 Third set

In this set a $k = 6\ N/m$ probe was used with all other specifications like the previous stiffer one. Due to its softness, this probe bended heavily and kept twisting due to the electrostatic field of the polycarbonate causing huge distortions in the force-displacement graphs yielding them unusable.

4.8.3.3 Fourth set

The same $k = 6\ N/m$ probe was utilised but the sample in this case was copper to negate the impact of the electrostatic field. And indeed, it did, the probe behaved normally. However, due to its softness and hardness of the copper sample the results were also unreliable as the slopes extracted were way off which in turn can be explained by the fact that the probe itself was bending and it wasn't actually penetrating the material. Due to the AFM design, it cannot differentiate between indentation and upward bending as it only detects changes on the reflected laser off the probe and onto the position sensitive photodiode detector (PSPD). The standard deviation in this set was 0.02 which is logical given the crystalline nature of polished copper sample and how it is unlikely for the probe to behave differently at different indentation sites.

4.8.3.3 Fifth set

This set utilised probe number 4 with specifications similar to the one in the first set. The sample was also the crystalline copper one. This set had better average d values than the previous one but given the fact that a large standard deviation in d values indicated that the same issue as above is faced where it is more likely that the probe itself bends instead of real indentation within the copper sample.

4.8.3.3 Sixth set

The same probe used in the fifth set was utilized but this time on a polycarbonate sample making this set a validation one to the first set with a 10 second holding time in this case instead of non as in the first.

Here, the average m value was 1.36 with 0.14 standard deviation. Regarding the d values, the average was 2.42 having 3.50 standard deviation

4.8.3.4 Average *m* and *d* values

Table 4.1 below shows average *m* and *d* values for all sets mentioned. Where, sets with significantly high *d* values were referred to as 'flat' and all *d* values were calculated using Eq. 4.10.

Table 4.1 average *m* and *d* values for test sets

Set no.	***m* value**	***d* value**
1	1.41	2.73
2	1.27	3.79
3	Flat	Flat
4	Flat	Flat
5	Flat	Flat
6	1.36	2.42

Regarding the flat values, Figure 4.22 shows the raw force-displacement data of one of the tests that exhibited a linear relation. This consequently resulted in significantly high *d* values of more than 60 (i.e., flat contact). A plausible explanation of the linear relations observed in many tests during the experiment, including the example in the figure below that shows one test conducted in the first set, may be explained due to the nature of the soft polymer used containing weakly connected macromolecules that may stick to the nose of the indenter creating some sort of a stagnant zone that moves together with the indenter.

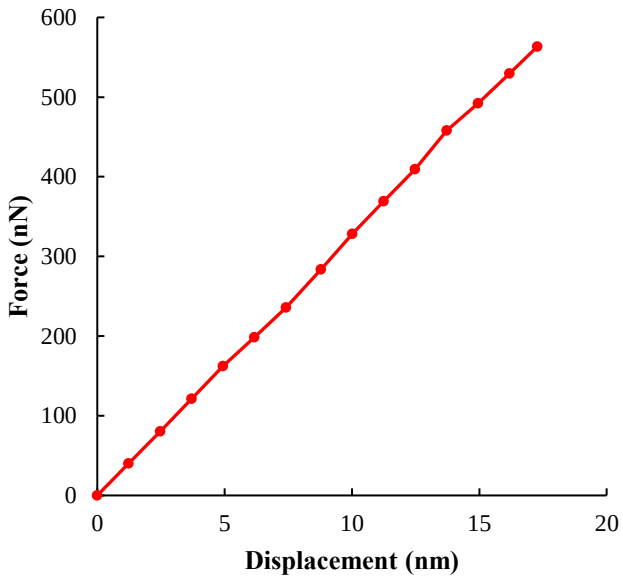

Figure 4.12 Linear force-displacement curve caused by a flat contact

In fact, the existence of a stagnation zone was observed for many materials as in Shaw (2005). In the case under consideration, the stagnation zone forms a pseudo-nose of the indenter that penetrates together with the indenter without widening the size of the deformed zone, i.e., it acts similarly to a flat-ended cylindrical indenter in the Boussinesq problem. As a result, a Hertz-type contact problem with a continuously increasing contact zone is not observed, but a contact region of a constant size, i.e., a Boussinesq-type contact problem for flat-ended cylinder. A copper sample was also tested; however, no useable data were extracted due to the material's hardness.

4.8.4 Impact of tip bluntness on pull-off force

Given that the experiments are done using workpieces made of soft materials, the JKR-n model is most suitable. Substituting values obtained in equation 4.16 into equation 4.15 gives the graph in Figure 4.23.

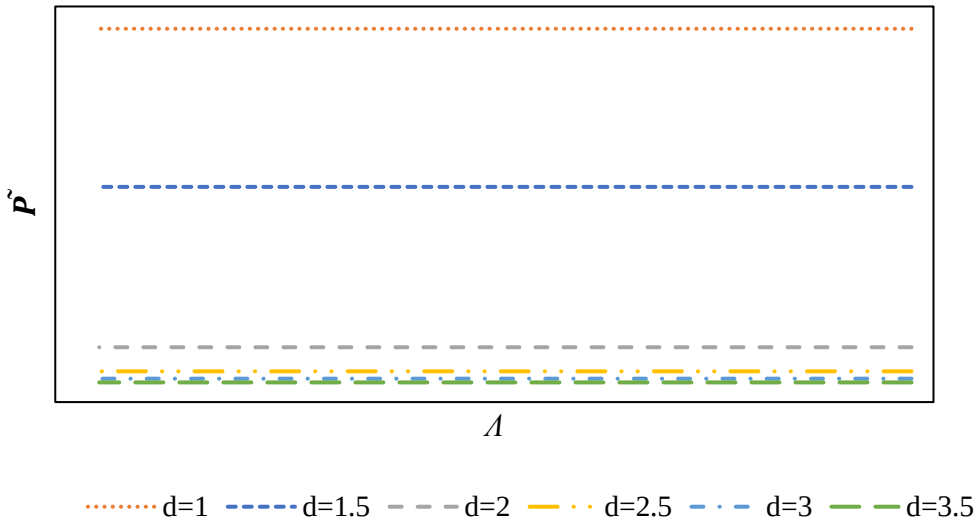

Figure 4.13 $\tilde{P}$ – Λ graph for bluntness values from 1 to 3.5

Results are presented by comparing the pull-off force corresponding to d values obtained with integer values above and below estimated value. So, when considering that:

The vertical orientation **left-hand** side of tip which has a bluntness degree $z(r) = r^{2.2}$:

- If bluntness is assumed 2 instead of 2.2 this yields a 6% error in the estimation
- If bluntness is assumed 3 instead of 2.2 this yields a 7% error in the estimation

The vertical orientation **right-hand** side of tip which has a bluntness degree $z(r) = r^{2.5}$:

- If bluntness is assumed 2 instead of 2.5 this yields a 10% error in the estimation
- If bluntness is assumed 3 instead of 2.5 this yields a 3% error in the estimation

Also,

Also, considering the tilted orientation **left-hand** side of tip with $z(r) = r^{2.4}$:

- If bluntness is assumed 2 instead of 2.4 this yields a 9% error in the estimation
- If bluntness is assumed 3 instead of 2.4 this yields a 4% error in the estimation

And the tilted orientation **right-hand** side of tip with $z(r) = r^{1.7}$:

- If bluntness is assumed 1 instead of 1.7 this yields a 222% error in the estimation
- If bluntness is assumed 2 instead of 1.7 this yields a 12% error in the estimation

Variation in pull-off force from the vertical assumption, and the tilted one is also analysed:

Tilted orientation **left-hand** side of tip $z(r) = r^{2.4}$ vs $z(r) = r^{2.2}$ vertical orientation:

- If tip is assumed vertical instead of tilted this yields a 3% error in the estimation

Tilted orientation **right-hand** side of tip $z(r) = r^{1.7}$ vs $z(r) = r^{2.5}$ vertical orientation:

- If tip is assumed vertical instead of tilted this yields a 20% error in the estimation

Finally, by comparing the bluntness value 2.3 extracted using AFM nanoindentation that represents a 3D value with 2 provided by the manufacturer it is easy to realise that if tip is assumed perfectly spherical instead of the actual blunter shape this yields a 6% error in the estimation.

Table 4.2 below summarises the effect of inaccurate estimation of the tip bluntness on the estimation of the pull-off force.

Table 4.2 The P(actual)/P(assumed) ratios and their respective error percentages

P(actual)/P(assumed)	**Pull-off force error percentage**
2.2/2	6%
2.2/3	7%
2.5/2	10%
2.5/3	3%
2.4/2	9%

2.4/3	4%
1.7/1	222%
1.7/2	12%
2.4/2.2	3%
1.7/2.5	20%
2.3/2	6%

And to highlight the issue further, Table 4.3 below demonstrates pull off force estimation error percentages for arbitrary bluntness values.

Table 4.3 The P(actual)/P(assumed) ratios and their respective error percentages for arbitrary values

P(actual)/P(assumed)	**Pull-off force error percentage**
1.5/1	90%
1.5/2	48%
2.5/2	14%
2.5/3	3%
3.5/3	<3%
3.5/4	<3%
4.5/4	<3%
4.5/5	<3%

4.9 Exploring the effective rake angle effect on ideal AFM tips

Four theoretical tips are used in this investigation which are created using equation 4.1 as in Figure 4.24 (a) and are rotated 12° using the rotation matrix as Figure 4.24 (b) shows.

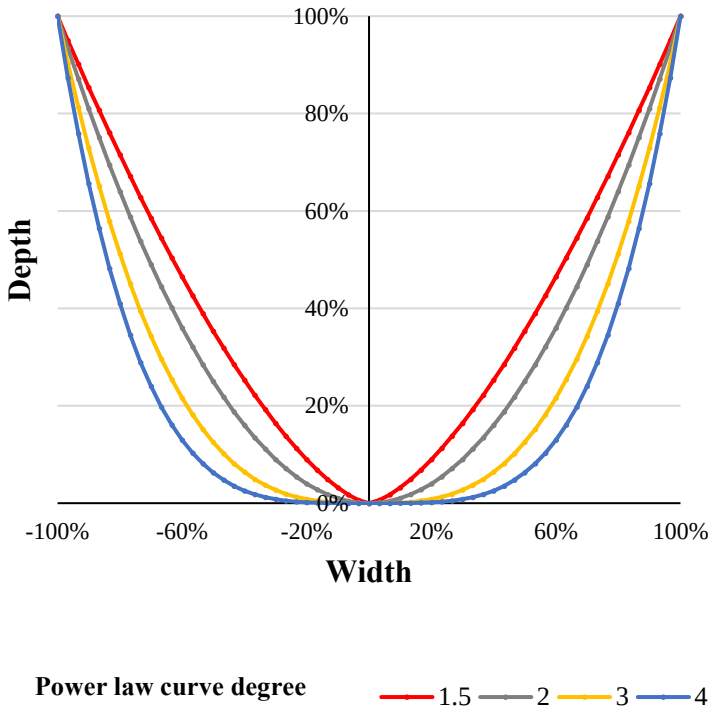

(a)

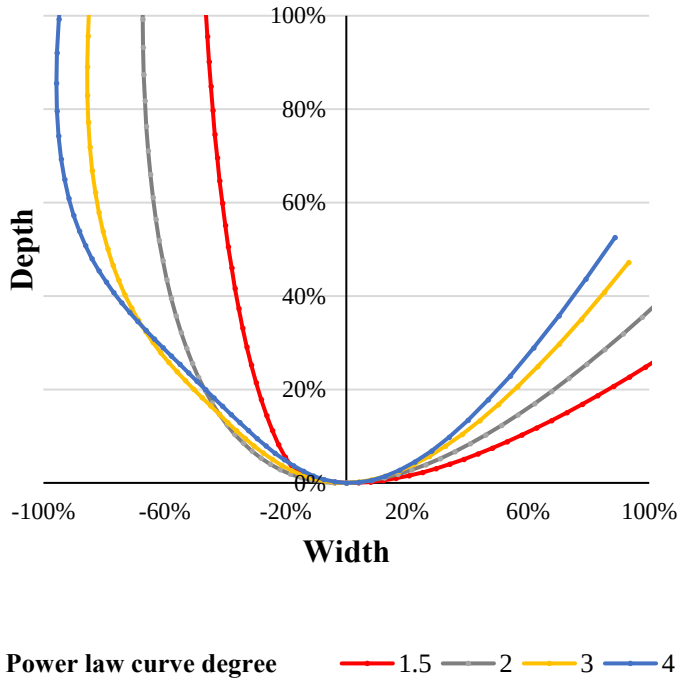

(b)

Figure 4.14 Idealised AFM tip profile curves of degrees 1.5, 2, 3 and 4 (respectively referred to as $r^{1.5}$, r^{2}, r^{3}, and r^{4}): (a) in the vertical orientation and (b) tilted 12° clockwise.

The evolution of the effective rake angle as a function of the change in penetration depth was studied by considering different scenarios where 20%, 40%, 60% and 80% of the tip depth is in contact with the material in the vertical and tilted orientations as shown in Figure 4.25.

The data points from both orientations were used to calculate and measure the effective rake angle. More specifically, this angle was calculated using trigonometry as the angle between a vertical line and the line connecting the lowest point of the tip to the point where workpiece material separates from the tip face (see Figure 4.25). This figure illustrates such an angle for a tilted tip profile with a power law exponent of 1.5 in the configuration where the workpiece velocity is oriented in a direction parallel to the long axis of the AFM probe cantilever and pointing away from it.

Figure 4.25 highlights how the negative effective rake angle is defined using separation point *S*. When connecting the lowest point of the cutting tool with the separation point, the effective rake angle is estimated as the angle between this line and the vertical line normal to the cutting plane, as also applied in Vogler (2003) for

instance. This separation point can be challenging to estimate in practice. Hence why Manjunathaiah and Endres (2000) suggested using a multiplication factor of the uncut chip thickness to approximate it, with $1.5a$ being an acceptable estimate.

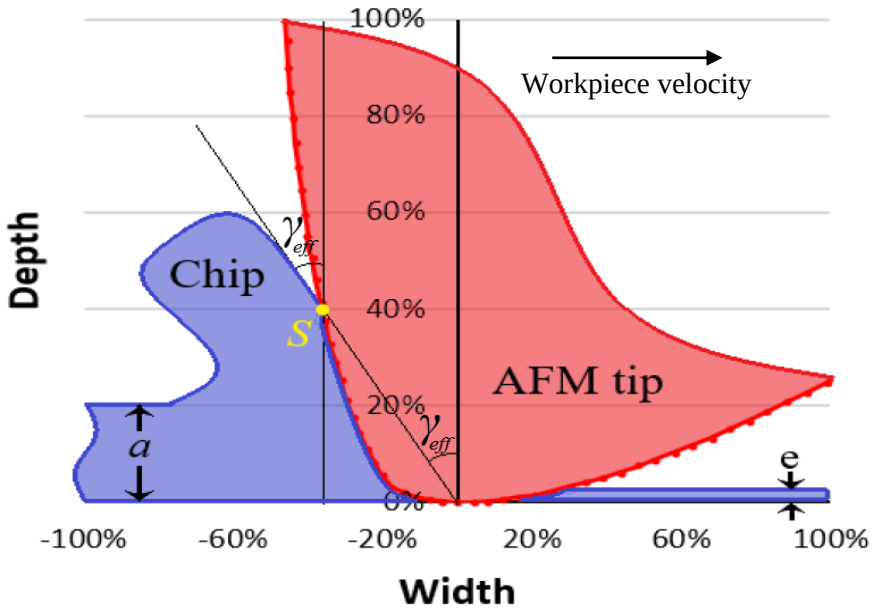

Figure 4.15 Representation of a 12° tilted AFM tip with bluntness of $r^{1.5}$ during nanomachining highlighting the effective rake angle (γ_{eff}), the uncut chip thickness (a), the elastic recovery (e) and separation point S. (angles not to scale)

4.9.1 Theoretical analysis outcome

The changes of the rake angle due to variations of the depth of contact between the tip and the material are presented in Figure 4.26 and Figure 4.27. The data given with Figure 4.26 are for the simplification where the tip is assumed to be in a vertical orientation. The results reported in the titled orientation with Figure 4.27 are for the case already illustrated in Figure 4.25, i.e., when the workpiece velocity is oriented in a direction parallel to the long axis of the AFM probe cantilever and moving away from the fixed end of the cantilever.

It can be observed that for both orientations of the tip, a smaller penetration into the workpiece material results in a more negative rake angle for the same tip profile, as expected. Also, as the tip shape becomes blunter, i.e., when the value of power law exponent, *d*, increases, the rake angle also becomes more negative for the same depth.

This is true for both orientations and again, this is an expected result. However, it is worth noting that this effect becomes less pronounced as the penetration depth becomes larger.

With respect to the influence of the tilt of the AFM probe on the effective rake angle, two main observations can be made. First, the angle is less negative for all values of tip bluntness and penetration depth in the tilted orientation. Second, and importantly, for a given penetration depth, the wear of the tip (i.e., the increase in bluntness) has a more important effect on the effective angle when taking into account the tilt of AFM probes. This is an important result given that this tilt is often overlooked in AFM-based nanomachining studies.

For example, in the tilted orientation, the change in rake angle between a sharper tip with d = 1.5 and a blunt tip with d = 4 is 72% for a condition of 20% contact between the material and the tip. This change in rake angle is much less, 22%, for the same contact condition when the tip is assumed to be vertical. It is also important to remember that this conclusion applies when the machining velocity of the workpiece is considered to be parallel to the long axis of the cantilever and pointing away from it.

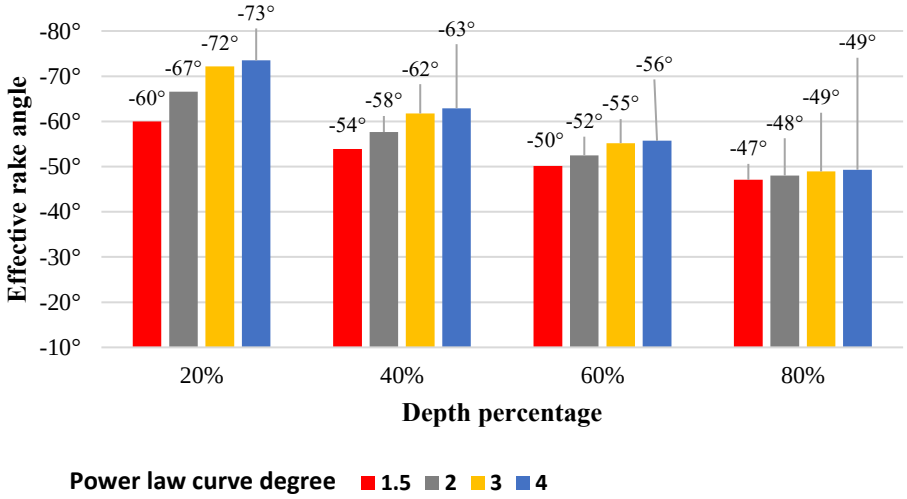

Figure 4.16 Effective rake angles for tip profile curves $z \sim r^{1.5}$, r^2, r^3, and r^4 at depths of 20%, 40%, 60% and 80% of the vertical orientation

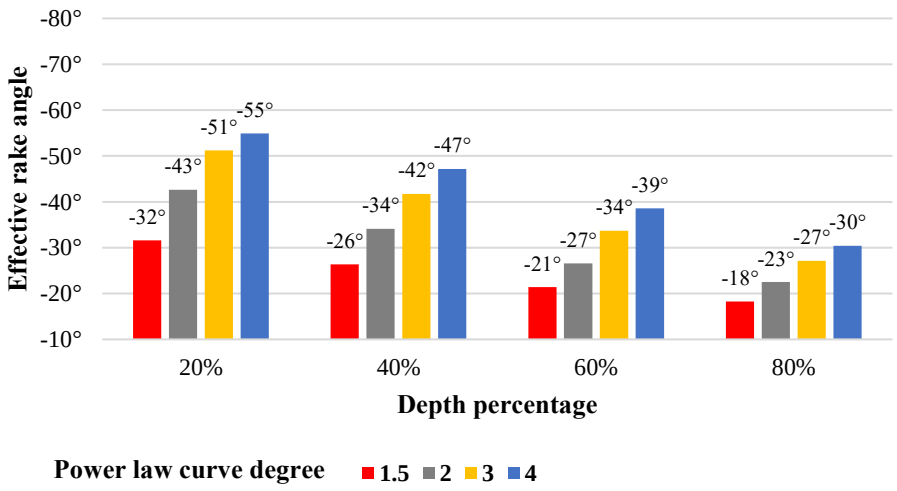

Figure 4.17 Effective rake angles for tip profile curves $z \sim r^{1.5}$, r^2, r^3, and r^4 at depths of 20%, 40%, 60% and 80% of the tilted orientation

4.10 Summary

With the increasing need for more accurate AFM probes as measuring tools while not being able to rely on the specification provided by manufacturers, our work provides an accurate tip characterisation tool. The novelty of this approach is that it enables representing the tip bluntness with real positive numerical values instead of integers only. For example, if a tip has an n value of around 2.5 whether to approximate it to 2 or 3 will be a difficult task, and in either case the error or difference will be quite considerable.

Also, this approach analysed the tip both in its vertical and working (12° clockwise orientation) positions and highlighted how erroneous if it is assumed that those two orientations are equivalent and interchangeable.

Noting that the data extracted from load-displacement data is 3D representation of the tip shape and its value can be considered as a benchmark for the other results.

Another noticeable outcome was the inverse relationship between the increase in the tip bluntness and the change in the pull-off force. This was corroborated using the work of adhesion analysis, in which the error percentage resultant from assuming integer values rather than real numbers was calculated. Such was done for a wide range of bluntness values where the error was more significant in cases where the tip is sharper (i.e., bluntness values closer to 1). This supporting the notion that adhesive interactions play bigger roles due to how ‘sticky’ interactions are at the nanoscale.

Moreover, considering each side of the tip individually plays a bigger role in nanomachining applications where the direction of the machining process does in fact impact the process’s outcome Al-Musawi and Brousseau (2016).

In turn, tests with significantly high *d* value were referred to as ‘flat’, which in turn was attributed to the existence of stagnation zones in the tested material, causing what is hypothesised to be a Boussinesq-type contact problem for a flat-ended cylinder.

The number of various applications of AFM-based nanomachining is rapidly increasing. Consequently, the need also increases for accurate characterisation of the AFM probe tip that works as the cutting tool. Here the impact of the tip shape, depth of penetration and orientation of AFM probes on the effective rake angle during AFM-based nanomachining has been studied. The main features of the models under

consideration are the following: (i) the AFM tip model used in the analysis is assumed to be axisymmetric; (ii) the impact of the tilt angle is studied for a single direction of AFM machining; and (iii) the surface of the tip is assumed to be completely smooth.

It is highlighted that care should be taken when representing an AFM tip in its working conditions, whether the application is practical and/or concerned with numerical studies. The effects of each of the abovementioned three factors have been analysed separately. It has been shown that each of these factor affects the rake angle, especially the AFM probe tilt angle. The analysis presented is dimensionless, allowing researchers to apply the results to various tip sizes because the model can be scaled up or down to fit any specific application.

The importance of the results presented becomes more prominent as the scale decreases, i.e., the results are more important on the nanoscale than on the microscale where undeformed chip thickness becomes increasingly close to or smaller than the edge radius of the tool. It is shown that the results are also vital for AFM nanomachining applications that may be affected by tip wear.

Chapter 5

Vibration-assisted Nanomachining Experimental Setup

5.1 Introduction

In this chapter, the one direction vibration-assisted nanomachining is analysed. After that, the test setup with all of the hardware and software needed to complete the experiments are presented. Subsequently, the conditions of the tests as well as the parameters are discussed. Finally, a brief explanation of how the SEM images and the AFM scans of the grooves are taken, in addition to some inherent limitations are presented.

5.2 Test Setup

In order to investigate the impact of the induced vibrations on the ultraprecision machining process of single crystal copper, nine tests with different amplitudes and frequencies of vibrations were conducted, in addition to the conventional nanoscratching tests that were used as a benchmark to compare which testing conditions provided the best results. Figure 5.1 demonstrates the motion of the proposed vibration-assisted nanomachining tests. The one-direction vibrations occur along the longitudinal axis of the probe, highlighted by the two-headed black arrow in Figure 5.1. Meanwhile, the cutting direction illustrated in Figure 5.1 goes along the longitudinal axis of the probe and away from its base (chip), as shown by the red arrow in Figure 5.1.

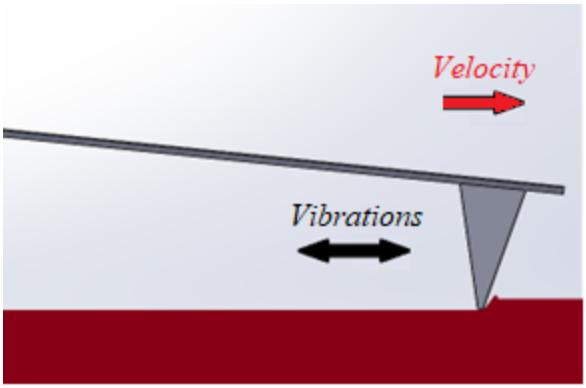

Figure 5.4 Proposed nanomachining method with one direction vibrations and showcasing the feedforward case

Figure 5.2 and Figure 5.3 show the setup used for testing and the corresponding signal flow graph, respectively. As Figure 5.3 demonstrates, the signal flow starts from the signal generator with a specific amplitude and frequency. Then, the amplitude of the signal is amplified using the voltage amplifier. Finally, the signal is sent to both the piezoelectric shear stack within the AFM to generate the vibrations, and to the oscilloscope to validate that the desired signal is being sent.

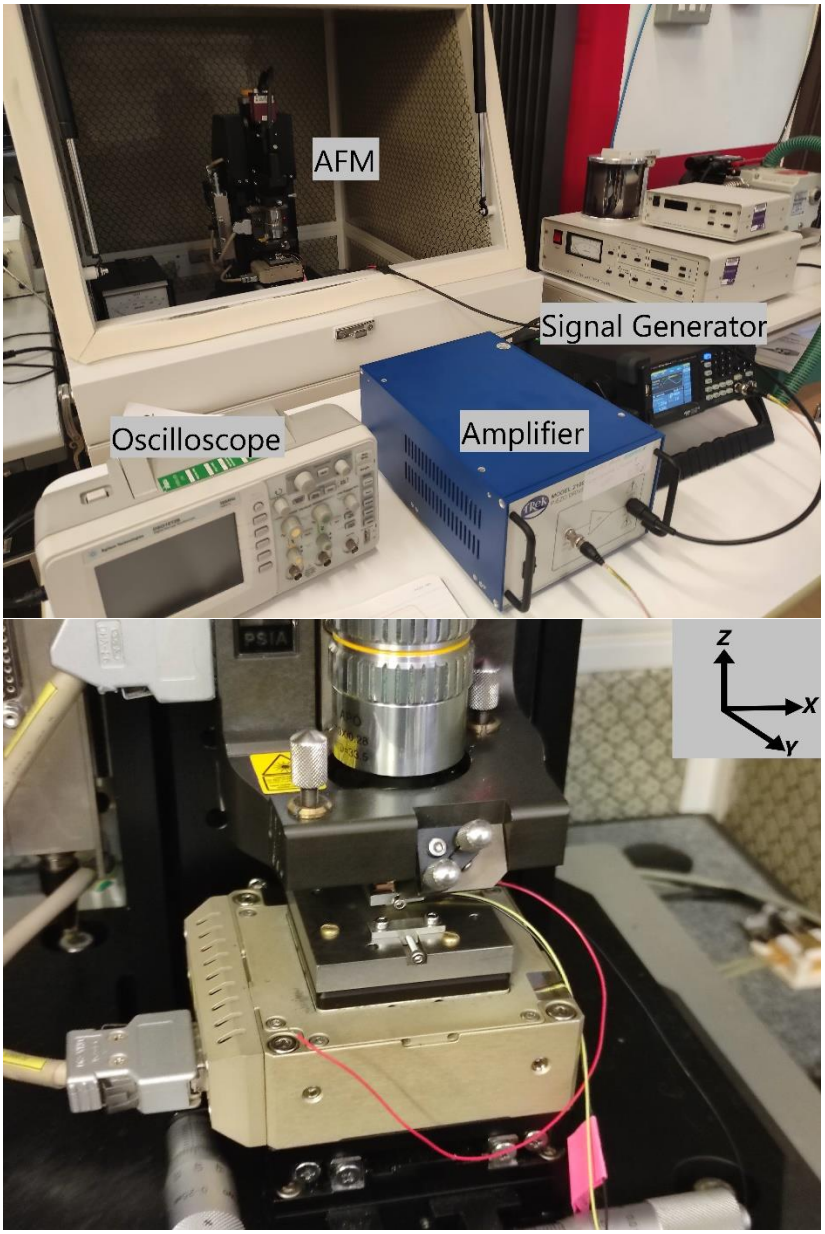

Figure 5.5 The set-up used for testing

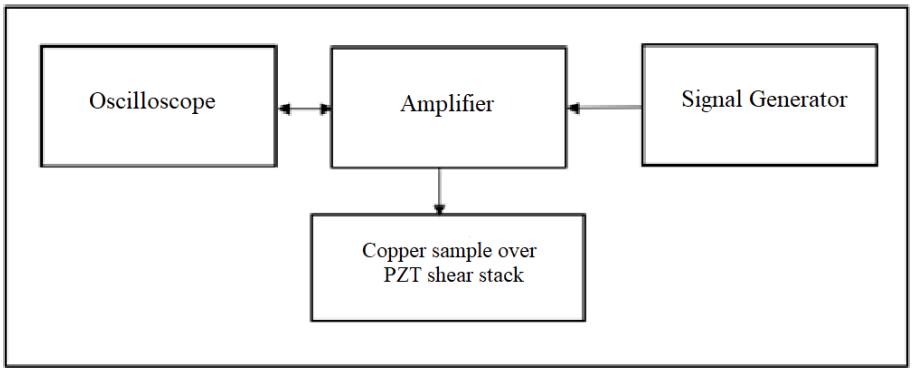

Figure 5.6 Signal flow diagram of the test setup

Three independent sources of data were used to collect information, details of which are explain later on in the chapter:

- LabVIEW data: From which four types of data were collected
- SEM Images: Highly magnified images of the grooves
- AFM scans: Topographical scans of the grooves that give detailed 3D information

5.2.1 Atomic Force Microscope

The AFM in this set of tests used both a cutting tool and a topography measurement tool. In specific, the model utilised was Park Systems' XE-100. To minimise any noise or external factors, the AFM is fixed over an active anti-vibration table from Table Stable Ltd of model TS 150 and all are protected by an acoustic enclosure that can fully seal the AFM during operation.

Also, it can measure and move in all three directions, the Z-scanner is used for motion normal to the workpiece, and the XY-scanner is used for planar motion. The Z-scanner which holds the scanning probe has a range of motion up to $12\ \mu m$. In addition, the applied voltage and control units used in the AFM software dictate the resolution of the Z-scanner.

The XY-scanner, in turn, has a flexure hinge mechanism that minimises unforeseen Z-axis motion and can move up to $50\,\mu m$ in both vertical and horizontal axes. This range of motion was utilised both during the ultraprecision machining and the following surface topography scans of the finished grooves.

5.2.1.1 AFM Probes

Since this set of experiments utilised the AFM for two purposes: surface scratching and surface topography scanning, two different types of probes were used to accommodate the two different applications.

A probe with a relatively high spring constant is needed for dynamic applications such as nanomachining otherwise softer probes would simply break. Hence, Bruker's DNISP probe was used in the ten tests conducted as it has a spring constant of 221 N/m according to the manufacturer.

The tip of the probe had a 3-sided pyramidical shape consisting of three right-angle planes. The apex of the tip can be approximated to a sphere with a 40 nm radius when measured using the images of the Scanning Electron Microscope (SEM), Figure 5.4 shows the probe used.

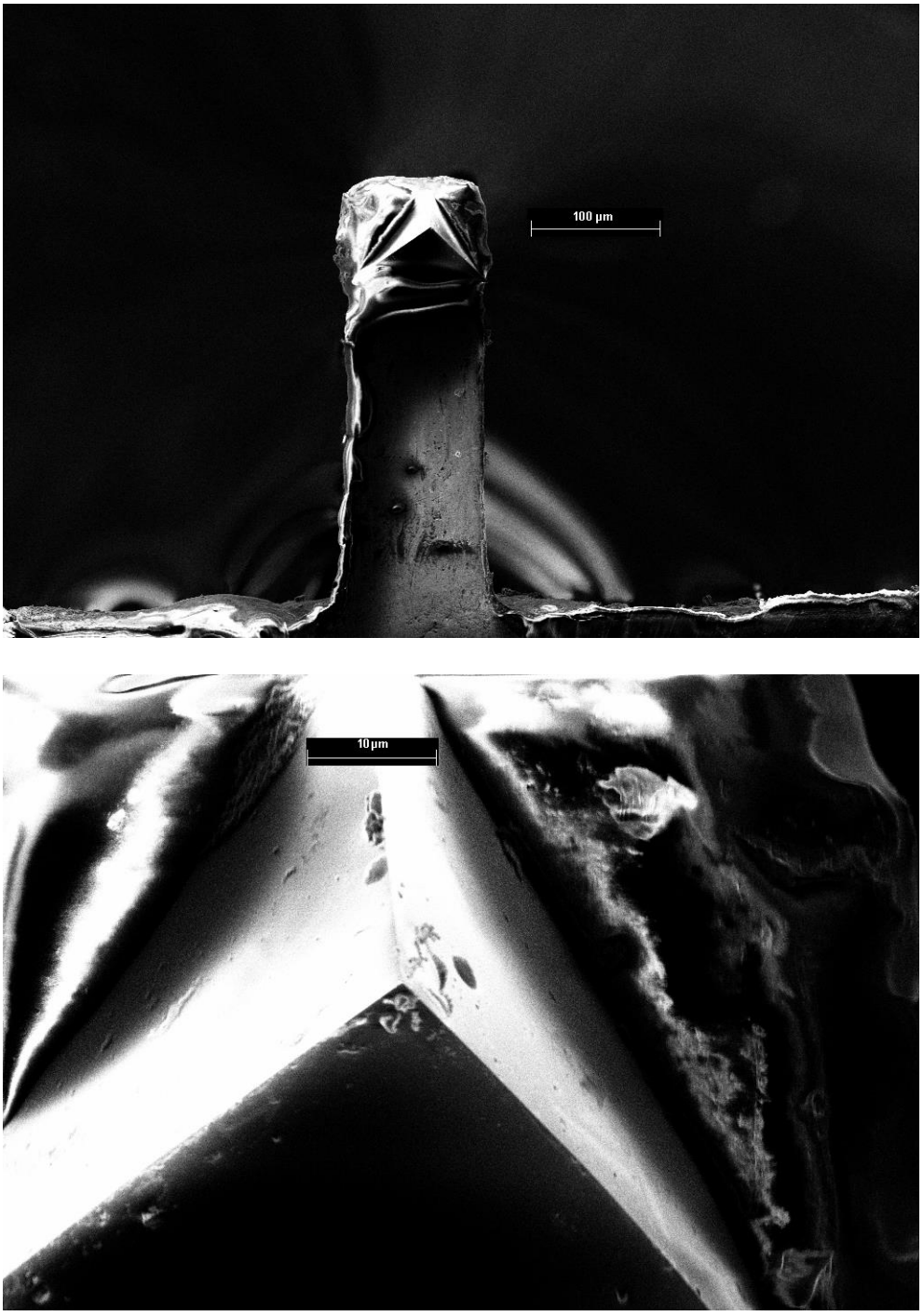

Figure 5.7 SEM images of the DNISP tip

After the nanomachining process is complete and grooves are well defined, studying their topography is the important next step. To achieve that, the probe was replaced by the softer CSG30 made by NT-MDT while using surface imaging function of the same AFM with the contact mode scanning.

Table 5.1 below highlights the specifications of both probes used.

Table 5.1 Probes used and their respecitve specifications

		DNISP	**CSG**
Tip	**Material**	Diamond	Silicon (Monocrystal)
	Shape	Three-sided pyramid	Three-sided pyramid
	Height	50 µm	14.4 µm
	Radius	40 nm (Typ.) 50 nm (Max.)	6 nm (Typ.) 10 nm (Max.)
Cantilever	**Material**	Stainless steel	Silicon
	Shape	Rectangular	Rectangular
	Length	352 µm	190 µm
	Width	110 µm	30 µm
	Thickness	10.7 µm	1.5 µm
	Spring Constant	221 N/m	0.6 N/m

AFM software

Park System's XE-100 AFM comes bundled with a software suite enabling the user to control the machine in addition to many tools to edit and manipulate the data it extracts:

- XEP: Used to operate the AFM in imaging mode
- XEL: Used for the ultraprecision machining tests
- XEI: Used for the post processing of the acquired AFM scan images

5.2.2 Data Acquisition System (DAQ)

Data acquisition from the AFM is done at three stages, data extracted using Park System's XE Signal Access Module, which sends signal to National Instruments' NI 9223 module which in turn sends data to a PC via a USB cable for the where the data is recorded is-situ using National Instruments' LabVIEW software.

5.2.2.1 Signal Access Module (SAM)

The signal access module as the name suggests, gives access to the numerous signals produced by the AFM, as Figure 5.5 below shows. It is worth mentioning that all signals discussed below are received as voltages.

This SAM is divided mainly into two sections, Driving Signal which can be used to input signal into the AFM to control it. There is also the Monitoring Signal section, which was utilised in this case as it is used to pick up (monitor) signal from the AFM and export it as output.

As seen in Figure 5.5, the ports used were 'X DET1', 'Y DET1', 'LFM', and 'AB (RAW)'. The first two ports provide data that detect the position and the changes in the X and Y axes, respectively. They are recorded to ensure that the XY scanner does in fact follow the path it was set to follow during the nanomachining process, and at the same time guarantee consistency over all tests, by comparing and noticing if there are any deviations of these two signals across the ten tests conducted.

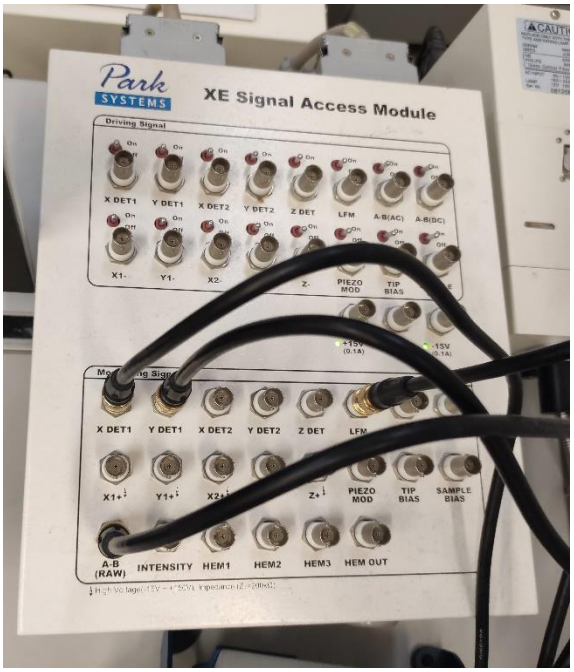

Figure 5.8 Park System's XE Signal Access Module

On the other hand, signal coming from the Lateral Force Microscopy (LFM) is crucial for picking up any lateral and torsional forces that represent the C-D voltages changes on the PSPD. Finally, the A-B (RAW) signal is in turn important for changes in the A-B signal of the PSPD occurring due to the deflections of the free end of the cantilever probe that in turn correspond to changes in the normal force exerted.

5.2.2.2 NI 9223 Module

This four channel module receives the various signals from the SAM simultaneously, handling sampling rates up to 1 MS/s and concurrently converts analog data to digital data such data a PC can handle.

5.2.2.3 LabVIEW Software

Finally, the digital data received from the NI 9223 module is sent to a PC that runs the LabVIEW software. This software allows the users to create a virtual laboratory with measurement tools that monitor data instantly and save them for post processing later on.

5.2.3 Piezoelectric shear stack

In order to produce the vibrations, a custom made piezoelectric shear stack was used that was fitted on an in-house made base that allows for high speed motion in both X and Y directions. The stack has a 3.8 mm height and a 5x5 mm surface area and can move up to 1.5 μm in X and Y axes each stroke.

The piezoelectric shear stack was made from the piezoceramic material NCE51 that is soft and is best suited for low power applications away from resonant frequencies, as Figure 5.6 shows.

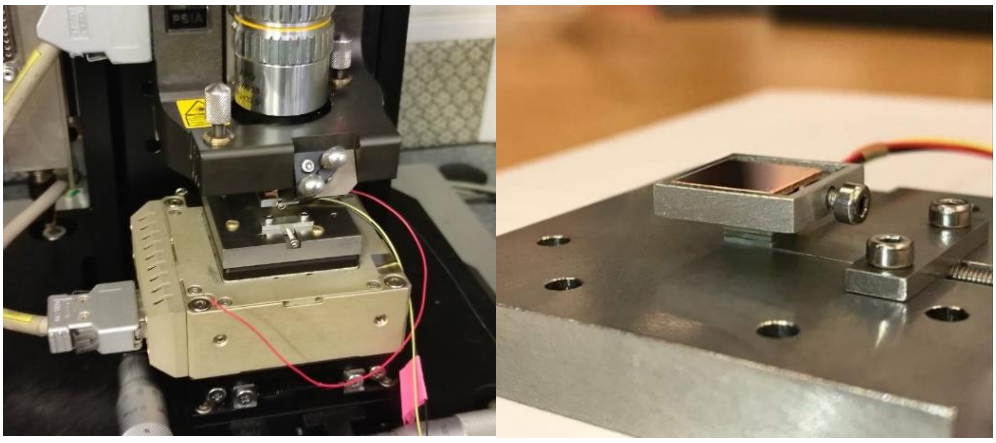

(a) (b)

Figure 5.9 (a) Piezoelectric shear stack with the copper workpiece fixed above it (b) the piezoelectric positioned within the AFM

5.2.4 Signal Generator

WaveStation 2012 from Teledyne LeCroy was used to generate the vibrational signal. This device provided live feedback of the signal being sent clearly showing the generated signal's frequency in Hertz and amplitude in Volts.

The range of frequencies this device provided was large enough to cover the range needed for the experiments. However, the amplitudes could only reach up to 6V which is not enough for the peak 125V needed, hence an amplifier was necessary. Figure 5.7 demonstrates the signal generator used during testing.

Figure 5.10 Signal Generator producing 1 KHz frequency and 2 V amplitude

5.2.5 Voltage Amplifier

Trek's 2100HF high voltage and high frequency amplifier (Figure 5.8) was utilised to provide sufficient amplitude voltage for the intended testing purposes. This device amplifies by a multiplication factor of 25.

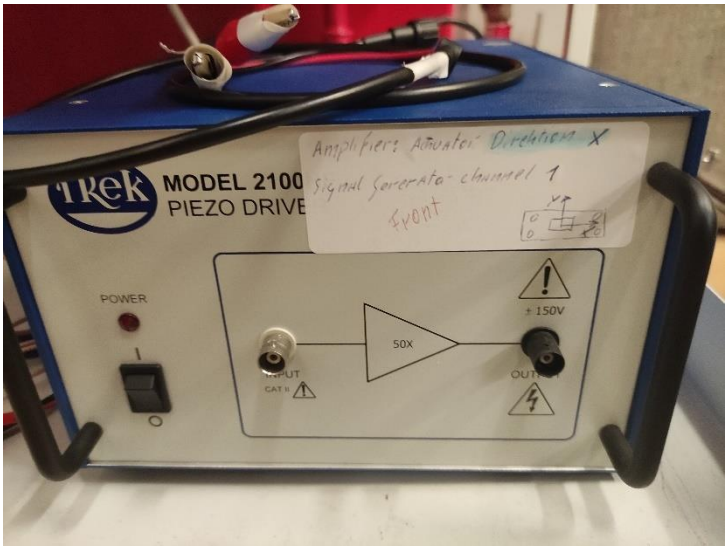

Figure 5.11 TRek Voltage Amplifier

5.2.6 Digital Oscilloscope

To guarantee that the correct amplification of amplitude voltage is applied, and that the frequency is not changed, an oscilloscope was used. Agilent technologies' DSO1072B oscilloscope in Figure 5.9 was utilised that has a live feed screen that any noise or signal deviation would have been picked up on the spot.

Figure 5.12 Digital Oscilloscope (keysight.com)

5.2.7 Workpiece material

A single crystal copper specimen with (111) crystallographic orientation and 99.999% purity was used for this study. This workpiece had a 5x5 mm dimensions and had a well-polished surface suitable for nanoscale applications including nanomachining. Figure 5.6 (b) clearly shows this copper workpiece.

5.3 Vibration assisted machining geometrical conditions

Referring to the analysis done in section 2.5.2 including the equations within with the values as in Figure 5.10 below, while following figures are used to demonstrate the impact of the variation of frequency on V_{crit}, F_{up} and the HSR. Afterwards, this information will be used to select the parameters used for the VANM tests.

Figure 5.10 below, which is courtesy of "EP/T01489X/1 - AFM-based nano-machining: developing and validating a novel modelling approach for effective process implementation in nanotechnology applications" project, shows a graph of the displacements acquired ranging from 2 Hz to 10 kHz with voltages also ranging from 50 V to 125 V. The piezoelectric plate used relied on a single shear-type.

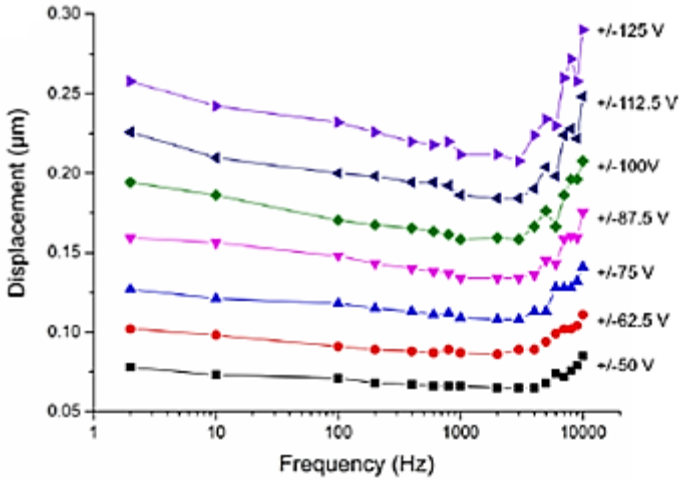

Figure 5. 13 Graph of displacements along the y-axis of the piezoelectric against logarithmic frequencies using different applied voltages

However, the frequency values used are up to 2000 Hz only as above values near resonance and as values increase, they follow random patterns. Figure 5.11 to 5.13 highlight the effect of changing the frequency on V_{crit}, F_{up} and the HSR at constant voltages. Not all voltages represented in Figure 5.10 were graphed as to improve readability. In turn, the cutting used both during the following analysis and consequent testing is $V = 5\ \mu m/s$.

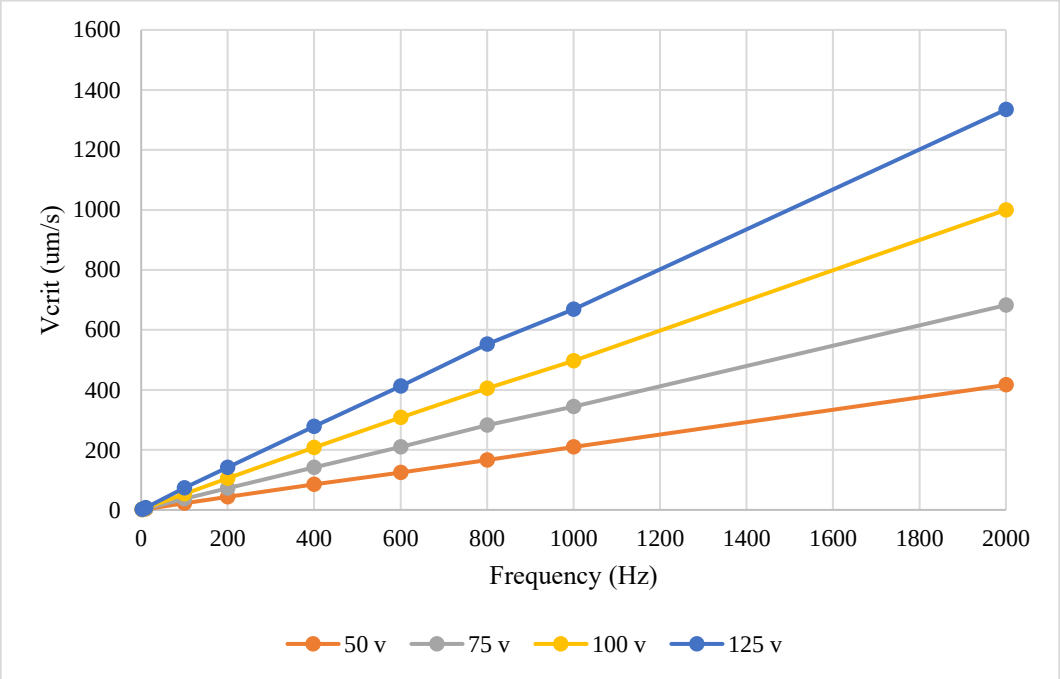

Figure 5.14 The effect of changing the frequency on V_{crit} with fixed voltages of 50 v, 75 v, 100 v and 125 v

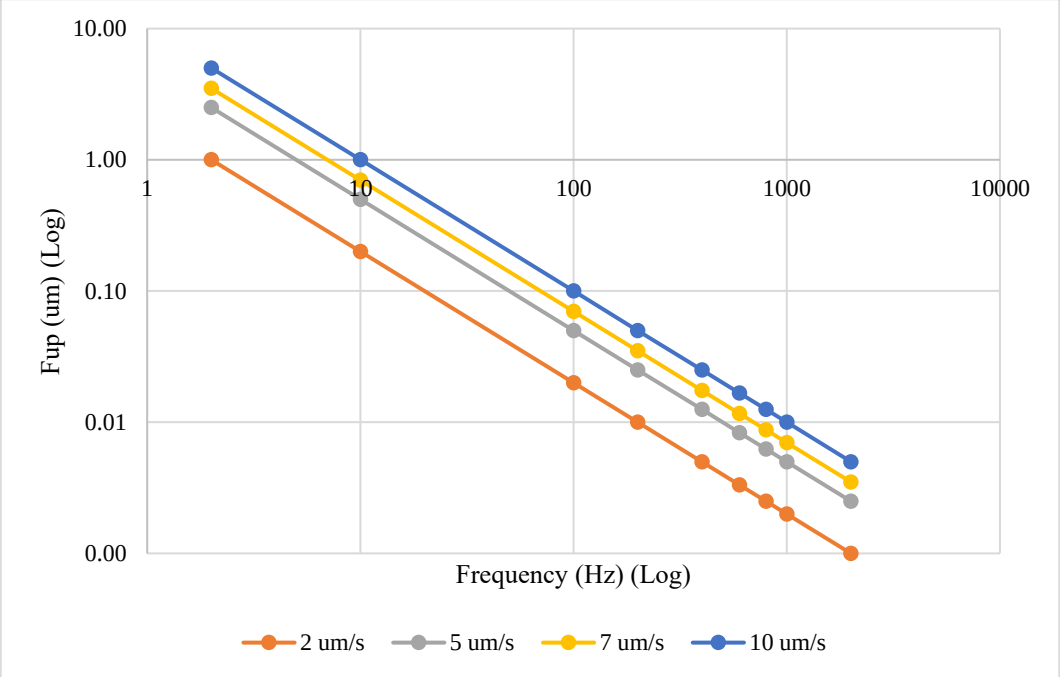

Figure 5.15 The effect of changing the frequency on F_{up} on all fixed voltages but with varying cutting speeds

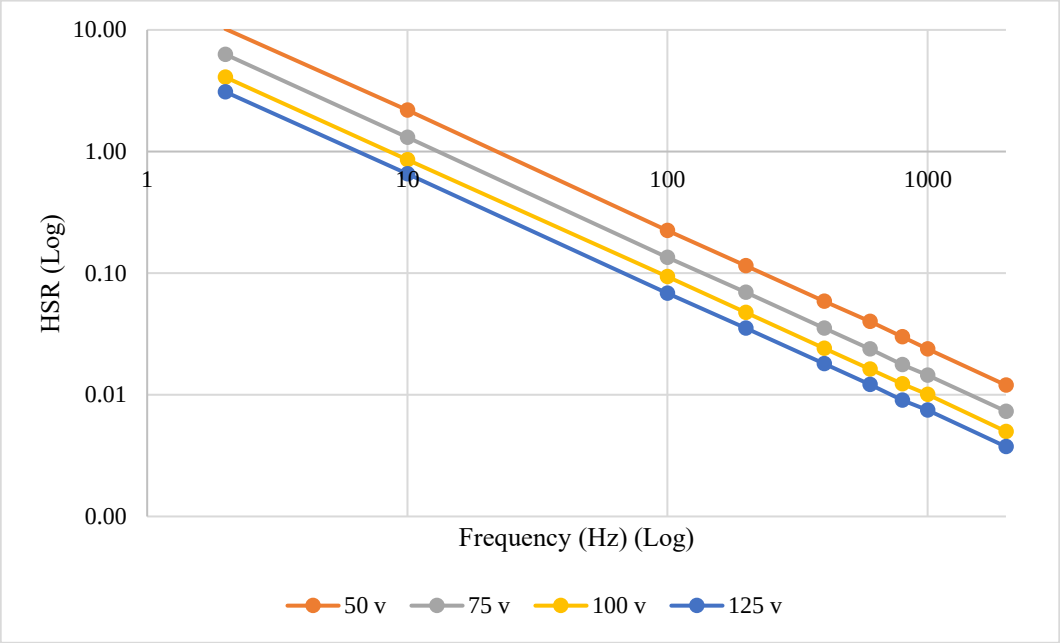

Figure 5.16 The effect of changing the frequency on HSR with fixed voltages of 50v, 75v, 100v and 125v

Moreover, the impact of changing the voltages (the displacement consequently) again V_{crit}, F_{up} and the HSR at constant frequencies was analysed and Figure 5.14 to Figure 5.16 demonstrate.

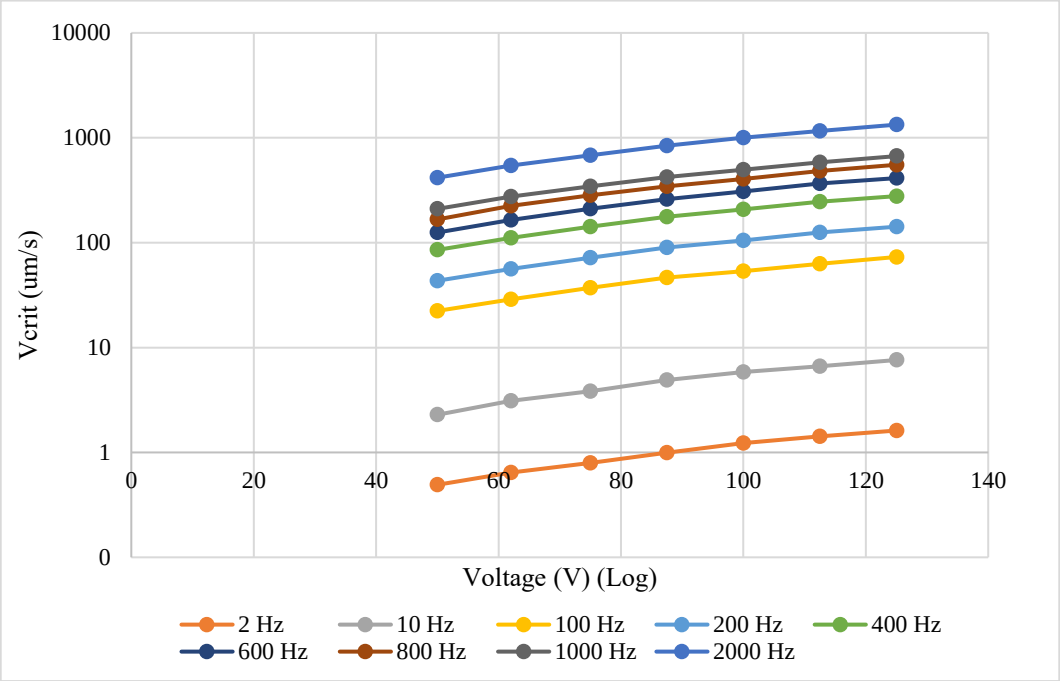

Figure 5.17 The effect of changing the voltage on V_{crit} with fixed frequencies from 2 Hz to 2000 Hz

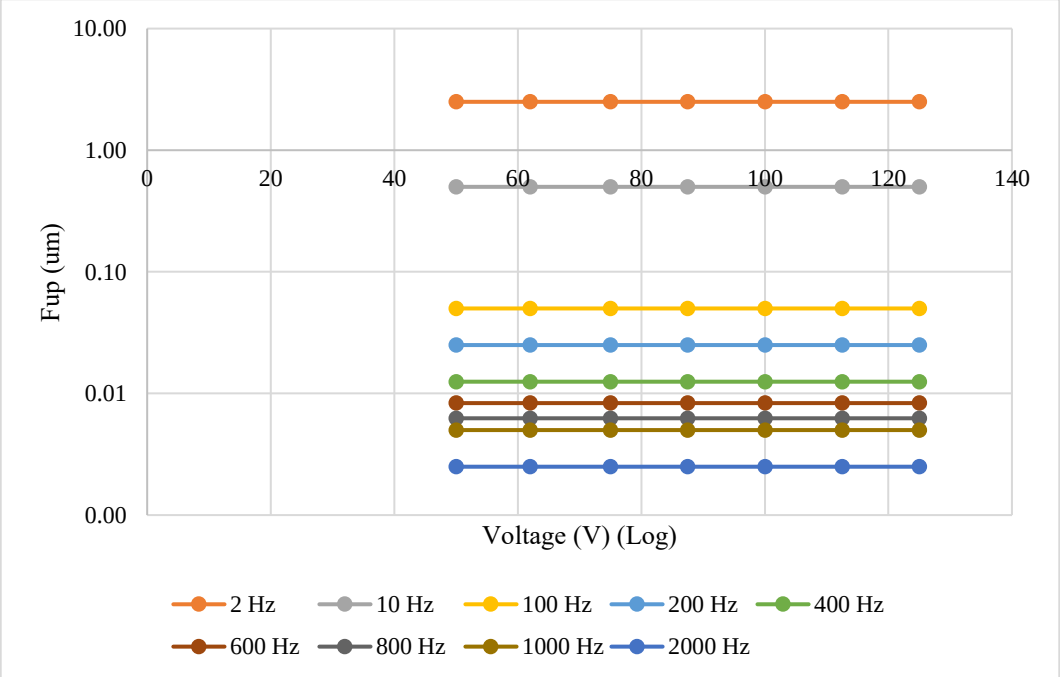

Figure 5.18 The effect of changing the voltage on F_{up} with fixed frequencies from 2 Hz to 2000 Hz

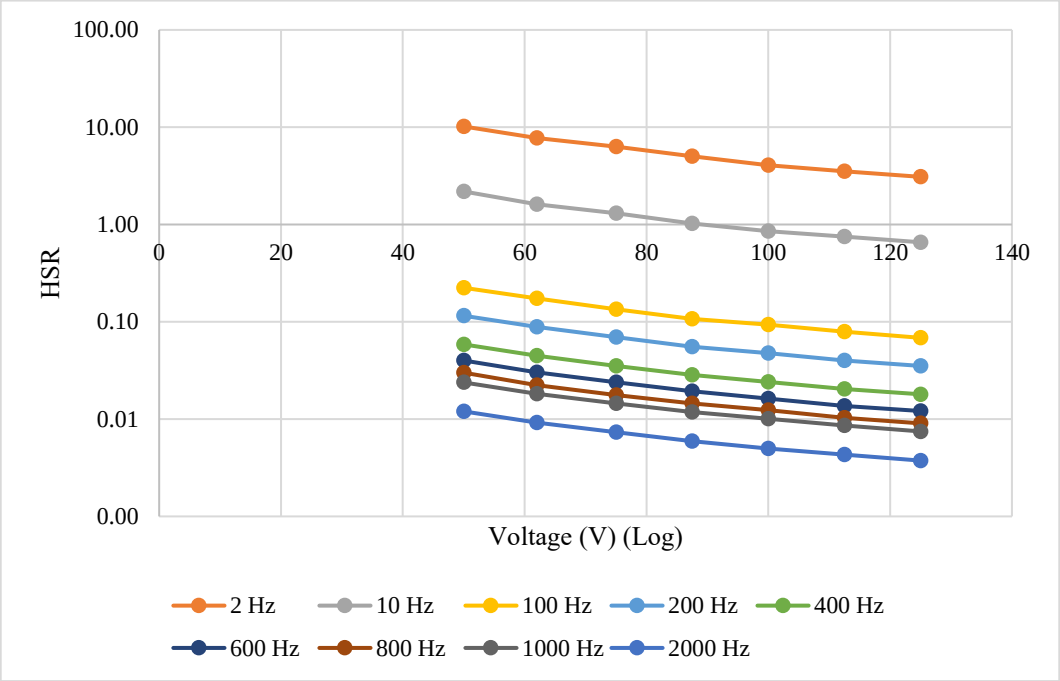

Figure 5.19 The effect of changing the voltage on HSR with fixed frequencies from 2 Hz to 2000 Hz

5.4 Cutting conditions and parameters used in testing

To investigate whether vibration-assisted nanomachining (VANM) provides improvements when compared to conventional nanoscratching and what combination of amplitude and frequency produce the best results, for a given application. In addition to the analysis done in the previous section, three different amplitudes and three different frequencies were investigated, making up a total of nine possible set-ups plus the conventional method, as Table 5.2 below shows.

Table 5.2 Test numbers with corresponding frequencies and amplitudes

n	Frequency (Hz)	Amplitude (nm)
0	0	0
1	100	40
2	1000	40
3	2000	40
4	100	80
5	1000	80
6	2000	80
7	100	130
8	1000	130
9	2000	130

It is worth noting that it was possible to utilise lower frequencies than 100 Hz (e.g., 10 Hz). However, when calculating V_{crit} it was found that lower frequencies are not sufficient to ensure cyclic detachments which are proven to provide improved cutting performance. Hence, due to the fact that this thesis explores the optimal vibrational parameters from what is available, the low frequencies were ignored. Also, knowing that within all tests cyclic detachments was achieved improves comparability.

In addition to the investigation of the impact of both the amplitude and frequency, the impact of which side of the pyramidal AFM tip in each condition was also examined. With each of the ten different tests having two grooves: Edge Forward (EF) and Face Forward (FF) as Figure 5.17 explains. Making the total of the grooves to be studied twenty.

Figure 5.20 Face Forward and Edge Forward directions of cut

5.4.1 Setting up the experiment

Before starting the ultraprecision machining process, multiple steps must be taken to ensure the machining goes to plan and that repeatability is not compromised. This first step starts by locating a relatively pristine spot as no matter how good the surface polishing process is, it is almost impossible to produce a surface defect-free workpiece. Such imperfections vary in shape and size and can be external such as contaminants or internal such as pre-existing grooves or protrusions that the polishing process missed.

Hence, as a rule of thumb, a surface defect that is recognisable enough and is adjacent to a relatively pristine surface is turned from a hindrance to an advantage by using it as a beacon to indicate the location of the machined grooves which tend to be small and hard to locate during further ex-situ analysis (i.e., taking SEM images and AFM scans of said grooves).

Once the location for the process is determined, the force applied during nanomachining is set using the XEL software. Within the software, the “set-point” is chosen in which the behaviour of the AFM probe and its interaction force with the workpiece is determined. This is done using the AFM’s built-in feedback loop mechanism that detects any variations occurring during the machining process (disturbance) from the set-point determined beforehand and then tries to adjust the applied force via the Z scanner to that original point, as depicted in Figure 5.18.

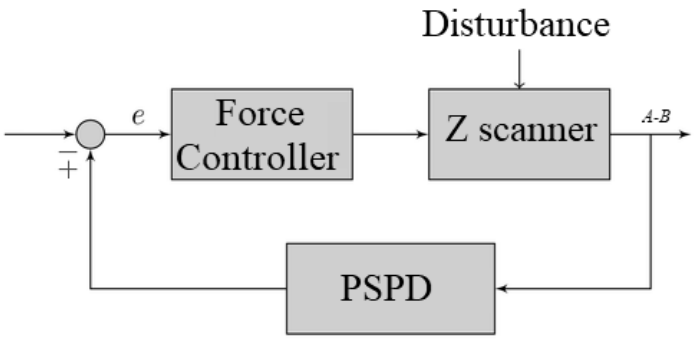

Figure 5.21 Feedback loop for the force-controlled process

In addition, the XEL software also allows for the creation of multiple machining path maps. Each map can be unique and in this set of tests ten different maps each having their unique number ranging from 0-9 and corresponding to the test conditions with varying frequencies and amplitudes as explained in Table 5.1.

Figure 5.19 is a template of the machining path maps, where the two grooves of interest are named FF (Face Forward) and EF (Edge Forward) each spanning 20 µm with a surrounding frame to easily identify the grooves, in addition to the numbering section in which N is replaced by values from 0 to 9 related to their corresponding tests.

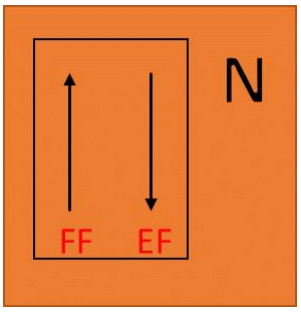

Figure 5.22 Machining path map template wherein tests is replaced by numbers 0-9

The final part of the AFM set-up process is doing the "approach" procedure in which the probe descends towards the workpiece's surface, allowing it to

pinpoint its position on the z-axis accurately. However, the software will not initiate this process unless the laser pointer is well calibrated at the centre of the PSPD.

With regards to data recording, a DAQ assistant module was set up to receive voltage data from four channels A-B (RAW), X DET 1, Y DET 1, and LFM, with each having its live feed monitor and a "Write to measurement file" extension that allows for the recording of data in the preferred format and using a convenient file extension, as Figure 5.20 shows. During the set-up of the DAQ assistant, the acquisition mode of 'N Samples' was chosen as it allows for the configuration of 'Samples to Read' and 'Rate (Hz)' with the values chosen to be 900,000 and 30,000, respectively. These choices mean that a total of 900,000 samples will be taken during each test with a rate of 30,000 samples per second for 30 seconds.

The relatively long duration of 30 seconds was done to guarantee that no points are not recorded at the start or end of the tests, with redundant data points being easily removed during data processing. As for the huge sampling rate of 30 kHz, this, in turn, was done to ensure that differences between induced vibrations of 100 Hz, 1000 Hz, and 2000 Hz are as noticeable as possible.

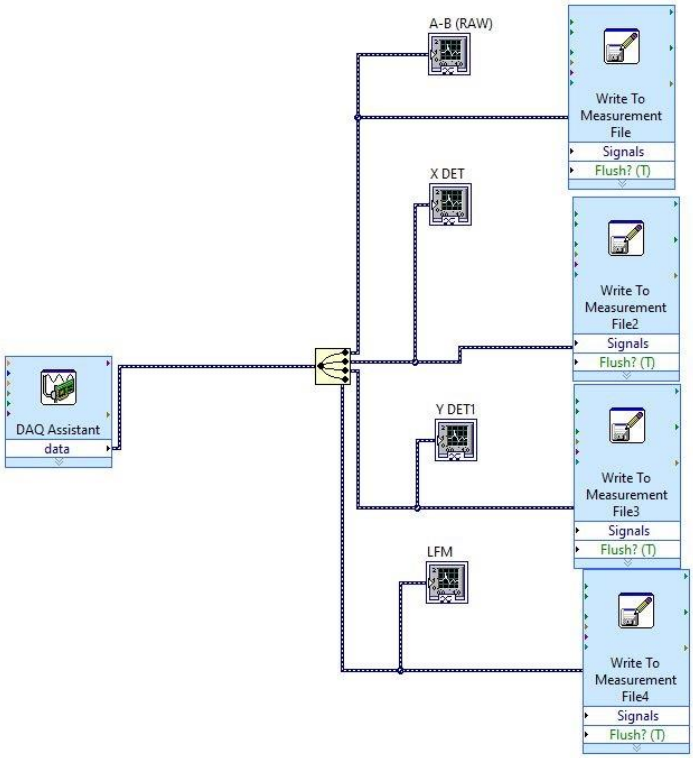

Figure 5.23 A screenshot of the LabVIEW's interface used

5.4.2 Cutting Parameters

The following cutting parameters were used in all ten tests:

- Cutting Direction: As mentioned earlier, two directions of cutting were investigated in each test, Face Forward (FF) and Edge Forward (EF) with both coinciding with the long axis of the probe's cantilever. As Figure 5.17 demonstrates, with the FF direction the probe moves towards the fixed end of the cantilever within the longitudinal axis of the probe. Meanwhile, the EF direction moves towards the exact opposite way directed towards the free end of the cantilever.
- Applied Force: Referred to as the set point, it is the static normal force (i.e., calculated without consideration of the horizontal motion) exerted by the AFM's tip on the workpiece. Since the aim of this study is to investigate the impact of the induced vibrations on the nanomachining process, a suitable set point should be high enough to induce a noticeable

plastic deformation but not too high that damage is caused to the tip and the impact of the variation of amplitude and frequency is overshadowed by the large-induced force.

- Machining path map dimension: As Figure 5.19 depicts, each test consists of two grooves, a rectangular frame surrounding them, and a test-indicative number. The grooves are each 30 µm separated by a 10 µm gap. The surrounding frame is 40 µm long and 20 µm wide. Finally, the test-indicative numbers have 10x6 µm dimensions. Enough spacing between grooves was guaranteed to ensure no groove influences the other by chip cross-contamination or any stress residuals.
- Machining path map timeline: When used to draw a machining map, the XEL software allows the user to reorder when each groove is made, depending on the user's preference. Hence, the first groove created for all tests is the Face Forward one, starting from the bottom and going upwards. Then, the probe is lifted and shifted 10 µm horizontally to the left, where it descends towards the sample, and the Edge Forward groove is made as the tip scratches the surface going downwards. Afterwards, the probe ascends and descends to create the rectangular frame. Finally, the test-indicative number is machined at the top-right side of the frame, at which point an individual test concludes.

Table 5.3 Cutting parameters for the copper sample

Probe	DNISP
Cutting Directions	FF and EF
Cutting Speed	5 µm/s
Groove Length	30 µm
Set-point Force	30 µN

5.4.3 Initiation of the VANM tests

Once the "approach" process is complete and the machining path maps are ready, the testing could commence. Initiating the machining process via the XEL software and the recording of data using LabVIEW is done simultaneously to ensure all data from both grooves are recorded and that future benchmarking is done with relative ease. And this is the reason why when machining path map was created, the first two grooves made were the FF and EF as the data of these two grooves are the only ones of interest.

For test no.0, which is the conventional nanoscratching and is used as a benchmark for the other tests, the signal generator was switched-off and the test was run.

After that, and for tests 1-9 the signal generator was switched-on and the frequencies and amplitude voltages that correspond to the amplitudes measured in nm were used with the aid of data collected from Figure 5.10.

5.5 Imaging and scanning of resultant grooves

After the completion of the ten different tests, the resultant grooves needed further analysis which were done by taking SEM images as well as AFM scans. With the latter using a different probe than the one used for the nanomachining, as explain earlier. In this experiment, SEM images were taking prior to the AFM scans due to time constraints as AFM scans take considerably more time to complete than SEM images.

5.5.1 SEM Images

Carl Zeiss' XB 1540 scanning electron microscope was utilised in this experiment to allow for a qualitative assessment of the resultant grooves. Four different magnification values were used for this inspection. Firstly a 3,000 magnification factor was used with each image encompassing a single test including every part within the machining path map. Then 20,000 followed by 50,000 and finally 100,000 magnification factor for each end of the two grooves. When chip formations were noticed, custom and arbitrary magnifications were used to take the best images for such incidents.

5.5.2 AFM Scans

In the end, the topographical information of the grooves is collected via an AFM scan done using the same XE-100 AFM machine but with CSG probes rather than the DNISP used for the nanomachining. Two scans were performed, one spanning 35x20 µm that scans the entirety of the two grooves, followed by close-up scans sized 2x2 µm for different parts of each groove. The close-up scans provide more detailed information for the specific section they cover.

The AFM scans not only provide a comprehensive 3D map of the grooves and their surroundings, but they also provide cross-sectional groove depth and pile-up height data as well as roughness parameters. Such information can be useful for comparing the different machining conditions.

The resultant images are available in the .tiff extension and can be analysed either using Park System's XEI software or using the free and open source modular program for SPM (Scanning Probe Microscopy including AFMs) software Gwyddion. The latter was chosen due to it being readily available for use off-campus as per government health guidance during Covid-19 to work from home in addition to its intuitive user interface as well as excellent support and tutorials also available freely on the software's official website.

When using Gwyddion, the first and most important step is to level the image. As when the workpiece is fixed in place some unavoidable tilt will be present and such inclination can be fixed using a functionality called “Three Point Level” within Gwyddion that allows the user to choose any three points (preferably as spread apart as possible) creating a triangle that in turn levels the image by putting all points at the same elevation. The software also allows for using circles instead of points with adjustable radii, larger radii provide better levelling. For example, Figure 5.21 shows the AFM scan of the end of the EF groove of the second test. In this figure, the three points that create the largest triangle were chosen, as the three circles within the figure demonstrate.

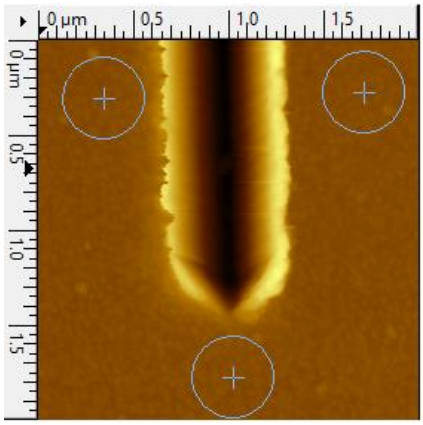

Figure 5.24 Three point level functionality in Gwyddion

Regarding the cross-sectional profiles of the grooves, the software can either extract the profile using a line or a segment with a user-defined thickness. When a segment is used, the software compounds all the profiles contained within and averages them linearly rather than a line that only represent an instant compromising the repeatability of the process. A segment with a 0.5 µm thickness was used in this experiment for the 2x2 µm scans, and all were 1.5 µm wide to ensure all groove profiles were captured without any unnecessary extra information.

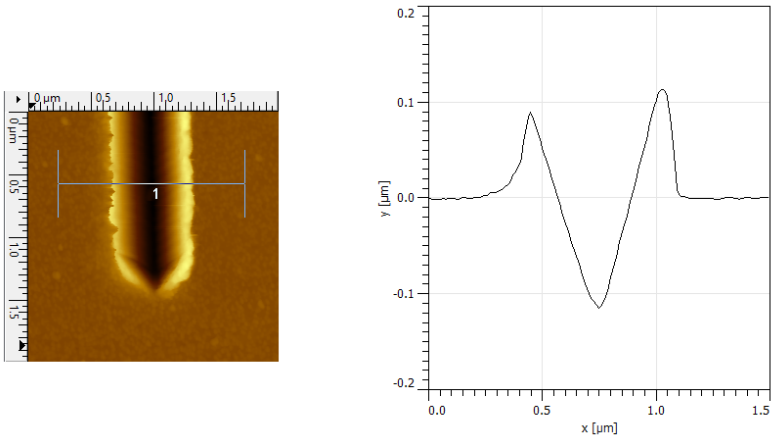

Figure 5.25 AFM scan of the end of the EF groove of the second test (a) selected segment (b) resultant cross-section

An important aspect to consider is the overestimation of the volume of the pile-ups, especially for the edge forward grooves. Figure 5.23 is an arbitrary groove with sections “e” representing the extra volume the scan adds, which in reality does not exist. Such issues arise from the normal angle between the tip and the scanned surface and the size of the radius of the tip when compared to the pile-ups. Hence, volumetric comparisons should be avoided when comparing pile-ups for different tests, but parameters such as height are unaffected. This phenomenon is closely related to what is known as the convolution principle discussed by Atamny and Baiker (1995) and is explained early on within the thesis.

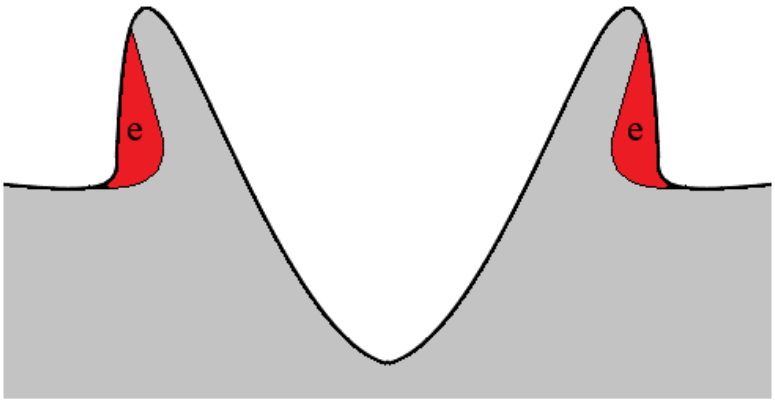

Figure 5.26 AFM scans pile-up volume overestimation

As for the surface roughness R_a analysis, Gwyddion has a specific tool for it as well. This tool also allowed choosing between using a line or a segment where the latter was chosen due to the same reasons mentioned earlier. However, the thickness of the segments here was not fixed and depended on the thickness of the groove analysed. The centre of the segment coincided with the centre (i.e., deepest point) of the groove and expanded from the highest point of one side of the pile-up to the other. The length of the segment taken was 1 µm, except for cases where removing noise in the AFM scans was impossible. In such cases, the length was less than 1 µm but more than 0.5 µm, as Figure 5.24 shows.

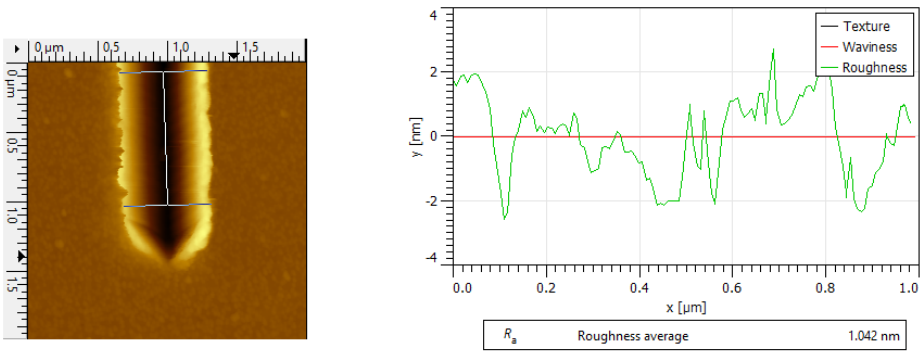

Figure 5.27 AFM scan of the end of the EF groove of the second test (a) selected segment (b) resultant roughness profile and average

The software also enables the use of a cut-off that was used only for cases where a 100% levelling was not possible and the cut-off functionality at its minimal settings was used to overcome the tilting present. Without the cut-off, the software tends to mistake tilt for roughness ending up significantly overestimating its values. Visual inspection is done to ensure that the cut-off is only rotating the roughness profile and that it is not altering its actual shape.

Chapter 6

Benchmarking Vibration-Assisted Tests Against the Conventional Nanomachining Counterpart

6.1 Introduction

The impact of the introduced vibrations, and their respective amplitudes and frequencies, during the nanomachining is investigated. This is done with special emphasis on its effect on surface roughness, groove depth, pile-up height, chip formation, and the signal acquired during the nanomachining process.

Also, investigated is the impact of the direction of machining, by comparing the face forward (FF) and edge forward (EF), and what causes such a noticeable difference in grooves produced.

In turn, the cutting speed used was 5 um/s. This speed was chosen to guarantee detachment in each vibrational motion with the available range of vibrational amplitudes and frequencies.

Finally, the impact of nanomachining of single crystal copper, the significance of the dead zone region and how the process compares to the widely investigated silicon are discussed.

6.2 Experimental results

In this section, the results of the conventional nanomachining test are presented, with detailed explanation of the presented outcomes. Each test starts with the corresponding SEM images followed by AFM scans

6.2.1 Conventional nanomachining

Within this sub-section, the conventional nanomachining test (i.e., test no.0) is analysed in detail with three specific sources of information: SEM images, AFM scans, and DAQ signals (LabVIEW data). Afterwards, each of the following nine tests will be analysed and compared to test no.0, which will be used as a benchmark. This investigates the impact of inducing vibrations and the corresponding effect of specific

frequency values and amplitudes. The degree of detail in comparisons will vary depending on how significant the change is from test no.0 (whether it is an improvement or the opposite).

In addition, as mentioned in chapter 5, every test is composed of two grooves: Face Forward (FF) followed by an Edge Forward (EF). Each groove's start and end are analysed and compared throughout this section. The following acronyms are used throughout this chapter:

- FF1: Start of Face Forward
- FF2: End of Face Forward
- EF3: Start of Edge Forward
- EF4: End of Edge Forward

Test no.0

SEM Images

In this test as well as all other tests, a noticeable trend emerges. The shape of the FF groves changes significantly when comparing the start versus the end of the groove. In contrast, for the EF groove although a slight change the in LabVIEW signal and the cross-sectional profiles were observed, these changes are not noticeable enough in the SEM images. Hence, when discussing SEM images, the start and end of the FF groove in addition to single EF images are accompanied by zoomed-in versions (further 7.5x magnification factor) as shown with the inset images in Figure 6.1.

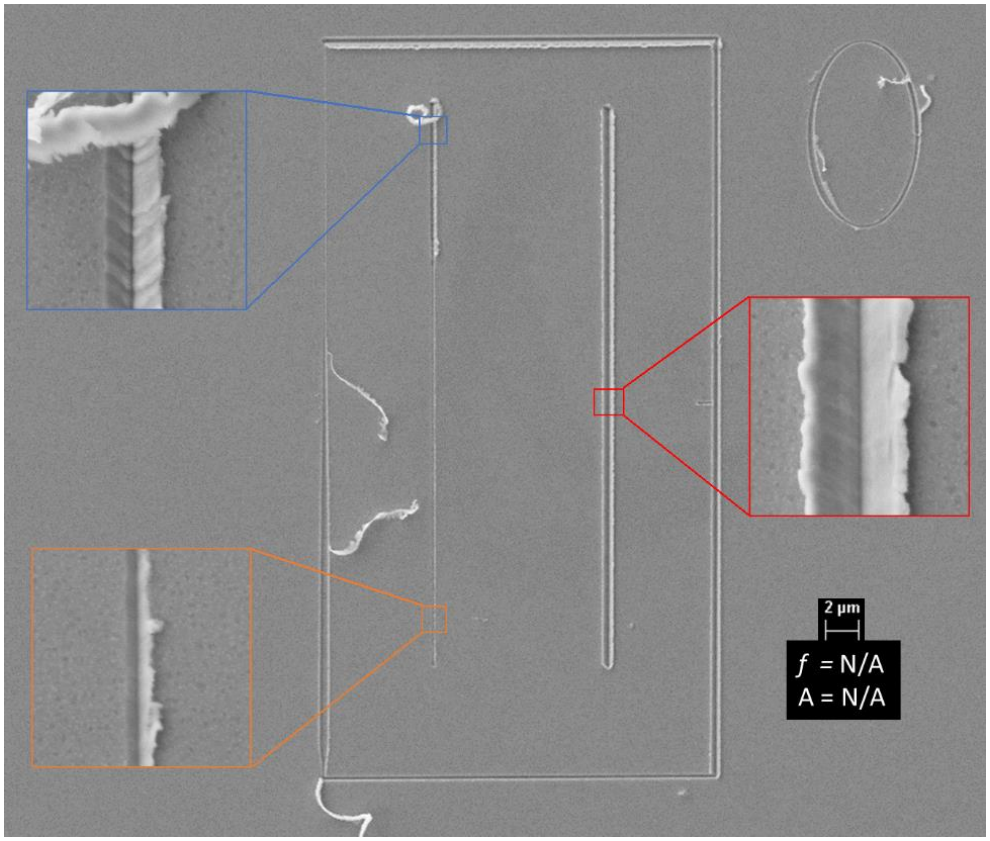

Figure 6.1 SEM image of test no.0

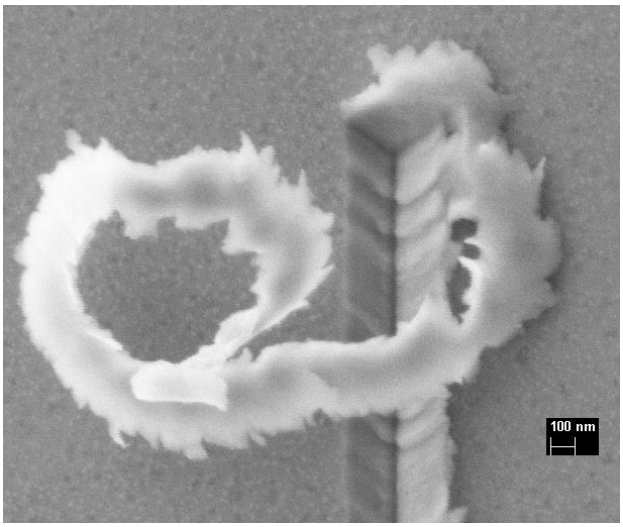

Figure 6.2 Chip morphology of the end of FF groove

AFM Scans

As mentioned in the previous chapter, the surface topography of each test was acquired using a CSG probe with the Atomic Force Microscope. 3D scans of the grooves were extracted to give a general view of each test. In addition, quantitative data was also extracted including the grooves' surface roughness as well as the cross-sectional profile of the grooves which in turn give both the depth and pile-up height measurements. The three mentioned parameters were extracted for the start (FF1) and end (FF2) of the Face Forward groove as well as the start (EF3) and end (EF4) of the Edge Forward groove. Unlike the qualitative nature of SEM images, quantitative data obtained is extracted for both start and end of the EF groove as there are differences in all groove depth, pile-up height and roughness, although these differences are not as pronounced as in the FF groove.

Figure 6.3 shows a 3D isometric view of the grooves made in test no.0, with a scanning size of 35x20 µm. Meanwhile, Figure 6.4 shows the raw .tiff images of FF1, FF2, EF3, and EF4 with a scanning size of 2x2 µm for each.

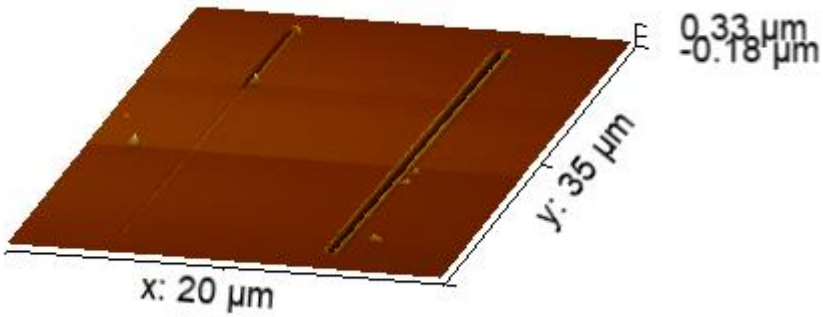

Figure 6.3 3D map of test no.0

Images in Figure 6.4 contain the information needed to extract the cross-sectional profiles as well as the roughness values. Figure 6.5 shows the average cross-section of the FF groove and Figure 6.6 of the EF counterpart, both of test no.0.

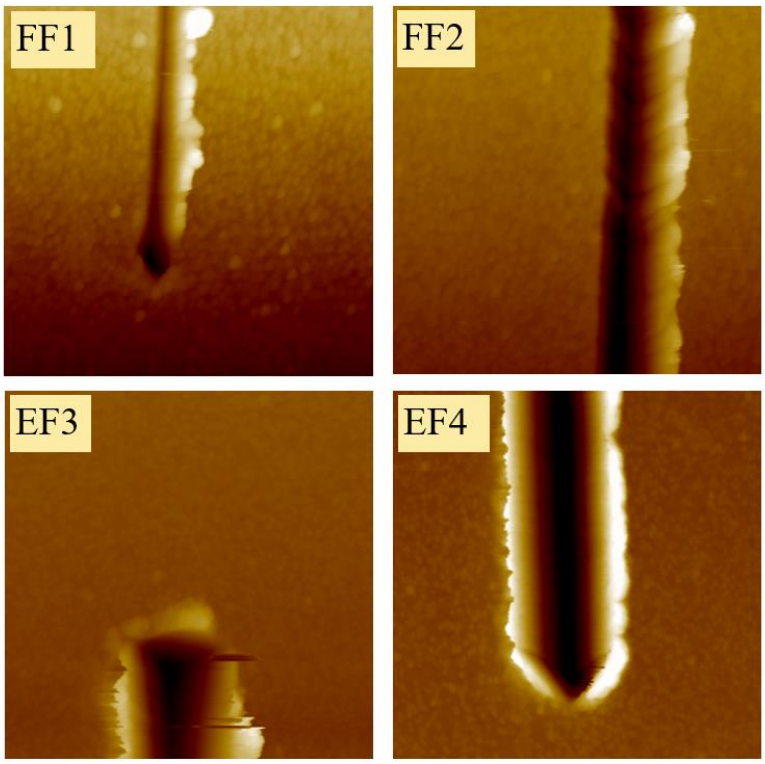

Figure 6.4 AFM scans of FF1, FF2, EF3, and EF4 respectively

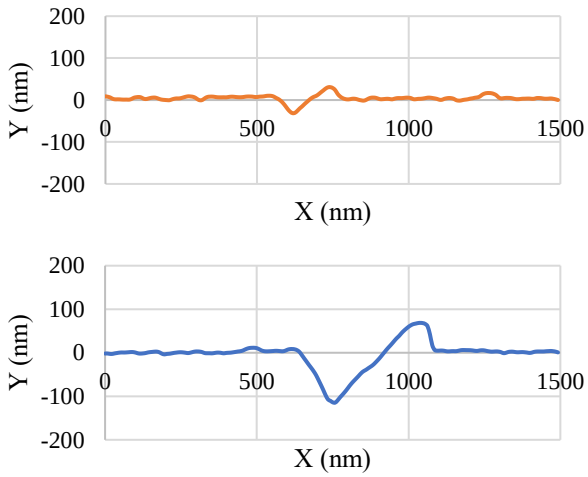

Figure 6.5 Average cross-sectional profile of (a) FF1 and (b) FF2

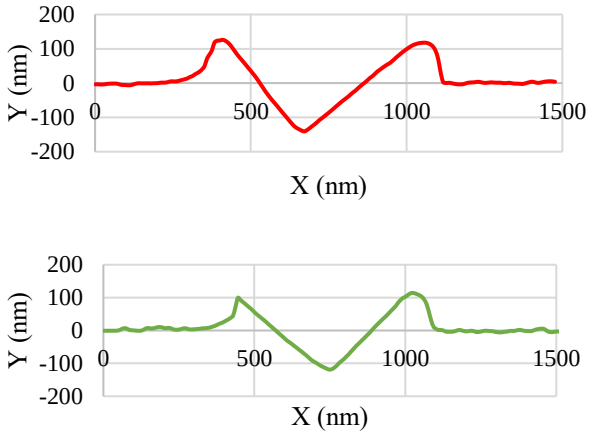

Figure 6.6 Average cross-sectional profile of (a) EF3 and (b) EF4

For both the face forward and edge forward grooves, Table 6.1 below shows the average maximum pile up height and groove depth. In addition, Table 6.1 shows the surface roughness R_a for both grooves however not average but the start and end of each groove, to highlight the difference. With the values appearing in the table comprising of the average value calculated for the start and end of FF (FF1 and FF2) and EF (EF3 and EF4), respectively.

Table 6.1 Cross sectional profile parameters of test no.0

	FF	**EF**
Pile up height (nm)	58.6	121.4
Groove depth (nm)	75.2	138.7
Roughness Start / End (nm)	2.4 / 4.4	4 / 2.1

DAQ Signals

The data extracted from the AFM and recorded using LabVIEW can be divided into two types:

- Positional data: X DET1 and Y DET1 that detect the horizontal and vertical motion of the workpiece relative to the tip, respectively.

- Cantilever deflection data: A-B (RAW) and LFM that record vertical deflection (up and down) and torsional deflection (rotations) about the longitudinal axis of the cantilever, respectively.

The latter type of data is what can be observed on the PSPD monitor within the AFM software. Figure 6.7 shows a schematic of PSPD monitor with the laser well positioned in the middle, which means that it was well calibrated and still not in contact with the workpiece.

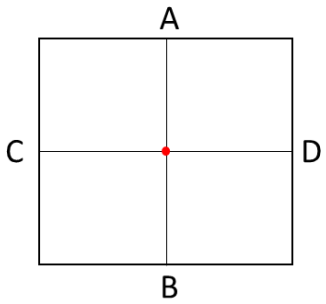

Figure 6.7 Schematic of a PSPD monitor in its idle position

As the test commences, the probe is lowered until contact is made. The distance travelled downwards is predetermined via a maximum force setpoint of 30 μN and is assigned using the XEL software.

Figure 6.8 below illustrates the cantilever deflection (PSPD) data recorded during the machining of the two grooves. Given that each groove was 30 μm with a machining speed of 5 μm/s, each groove takes 6 s to complete. In turn, Figure 6.9 illustrates the cantilever's beam torsional motion for both clockwise and anti-clockwise motions.

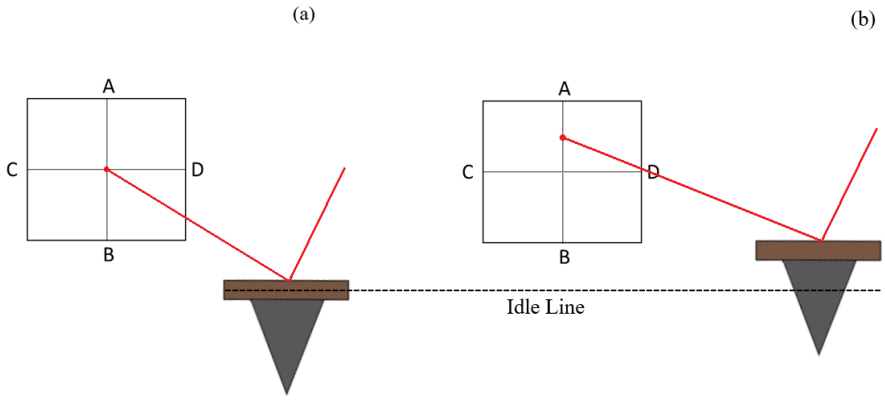

Figure 6.8 Vertical deflection of the beam and how the A-B (RAW) is seen on the PSPD: (a) Idle position before contact but after calibration (b) After deflecting upwards

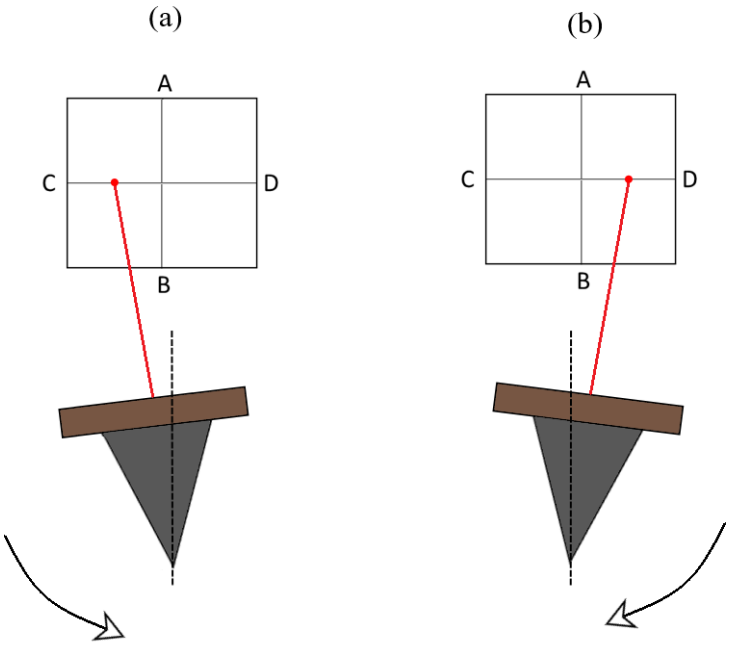

Figure 6.9 Torsion of the beam and how LFM signal is recorded on the PSPD: (a) Anti-clockwise (b) Clockwise (Adapted from parksystems.com)

Figure 6.10 shows the A-B (Raw) and LFM data recorded during test no.0, for a 30 second duration. The two grooves can be easily recognised in both Figure 10 (a) and (b), where the face forward starts just before the 3rd second and the edge forward one starts just after the 13th second.

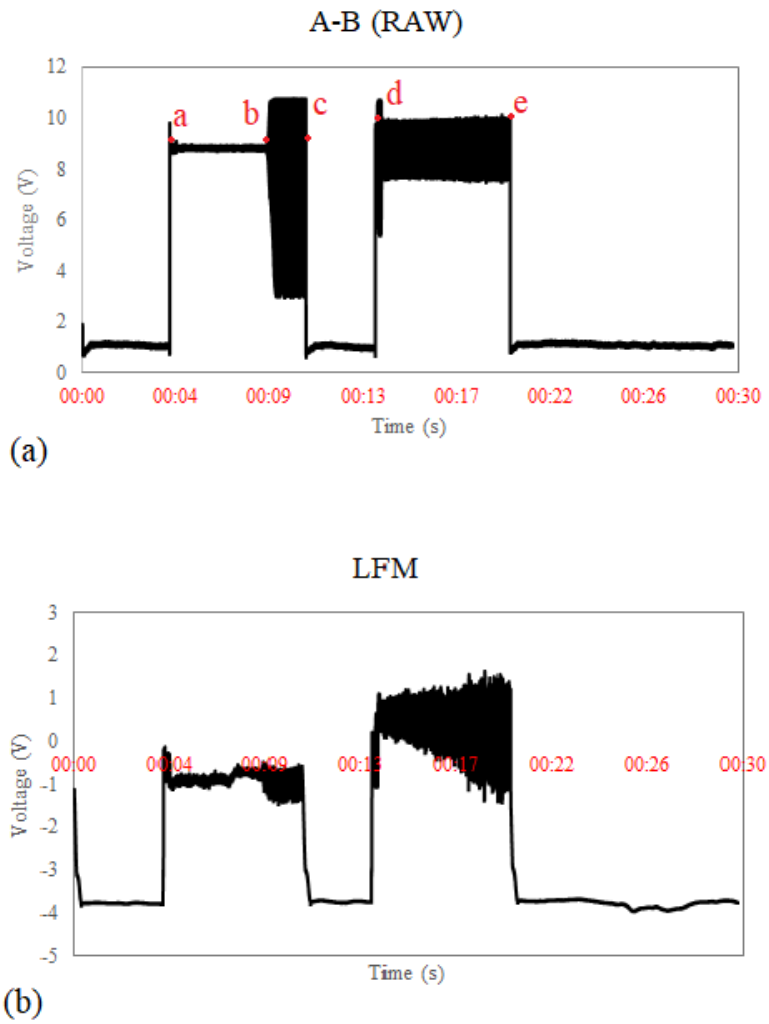

Figure 6.10 A-B Raw and LFM signals of test no.0

Following the timeline of the A-B (RAW) signal in Figure 6.10 (a) and LFM in Figure 6.10 (b). It is possible to divide it into four sections starting with point a and ending with point e, as follows:

- **a to b**: the first flat line with a voltage value of about 1 V indicates that the tip is in contact with the surface following the approach but that the interaction force between the tip and the surface is quite small at 50 nN. Then, in both A-B (RAW) and LFM an off-shoot in the signal is noticeable. This off-shoot (Point a) is followed by a slight decrease in the signal then a steady-state until around the 9th second (Point b). The off-shoot seen at Point a is explained physically by the start of the indentation process until a thrust force of 30 μN is reached. Then the lateral

motion between the tip and the workpiece is initiated and this is accompanied by a change from a static coefficient of friction to a dynamic one, with the latter know to be always smaller.

- **b to c**: Around the 9th second, a sharp and sudden increase in the variability of the A-B signal is noticeable. This part of the groove is observed to be deeper and wider in the SEM image in Figure 6.1. Importantly, this SEM image also suggests that chip formation took place during point b and point c. The reason why chip formation took place only at some point during the formation of the groove, and not earlier, could be the result of a dead zone accumulating in front of the tip as it progressed along the groove. The consequence of having such accumulated and relatively stagnant material ahead of the tip is that it may change the effective rake angle of the tip, making it less negative and eventually favouring the onset of chip formation. It is also observed from the SEM image in Figure 6.1 that the roughness at the bottom of this FF groove is much more pronounced at the end compared to that at the beginning. This should be the result of the chip formation process where successive thin portions of the workpiece material are successively sheared to form a chip. It should also be kept in mind that the flattening of the top part of the signal between b and c (also seen at Point d) is due to voltage-reading limitation as the range cannot exceed and is capped to 10 V (i.e., the distance between the lowest and highest in any A-B (RAW) graph will always be limited to 10 V). This increase in signal fluctuation is less pronounced in the LFM signal (i.e., less torsion in the cantilever). At Point c the first groove is complete the probe is lifted until the set point force value of 50 nN is reached.
- **c to d**: The probe is moved between the end of the first groove to the start of the second one via the displacement of the AFM stage 10 µm horizontally. The tip is lowered into the workpiece until a pre-set force is reached. This leads to a brief off-shoot, as was the case for the first groove, albeit to a higher degree here. The larger initial off-shoot in the edge forward than the face forward is consistent in all tests, which indicate that the orientation of the tip could play a major role in this phenomenon rather than contaminants, i.e., chips stuck on the tip or impurities on the surface of the workpiece.
- **d to e**: Fluctuations in the A-B signal are observed but to a lesser extent than those recorded between c and d, which were for the last part of the first groove.

Qualitatively, the SEM image of this test (see Figure 6.1) confirms that the roughness of this EF groove is less than that at the end of the FF groove. This suggests that there may be a correlation between the variability of the A-B signal and the obtained surface roughness. The SEM image of this groove also indicates that no chips were formed along this groove and that machining took place entirely via ploughing. Given that it is essentially one of the three edges of the pyramidal tip, and not a face, which progresses into the material, this result is not surprising. The LFM signal's fluctuation is seen to increase gradually along this groove. Finally, the probe is lifted at Point e. The data acquisition carried on until the 30th second was reached, at which point the data acquisition stops.

As seen in Figure 6.10, data was recorded for 30 seconds which was a considered comfortable estimate. However, in the following tests in which comparisons are made, individual grooves will be compared, and periods of noncontact will be cropped out.

Figure 6.11 shows the signal recorded by the sensors that monitor the lateral motion of the stage that holds the workpiece. Discussing Figure 6.11 (a), in the X-Detector, any increase in the voltage translates into a movement to the left and vice-versa for the right. In addition, a horizontal line (i.e., no change in voltage) means no positional change in the x-axis. The first two horizontal lines correspond to the machining of the FF and EF grooves.

As for Figure 6.11 (b), an increase in voltage in the Y-Detector means that upward movement, and the opposite applies to the downward movement. Only one portion of the graph has a horizontal line (i.e., no change in the y-axis) which is between the end of the FF groove and the start of the EF groove in which the probe was lifted.

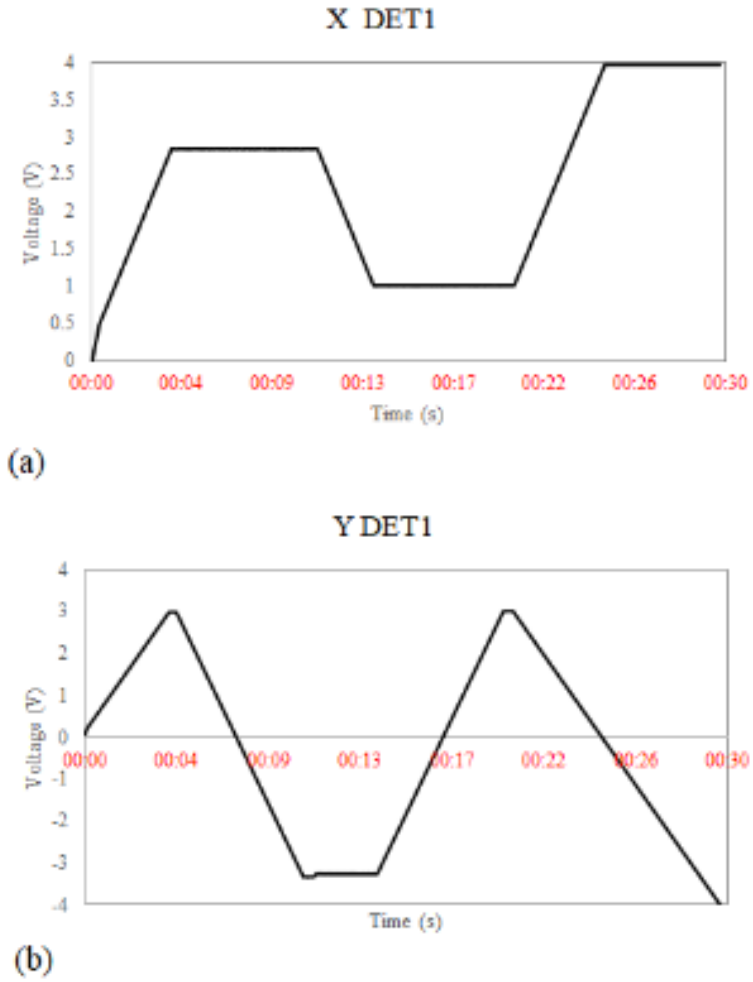

Figure 6.11 X DET1 and Y DET1 data of test no.0

6.2.2 Vibration assisted nanomachining tests

In this part, all vibration-assisted nanomachining test are presented seperatly. Within, SEM images of each are shown with emphasis on the grooves topography as well as as the resultant chip formation. Also, tables highlighting percentage in variations in groove depth, pile up heights, and roughess are presented.

Test no.1

Figure 6.12 below shows the grooves resulting from test no.1 which was the first test with induced vibrations. This test had the minimum settings for both the frequency and amplitude which were 100 Hz and 40 nm, respectively.

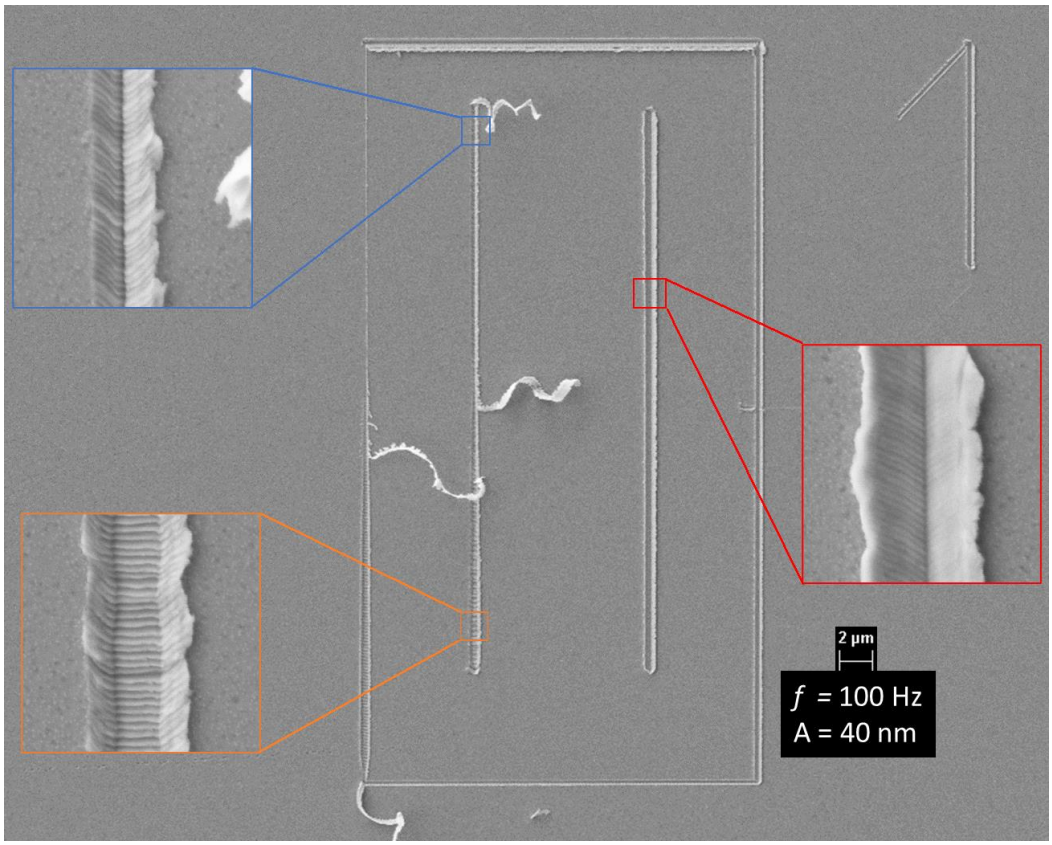

Figure 6.12 SEM image of test no.1

The first major difference can be seen at the first half of the face forward (i.e., FF1) portion, in which the groove was both deeper and wider with a visible "stacking" effect. This pattern persisted in all following vibration assisted tests.

In addition, continuous chips were also observed in this test. With the first one seemingly wider than the second, as Figure 6.13 demonstrates.

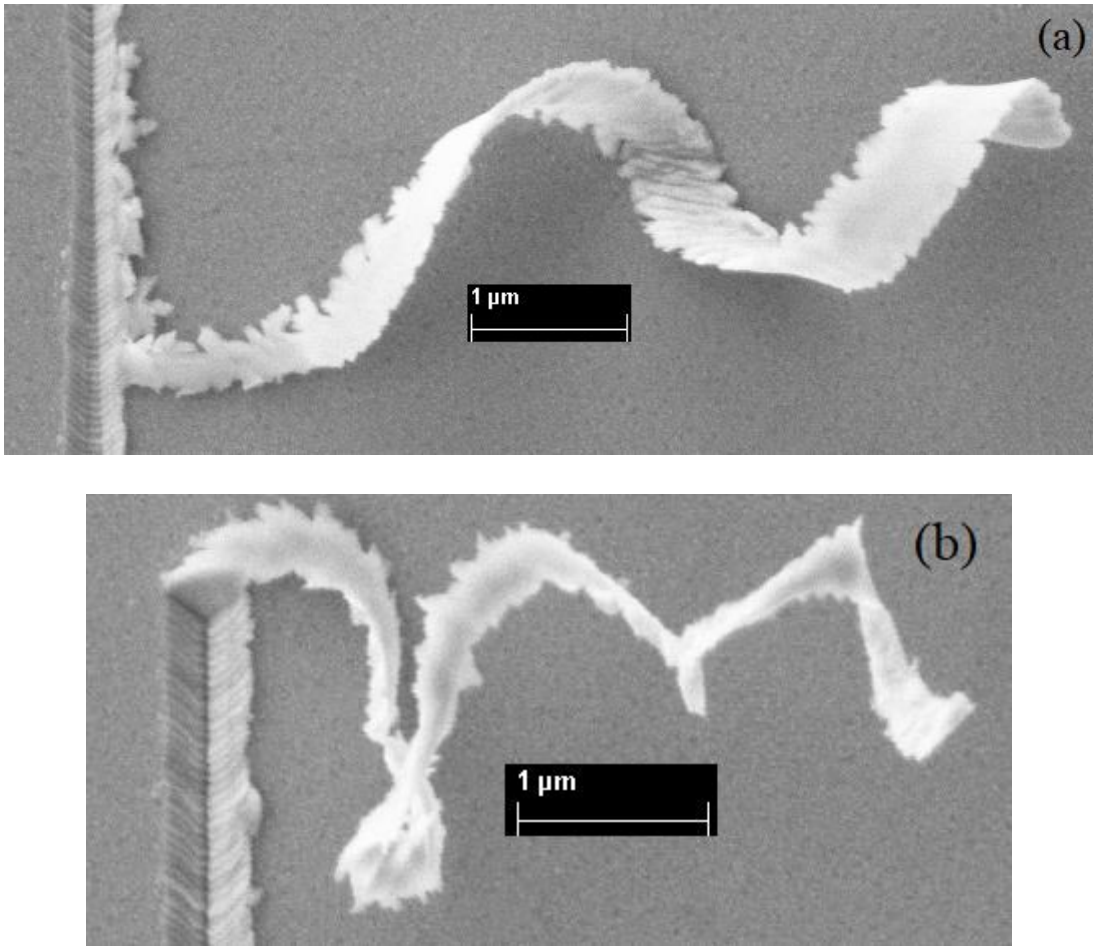

Figure 6.13 Magnification of the SEM image of the chip formed at (a) middle (b) end of the FF groove

AFM Scans

Comparing the pile-up height, the groove depth and the surface roughness of tests no.1 and no.0 gives:

Table 6.2 Cross sectional profile parameters of test no.1

	FF (% change)	**EF (% change)**
Pile up height (nm)	57.2 (-2%)	118.8 (-2%)
Groove depth (nm)	99.1 (32%)	131.1 (-6%)
Roughness Start / End (nm)	3.6 (50%) / 4.2 (-3%)	5.6 (38%) / 2.2 (9%)

Explanation of % signs:

- Pile up height: +ve is more height and -ve less height
- Groove depth: +ve is deeper -ve is shallower
- Roughness: +ve is increase in roughness and -ve is decrease in roughness

DAQ output

DAQ signal extracted from test no.1 compared to test no.0 for A-B (Raw) is demonstrated in Figure 6.14 and for LFM in Figure 6.15:

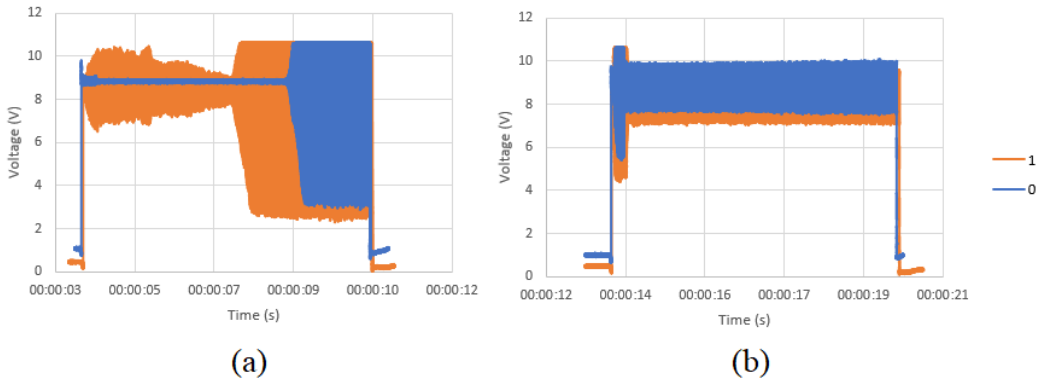

Figure 6.14 Comparison between the extracted A-B (RAW) data between tests 0 (blue) and 1 (orange) with: (a) Face forward (b) Edge forward

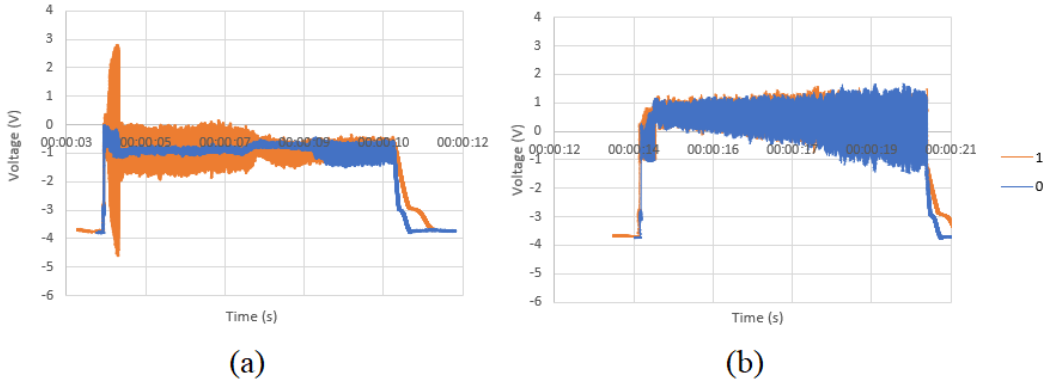

Figure 6.15 Comparison between the extracted LFM data between tests 0 (blue) and 1 (orange) with: (a) Face forward (b) Edge forward

Test no.2

Figure 6.16 shows the second test wherein the same amplitude of 40 nm was used but a 1000 Hz frequency rather than 100 Hz. As for the chip formation, Figure 6.17 (a) shows the creation of a continuous chip followed by serrated ones on one side of the groove as in Figure 6.17 (b).

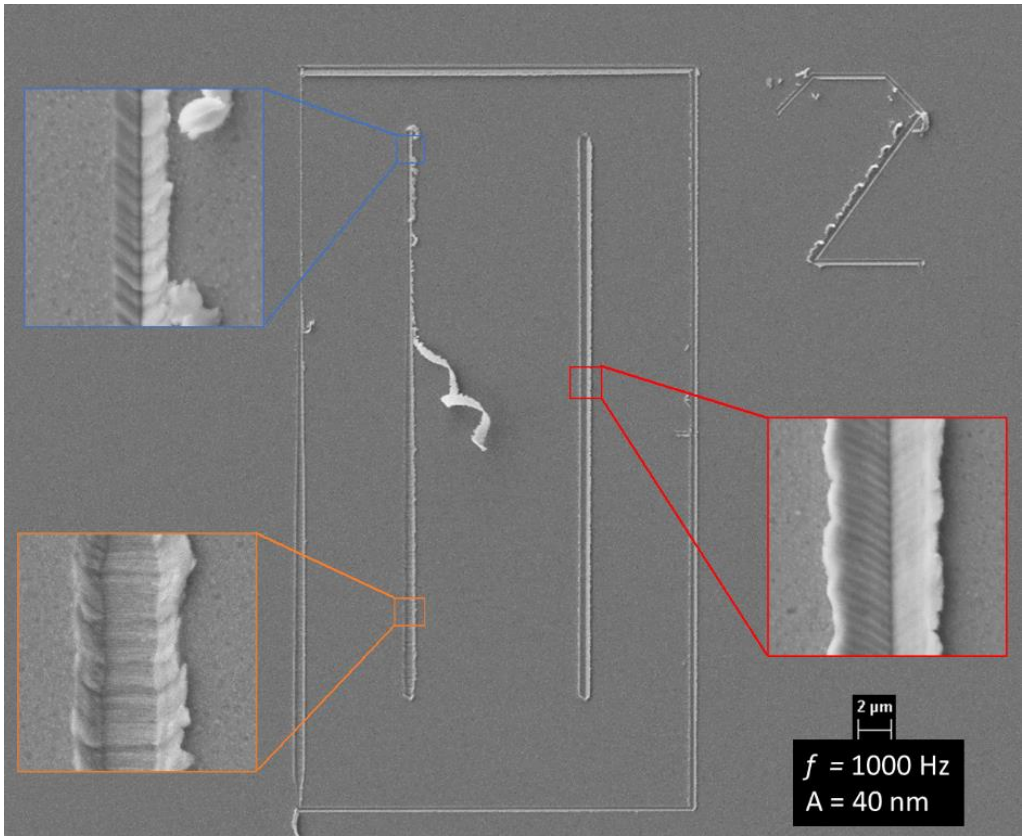

Figure 6.16 SEM image of test no.2

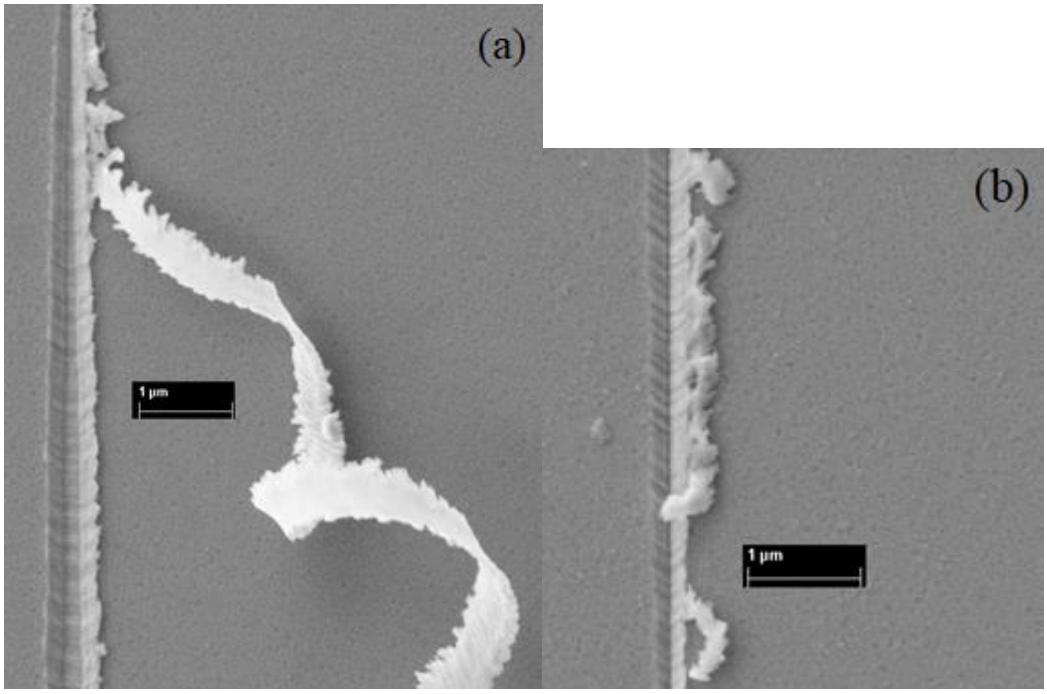

Figure 6.17 Magnified image of the chip formed at (a) middle (b) near the end of the FF groove

AFM Scans

Comparing the pile-up height, the groove depth and the surface roughness of tests no.2 and no.0 gives:

Table 6.3 Cross sectional profile parameters of test no.2

	FF (% change)	**EF (% change)**
Pile up height (nm)	73.8 (26%)	137.4 (13%)
Groove depth (nm)	79.8 (6.1%)	127.9 (-7.8%)
Roughness Start / End (nm)	2.3 (-2%) / 3 (-3%)	1.6 (-60%) / 1 (-52%)

DAQ output

DAQ signal extracted from test no.2 compared to test no.0 for A-B (Raw) is demonstrated in Figure 6.18 and for LFM in Figure 6.19:

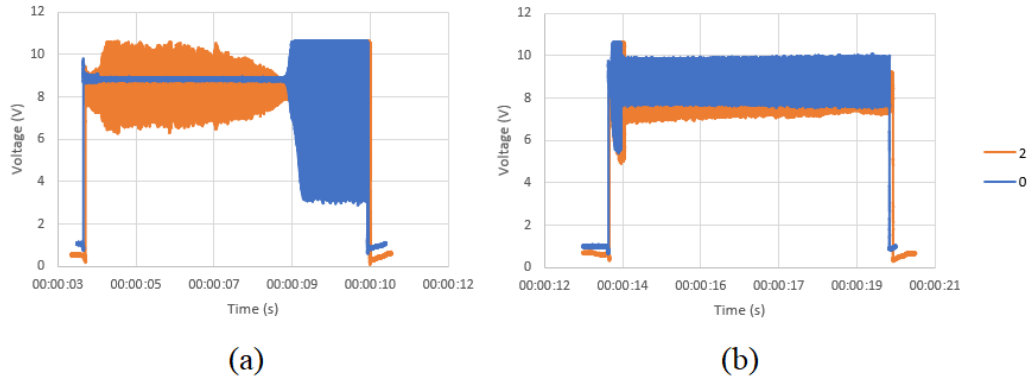

Figure 6.18 Comparison between the extracted A-B (RAW) data between tests 0 (blue) and 2 (orange) with: (a) Face forward (b) Edge forward

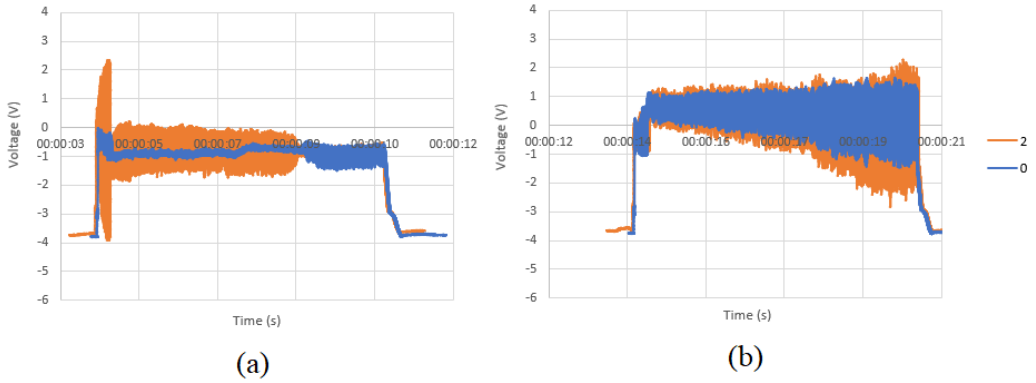

Figure 6.19 Comparison between the extracted LFM data between tests 0 (blue) and 2 (orange) with: (a) Face forward (b) Edge forward

Test no.3

As for the third test with its SEM image shown in Figure 6.20, the maximum applicable frequency of 2000 Hz was used while the amplitude stayed at 40 nm. Meanwhile, Figure 6.21 (a) shows a chip that probably was created during the previous groove, was stuck to the probe, and got detached as the probe started the EF groove. Figure 6.21 (b) on the other hand shows serrated chips as in the previous test.

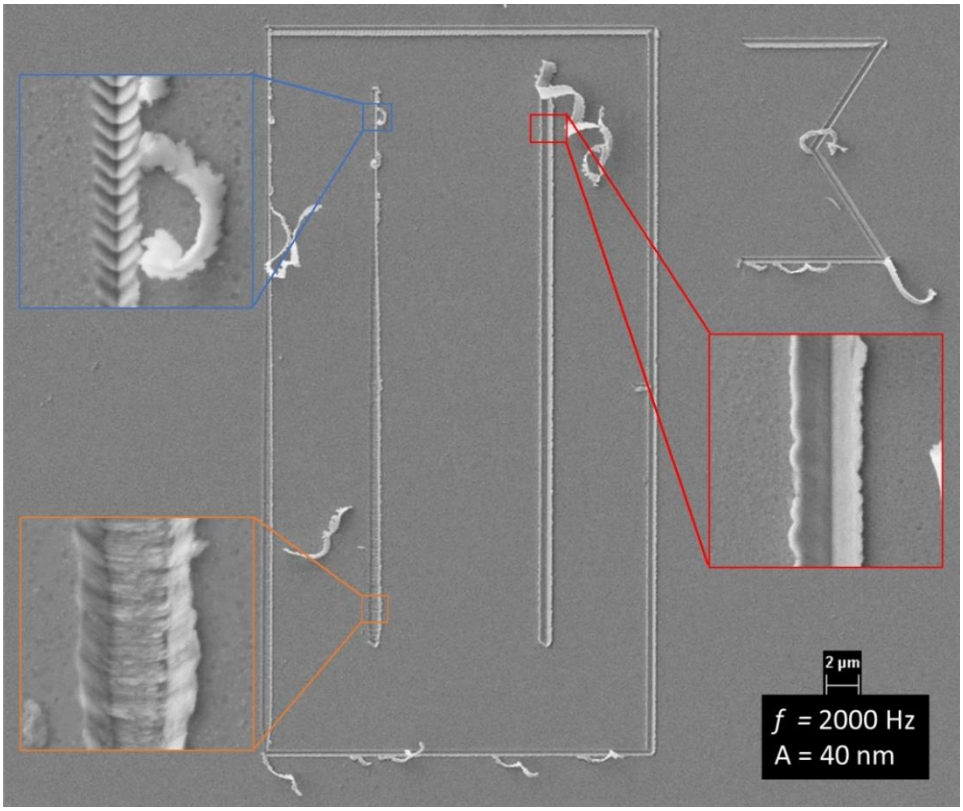

Figure 6.20 SEM image of test no.4

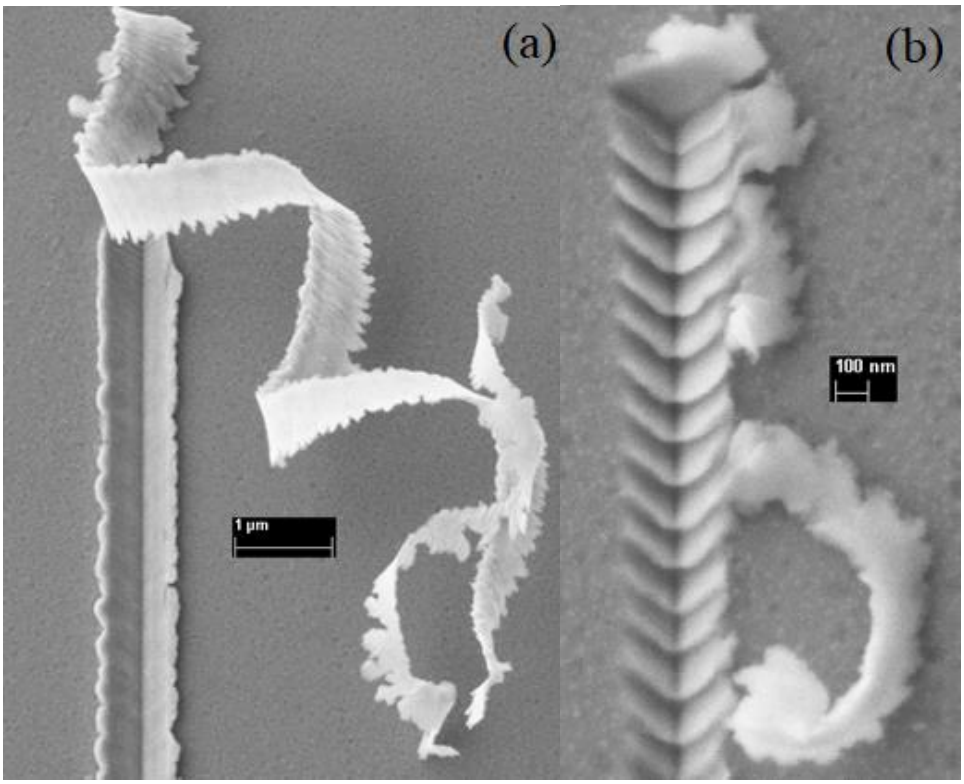

Figure 6.21 Magnified image of the chip formed at (a) middle of the EF groove (relocated from the previous FF groove) (b) end of the FF groove

AFM Scans

Comparing the pile-up height, the groove depth and the surface roughness of tests no.3 and no.0 gives:

Table 6.4 Cross sectional profile parameters of test no.3

	FF (% change)	**EF (% change)**
Pile up height (nm)	58.4 (-0.4%)	149.8 (23%)
Groove depth (nm)	92.6 (23%)	139.9 (1%)
Roughness Start / End (nm)	4.7 (97%) / 3.2 (-28%)	0.97 (-76%) / 1.7 (-18%)

DAQ output

DAQ signal extracted from test no.3 compared to test no.0 for A-B (Raw) is demonstrated in Figure 6.22 and for LFM in Figure 6.23:

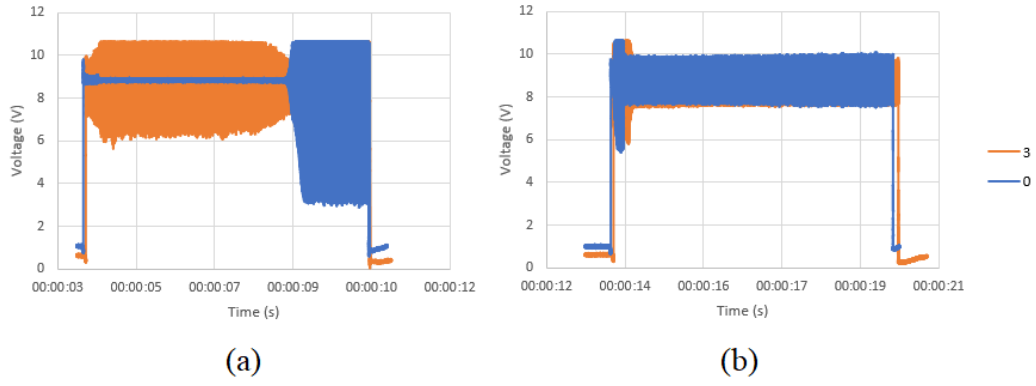

Figure 6.22 Comparison between the extracted A-B (RAW) data between tests 0 (blue) and 3 (orange) with: (a) Face forward (b) Edge forward

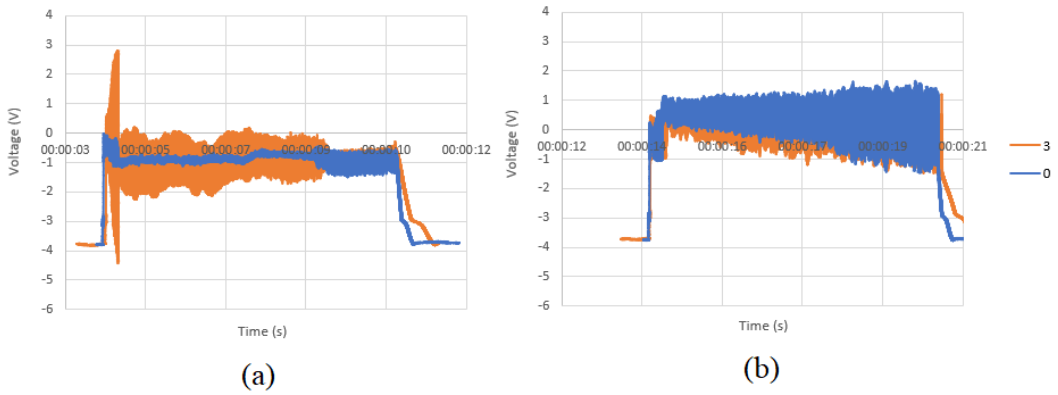

(a) (b)

Figure 6. 23 Comparison between the extracted LFM data between tests 0 (blue) and 3 (orange) with: (a) Face forward (b) Edge forward

Test no.4

The fourth test was the first to use 80 nm amplitude vibrations while using the minimum frequency of 100 Hz, as shown in Figure 6.24. Continuous and long chips were formed during the FF groove with no noticeable serrated or discontinuous chips.

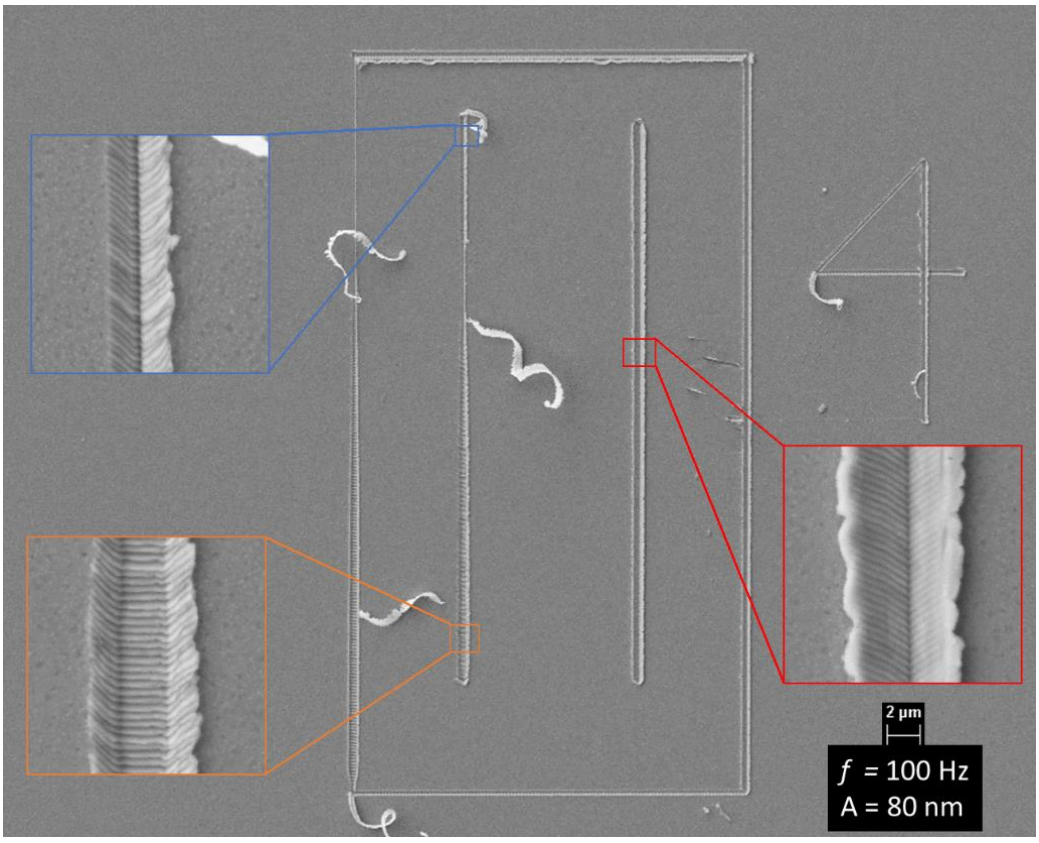

Figure 6.24 SEM image of test no.4

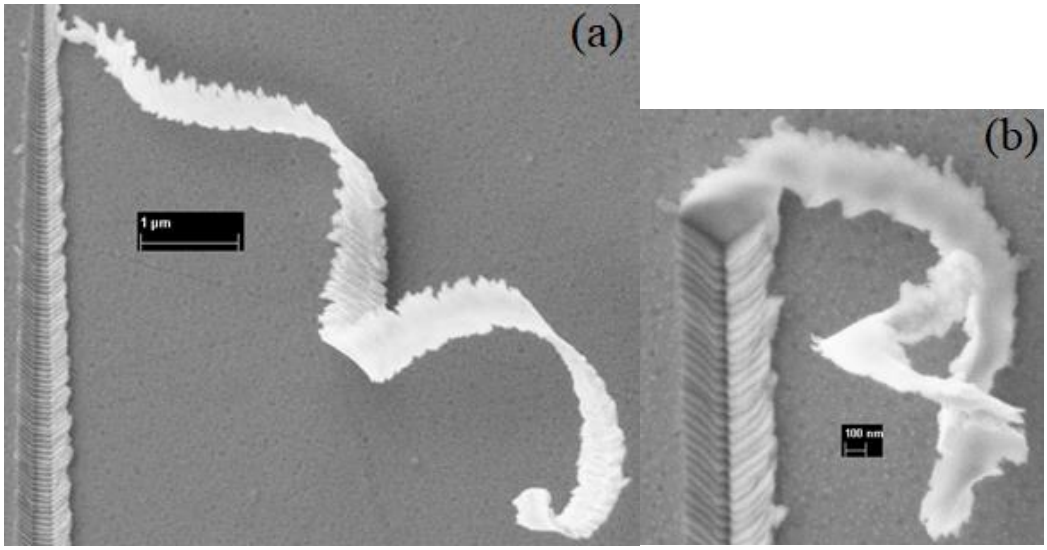

Figure 6.25 Magnified image of the chip formed at (a) middle (b) end of the FF groove

AFM Scans

Comparing the pile-up height, the groove depth and the surface roughness of tests no.4 and no.0 gives:

Table 6.5 Cross sectional profile parameters of test no.4

	FF (% change)	**EF (% change)**
Pile up height (nm)	67.2 (15%)	139.7 (15%)
Groove depth (nm)	99.3 (32%)	131.6 (-5%)
Roughness Start / End (nm)	3.7 (58%) / 2.6 (-40%)	1.1 (-73%) / 2.9 (39%)

DAQ output

DAQ signal extracted from test no.4 compared to test no.0 for A-B (Raw) is demonstrated in Figure 6.26 and for LFM in Figure 6.27:

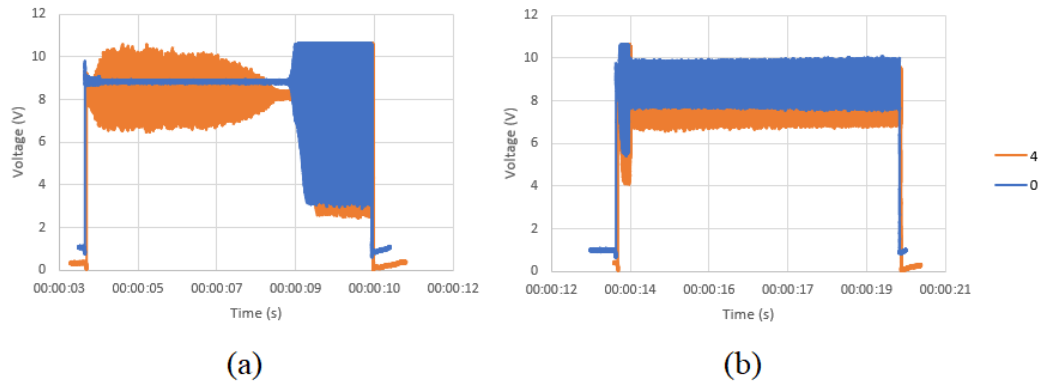

Figure 6.26 Comparison between the extracted A-B (RAW) data between tests 0 (blue) and 4 (orange) with: (a) Face forward (b) Edge forward

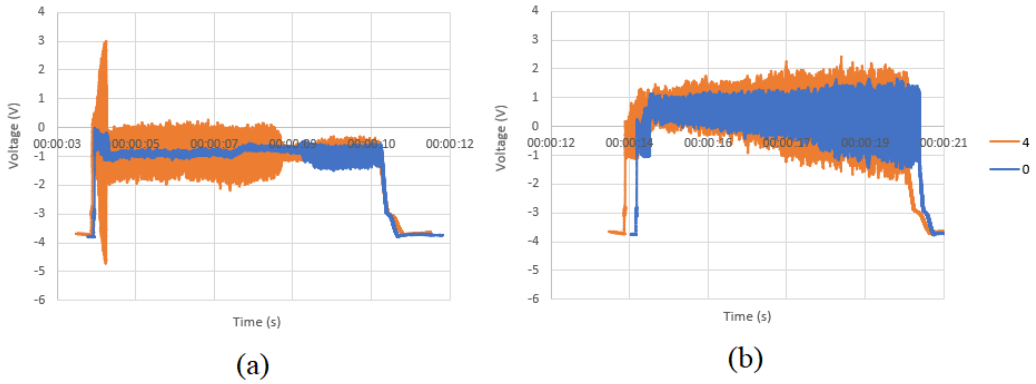

Figure 6.27 Comparison between the extracted LFM data between tests 0 (blue) and 4 (orange) with: (a) Face forward (b) Edge forward

Test no.5

The middle settings (values) of both the amplitude and frequency were used in this test, 80 nm and 1000 Hz, respectively. Figure 6.28 shows the SEM image of the fifth test. The trend of long chips then shorter serrated ones can be seen in Figure 6.29.

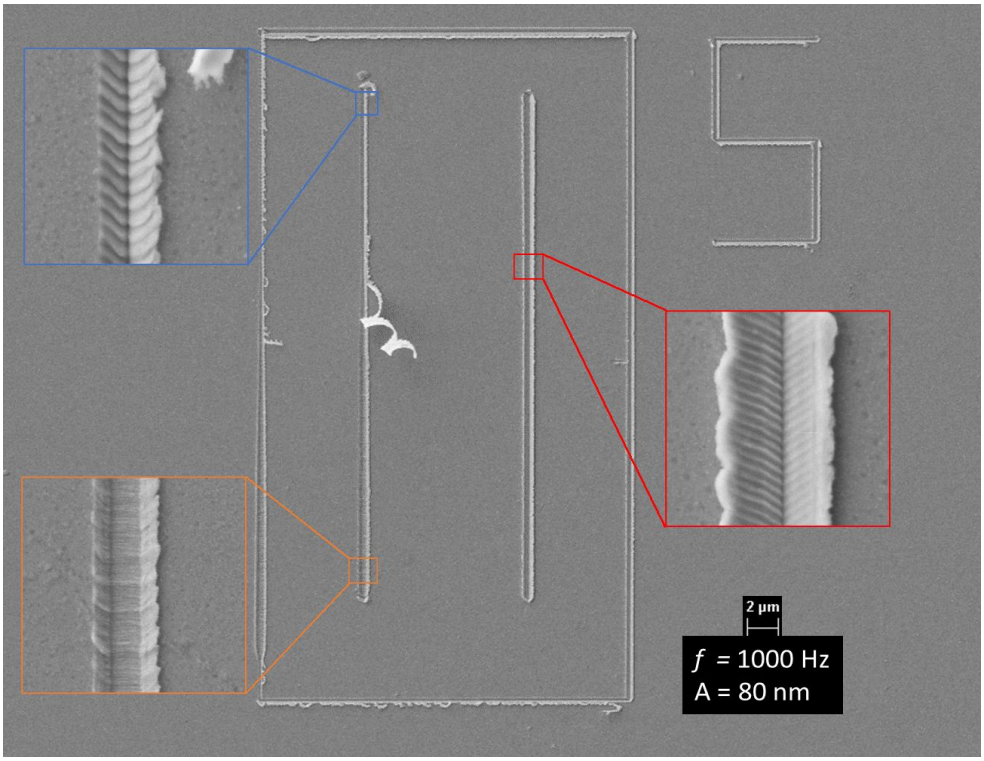

Figure 6.28 SEM image of test no.5

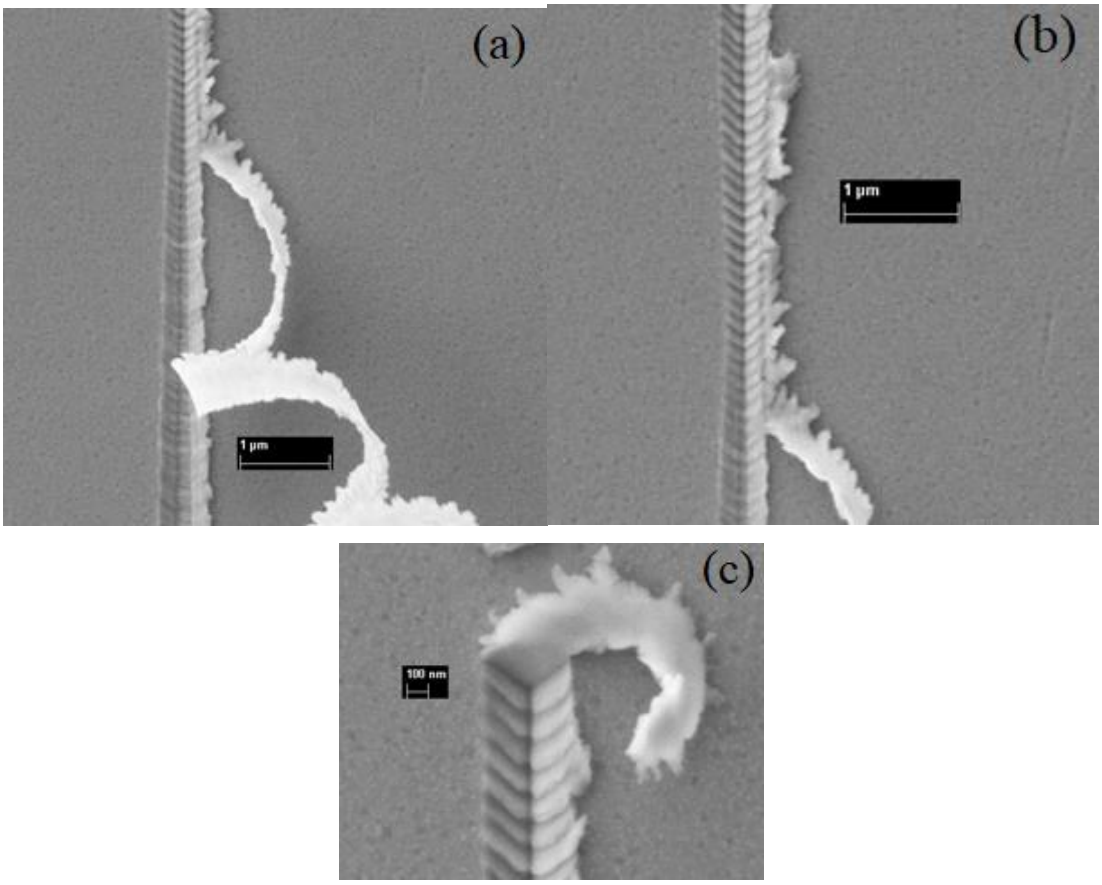

Figure 6.29 Magnified image of the chip formed at various locations within the FF groove

AFM Scans

Comparing the pile-up height, the groove depth and the surface roughness of tests no.5 and no.0 gives:

Table 6.6 Cross sectional profile parameters of test no.5

	FF (% change)	**EF (% change)**
Pile up height (nm)	67.2 (15%)	91.9 (-24%)
Groove depth (nm)	110.6 (47%)	122.4 (-12%)
Roughness Start / End (nm)	2.4 (3%) / 4.5 (3%)	3.4 (-14%) / 1.3 (-38%)

DAQ output

DAQ signal extracted from test no.5 compared to test no.0 for A-B (Raw) is demonstrated in Figure 6.30 and for LFM in Figure 6.31:

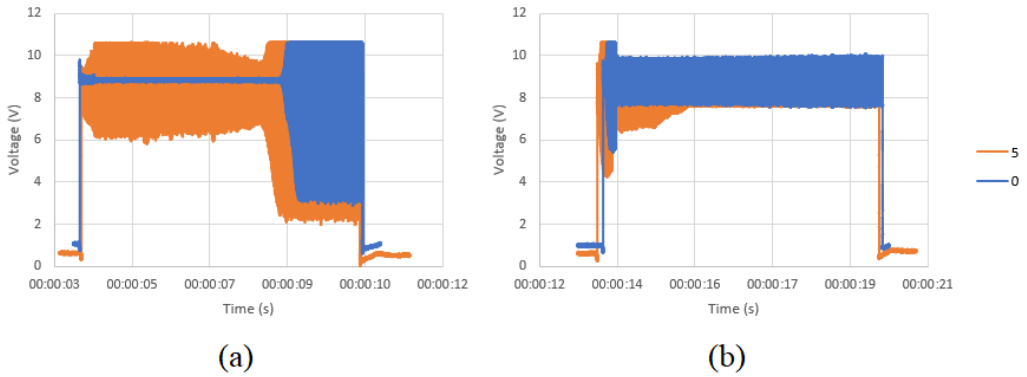

Figure 6.30 Comparison between the extracted A-B (RAW) data between tests 0 (blue) and 5 (orange) with: (a) Face forward (b) Edge forward

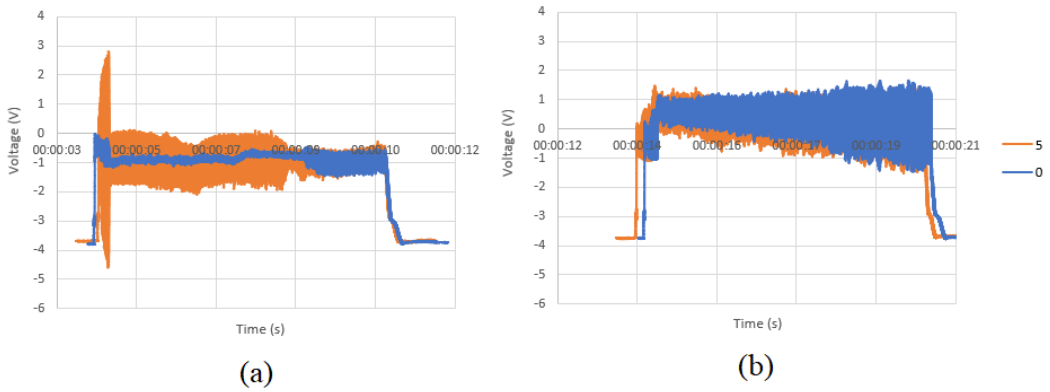

Figure 6.31 Comparison between the extracted LFM data between tests 0 (blue) and 5 (orange) with: (a) Face forward (b) Edge forward

Test no.6

The sixth test was the last to use 80 nm amplitude along with the highest frequency of 2000 Hz, as shown in Figure 6.32. However, this figure does not show a long continuous chip like previous tests. This is probably caused by the attachment of the chip to the probe's tip causing its relocation. Meanwhile, Figure 6.33 shows no serrated chips but rather a continuous one.

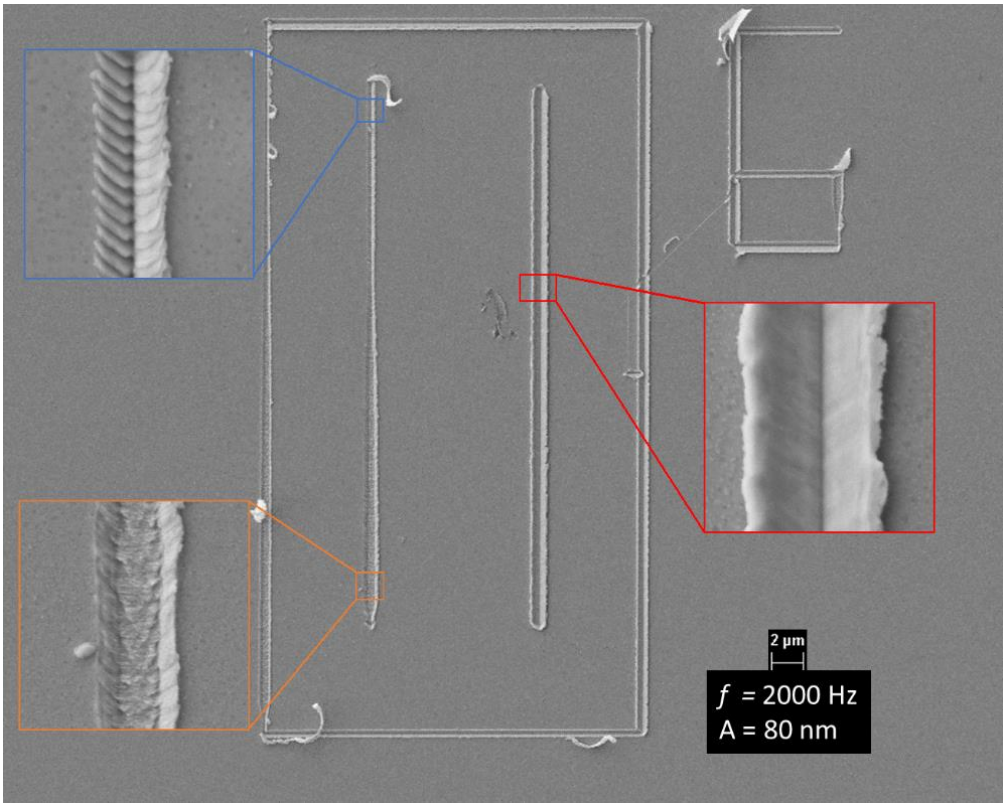

Figure 6.32 SEM image of test no.6

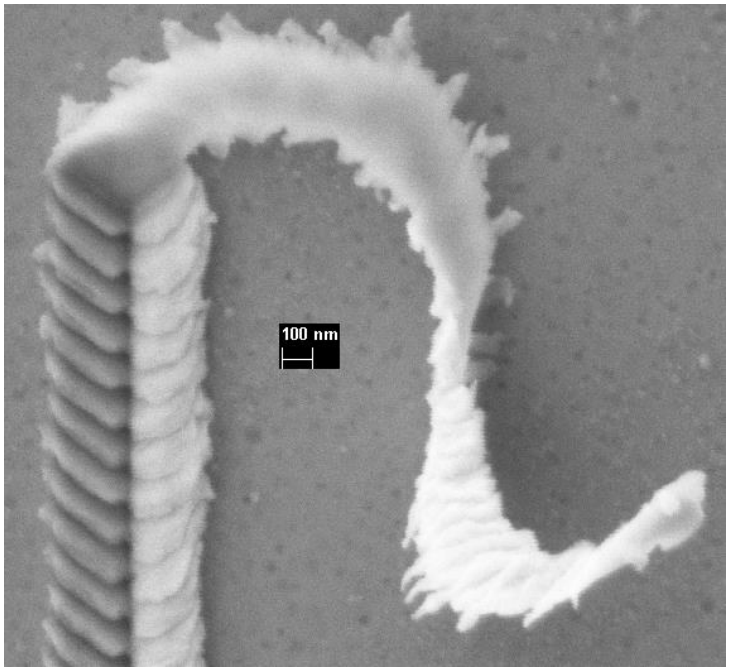

Figure 6.33 Magnified image of the chip formed at the end of the FF groove

AFM Scans

Comparing the pile-up height, the groove depth and the surface roughness of tests no.6 and no.0 gives:

Table 6.7 Cross sectional profile parameters of test no.6

	FF (% change)	**EF (% change)**
Pile up height (nm)	66.4 (13%)	151.3 (25%)
Groove depth (nm)	107.4 (43%)	156.5 (13%)
Roughness Start / End (nm)	4.1 (72%) / 3 (-32%)	1.7 (-58%) / 2.1 (-1%)

DAQ output

DAQ signal extracted from test no.6 compared to test no.0 for A-B (Raw) is demonstrated in Figure 6.34 and for LFM in Figure 6.35:

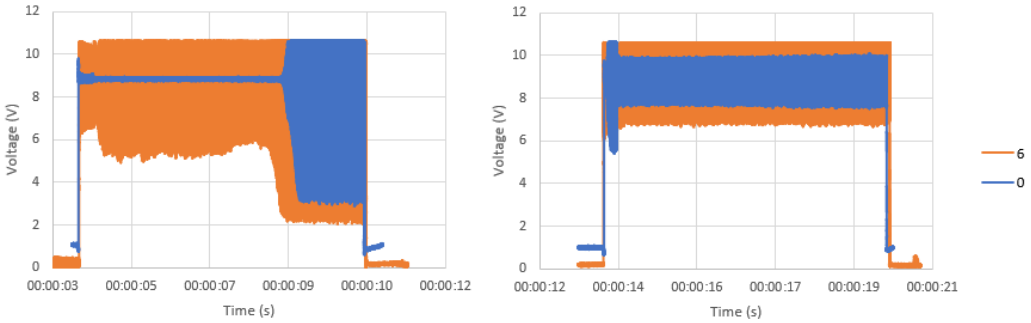

Figure 6.34 Comparison between the extracted A-B (RAW) data between tests 0 (blue) and 6 (orange) with: (a) Face forward (b) Edge forward

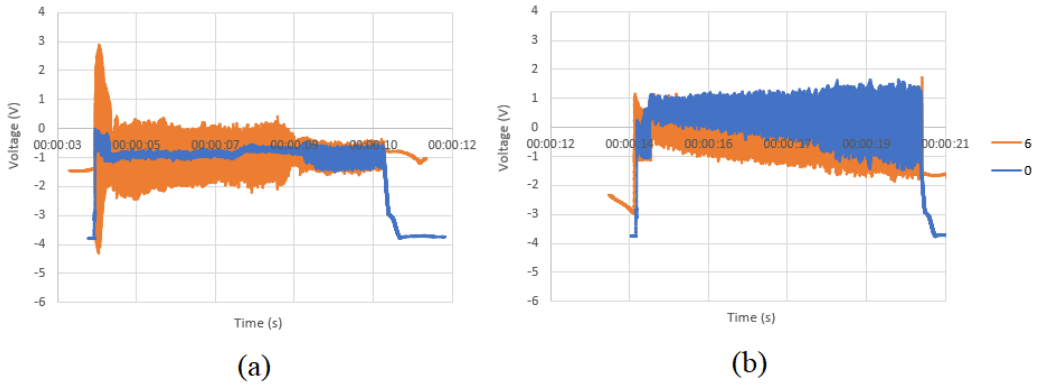

Figure 6.35 Comparison between the extracted LFM data between tests 0 (blue) and 6 (orange) with: (a) Face forward (b) Edge forward

Test no.7

The seventh test uses the maximum amplitude of 130 nm with the minimum frequency of 100 Hz. Figure 6.36 show the SEM image of this test. As Figure 6.37 shows, three continuous chips were formed, albeit with varying lengths.

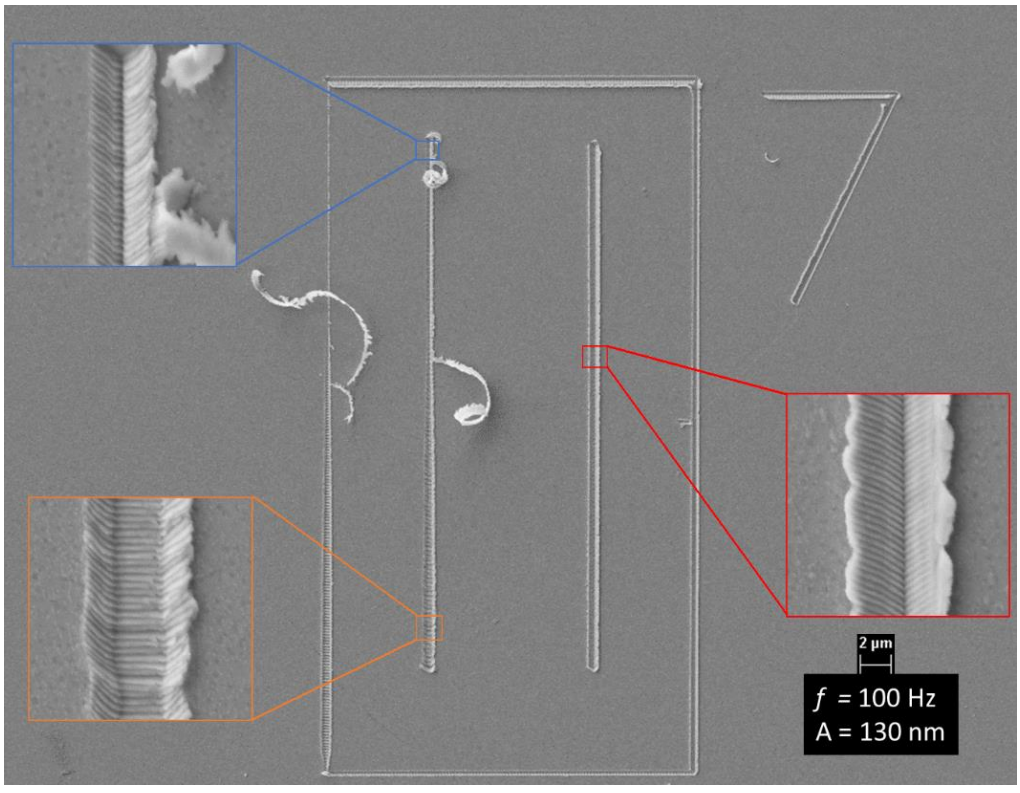

Figure 6. 36 SEM image of test no.7

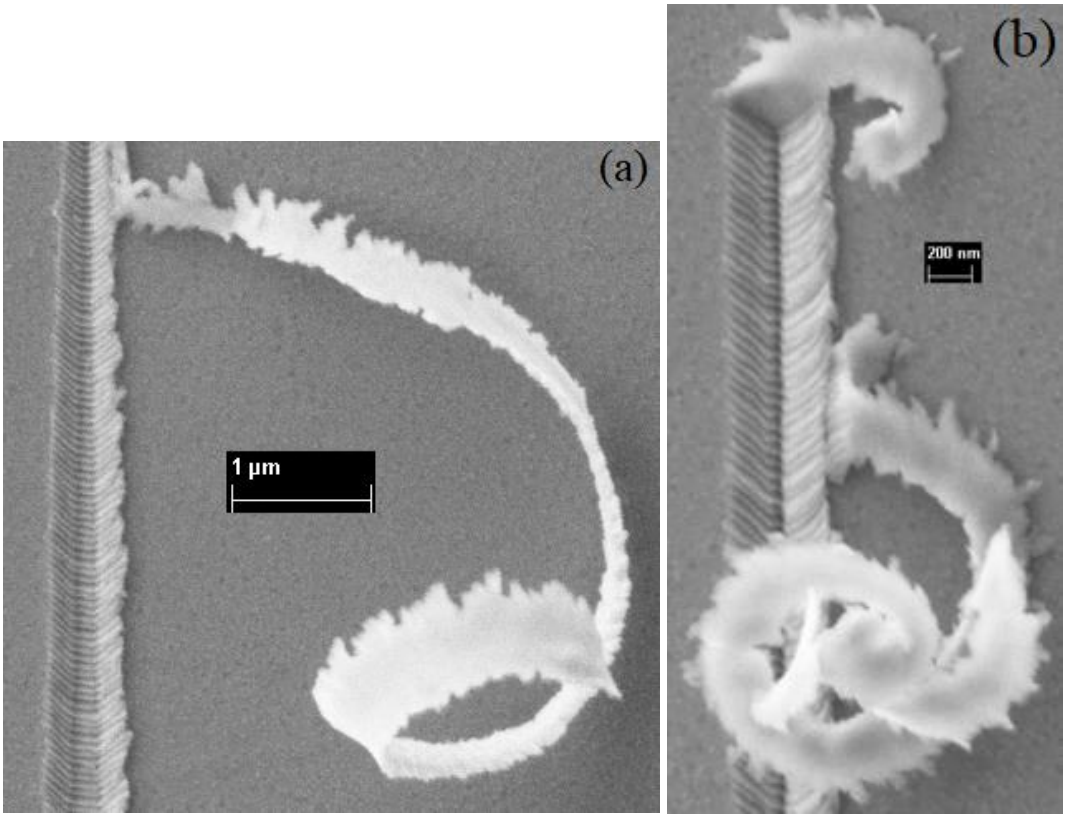

Figure 6.37 Magnified image of the chip formed at (a) middle (b) end of the FF groove

AFM Scans

Comparing the pile-up height, the groove depth and the surface roughness of tests no.7 and no.0 gives:

Table 6.8 Cross sectional profile parameters of test no.7

	FF (% change)	**EF (% change)**
Pile up height (nm)	65.5 (12%)	112.7 (-7%)
Groove depth (nm)	100.1 (33%)	129.1 (-7%)
Roughness Start / End (nm)	3.4 (42%) / 3 (-31%)	1.8 (-57%) / 2.8 (34%)

DAQ output

DAQ signal extracted from test no.7 compared to test no.0 for A-B (Raw) is demonstrated in Figure 6.38 and for LFM in Figure 6.39:

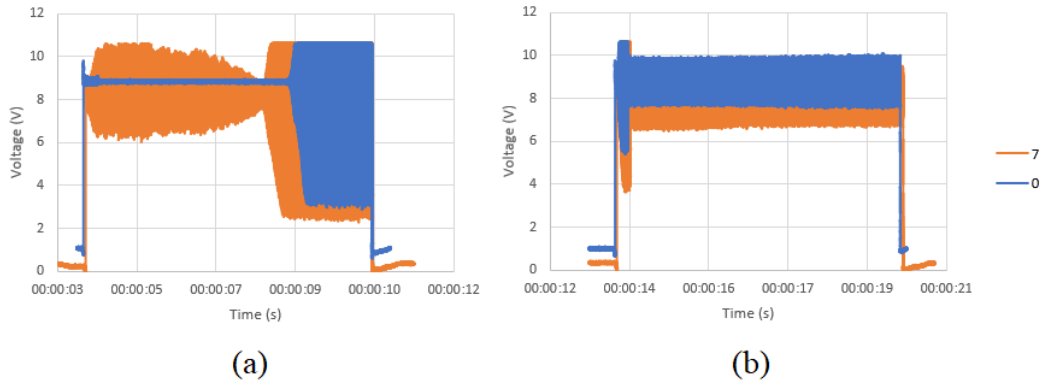

Figure 6.38 comparison between the extracted A-B (RAW) data between tests 0 (blue) and 7 (orange) with: (a) Face forward (b) Edge forward

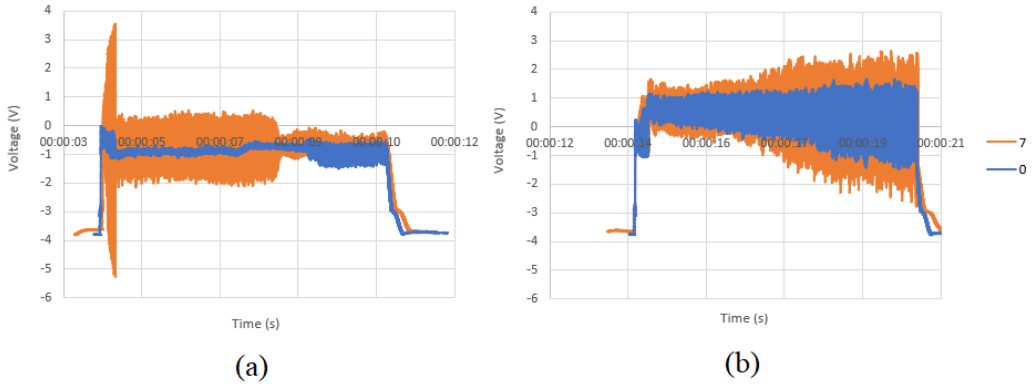

Figure 6.39 comparison between the extracted LFM data between tests 0 (blue) and 7 (orange) with: (a) Face forward (b) Edge forward

Test no.8

This test uses 1000 Hz frequency while using 130 nm amplitude, as shown in Figure 6.40. With regards to chip formation, Figure 6.41 shows a continuous chip but the return of serrated chips along the last third of the FF groove.

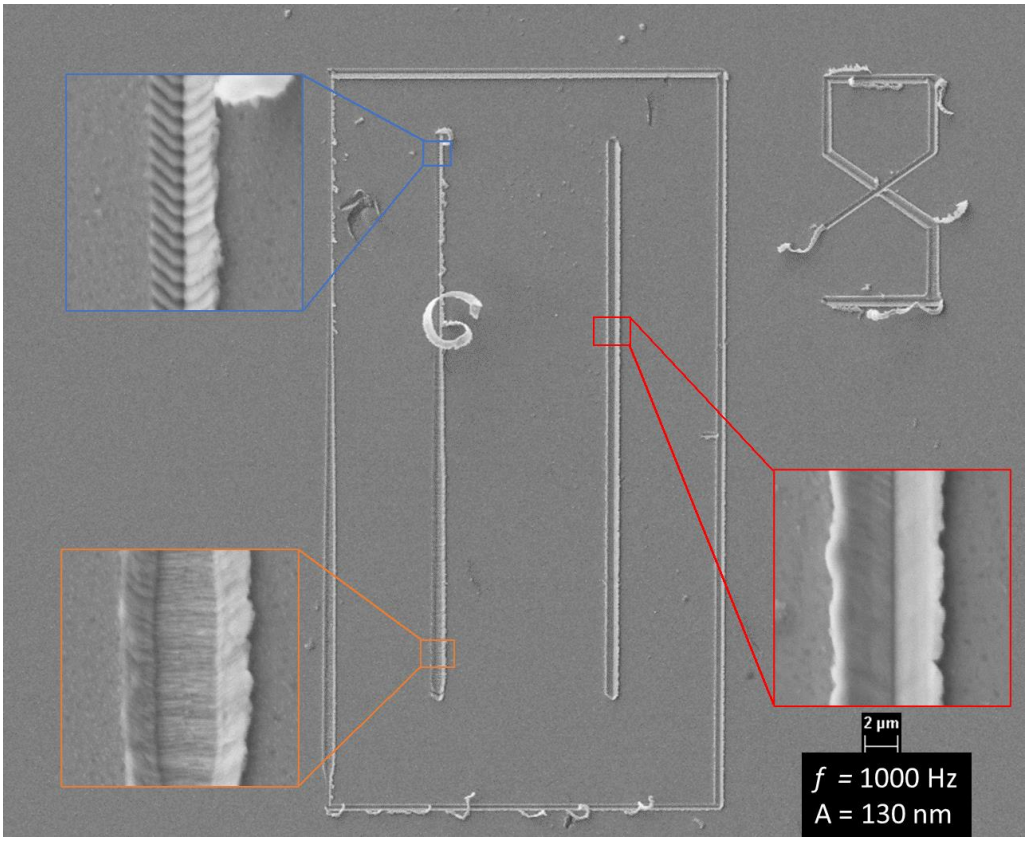

Figure 6.40 SEM image of test no.8

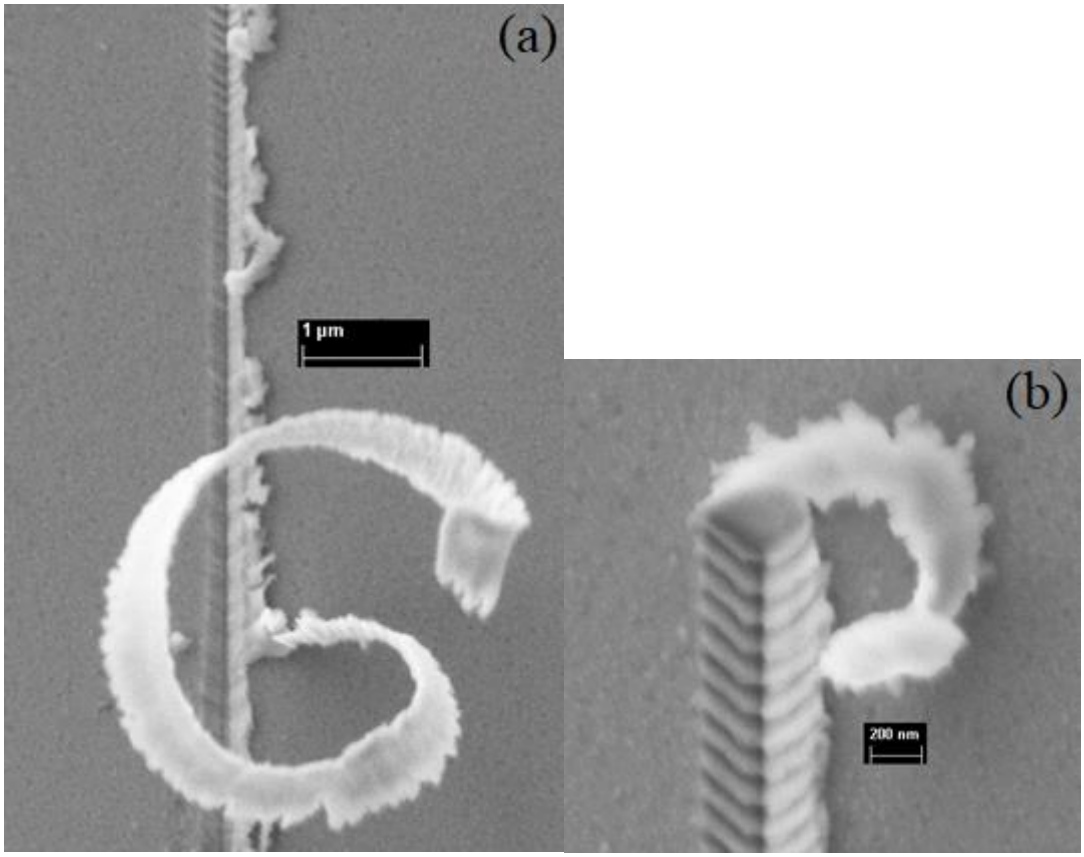

Figure 6.41 Magnified image of the chip formed at (a) middle (b) end of the FF groove

AFM Scans

Comparing the pile-up height, the groove depth and the surface roughness of tests no.8 and no.0 gives:

Table 6.9 Cross sectional profile parameters of test no.8

	FF (% change)	**EF (% change)**
Pile up height (nm)	83.4 (42%)	139.3 (15%)
Groove depth (nm)	114.1 (52%)	137.0 (-1%)
Roughness Start / End (nm)	2.1 (-12%) / 3.6 (-19%)	3.3 (-18%) / 1.3 (-38%)

DAQ output

DAQ signal extracted from test no.8 compared to test no.0 for A-B (Raw) is demonstrated in Figure 6.42 and for LFM in Figure 6.43:

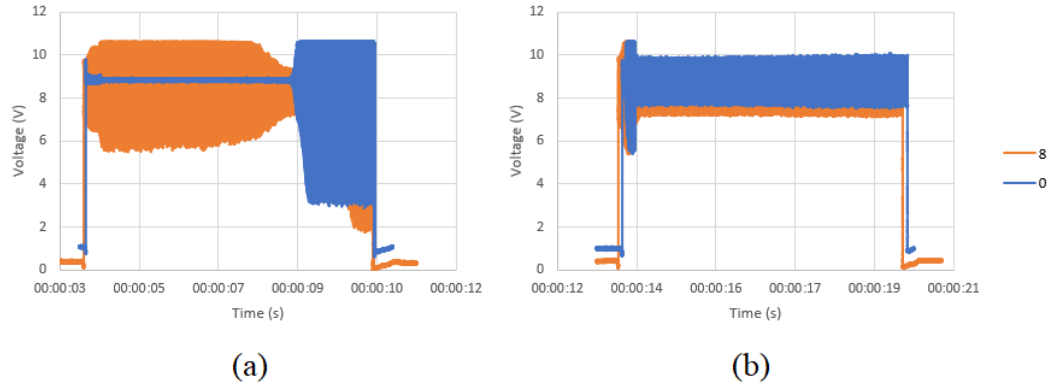

Figure 6.42 Comparison between the extracted A-B (RAW) data between tests 0 (blue) and 8 (orange) with: (a) Face forward (b) Edge forward

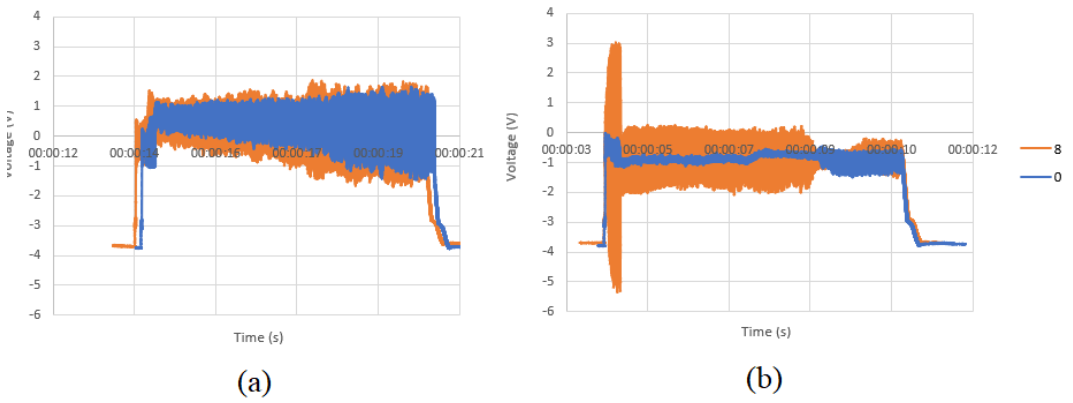

Figure 6.43 Comparison between the extracted LFM data between tests 0 (blue) and 8 (orange) with: (a) Face forward (b) Edge forward

Test no.9

The maximum settings for both the amplitude and frequency are used in this final test, with 130 nm and 2000 Hz values, respectively. SEM image of the test is shown in Figure 6.44. Similar to test no.6, the first chip formed was probably relocated due to its adhesion to the tip, while the last chip remained, as Figure 6.45 shows.

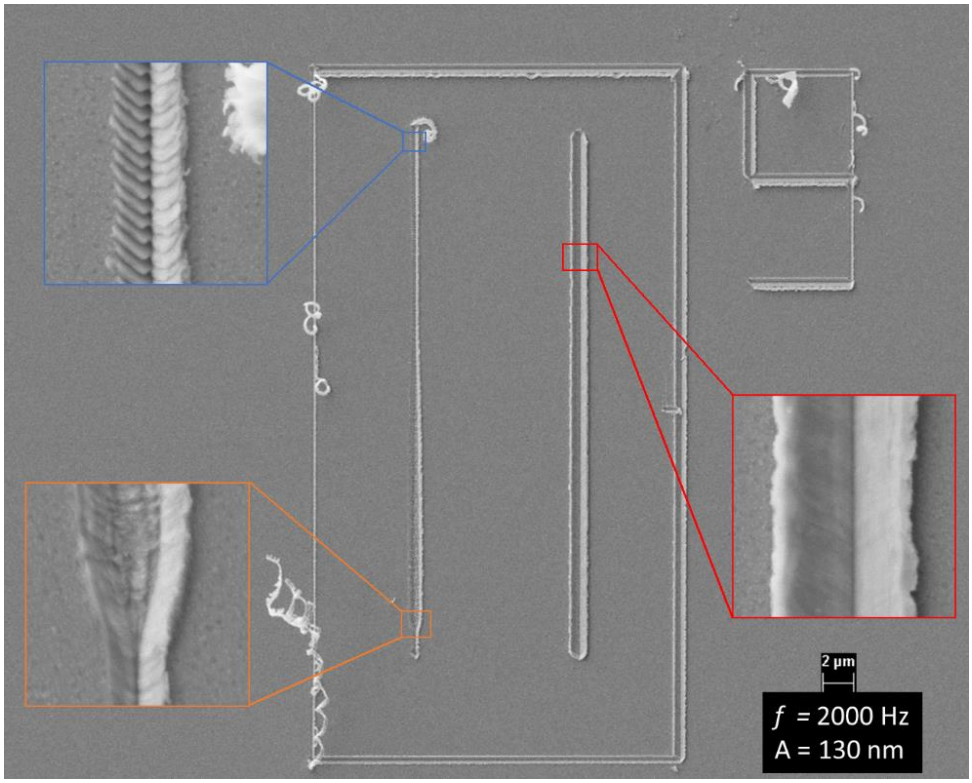

Figure 6.44 SEM image of test no.9

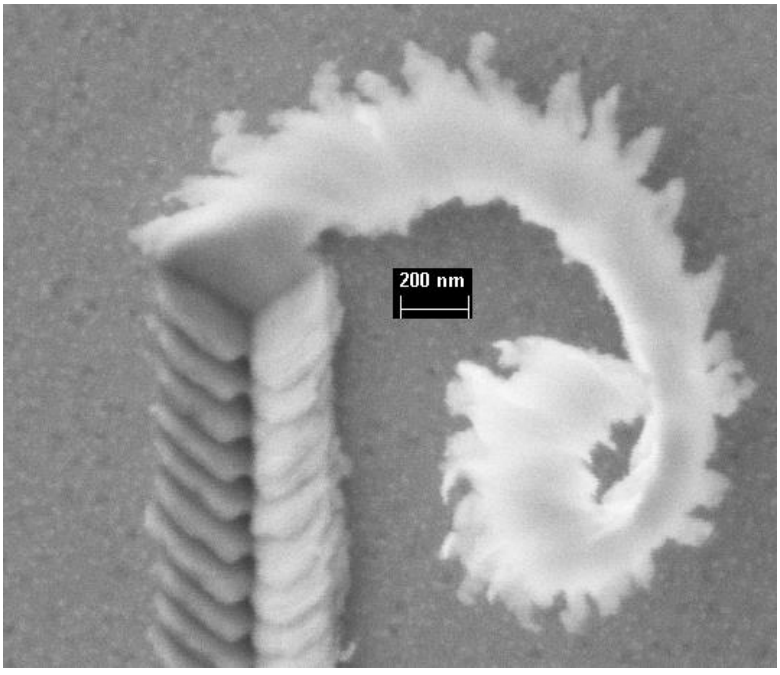

Figure 6.45 Magnified image of the chip formed at the end of the FF groove

AFM Scans

Comparing the pile-up height, the groove depth and the surface roughness of tests no.9 and no.0 gives:

Table 6.10 Cross sectional profile parameters of test no.9

	FF (% change)	**EF (% change)**
Pile up height (nm)	77.3 (32%)	166.9 (37%)
Groove depth (nm)	127.2 (69%)	187.7 (35.3)
Roughness Start / End (nm)	4.1 (71%) / 3.6 (-18%)	1.4 (-66%) / 1.3 (-36%)

DAQ output

DAQ signal extracted from test no.9 compared to test no.0 for A-B (Raw) is demonstrated in Figure 6.46 and for LFM in Figure 6.47:

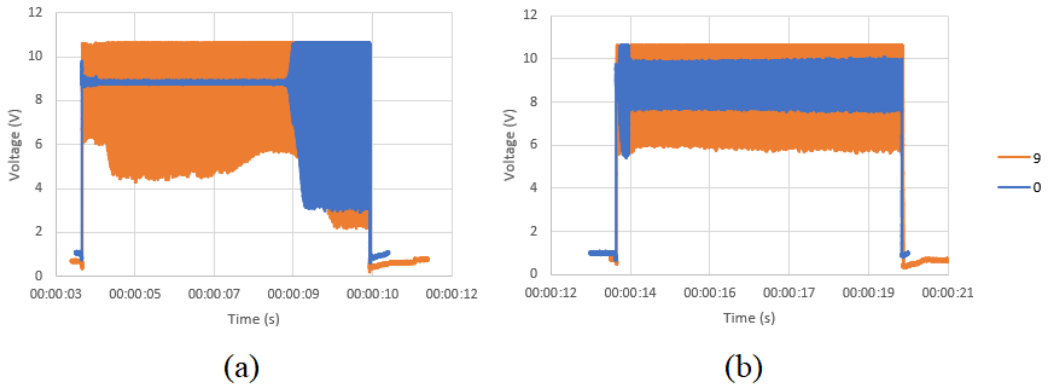

Figure 6.46 Comparison between the extracted A-B (RAW) data between tests 0 (blue) and 9 (orange) with: (a) Face forward (b) Edge forward

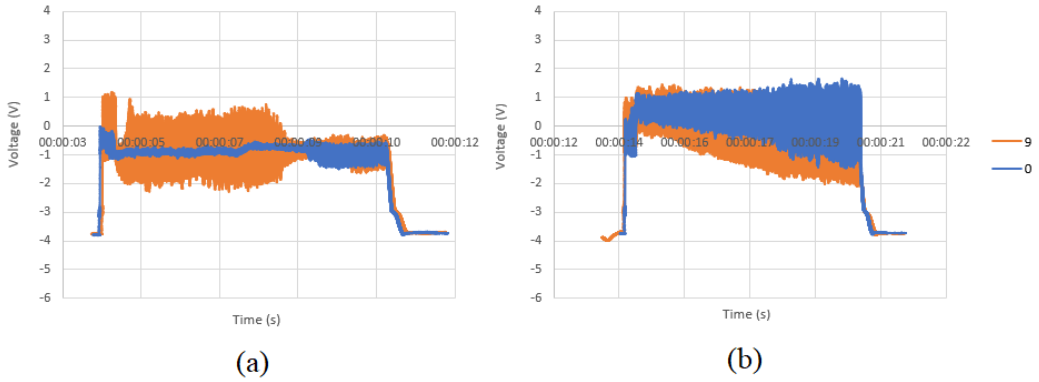

Figure 6.47 Comparison between the extracted LFM data between tests 0 (blue) and 9 (orange) with: (a) Face forward (b) Edge forward

6.3 Exploring the effect of introducing vibrations against conventional nanomachining

In this section, the first test (i.e., test no.0) will be used as a benchmark for further analysis.

Figure 6.48 compares the groove depths and pile-up heights for the different tests and different portions of each groove in which:

- h_{min} FF1: The lowest point of the start of the FF groove
- h_{max} FF1: The highest point of the start of the FF groove
- h_{min} FF2: The lowest point of the end of the FF groove
- h_{max} FF2: The highest point of the end of the FF groove

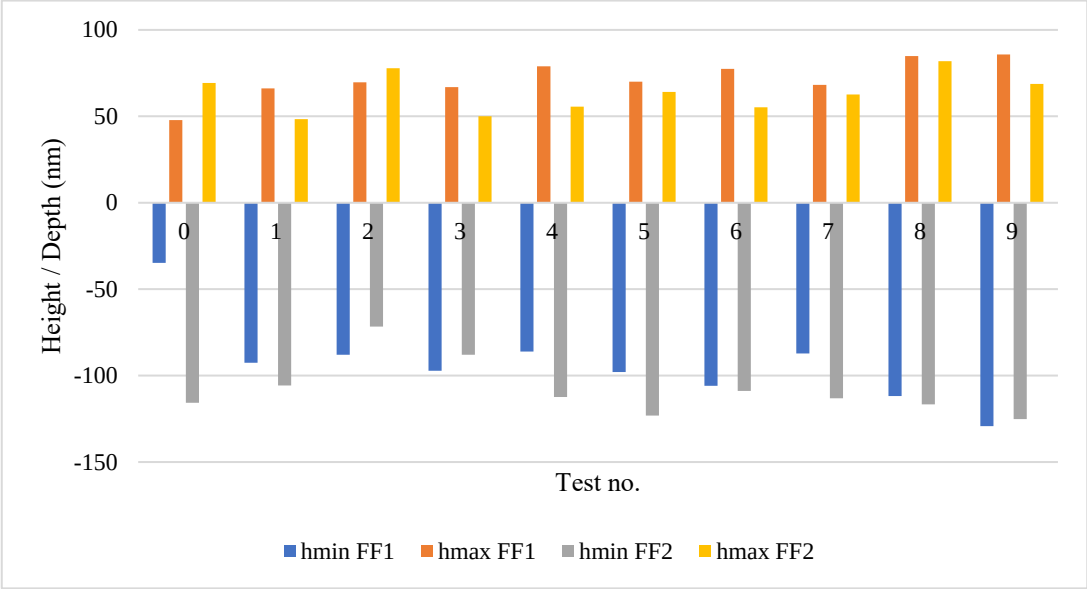

Figure 6.48 Face forward groove depths and pile-up heights comparison

Also applies for the EF groove (Figure 6.49), where:

- h_{min} EF3: The lowest point of the start of the EF groove
- h_{max} EF3: The highest point of the start of the EF groove
- h_{min} EF4: The lowest point of the end of the EF groove
- h_{max} EF4: The highest point of the end of the EF groove

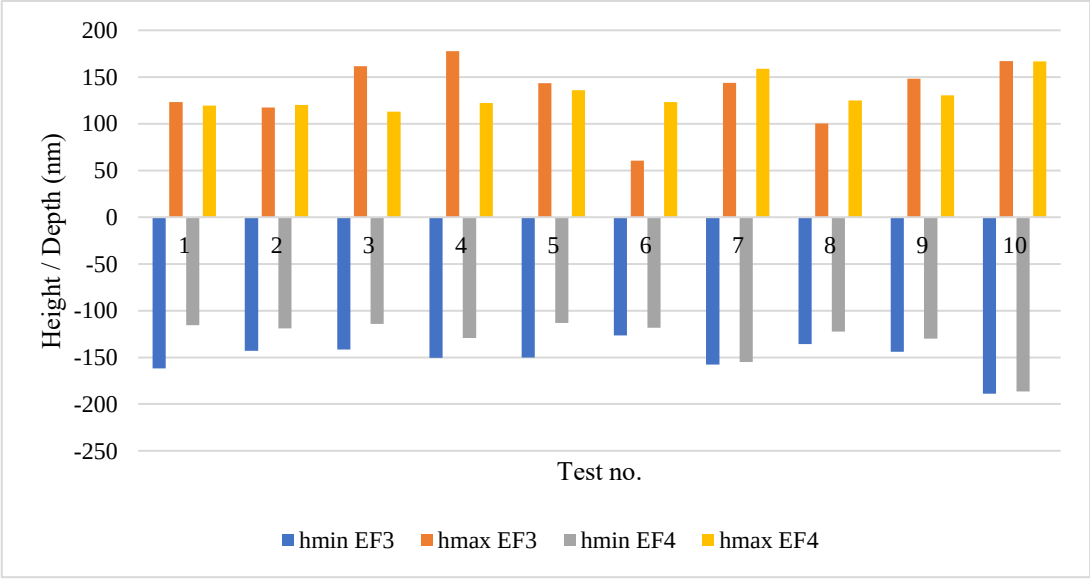

Figure 6.49 Edge forward groove depths and pile-up heights comparison

Consistency comparison

Table 6.11 shows consistency values for different grooves in which the bigger the values the less consistent the test is (shows bigger difference between start and end of groove), where:

- Shaded highlight the least consistent
- Underlined boxes highlight the most consistent

Table 6.11 Consistency values across all tests

	ΔFF (nm)		**ΔEF(nm)**	
	Δh_{min}(nm)	**Δh_{max}(nm)**	**Δh_{min}(nm)**	**Δh_{max}(nm)**
0	80.9	21.4	46.5	3.9
1	13.0	17.7	24.0	2.9
2	16.3	8.3	27.2	48.7
3	9.3	16.8	21.0	55.5
4	26.4	23.3	37.0	7.5
5	25.3	5.9	8.0	62.7
6	2.9	22.2	2.7	15.2
7	26.1	5.5	13.3	24.8
8	4.8	2.9	13.8	17.7
9	3.9	17.0	2.7	0.2

If a practitioner values a minimal change in pile-up heights and valley depths between the start and end of a groove, then consistency will be a useful tool for them.

Figure 6.50 below shows the difference between the lowest point (valley depth) at the start and end for both the FF and EF grooves, referred to as Δh_{min} FF and Δh_{min} EF, respectively. As well as the difference between the highest point (pile-up height)

at the start and end for both the FF and EF grooves, referred to as Δh_{max} FF and Δh_{max} EF, respectively as well.

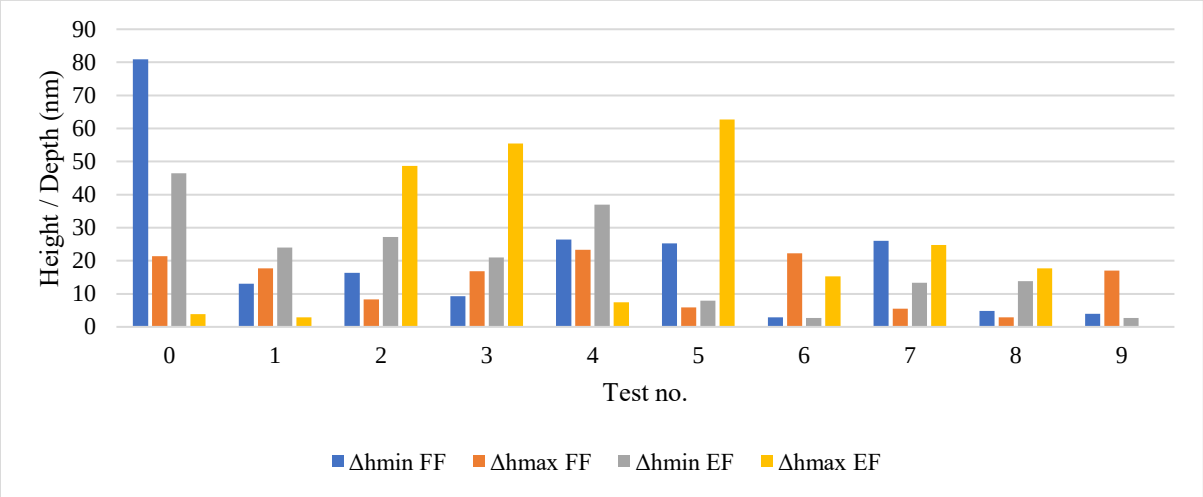

Figure 6.50 Inconsistency chart, higher values mean increased inconsistency

In addition, to give better perspective regarding the depth of the groove or height of the pile-up with respect to their corresponding average across the groove, as Figure 6.51 shows for the FF grooves and Figure 6.52 for the EF ones.

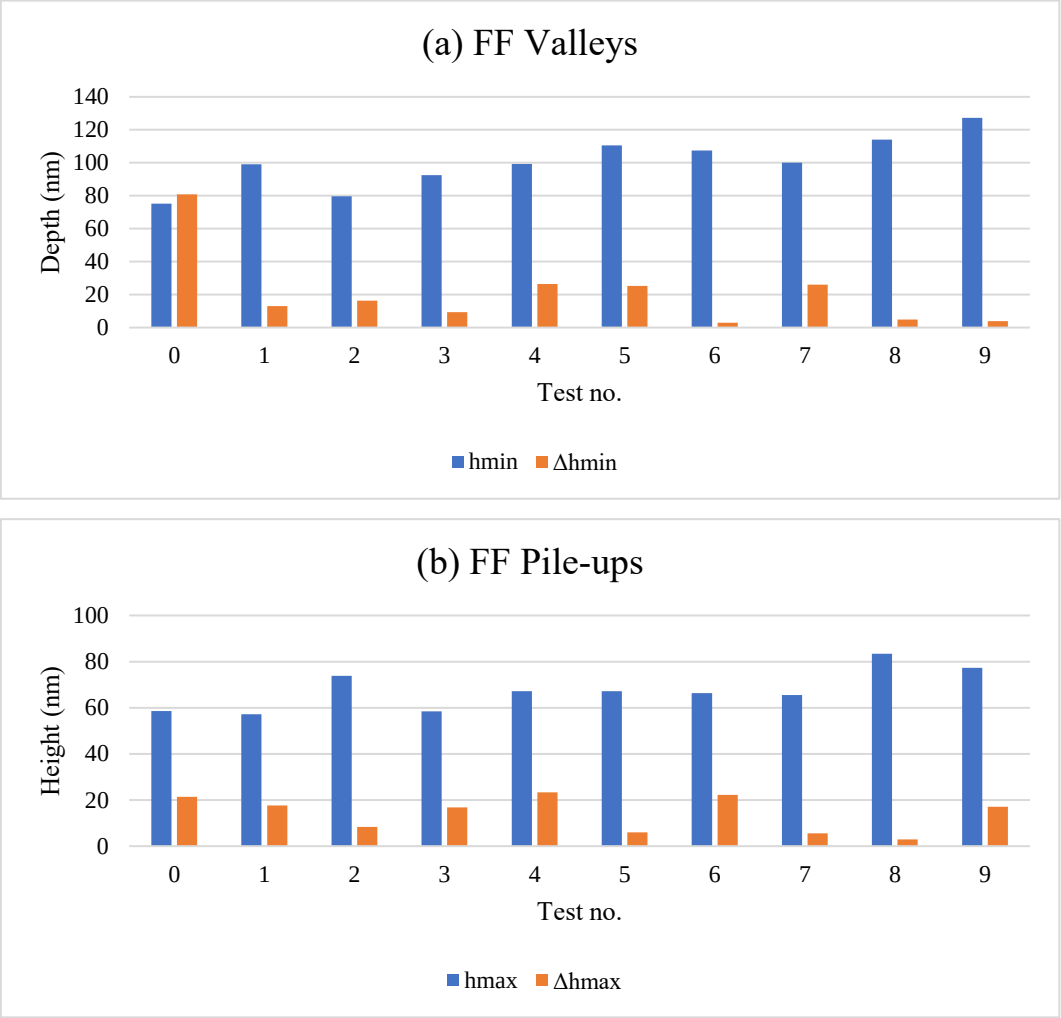

Figure 6.51 The Face Forward (a) depth of the grooves and (b) height of the pile-ups with their average values within the groove

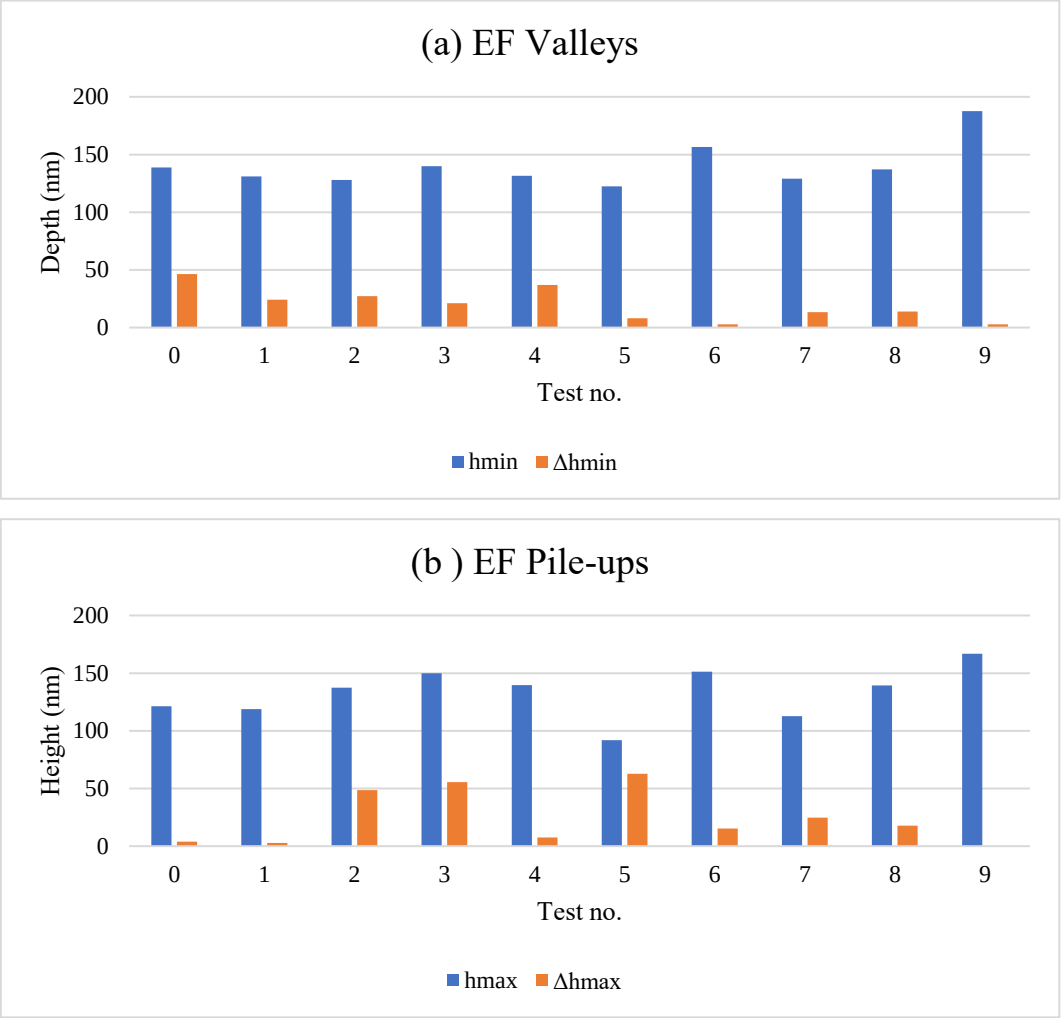

Figure 6.52 The Edge Forward (a) depth of the grooves and (b) height of the pile-ups with their average values within the groove

Roughness analysis

Another important parameter that can be used to assess the impact of inducing vibrations into the ultraprecision machining process is roughness. Table below compares each VANM test with the conventional test no.0.

As seen in Table 6.12, where positive percentages reflect an increase in roughness (i.e., worsening) and negative a decrease (i.e., improvement) with the last row showing the average value for all the tests. Graph in Figure 6.53 shows the data presented in Table 6.12.

Table 6.12 Roughness changes when compared to conventional nanomachining

	FF	**EF**
1-0	23.3%	23.5%
2-0	-17.2%	-55.6%
3-0	34.8%	-46.8%
4-0	8.8%	-17.2%
5-0	3.2%	-26.5%
6-0	20.1%	-29.6%
7-0	5.4%	-11.2%
8-0	-15.6%	-27.9%
9-0	26.4%	-50.9%
Average	9.9%	-26.9%

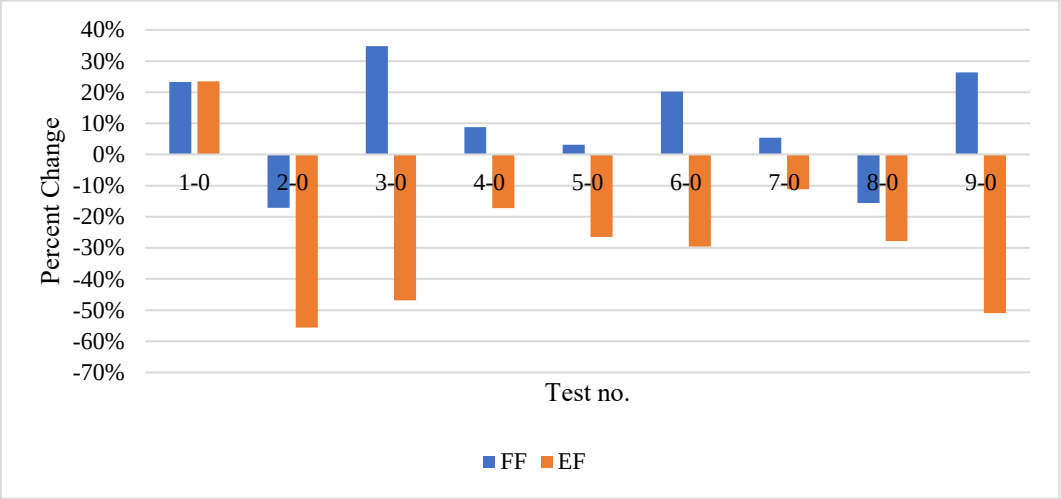

Figure 6.53 Summary of the change in roughness

Now, to give a better perspective on how a certain amplitude (Table 6.13 and Figure 6.54) and a certain frequency (Table 6.14 and Figure 6.55) impact roughness, data is rearranged as following tables and bar chart figures show.

Table 6.13 Impact of amplitude change on surface roughness

	40 nm		**80 nm**		**130 nm**		**All (nm)**	
	FF	**EF**	**FF**	**EF**	**FF**	**EF**	**FF**	**EF**
100 Hz	23.2%	26.8%	8.7%	-14.3%	5.4%	14.0%	12.5%	-0.5%
1000 Hz	-17.1%	-17.3%	3.1%	-30.8%	-15.6%	-27.8%	-9.9%	-25.3%
2000 Hz	34.8%	-46.8%	20.1%	-25.0%	26.4%	-39.8%	27.1%	-37.2%

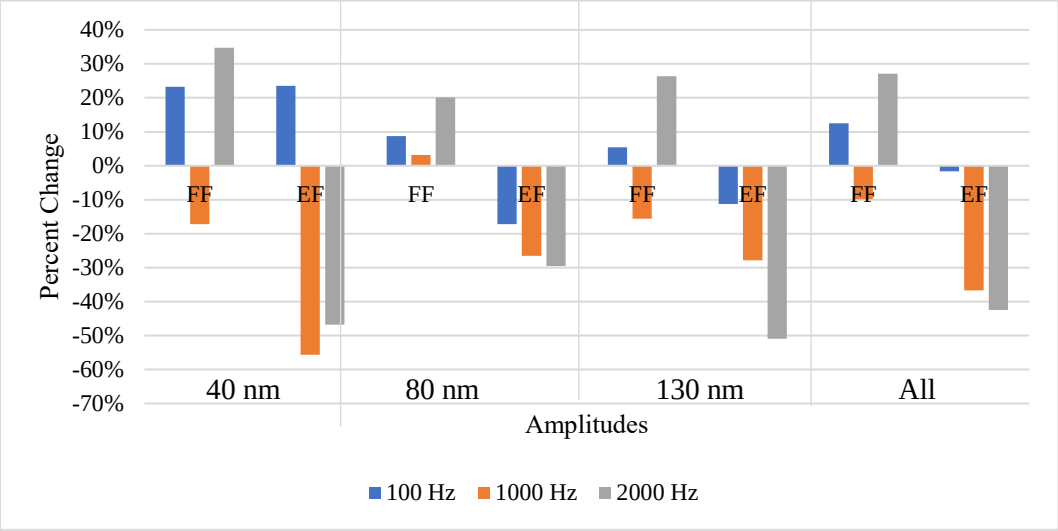

Figure 6.54 Bar chart of the impact of amplitude on surface roughness

Table 6.14 Impact of frequency change on surface roughness

	100 Hz		**1000 Hz**		**2000 Hz**		**All**	
	FF	**EF**	**FF**	**EF**	**FF**	**EF**	**FF**	**EF**
40 nm	23.2%	26.8%	-17.2%	-17.4%	34.8%	-46.8%	13.6%	-12.5%
80 nm	8.8%	-14.3%	3.2%	-30.8%	20.1%	-25.0%	10.7%	-23.4%
130 nm	5.4%	-14.0%	-15.6%	-27.8%	26.4%	-39.8%	5.4%	-27.2%

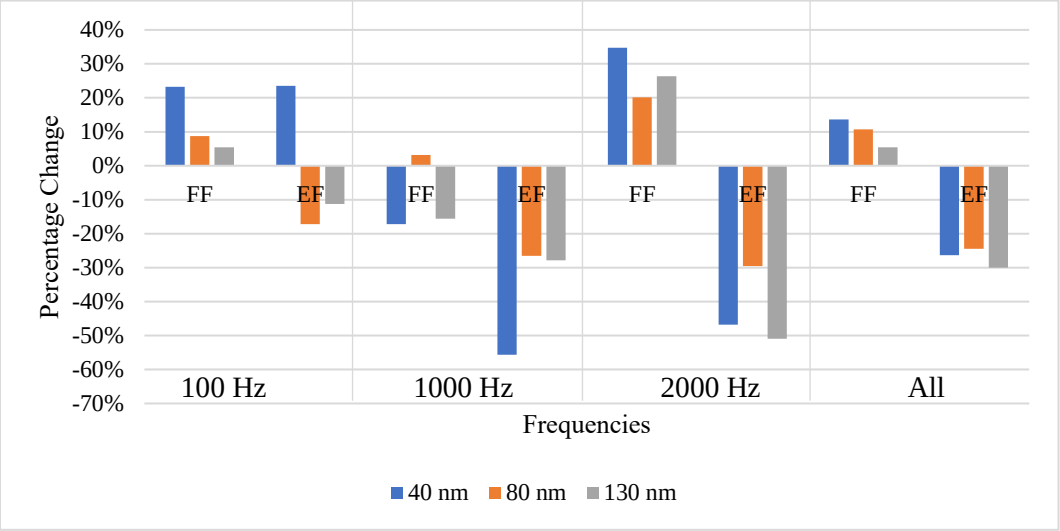

Figure 6.55 Bar chart of the impact of frequency on surface roughness

6.4 Discussion and Analysis

In this section the results of the nine vibration assisted nanomachining tests will be discussed and compared to the benchmark test (i.e., test no. 0). The parameters used for comparisons are:

- Groove depth and pile up height: In which the increase and decrease of both is discussed in addition to how consistent each was by comparing the start and end of each groove
- Roughness: Straightforward comparison between the start and end of each groove
- Chip formation: Since no chips were formed in any of the EF grooves, chips formed in FF grooves will be discussed. Continuous serrated chips, continuous smooth chips, and discontinuous chips were observed to varying degrees
- DAQ data: A-B and LFM signals acquired during each test is benchmarked against test no.0 to observe any significant change in voltage trends and any increases or decreases and how they relate to cross sectional profiles of the grooves

6.4.1 Groove depth and pile up height

The following was observed regarding the groove depths and pile up heights:

1. Changes in the profile of the groove between the two tests were mainly insignificant, except for the depth of the start of the Face Forward groove. However, test no.1 was more consistent in both parameters in all investigated parts of the grooves.
2. For the face forward groove, test no.2 achieved the worst, increasing the pile-up height by 25% with an insignificant increase in depth. As for the edge forward, the depth was shallower and the pile-up higher. However, consistency improved in test no.2 for both grooves and both groove depth and pile-up height. Consistency was good for the depth of the FF groove, the average for the pile-up height of the FF groove and the depth of the EF groove, but significant worsening for the pile-up height.
3. Test no.03 had contrasting results when comparing FF and EF grooves. Wherein the FF groove depth increased 23% without a significant change in the pile-up height and the opposite occurred in the EF groove where the depth didn't change meanwhile the pile-up increased by more than 23%. With a similar trend, consistency pile-up height had good consistency for FF and which cannot be said for the EF groove. Groove depth consistency was average for both grooves.
4. A 32% deeper groove and a 15% higher pile-up can be seen in this test when compared to the benchmark one regarding the FF groove. Similar pile up is seen for the EF groove with a slight decrease in depth. Consistency was bad for the depth of both grooves, the worse consistency value for the pile-up height of the FF in contrast to the good consistency in the EF counterpart.
5. A significant increase in average depth of the FF groove is noticed in this groove, reaching almost 50% with a less significant increase of near 15% in the pile-up height is seen. As for the EF groove, although the groove is 11% shallower a considerable 25% decrease in pile-up height had resulted. However, the pile-up in the EF groove was the least consistent with its values increasing significantly towards the end, however the groove depth was more consistent. As for the FF groove, the consistency of the depth was average and good for the pile-up.

6. A 43% deeper groove accompanied by a 13% increase in pile-up height is seen in the FF groove. Meanwhile, unfavourable 25% increase in the pile-up height is seen with only 13% deeper groove in the FF counterpart. This test however produced the best groove depth consistency for in each groove producing almost similar depths at the start and end of the two grooves. As for the pile-up heights it had an average result for the FF groove and slightly better outcome for the EF one.
7. Similar to the previous two tests, a 33% increase in the depth and 12% increase in the pile-ups for the FF was found. As for the EF, both the depth and pile-up heights are ever so slightly reduced. Average FF depth and EF pile-up height consistencies were recorded, whereas the FF pile-up and EF depths were good.
8. Major increase in depth is noticed depth of the groove and the pile-up height for the FF groove. Whereas no change in the depth for EF and a small increase in the pile-up height is seen. Excellent consistency figures are recorded for the FF groove and good ones for the EF counterpart.
9. The highest FF groove depth average increase was recorded in this test being around 70% deeper while the pile-up height increasing by just above 30%. The deepest EF groove at 35% increase was also recorded in test no.9 with a pile-up increase at 37%. Best overall consistency was also recorded in this test wit close to perfect results for the groove depth of both grooves and the pile-up height of the EF groove. Nonetheless, the consistency for the pile-up height of the FF groove was still better than average.

6.4.2 Roughness

Meanwhile, the following was observed regarding the surface roughness of the grooves:

1. Test no.1 produces significantly worse roughness at the beginning of both grooves. At the same time, the differences towards the ends of each groove are insignificantly different from test no.0.
2. This test is one of two only to improve roughness in all cases, albeit slightly at the start of the face forward groove. A 32% improvement, however, can be seen at the

end of this groove. As for the edge forward, improvement exceeding 50% across the groove is noticed.

3. Roughness almost doubled for the start of the FF groove, which is the worst across all tests. Meanwhile, more than 75% improvement was noticed at the beginning of groove EF. The end of both grooves produced a noticeable improvement in roughness.
4. This test provided the least predictable outcomes as it produced significantly worse roughness at the FF's and EF grooves' start and end. In contrast, it produced significant improvement for the end of the FF and the start of the EF grooves.
5. Roughness parameters for the FF groove have practically the same values as test no.0. Regarding the EF, a gradually increasing average of over 25% is seen.
6. A large increase is noticed at the start of the FF groove that changes into an improvement towards the end. Meanwhile, the EF groove has improved roughness across the groove.
7. A significant roughness increase is noted at the beginning, contrasted by an improvement towards the end. Meanwhile, an improvement nearing 50% is observed across the EF groove.
8. The best roughness results for the start of the FF groove are recorded, and this test, in addition to test no.2 is the only one to record roughness improvements across the entirety of both grooves.
9. A large increase in roughness at the start of the FF, then improvement towards the end, consistent with 2 kHz tests. Also consistent with the 2 kHz test is the improvement of roughness across the EF groove, especially at the start.

6.4.3 Chip Formation

As for chip formation, the following was found:

1. For the FF groove, test no.1 produced more chips than test no.0 which is to be expected as the groove depth of the latter was much shallower. However, when comparing the two chips, the one in test no.0 was smoother and less serrated. As for the EF groove, none of the 10 tests conducted had chips formed.

2. A continuous serrated chip is formed for the first two thirds of the FF groove, followed by discontinuous chips sticking to the side of the groove. No chip formed in the EF groove.
3. A long chip can be observed at the beginning of the EF groove, however this is most likely to be the chip formed during the cutting of the FF groove and detached as the probe moved towards the EF groove. Chip morphology is similar to test no.2 with an initial long continuous and serrated chip then followed by discontinuous chips stuck to the side of the groove. No chips in the EF groove.
4. Similar to test no.1, two continuous chips were produced for the FF groove without any noticeable discontinuations. No chips in the EF groove were observed.
5. The improvement in the pile up heights noticed for the FF groove can be attributed to the creation of two continuous chips with the larger one appearing less serrated when compared to the previous tests.
6. Although a long continuous chip is not to be seen in the SEM images, most likely one was created regardless but was stuck to the tip and was relocated. However, a small highly serrated one is seen towards the end of the FF groove. Pile ups on the sides are big and are close to discontinuous chips in size.
7. In this test three continuous chips are noticed with a small region of small, discontinued chips piling up on one side right after the first continuous chip.
8. Two continuous chips are formed a one that is less serrated than previous tests are seen, a relatively small one at the end and between the two a small section with small discontinuous chips sticking to the side of the end of the groove is seen here as well.
9. The long continuous chip cannot be seen in the SEM images and suspicion that it was relocated is very plausible. However, no small discontinuous chips are observed within the last third of the FF groove. The chip at the end of the groove is serrated.

6.4.4 DAQ Output

As for DAQ signal output, the following was observed:

1. An increase proportional to the increase in the groove size is noticed in both the AB and LFM signals at the FF groove, especially at the first two-thirds. As for the EF signal, an almost identical signal is observed.
2. Similar to the previous test, a proportional increase is observed in the first two-thirds of the A-B signal as well as the LFM at the FF groove with a slight decrease at the last third (FF2). As for the A-B signal, a gradual although small decrease is noticeable with the end showing lower values than test no.0. Reversely, a small gradual increase in the LFM is noticed. In practice, this means that the normal exerted force decreased while the torsional counterpart increased. This explains the shallower, yet wider groove produced when compared to test no.0.
3. The A-B signal increases significantly compared to all other previous tests then reduces to values below test no.0 towards the end of the FF groove, same applies to the LFM signal. As for the EF groove, lower A-B signal is seen all across the tests, meanwhile close values are seen for the LFM signal on average.
4. For the A-B, again a signal proportional to the size of the groove is observed in the FF groove. Meanwhile similar signal for the EF groove is observed, however, given that the test no.0's groove is both deeper and has lower pile-up, test no.4 hence gives less favourable outcome in that regard. As for the LFM signal, proportionality persists where a larger LFM signal is noticed at the start of the FF groove resulting in a wider groove.
5. The proportionality trend proceeds in the FF groove in both A-B and LFM signals. However, gradual improvement in both signals in the EF groove is observed. Wherein the at the start test no.5 produces more normal and torsional force than test no.0 then gradually performs better where it clearer towards the end of the test.
6. Significant increase in the A-B data is seen across both grooves, however still proportional to the size of the grooves. As for the LFM groove width proportionality still applies for the FF groove and a slight improvement towards the end of the EF groove.

7. The A-B data still follows the proportionality of the size of the grooves. A sizable increase in the LFM EF groove's signal whereas the FF's is similar to the equivalent test with the same frequency but lower amplitude.
8. Proportionality continues here however the signal is more condensed here meaning the probe deflects up and down at higher rates than previous tests for the FF's A-B data, the LFM data follows suit with more condensed signal and size proportional. As for the EF's A-B, this test is the first and only test where a significant decrease in the A-B data is seen meaning that less for is exerted to produce the groove, the LFM data is slightly bigger at the beginning and becomes the same towards the end.
9. Significant increase in the signal for the FF groove for both A-B and LFM. As for the EF groove, and when compared to previous tests, although an increase in the signal is seen, it is not proportional to the increase in size of the grooves, indicating that less normal force and torsion were exerted to produce the groove in proportion to test no.0.

6.5 Trends obtained from comparing VANM tests to the conventional one

In this section, various trends observed when the nine VANM were benchmarked against test no.0.

6.5.1 Groove depth, pile-ups, and consistency

For the EF grooves, increasing the frequency results in deeper grooves, as seen in Figure 5.56.

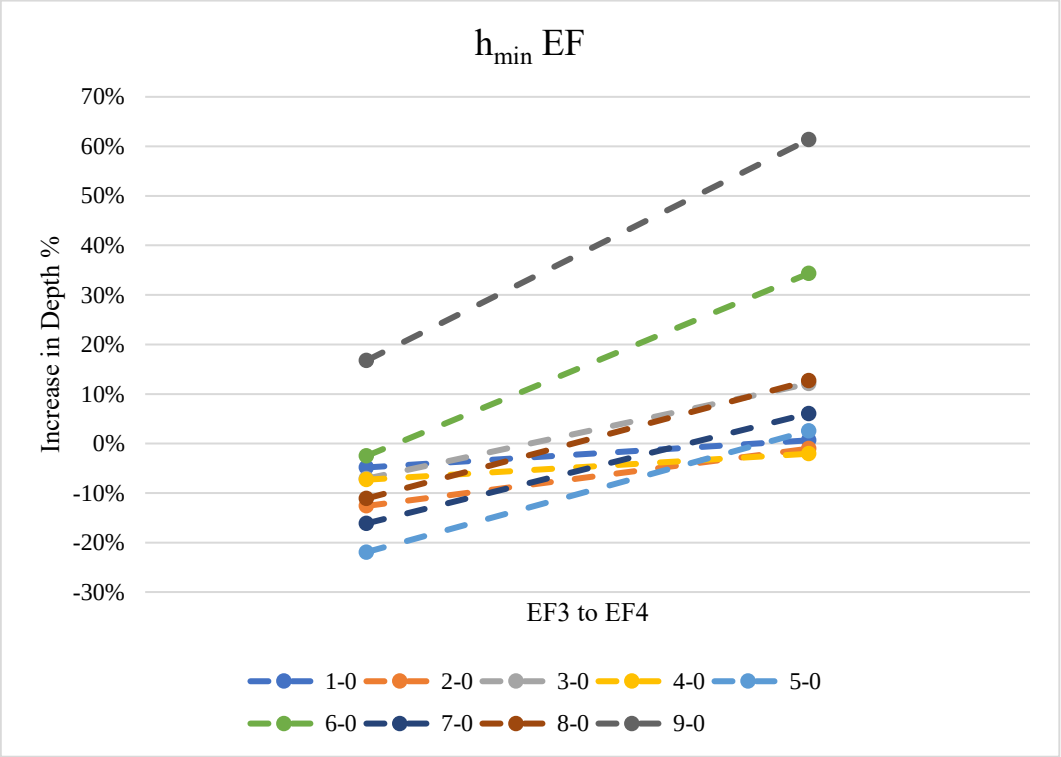

Figure 6.56 Percentage change in groove depth from start to end of EF groove

Change in pile up height from start to end of EF grooves did not follow any clear trend. As Figure 6.57 shows.

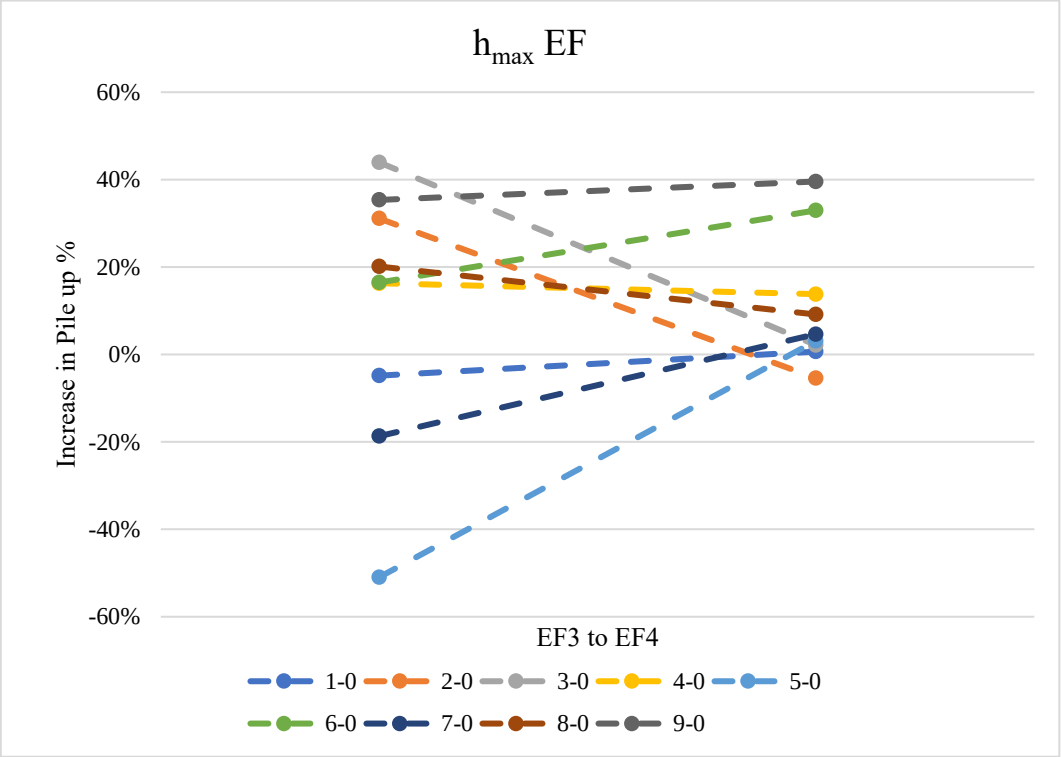

Figure 6.57 Percentage change in pile up height from start to end of EF groove

For the FF cases, grooves increase in depth more than they do in pile up heights are seen for all tests except test no.2, in which a slight increase in depth is overshadowed by a sizeable increase in pile up height. As Figure 6.58 and Figure 6.59 show.

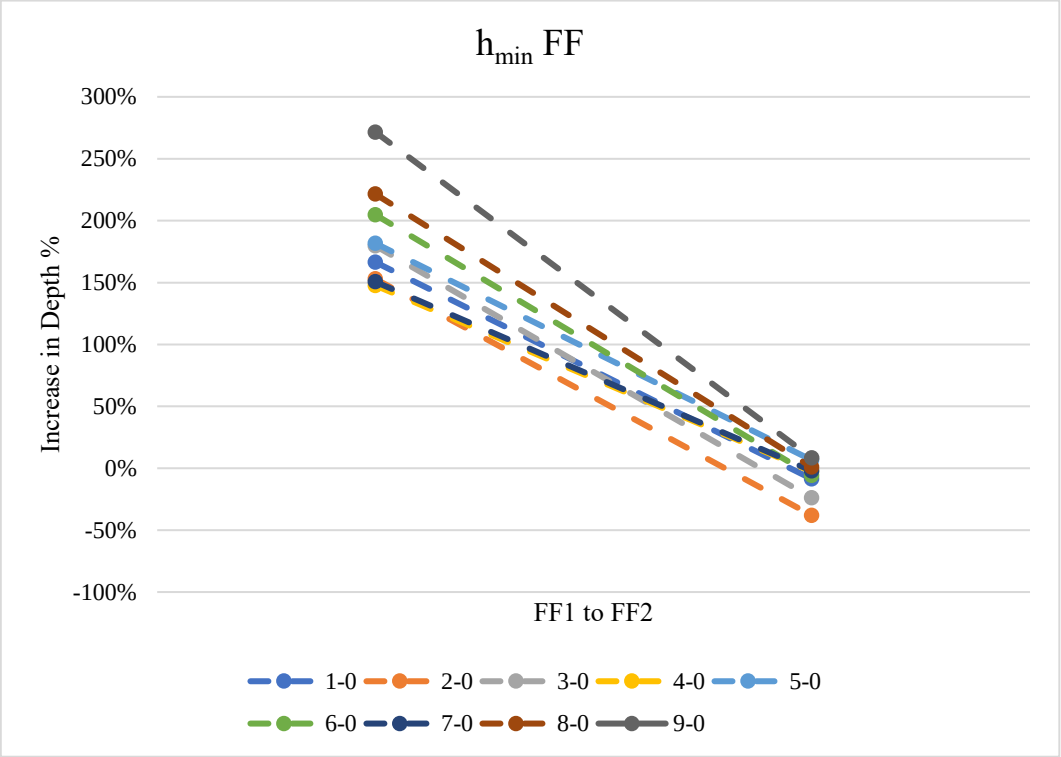

Figure 6.58 Percentage change in groove depth from start to end of FF groove

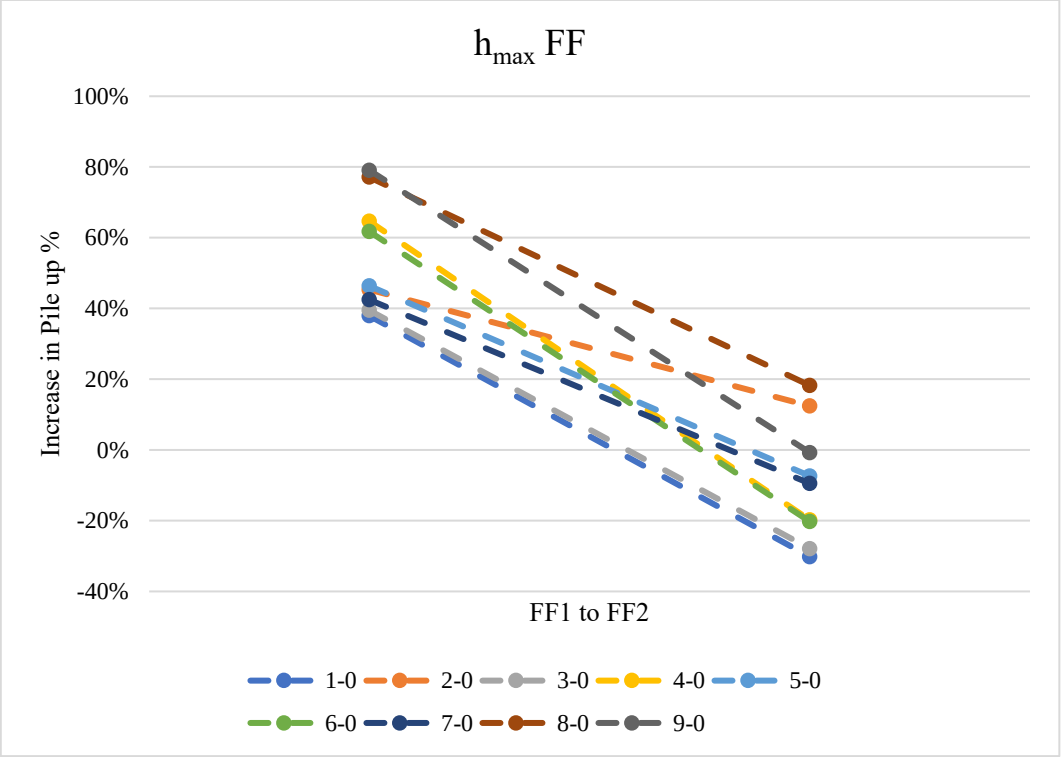

Figure 6.59 Percentage change in pile up height from start to end of FF groove

No EF groove provided a deeper groove with less pile-up height when compared to test no.0. Hence, conventional nanomachining provides the best groove depth to pile up height when the direction of machining is edge forward.

EF grooves with 100 and 1000 Hz frequencies tend to be shallower, with the only increase in depth occurring at the 2000 Hz.

For FF grooves, 1000 Hz tends to create the highest pile-ups. Amplitude of 40 nm tends to provide the best depth/pile-up performance in the cases of 100 Hz and 2000 Hz.

Grooves with 2000 Hz frequencies produced the most consistent groove depths between the two tests and for both directions.

However, the 1000 Hz tests produced the most consistent pile-up heights for the FF grooves. The last test (2000 Hz and 130 nm) gave an almost perfect consistency score, but no specific frequency or amplitude gave a clear advantage.

The least consistency by a significant margin was test no.0, in both the depth of FF and EF grooves. It was also inconsistent in the pile-up height of the FF groove; the opposite can be said to its EF counterpart.

6.5.2 Roughness

With the exception of test no.5, in which roughness did not change, all other tests go through significant improvement in roughness progressing from the start towards the end of the face forward groove, when compared to test no.0.

On average, across the whole of FF grooves, vibration-assisted nanomachining tends to produce more rough surfaces than the conventional counterpart. Meanwhile, the opposite applies to the EF grooves where VANM provides significant improvements in roughness. FF grooves' roughness worsens by 10%, while the EF grooves improve by 27%. Hence, considering both directions, VANM improves surface roughness by 17% overall.

For the start of the FF groove (FF1), tests with 2 kHz frequencies tend to produce the worst roughness values. As for 100 Hz tests, they also tend to worsen the roughness for the same position but not as bad as 2 kHz. Finally, 1 kHz tend to provide improvement in roughness at the same case (two test provide clear improvement and one with no significant change).

Increasing the frequency in both groove directions tends to improve the surface roughness, where the impact is clearer in the FF than in the EF.

Increasing the amplitude in the EF direction tends to improve roughness, such a trend is not observed in the FF direction, where the 80 nm does provide improvement, but the other two do not.

6.5.3 DAQ signal

Revising the positional signal provided by X DET1 and Y DET1, it is clear that all tests behaved as expected and followed through the path set out by the AFM software without any noticed deviations.

There is a clear proportionality between the depth of each groove and the strength of the A-B signal.

The A-B signal of the FF groove shows that with the pre-set applied 30 µm force, the tip struggles to penetrate the material creating a small groove via ploughing and then suddenly switching to cutting where a chip is formed at the end. On the contrary, VANM tests tend to start the cutting process straight away. However, the sudden increase in groove depth still persists but is less impactful as both frequency and amplitude increase.

At practically the same depth, test no.8 is the only test that needed less normal force to create the same groove, which also has a smoother surface, however, at the expense of higher pile-ups.

6.6 Cutting direction impact on ploughing and chip formation

As seen in the SEM images of the various tests, grooves in the face forward (FF) direction observe the creation of chips, in contrast to the edge forward (EF) in which the cutting regime is confined to ploughing without any chips present.

To explain these phenomena, it is necessary to keep in mind the geometry of the DNISP tip and how its apex spherical with 40 nm radius but above this a three sided pyramid is present.

Figure 6.60 below represents the tip with its spherical apex, including both top and side views. Taking test no.0 as an example and observing the AFM scan of test no.0 (Figures 6.5 and 6.6), the depth of the face forward groove increased almost four-fold from start to end while the same depth was maintained for the edge forward groove. A similar tendency has also been observed in the change of the groove widths. The width has almost doubled for the face forward groove, while the width for the edge forward groove was practically the same. Hence, it can be reported that based on this data alone, using the edge forward direction provided a more consistent groove throughout.

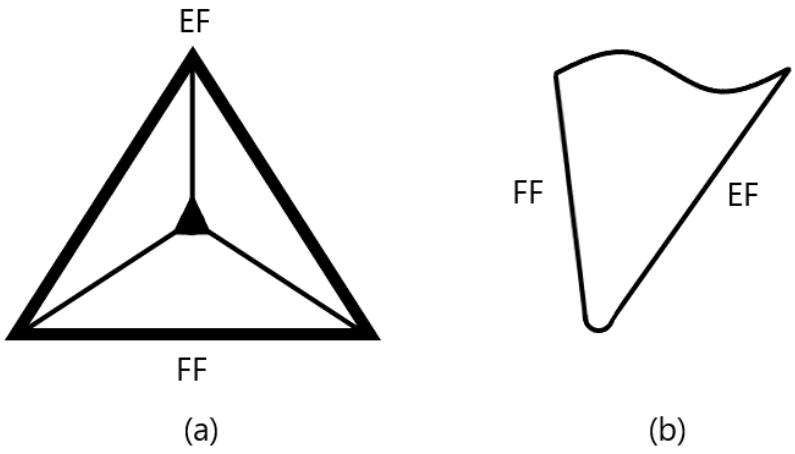

Figure 6.60 DNISP tip with spherical apex (not to scale) with (a) as top view (b) as side view

In addition, an improvement was observed with respect to the surface roughness for the start of the EF groove compared to FF counterpart, and no significant change

when considering the start of the respective grooves. One major difference between the two directions of cutting is regarding chip formation. In the face forward direction, continuous chips could be observed, albeit starting from the last quarter of the groove. Indeed, the initial part of the cut took place via ploughing as was also observed throughout the entirety of the edge forward groove, without any traces of chips formed. This contrast between the two directions is attributed to the non-axisymmetric nature of the AFM probe.

Here, the case where no vibrations are induced during the nanomachining process was discussed. However, differences caused by a change in direction when a three-sided pyramidal tip is used can be observed even when induced vibrations are utilised, albeit at varying degrees, as section 6.5 discussed. Nevertheless, the point being is that researchers and practitioners need to keep in mind that when the face forward or edge forward directions are implemented during AFM tip-based nanomachining of metals such as copper while using a three-sided pyramidal probe tip, the aforementioned differences need to be kept in mind.

6.6.1 Smoother surfaces indicate higher dislocation density

As explained in the literature review in which Ye et al. (2003) investigated the impact of cutting velocity on the surface roughness and dislocation density. Where, increased velocities resulted in smoother surfaces and higher dislocation densities.

Referring to section 2.5.1, where Zhu et al. (2016) conducted a molecular dynamics study on the effect of introducing vibrations to the nanomachining of single crystal copper. Where the study concluded that vibrations with higher frequencies produce smoother surfaces, this was explained by the increased number of times the tip presses the machined material. The higher frequency, in turn, contributed to the dislocation growth, making tip penetration into the material in each cycle easier. These observations were confirmed in the tests conducted in this thesis, with higher

frequencies improving the surface roughness. However, as results show, the improvements mainly occurred when the EF direction was used.

Meanwhile, although the FF grooves provided better results in two tests, in most cases, roughness values were worse off when compared to conventional nanomachining. Hence, the cutting direction must be considered when non-axisymmetric tips are used. Regarding the impact of increasing the amplitude, the test results showed no direct correlation between the surface roughness and the gradual change of amplitude.

This all, in turn, is consistent with the argument that dislocation nucleation is the main cause for deformation at such a scale as vibrations are an additional dislocation source due to kinetic energy provided to adjacent atoms in each cycle, increasing the probability of dislocation nucleation, as explained in chapter 3.

6.6.2 An explanation to the hourglass shape of the face forward grooves

Following the progression of the FF grooves, it can be noticed that the groove has a wide profile with chip formation until a certain point where the chip formation stops, and the grooves become visibly narrower. After that, the grooves widen again with another continuous chip is formed at the end. One explanation is the inverse relationship between the dead zone size and the amount of chip formation discussed in chapter 2 (Hosseini and Vahdati 2012). This occurrence could be attributed to the fact that a part of the dead zone leaves the material as chips separate from the workpiece wherein a critical size is reached in which the dead zone is so small it cannot act as an additional cutting edge causing the narrowing. Following that, a new dead zone is created, acting as a new additional cutting edge. However, more work would be needed to confirm this hypothesis.

Also, the LFM signal (see, for example, Figure 6.15) of the vibration-assisted FF groove indicates that pronounced torsion fluctuation took place at the beginning of the groove. This is in line with the increased width observed at the beginning of the FF groove. A possible explanation for this phenomenon which can be attributed to the creation of a dead zone, is the increased hardness in this region which was discussed

in Kümmel et al. (2014). Here, the hypothesis is that at every cycle of vibration, the rake face is hitting part of the dead zone and part of the surrounding copper material, which have varying hardness values. This difference in hardness makes the tip (and thus the cantilever twist) until the dead zone is large enough later on along the groove for this phenomenon to stop. If this is the case, this would suggest that the dead zone remains in front of the tip, although a chip formation is seen halfway along the groove.

Meanwhile, analysing the step-like (stacking) pattern observed in the FF grooves, low-cycle fatigue cannot be used as an explanation due to each step being smaller or shorter than the length of stroke (i.e., amplitude) for each vibration.

6.7 Conclusion and Summary

Modes of operation, how the data extracted was interpreted in addition to in depth comparison and trends were presented throughout this chapter. And as was seen throughout, introducing vibrations to the AFM tip-based nanomachining of single crystal copper does -depending on the frequency and amplitude chosen- provide certain improvements over conventional nanoscratching. The impact of choosing a certain frequency and amplitude affects groove depths, pile-up heights, surface roughness and chip formation.

For example, the change in the depths and heights between the start and end of each groove (referred to as consistency) was affected by the induced vibrations. Wherein, groove depth consistency was significantly worse in the conventional nanoscratching when compared to any vibration-assisted one. On the other hand, considerable improvements were seen when higher vibrational frequencies were utilised.

In addition, surface roughness of the grooves improved significantly with induced vibrations in the EF grooves, but the opposite occurred in the FF ones. Exceptions can be seen in the first test where it did worse in both directions, and improvements in both directions in the 2^{nd} and 8^{th} (both with 1000 Hz) were present. So, when surface

roughness is considered, and regardless of direction and amplitude, utilising 1000 Hz vibrations tend to provide enhanced results over conventional nanomachining.

SEM images on the other hand were utilised to study chip formation as well as the shape of the grooves produced. The effect of the uncut chip thickness on the grooves was significant due to its variation between FF and EF grooves. Hypotheses based on research reviewed in chapters 2 and 3 were introduced including comparisons with previous research.

Chapter 7

Contributions, Conclusions and Future Work

This thesis's main aim was to gain further understanding of the AFM tip-based vibration-assisted nanomachining process.

While chapter 2 states the theoretical framework under which the deformation mechanism governs nanoindentation and nanomachining, chapter 3 explains it theoretically. Chapters 4, 5 and 6, on the other hand, provided the experimental investigations. This chapter summarises the main contributions, conclusions, and suggestions for future work that builds upon the results obtained in this thesis.

7.1 Contributions

The following novel contributions were made in the field of AFM tip-based vibration-assisted nanomachining:

- Linear force-displacement curves due to stagnation zones. It was found that AFM machining of some polymer materials may cause large stagnation zones that may remove any influence of the AFM tip shape on nanomachining processes. Hence, regardless of how sharp the tip is, it acts as a blunt tool. In particular, it was experimentally discovered that AFM depth-sensing nanoindentation of such polymers might lead to an almost linear force-displacement curve. This linear relation was theoretically explained as a curved AFM probe creating a large stagnation zone in front of its tip and, hence, the adequate theoretical model is not the Hertz-type contact having an increasing contact region but rather the Boussinesq problem for effective flat-ended cylindrical punch having a constant contact zone.
- Tip bluntness impact on the pull-off force and the effective rake angle. In addition to providing a detailed and straightforward methodology for extracting AFM tip bluntness from SEM images, supported by bluntness values extracted via AFM depth-sensing nanoindentation, such bluntness values were used to investigate their impact on the work of adhesion. Wherein it was found that using integer values leads to significant error in

pull-off force estimations, especially when sharper tips are considered. Also, factors such as the tilt angle and depth were found to impact the effective rake angle in addition to the tip's bluntness.

- Novel experimental approaches and detailed analysis of AFM tip-based vibration-assisted nanomachining of single crystal copper. Recent experimental studies dedicated to the application of the vibration-assisted nanomachining to single crystal silicon (Wang et al. 2021), the silicon-based organic polymer Polydimethylsiloxane (Deng et al. 2021), and silicon nitride ceramics (Qiao et al. 2021)., show that this nanomachining technique is very timely and intensively developed research field. However, to the best of the author's knowledge, there are no publications related to applying this technique to metals. Hence, there were obtained novel results and developed novel experimental approaches for a detailed analysis of vibration-assisted nanomachining of metals, especially single copper crystals.

7.2 Conclusions

The main goal of this thesis is to optimise and better understand the AFM tip-based nanomachining process of copper. Vibration-assisted nanomachining is proven to provide improvements over the conventional counterpart. However, research on metals in this area is limited hence the utilisation of a single crystal copper workpiece in this thesis.

However, before that, the tip condition had a significant impact on nanomachining processes; hence characterisation of AFM tips' bluntness was done. Hence, based on this, the following conclusions can be drawn:

- An AFM tip shape characterisation method that represented the tip's bluntness using real numbers rather than integers was utilised. The analysis included the tip's bluntness in the vertical position as well as its 12° clockwise working orientation.

- Three-dimensional data of the tip bluntness were extracted using force-displacement graphs, which were used to verify the data from the 2D SEM images. Good agreement between the two approaches was found.
- Some of the force-displacement graphs had an almost linear-like behaviour. This, in turn, was explained by the existence of a stagnation zone just beneath the indenter, which moves into the material during indentation hence acting as a flat-ended cylindrical indenter in the Boussinesq case. Indentation of a copper sample was done; however, the hardness of copper yielded unusable results.
- Using integers rather than real numbers to characterise AFM tip bluntness was found to be significant errors in the estimation of the pull-off force. Specifically, errors were more pronounces when tips were sharper.
- The impact of the tip bluntness, depth of penetration and orientation of AFM probes on the effective rake angle during AFM-based nanomachining was analysed. It was found that all had varying degrees of impact however the consideration of the tilt angle was the most significant.
- Nine vibration-assisted nanomachining tests were conducted. These tests were benchmarked against one with no induced vibrations. Comparisons were made using grooves' depths, pile-up heights, surface roughness, and chips formed.
- Significant changes in all above-mentioned parameters were observed depending on which frequency-amplitude combination was used. For example, consistency of both groove depths and pile-up heights on average improved as frequency increased.
- The direction of the groove cutting had the most pronounced effect. For example, chip formation was observed in all FF grooves and non in the EF ones. This was attributed to the minimum uncut chip thickness effect.
- It was also concluded that induced vibrations provided an average of 27% improvement across all combinations in the EF direction. Meanwhile, a 10% worsening was seen on average when FF grooves were considered. The only exception was when 1000 Hz vibrations were used as they provided improvements regardless of cutting direction.

- Several observations were discussed, such as explanations provided in previous works, such as smoother surfaces indicating higher dislocation density. It was also concluded that some materials which are macroscopically brittle materials behave similarly to the ductile copper tested in this thesis brittle-to-ductile transition occurring at the nanoscale. Hypotheses that try to explain the hourglass shape of the face forward grooves were also put forward, with the dead zone being a probable important factor.

7.3 Future work

In this thesis, multiple novel contributions were introduced in the characterisation of AFM tip bluntness as well as in the vibration-assisted nanomachining of metals. However, some further investigations are worth considering, including:

- Experimentally verifying the pull-off force values. This could be done if a soft probe is used. This probe is scratched under controlled conditions to gradually increase its bluntness while ensuring that such a soft probe's cantilever does not break under the applied load or its tip. And at certain intervals, the pull-off force is calculated with data obtained from force-displacement tests.
- Utilising gradually increasing applied forces for select frequency-amplitude. This addition would provide more information regarding elastic, ploughing, and chip forming cutting regimes during nanomachining.
- Using an axisymmetric probe for vibration-assisted nanomachining experiment. Then redo grooves in directions as done in this thesis, then investigate differences in outcome. This would highlight other factors than the minimum uncut chip thickness such as probe cantilever flexure and the impact of the probe's inclination. More investigation into the hourglass shape occurring during cutting of the FF grooves in case similar occurrences are observed.

- Utilising additional workpieces. This would include another crystalline copper workpiece with a different crystallographic orientation to understand its effect. Or other metals such as aluminium. Or even other completely different materials such as soft polycarbonate.

References

Agarwal, G., Naik, R.R. and Stone, M.O., 2003. Immobilization of histidine-tagged proteins on nickel by electrochemical dip pen nanolithography. *Journal of the American Chemical Society*, *125*(24), pp.7408-7412.

Al-Musawi, R. S. J., Brousseau, E. B., Geng, Y.,Borodich, F. M. (2016). Insight into mechanics of AFM tip-based nanomachining: Bending of cantilevers and machined grooves, *Nanotechnology*, **27**.

Al-Musawi, R. S. J.,Brousseau, E. (2016). Assessing the applied normal load during contact mode AFM: an issue with the conventional approach.

Alraziqi, Z. N. R., Brousseau, E.,Borodich, F. M. (2017). A new metric to assess the tip condition of AFM probes based on three-dimensional data. In 2016 International Conference for Students on Applied Engineering, ICSAE 2016, 24-29. Place (Published).

Amarouchene, Y., Boudet, J.,Kellay, H. (2001). Dynamic sand dunes, *Physical Review Letters*, **86**, 4286.

Arrazola, P., Özel, T., Umbrello, D., Davies, M.,Jawahir, I. (2013). Recent advances in modelling of metal machining processes, *CIRP annals*, **62**, 695-718.

Atamny, F.,Baiker, A. (1995). Direct imaging of the tip shape by AFM, *Surface science*, **323**, L314-L318.

Basquin, O. (1910). The exponential law of endurance tests. In Proc Am Soc Test Mater, 625-630. Place (Published).

Bei, H., Gao, Y., Shim, S., George, E. P.,Pharr, G. M. (2008a). Strength differences arising from homogeneous versus heterogeneous dislocation nucleation, *Physical Review B*, **77**, 060103.

Bei, H., Shim, S., Pharr, G. M.,George, E. P. (2008b). Effects of pre-strain on the compressive stress–strain response of Mo-alloy single-crystal micropillars, *Acta Materialia*, **56**, 4762-4770.

Berghezan, A.,Fourdeux, A. (1959). Transmission electron microscopy studies of the mechanism of plastic deformation, *Journal of Applied Physics*, **30**, 1913-1922.

Bhaskaran, H., Gotsmann, B., Sebastian, A., Drechsler, U., Lantz, M. A., Despont, M., Jaroenapibal, P., Carpick, R. W., Chen, Y.,Sridharan, K. (2010). Ultralow nanoscale wear through atom-by-atom attrition in silicon-containing diamond-like carbon, *Nature nanotechnology*, **5**, 181.

Bhushan, B., 2011. *Hand book of Nano-technology* 3rd editio., Springer-Verlag Berlin Heideiberg 2010.

Bhushan, B.,Nosonovsky, M. (2003). Scale effects in friction using strain gradient plasticity and dislocation-assisted sliding (microslip), *Acta Materialia*, **51**, 4331-4345.

Binnig, G., Quate, C. F.,Gerber, C. (1986). Atomic force microscope, *Physical Review Letters*, **56**, 930.

Blake, P. N.,Scattergood, R. O. (1990). Ductile-regime machining of germanium and silicon, *Journal of the American ceramic society*, **73**, 949-957.

Borodich, F. M. (1983). Similarity in the problem of contact between elastic bodies, *Journal of Applied Mathematics and Mechanics*, **47**, 440-442.

Borodich, F. M. (1989). Hertz contact problems for an anisotropic physically nonlinear elastic medium, *Strength of Materials*, **21**, 1668-1676.

Borodich, F. M. (1990). Hertz contact problems for elastic anisotropic halfspace with initial stress, *Soviet Applied Mechanics*, **26**, 126-133.

Borodich, F. M. (1993). The hertz frictional contact between nonlinear elastic anisotropic bodies (the similarity approach), *International Journal of Solids and Structures*, **30**, 1513-1526.

Borodich, F. M. (2011). Contact problems at nano/microscale and depth sensing indentation techniques. In Materials Science Forum, 53-76. Place (Published).

Borodich, F. M. (2014). The Hertz-Type and Adhesive Contact Problems for Depth-Sensing Indentation. In Advances in Applied Mechanics, 225-366. Place (Published).

Borodich, F. M., Galanov, B. A., Keer, L. M.,Suarez-Alvarez, M. M. (2014a). The JKR-type adhesive contact problems for transversely isotropic elastic solids, *Mechanics of Materials*, **75**, 34-44.

Borodich, F. M., Galanov, B. A.,Suarez-Alvarez, M. M. (2014b). The JKR-type adhesive contact problems for power-law shaped axisymmetric punches, *Journal of the Mechanics and Physics of Solids*, **68**, 14-32.

Borodich, F. M., Keer, L. M.,Korach, C. S. (2003). Analytical study of fundamental nanoindentation test relations for indenters for non-ideal shapes, *Nanotechnology*, **14**, 803-808.

Borodich, F. M.,Galanov, B. A. (2004). Molecular adhesive contact for indenters of non-ideal shapes.

Borodich, F. M.,Savencu, O. (2017). 'Hierarchical models of engineering rough surfaces and bio-inspired adhesives.' in, Bio-inspired Structured Adhesives (Springer).

Bouchonville, N.,Nicolas, A. (2019). 'Quantification of the Elastic Properties of Soft and Sticky Materials Using AFM.' in, Atomic Force Microscopy (Springer).

Brehl, D.,Dow, T. (2008). Review of vibration-assisted machining, *Precision Engineering*, **32**, 153-172.

Brenner, S. (1958). Growth and Properties of" Whiskers", *Science*, **128**, 569-575.

Bridgman, P. W. (1952). Physics of high pressure.

Broek, D. (1982). Elementary engineering fracture mechanics (Springer Science & Business Media).

Cahn, J. W.,Nabarro, F. (2001). Thermal activation under shear, *Philosophical Magazine A*, **81**, 1409-1426.

Carlton, C.,Ferreira, P. J. (2007). What is behind the inverse Hall–Petch effect in nanocrystalline materials?, *Acta Materialia*, **55**, 3749-3756.

Carpick, R. W., Agrait, N., Ogletree, D.,Salmeron, M. (1996). Measurement of interfacial shear (friction) with an ultrahigh vacuum atomic force microscope,

Journal of Vacuum Science & Technology B: Microelectronics and Nanometer Structures Processing, Measurement, and Phenomena, **14**, 1289-1295.

Chen, L., El-Wardany, T., Nasr, M.,Elbestawi, M. (2006). Effects of edge preparation and feed when hard turning a hot work die steel with polycrystalline cubic boron nitride tools, *CIRP annals*, **55**, 89-92.

Cheng, T. J., Han, J. H., Ziwisky, M., Lee, C. H.,Bhave, S. A. (2011). 6.4 GHz acoustic sensor for in-situ monitoring of AFM tip wear. In 2011 IEEE 24th International Conference on Micro Electro Mechanical Systems, 521-524. Place (Published), IEEE.

Chung, K.-H., Lee, Y.-H.,Kim, D.-E. (2005). Characteristics of fracture during the approach process and wear mechanism of a silicon AFM tip, *Ultramicroscopy*, **102**, 161-171.

Chung, K.-H.,Kim, D.-E. (2003). Fundamental investigation of micro wear rate using an atomic force microscope, *Tribology Letters*, **15**, 135-144.

Coffin Jr, L. F. (1954). A study of the effects of cyclic thermal stresses on a ductile metal, *Transactions of the American Society of Mechanical Engineers, New York*, **76**, 931-950.

Cordeiro, G. M.,Lemonte, A. J. (2011). The β-Birnbaum–Saunders distribution: an improved distribution for fatigue life modeling, *Computational Statistics & Data Analysis*, **55**, 1445-1461.

Cottrell, A. H. (1953). Dislocations and plastic flow in crystals.

De Oliveira, F. B., Rodrigues, A. R., Coelho, R. T.,De Souza, A. F. (2015). Size effect and minimum chip thickness in micromilling, *International Journal of Machine Tools and Manufacture*, **89**, 39-54.

Delph, T., Zimmerman, J., Rickman, J.,Kunz, J. (2009). A local instability criterion for solid-state defects, *Journal of the Mechanics and Physics of Solids*, **57**, 67-75.

Deng, J., Jiang, L., Si, B., Zhou, H., Dong, J.,Cohen, P. (2021). AFM-Based nanofabrication and quality inspection of three-dimensional nanotemplates for soft lithography, *Journal of Manufacturing Processes*, **66**, 565-573.

Deng, J., Zhang, L., Dong, J. Y.,Cohen, P. H. (2016). AFM-based 3D nanofabrication using ultrasonic vibration assisted nanomachining, *Journal of Manufacturing Processes*, **24**, 195-202.

Denkena, B., Koehler, J.,Rehe, M. (2012). Influence of the honed cutting edge on tool wear and surface integrity in slot milling of 42CrMo4 steel, *Procedia CIRP*, **1**, 190-195.

Denkena, B., Reichstein, M., Brodehl, J.,de León García, L. (2005). Surface preparation, coating and wear performance of geometrically defined cutting edges. In Proceedings of the 5th international conference the coatings in manufacturing engineering, 5-7. Place (Published).

Denkena, B.,Biermann, D. (2014). Cutting edge geometries, *CIRP annals*, **63**, 631-653.

Dimov, S., Brousseau, E., Minev, R.,Bigot, S. (2012). Micro-and nano-manufacturing: Challenges and opportunities, *Proceedings of the Institution of Mechanical Engineers, Part C: Journal of Mechanical Engineering Science*, **226**, 3-15.

Dongmo, L., Villarrubia, J. S., Jones, S. N., Renegar, T. B., Postek, M. T.,Song, J.-F. (2000). Experimental test of blind tip reconstruction for scanning probe microscopy, *Ultramicroscopy*, **85**, 141-153.

Eckert, J., Holzer, J., Krill, C.,Johnson, W. (1992). Structural and thermodynamic properties of nanocrystalline fcc metals prepared by mechanical attrition, *Journal of Materials Research*, **7**, 1751-1761.

Elkaseer, A.,Brousseau, E. (2013). Modelling the surface generation process during AFM probe-based machining: simulation and experimental validation, *Surface Topography: Metrology and Properties*, **2**, 025001.

Elmustafa, A., Ananda, A.,Elmahboub, W. (2004). Dislocation mechanics simulations of the bilinear behavior in micro-and nanoindentation, *Journal of Materials Research*, **19**, 768-779.

Erhart, P.,Albe, K. (2005). Analytical potential for atomistic simulations of silicon, carbon, and silicon carbide, *Physical Review B*, **71**, 035211.

Ernst, H.,Merchant, M. E. (1941). Chip formation, friction and finish (Cincinnati milling machine Company Cincinnati).

Fang, F., Zhang, N., Guo, D., Ehmann, K., Cheung, B., Liu, K.,Yamamura, K. (2019). Towards atomic and close-to-atomic scale manufacturing, *International Journal of Extreme Manufacturing*, **1**, 012001.

Fang, F.,Venkatesh, V. (1998). Diamond cutting of silicon with nanometric finish, *CIRP annals*, **47**, 45-49.

Fang, F.,Zhang, G. (2003). An experimental study of edge radius effect on cutting single crystal silicon, *The International Journal of advanced manufacturing technology*, **22**, 703-707.

Fang, N., Pai, P. S.,Mosquea, S. (2010). The effect of built-up edge on the cutting vibrations in machining 2024-T351 aluminum alloy, *The International Journal of advanced manufacturing technology*, **49**, 63-71.

Fleck, N., Muller, G., Ashby, M.,Hutchinson, J. (1994). Strain gradient plasticity: theory and experiment, *Acta Metallurgica et materialia*, **42**, 475-487.

Flores-Johnson, E.,Li, Q. (2010). Indentation into polymeric foams, *International Journal of Solids and Structures*, **47**, 1987-1995.

Forman, R. G., Kearney, V.,Engle, R. (1967). Numerical analysis of crack propagation in cyclic-loaded structures.

Galanov, B. A. (1981a). The approximate solution of certain problems of the elastic contact of two bodies, *Akademiia Nauk SSSR, Izvestiia, Mekhanika Tverdogo Tela*, 61-67.

Galanov, B. A. (1981b). Approximate solution of some contact problems with unknown contact area under conditions of power-law hardening of the material, *Akademiia Nauk Ukrains' koi RSR, Dopovidi, Seriia A-Fiziko-Matematichni ta Tekhnichni Nauki*, 35-40.

Galanov, B. A. (1981b). Approximate solution of some contact problems with unknown contact area under conditions of power-law hardening of the material,

Akademiia Nauk Ukrains' koi RSR, Dopovidi, Seriia A-Fiziko-Matematichni ta Tekhnichni Nauki, 35-40.

Galanov, B. A. (1993). Development of analytical and numerical methods for study of models of materials. In. Place (Published), Institute for Problems in Materials Science.

Gao, S.,Huang, H. (2017). Recent advances in micro-and nano-machining technologies, *Frontiers of Mechanical Engineering*, **12**, 18-32.

Geng, Y., Brousseau, E. B., Zhao, X., Gensheimer, M.,Bowen, C. R. (2018). AFM tip-based nanomachining with increased cutting speed at the tool-workpiece interface, *Precision Engineering*, **51**, 536-544.

Goel, S., Luo, X., Agrawal, A.,Reuben, R. L. (2015). Diamond machining of silicon: a review of advances in molecular dynamics simulation, *International Journal of Machine Tools and Manufacture*, **88**, 131-164.

Gope, P. (1999). Determination of sample size for estimation of fatigue life by using Weibull or log-normal distribution, *International Journal of Fatigue*, **21**, 745-752.

Gotsmann, B.,Lantz, M. A. (2008). Atomistic wear in a single asperity sliding contact, *Physical Review Letters*, **101**, 125501.

Gouldstone, A., Chollacoop, N., Dao, M., Li, J., Minor, A. M.,Shen, Y.-L. (2007). Indentation across size scales and disciplines: Recent developments in experimentation and modeling, *Acta Materialia*, **55**, 4015-4039.

Gozen, B. A.,Ozdoganlar, O. B. (2010). A rotating-tip-based mechanical nano-manufacturing process: nanomilling, *Nanoscale Research Letters*, **5**, 1403-1407.

Greer, J. R., Oliver, W. C.,Nix, W. D. (2005). Size dependence of mechanical properties of gold at the micron scale in the absence of strain gradients, *Acta Materialia*, **53**, 1821-1830.

Greer, J. R.,De Hosson, J. T. M. (2011). Plasticity in small-sized metallic systems: Intrinsic versus extrinsic size effect, *Progress in Materials Science*, **56**, 654-724.

Greer, J. R.,Nix, W. D. (2005). Size dependence of mechanical properties of gold at the sub-micron scale, *Applied Physics A*, **80**, 1625-1629.

Greer, J. R.,Nix, W. D. (2006). Nanoscale gold pillars strengthened through dislocation starvation, *Physical Review B*, **73**, 245410.

Grierson, D. S., Liu, J., Carpick, R. W.,Turner, K. T. (2013). Adhesion of nanoscale asperities with power-law profiles, *Journal of the Mechanics and Physics of Solids*, **61**, 597-610.

Griffith, A. (1924). The theory of rupture. In First Int. Cong. Appl. Mech, 55-63. Place (Published).

Han, X. S. (2006). Investigation micro-mechanism of dry polishing using molecular dynamics simulation method. In 2006 1st IEEE International Conference on Nano/Micro Engineered and Molecular Systems, 936-941. Place (Published), IEEE.

Han, X. S. (2006). Investigation micro-mechanism of dry polishing using molecular dynamics simulation method. In 2006 1st IEEE International Conference on Nano/Micro Engineered and Molecular Systems, 936-941. Place (Published), IEEE.

Han, X. S., Lin, B., Yu, S.,Wang, S. (2002). Investigation of tool geometry in nanometric cutting by molecular dynamics simulation, *Journal of Materials Processing Technology*, **129**, 105-108.

Hansma, P., Elings, V., Marti, O.,Bracker, C. (1988). Scanning tunneling microscopy and atomic force microscopy: application to biology and technology, *Science*, **242**, 209-216.

Heim, L.-O., Kappl, M.,Butt, H.-J. (2004). Tilt of atomic force microscope cantilevers: effect on spring constant and adhesion measurements, *Langmuir*, **20**, 2760-2764.

Hertz, H. (1895). Stresses and deflections of cylindrical bodies, *Lepzig ed*.

Hill, R. (1950). The Mathematical Theory of Plasticity, Oxford University Press, Oxford, 1950.

Honeycutt, J. D.,Andersen, H. C. (1987). Molecular dynamics study of melting and freezing of small Lennard-Jones clusters, *Journal of Physical Chemistry*, **91**, 4950-4963.

Horstemeyer, M., Plimpton, S.,Baskes, M. (2001). Size scale and strain rate effects on yield and plasticity of metals, *Acta Mater*, **49**, 4363-4374.

Hosseini, S. V.,Vahdati, M. (2012). Modeling the effect of tool edge radius on contact zone in nanomachining, *Computational Materials Science*, **65**, 29-36.

Huang, Y., Zhang, F., Hwang, K., Nix, W., Pharr, G.,Feng, G. (2006). A model of size effects in nano-indentation, *Journal of the Mechanics and Physics of Solids*, **54**, 1668-1686.

Hutchinson, J. W. (2000). Plasticity at the micron scale, *International Journal of Solids and Structures*, **37**, 225-238.

Hutter, J. L. (2005). Comment on tilt of atomic force microscope cantilevers: effect on spring constant and adhesion measurements, *Langmuir*, **21**, 2630-2632.

Irwin, G. R. (1957). Analysis of stresses and strains near the end of a crack transversing a plate, *Trans. ASME, Ser. E, J. Appl. Mech.*, **24**, 361-364.

Isaev, A. (1961). Ultrasonic vibration of a metal cutting tool, *Vest Mashinos*, **41**.

Jacobs, T. D., Wabiszewski, G. E., Goodman, A. J.,Carpick, R. W. (2016). Characterizing nanoscale scanning probes using electron microscopy: A novel fixture and a practical guide, *Review of Scientific Instruments*, **87**, 013703.

Jennings, A. T., Burek, M. J.,Greer, J. R. (2010). Microstructure versus size: mechanical properties of electroplated single crystalline Cu nanopillars, *Physical Review Letters*, **104**, 135503.

Kalinin, S. V.,Bonnell, D. A. (2002). Imaging mechanism of piezoresponse force microscopy of ferroelectric surfaces, *Physical Review B*, **65**, 125408.

Khurshudov, A.,Kato, K. (1995). Wear of the atomic force microscope tip under light load, studied by atomic force microscopy, *Ultramicroscopy*, **60**, 11-16.

Khurshudov, A.,Kato, K. (1997). Wear mechanisms in reciprocal scratching of polycarbonate, studied by atomic force microscopy, *Wear*, **205**, 1-10.

Kiener, D., Grosinger, W., Dehm, G.,Pippan, R. (2008). A further step towards an understanding of size-dependent crystal plasticity: In situ tension experiments of miniaturized single-crystal copper samples, *Acta Materialia*, **56**, 580-592.

Kim, J.-Y., Lee, B.-W., Read, D. T.,Kwon, D. (2005). Influence of tip bluntness on the size-dependent nanoindentation hardness, *Scripta Materialia*, **52**, 353-358.

Kindrachuk, V. M., Galanov, B. A., Kartuzov, V. V.,Dub, S. N. (2006). On elastic nanoindentation of coated half-spaces by point indenters of non-ideal shapes, *Nanotechnology*, **17**, 1104.

Kindrachuk, V. M., Galanov, B. A., Kartuzov, V. V.,Dub, S. N. (2006). On elastic nanoindentation of coated half-spaces by point indenters of non-ideal shapes, *Nanotechnology*, **17**, 1104.

Koch, C. (1999). 'Bulk behavior of nanostructured materials.' in, Nanostructure Science and Technology (Springer).

Kocks, U. (1975). Termodynamics and Kinetics of Slip, *Prog. in Mater. Sci.*, **242**.

Komanduri, R., Chandrasekaran, N.,Raff, L. (1999). Some aspects of machining with negative-rake tools simulating grinding: a molecular dynamics simulation approach, *Philosophical Magazine B*, **79**, 955-968.

Komanduri, R., Varghese, S.,Chandrasekaran, N. (2010). On the mechanism of material removal at the nanoscale by cutting, *Wear*, **269**, 224-228.

Kong, X., Deng, J., Dong, J.,Cohen, P. H. (2020). Study of tip wear for AFM-based vibration-assisted nanomachining process, *Journal of Manufacturing Processes*, **50**, 47-56.

Kong, X., Dong, J.,Cohen, P. H. (2017). Modeling of the dynamic machining force of vibration-assisted nanomachining process, *Journal of Manufacturing Processes*, **28**, 101-108.

Kountanya, R. K.,Endres, W. J. (2001). A high-magnification experimental study of orthogonal cutting with edge-honed tools. In Proceedings of 2001 ASME International Mechanical Engineering Congress and Exposition, New York, 11-16. Place (Published).

Krishnan, N., Boyd, S., Somani, A., Raoux, S., Clark, D.,Dornfeld, D. (2008). A hybrid life cycle inventory of nano-scale semiconductor manufacturing, *Environmental science & technology*, **42**, 3069-3075.

Kümmel, J., Gibmeier, J., Müller, E., Schneider, R., Schulze, V.,Wanner, A. (2014). Detailed analysis of microstructure of intentionally formed built-up edges for improving wear behaviour in dry metal cutting process of steel, *Wear*, **311**, 21-30.

Lai, M., Zhang, X.,Fang, F. (2012). Study on critical rake angle in nanometric cutting, *Applied Physics A*, **108**, 809-818.

Lantz, M., O'Shea, S.,Welland, M. (1998). Characterization of tips for conducting atomic force microscopy in ultrahigh vacuum, *Review of Scientific Instruments*, **69**, 1757-1764.

Lee, S.-W., Han, S. M.,Nix, W. D. (2009). Uniaxial compression of fcc Au nanopillars on an MgO substrate: The effects of prestraining and annealing, *Acta Materialia*, **57**, 4404-4415.

Li, C., Zhang, F., Meng, B., Liu, L.,Rao, X. (2017). Material removal mechanism and grinding force modelling of ultrasonic vibration assisted grinding for SiC ceramics, *Ceramics International*, **43**, 2981-2993.

Li, J. (2007). The mechanics and physics of defect nucleation, *MRS bulletin*, **32**, 151-159.

Li, J., Guo, J., Luo, H., Fang, Q., Wu, H., Zhang, L.,Liu, Y. (2016). Study of nanoindentation mechanical response of nanocrystalline structures using molecular dynamics simulations, *Applied Surface Science*, **364**, 190-200.

Li, J., Van Vliet, K. J., Zhu, T., Yip, S.,Suresh, S. (2002). Atomistic mechanisms governing elastic limit and incipient plasticity in crystals, *Nature*, **418**, 307.

Li, J., Van Vliet, K. J., Zhu, T., Yip, S.,Suresh, S. (2002). Atomistic mechanisms governing elastic limit and incipient plasticity in crystals, *Nature*, **418**, 307.

Liddle, J. A.,Gallatin, G. M. (2016). Nanomanufacturing: a perspective, *ACS nano*, **10**, 2995-3014.

Lim, Y. Y.,Chaudhri, M. M. (1999). The effect of the indenter load on the nanohardness of ductile metals: an experimental study on polycrystalline work-hardened and annealed oxygen-free copper, *Philosophical Magazine A*, **79**, 2979-3000.

Lim, Y. Y.,Chaudhri, M. M. (1999). The effect of the indenter load on the nanohardness of ductile metals: an experimental study on polycrystalline work-hardened and annealed oxygen-free copper, *Philosophical Magazine A*, **79**, 2979-3000.

Liu, J., Notbohm, J. K., Carpick, R. W.,Turner, K. T. (2010). Method for characterizing nanoscale wear of atomic force microscope tips, *ACS nano*, **4**, 3763-3772.

Liu, K., Li, X., Rahman, M., Neo, K.,Liu, X. (2007). A study of the effect of tool cutting edge radius on ductile cutting of silicon wafers, *The International Journal of advanced manufacturing technology*, **32**, 631.

Liu, Y.,Ngan, A. (2001). Depth dependence of hardness in copper single crystals measured by nanoindentation, *Scripta Materialia*, **44**, 237-241.

Lovsky, Y., Lewis, A., Sukenik, C. *et al.* Atomic-force-controlled capillary electrophoretic nanoprinting of proteins. *Anal Bioanal Chem* **396,** 133–138 (2010).

Lu, L., Shen, Y., Chen, X., Qian, L.,Lu, K. (2004). Ultrahigh strength and high electrical conductivity in copper, *Science*, **304**, 422-426.

Lucca, D., Seo, Y., Rhorer, R.,Donaldson, R. (1994). Aspects of surface generation in orthogonal ultraprecision machining, *CIRP annals*, **43**, 43-46.

Manjunathaiah, J.,Endres, W. (2000). A study of apparent negative rake angle and its effect on shear angle during orthogonal cutting with edge-radiused tools, *Transactions-North American Manufacturing Research Institution of Sme*, 197-202.

Manson, S. S. (1953). Behavior of materials under conditions of thermal stress (National Advisory Committee for Aeronautics).

Martin, Y., Williams, C. C.,Wickramasinghe, H. K. (1987). Atomic force microscope–force mapping and profiling on a sub 100-Å scale, *Journal of Applied Physics*, **61**, 4723-4729.

Masuzawa, T. (2000). State of the art of micromachining, *CIRP annals*, **49**, 473-488.

McWilliams, A. 2018. 'Nanodevices and Nanomachines: The Global Market', bccresearch.https://www.bccresearch.com/market-research/nanotechnology/nanodevices-and-nanomachines-market-report.html.

Merchant, M. E. (1945). Mechanics of the metal cutting process. I. Orthogonal cutting and a type 2 chip, *Journal of Applied Physics*, **16**, 267-275.

Meyer, G.,Amer, N. M. (1990). Optical-beam-deflection atomic force microscopy: The NaCl (001) surface, *Applied Physics Letters*, **56**, 2100-2101.

Miller, R. E.,Rodney, D. (2008). On the nonlocal nature of dislocation nucleation during nanoindentation, *Journal of the Mechanics and Physics of Solids*, **56**, 1203-1223.

Miller, R., Vesenka, J.,Henderson, E. (1995). Tip reconstruction for the atomic force microscope, *SIAM Journal on Applied Mathematics*, **55**, 1362-1371.

Miller, R., Vesenka, J.,Henderson, E. (1995). Tip reconstruction for the atomic force microscope, *SIAM Journal on Applied Mathematics*, **55**, 1362-1371.

Miner, M. (1945). Cumulative fatigue damage, *Journal of applied mechanics*, **12**, A159-A164.

Moriwaki, T.,Shamoto, E. (1991). Ultraprecision diamond turning of stainless steel by applying ultrasonic vibration, *CIRP annals*, **40**, 559-562.

Murthy, T. G., Gnanamanickam, E.,Chandrasekar, S. (2012). Deformation field in indentation of a granular ensemble, *Physical Review E*, **85**, 061306.

Nawaz, A., Mao, W., Lu, C.,Shen, Y. (2017). Mechanical properties, stress distributions and nanoscale deformation mechanisms in single crystal 6H-SiC by nanoindentation, *Journal of Alloys and Compounds*, **708**, 1046-1053.

Nieh, T.,Wadsworth, J. (1991). Hall-Petch relation in nanocrystalline solids, *Scripta Metallurgica et Materialia*, **25**, 955-958.

Niesłony, P., Grzesik, W., Chudy, R.,Habrat, W. (2015). Meshing strategies in FEM simulation of the machining process, *Archives of Civil and Mechanical Engineering*, **15**, 62-70.

Nishimatsu, Y. (1972). The mechanics of rock cutting. In International Journal of Rock Mechanics and Mining Sciences & Geomechanics Abstracts, 261-270. Place (Published), Elsevier.

Nix, W. D.,Gao, H. (1998). Indentation size effects in crystalline materials: a law for strain gradient plasticity, *Journal of the Mechanics and Physics of Solids*, **46**, 411-425.

Ogata, S., Li, J., Hirosaki, N., Shibutani, Y.,Yip, S. (2004). Ideal shear strain of metals and ceramics, *Physical Review B*, **70**, 104104.

Ogata, S., Li, J.,Yip, S. (2002). Ideal pure shear strength of aluminum and copper, *Science*, **298**, 807-811.

Oluwajobi, A.,Chen, X. (2011). The effect of interatomic potentials on the molecular dynamics simulation of nanometric machining, *International Journal of Automation and Computing*, **8**, 326-332.

Orowan, E. (1950). Fundamentals of brittle behavior in metals, *Fatigue and fracture of metals*, 139-167.

Palmgren, A. (1924). Die lebensdauer von kugellargern, *Zeitshrift des Vereines Duetsher Ingenieure*, **68**, 339.

Paris, P., Gomez, M.,Anderson, W. (1961). The trend in engineering, *University of Washington*, **13**.

Paris, P.,Erdogan, F. (1963). Basic engineering, *Trans ASTM J*, 528-534.

Pei, Q., Lu, C., Fang, F.,Wu, H. (2006). Nanometric cutting of copper: A molecular dynamics study, *Computational Materials Science*, **37**, 434-441.

Pen, H., Liang, Y., Luo, X., Bai, Q., Goel, S.,Ritchie, J. (2011). Multiscale simulation of nanometric cutting of single crystal copper and its experimental validation, *Computational Materials Science*, **50**, 3431-3441.

Piispanen, V. (1937). Lastunmuodostumisen teoriaa, *Teknillinen aikakauslehti*, **27**, 315-322.

Polonsky, I.,Keer, L. M. (1996a). 'Elastic-Plastic Microcontact Modeling Using Dislocations.' in, Tribology Series (Elsevier).

Polonsky, I.,Keer, L. M. (1996b). Scale effects of elastic-plastic behavior of microscopic asperity contacts.

Polonsky, I.,Keer, L. M. (1996c). Simulation of microscopic elastic-plastic contacts by using discrete dislocations, *Proceedings of the Royal Society of London. Series A: Mathematical, Physical and Engineering Sciences*, **452**, 2173-2194.

Prandtl, L. (1920). Theory of lifting surfaces.

Qiao, G., Yi, S., Zheng, W.,Zhou, M. (2021). Material removal behavior and crack-inhibiting effect in ultrasonic vibration-assisted scratching of silicon nitride ceramics, *Ceramics International*.

Qiu, C., Zhu, P., Fang, F., Yuan, D.,Shen, X. (2014). Study of nanoindentation behavior of amorphous alloy using molecular dynamics, *Applied Surface Science*, **305**, 101-110.

Ramirez-Aguilar, K. A.,Rowlen, K. L. (1998). Tip characterization from AFM images of nanometric spherical particles, *Langmuir*, **14**, 2562-2566.

Rester, M., Motz, C.,Pippan, R. (2007). Microstructural investigation of the volume beneath nanoindentations in copper, *Acta Materialia*, **55**, 6427-6435.

Rinaldi, A., Peralta, P., Friesen, C.,Sieradzki, K. (2008). Sample-size effects in the yield behavior of nanocrystalline nickel, *Acta Materialia*, **56**, 511-517.

Roters, F., Eisenlohr, P., Hantcherli, L., Tjahjanto, D. D., Bieler, T. R.,Raabe, D. (2010). Overview of constitutive laws, kinematics, homogenization and multiscale methods in crystal plasticity finite-element modeling: Theory, experiments, applications, *Acta Materialia*, **58**, 1152-1211.

Schmitz, S., Seibel, T., Beck, T., Rollmann, G., Krause, R.,Gottschalk, H. (2013). A probabilistic model for LCF, *Computational Materials Science*, **79**, 584-590.

Schmutz, J.-E., Fuchs, H.,Hölscher, H. (2010). Measuring wear by combining friction force and dynamic force microscopy, *Wear*, **268**, 526-532.

Scifo, J., Alesini, D., Anania, M.P., Bellaveglia, M., Bellucci, S., Biagioni, A., Bisesto, F., Cardelli, F., Chiadroni, E., Cianchi, A. and Costa, G., 2018. Nano-machining, surface analysis and emittance measurements of a copper photocathode at SPARC_LAB. *Nuclear Instruments and Methods in Physics Research Section A: Accelerators, Spectrometers, Detectors and Associated Equipment*, *909*, pp.233-238.

Sedin, D. L.,Rowlen, K. L. (2001). Influence of tip size on AFM roughness measurements, Applied Surface Science, 182, 40-48.

Shamoto, E.,Moriwaki, T. (1999). Ultaprecision diamond cutting of hardened steel by applying elliptical vibration cutting, *CIRP annals*, **48**, 441-444.

Shan, Z., Mishra, R. K., Asif, S. S., Warren, O. L.,Minor, A. M. (2008). Mechanical annealing and source-limited deformation in submicrometre-diameter Ni crystals, *Nature materials*, **7**, 115.

Shaw, M. C. (1984). Metal cutting principles (Oxford university press New York).

Shaw, M. C. (2005). Metal cutting principles (Oxford university press New York).

Shaw, M. C.,DeSalvo, G. J. (1970). On the plastic flow beneath a blunt axisymmetric indenter.

Shibata, T., Fujii, S., Makino, E.,Ikeda, M. (1996). Ductile-regime turning mechanism of single-crystal silicon, *Precision Engineering*, **18**, 129-137.

Shimada, S., Ikawa, N., Tanaka, H., Ohmori, G., Uchikoshi, J.,Yoshinaga, H. (1993). Feasibility study on ultimate accuracy in microcutting using molecular dynamics simulation, *CIRP annals*, **42**, 91-94.

Steigerwald J M, Murarka S P and Gutmann R J 1997 Chemical Mechanical Planarization of MicroelectronicMaterials (New York: Wiley)

Sieradzki, K., Rinaldi, A., Friesen, C.,Peralta, P. (2006). Length scales in crystal plasticity, *Acta Materialia*, **54**, 4533-4538.

Stephens, R. I., Fatemi, A., Stephens, R. R.,Fuchs, H. O. (2000). Metal fatigue in engineering (John Wiley & Sons).

Stukowski, A., Bulatov, V. V.,Arsenlis, A. (2012). Automated identification and indexing of dislocations in crystal interfaces, *Modelling and Simulation in Materials Science and Engineering*, **20**, 085007.

Sun, X., Chen, S., Cheng, K., Huo, D.,Chu, W. (2006). Multiscale simulation on nanometric cutting of single crystal copper, *Proceedings of the Institution of Mechanical Engineers, Part B: Journal of Engineering Manufacture*, **220**, 1217-1222.

Swadener, J., George, E.,Pharr, G. (2002). The correlation of the indentation size effect measured with indenters of various shapes, *Journal of the Mechanics and Physics of Solids*, **50**, 681-694.

Szlufarska, I., Kalia, R. K., Nakano, A.,Vashishta, P. (2007). A molecular dynamics study of nanoindentation of amorphous silicon carbide, *Journal of Applied Physics*, **102**, 023509.

Timoshenko, S. (1911). Festigkeitslehre.

Tordesillas, A.,Shi, J. (1999). Frictional indentation of dilatant granular materials, *Proceedings of the Royal Society of London. Series A: Mathematical, Physical and Engineering Sciences*, **455**, 261-283.

Tschopp, M.,McDowell, D. (2008). Influence of single crystal orientation on homogeneous dislocation nucleation under uniaxial loading, *Journal of the Mechanics and Physics of Solids*, **56**, 1806-1830.

Uhlmann, E., Henze, S.,Brömmelhoff, K. (2015). Influence of the built-up edge on the stress state in the chip formation zone during orthogonal cutting of AISI1045, *Procedia CIRP*, **31**, 310-315.

Van Vliet, K. J., Li, J., Zhu, T., Yip, S.,Suresh, S. (2003). Quantifying the early stages of plasticity through nanoscale experiments and simulations, *Physical Review B*, **67**, 104105.

Villarrubia, J. S. (1994). Morphological estimation of tip geometry for scanned probe microscopy, *Surface science*, **321**, 287-300.

Vogler, M. P. (2003). On the modeling and analysis of machining performance in microendmilling (University of Illinois at Urbana-Champaign).

Voigt, F., Krohs, F.,Gerbach, R. (2009). Flexural-torsional resonance mode of a chip cantilever system: Applications to nanomachining, *Journal of Vacuum Science & Technology B*, **27**, 958-963.

Wang, J., Geng, Y., Li, Z., Yan, Y., Luo, X.,Fan, P. (2021). Study on the vertical ultrasonic vibration-assisted nanomachining process on single-crystal silicon, *Journal of Manufacturing Science and Engineering*, **144**, 041013.

Wang, J., Zhang, X., Fang, F.,Chen, R. (2018). A numerical study on the material removal and phase transformation in the nanometric cutting of silicon, *Applied Surface Science*, **455**, 608-615.

Wang, Z.-J., Li, Q.-J., Cui, Y.-N., Liu, Z.-L., Ma, E., Li, J., Sun, J., Zhuang, Z., Dao, M.,Shan, Z.-W. (2015). Cyclic deformation leads to defect healing and strengthening of small-volume metal crystals, *Proceedings of the National Academy of Sciences*, **112**, 13502-13507.

Wang, W.,Lu, K. (2006). Nanoindentation study on elastic and plastic anisotropies of Cu single crystals, *Philosophical Magazine*, **86**, 5309-5320.

Wang, Z. Q., Jiao, N. D., Tung, S.,Dong, Z. L. (2010). Research on the atomic force microscopy-based fabrication of nanochannels on silicon oxide surfaces, *Chinese Science Bulletin*, **55**, 3466-3471.

Wang, Z.-J., Li, Q.-J., Cui, Y.-N., Liu, Z.-L., Ma, E., Li, J., Sun, J., Zhuang, Z., Dao, M.,Shan, Z.-W. (2015). Cyclic deformation leads to defect healing and strengthening of small-volume metal crystals, *Proceedings of the National Academy of Sciences*, **112**, 13502-13507.

Weibull, W. (1939). A statistical theory of strength of materials, *IVB-Handl.*

Weibull, W. (1951). A statistical distribution function of wide applicability, *Journal of applied mechanics*, **18**, 293-297.

Woon, K., Rahman, M., Fang, F., Neo, K.,Liu, K. (2008). Investigations of tool edge radius effect in micromachining: a FEM simulation approach, *Journal of Materials Processing Technology*, **195**, 204-211.

Wyen, C.-F., Knapp, W.,Wegener, K. (2012). A new method for the characterisation of rounded cutting edges, *The International Journal of advanced manufacturing technology*, **59**, 899-914.

Xu, F., Fang, F.,Zhang, X. (2017a). Side flow effect on surface generation in nano cutting, *Nanoscale Research Letters*, **12**, 1-11.

Xu, F., Fang, F., Zhu, Y.,Zhang, X. (2017b). Study on crystallographic orientation effect on surface generation of aluminum in nano-cutting, *Nanoscale Research Letters*, **12**, 1-13.

Xu, F., Wang, J., Fang, F.,Zhang, X. (2017c). A study on the tool edge geometry effect on nano-cutting, *The International Journal of advanced manufacturing technology*, **91**, 2787-2797.

Xu, G.,Argon, A. S. (2001). Energetics of homogeneous nucleation of dislocation loops under a simple shear stress in perfect crystals, *Materials Science and Engineering: A*, **319**, 144-147.

Yadav, S., Saldana, C.,Murthy, T. G. (2016). Porosity and geometry control ductile to brittle deformation in indentation of porous solids, *International Journal of Solids and Structures*, **88**, 11-16.

Yadav, S., Saldana, C.,Murthy, T. G. (2018). Experimental investigations on deformation of soft rock during cutting, *International Journal of Rock Mechanics and Mining Sciences*, **105**, 123-132.

Yan, J. (1999). Effects of cutting edge geometry on brittle-ductile transition in silicon machining. In Proceedings of the 9th international conference on precision engineering (ICPE), Osaka, Japan, 1999, 92-97. Place (Published).

Yan, J., Yoshino, M., Kuriagawa, T., Shirakashi, T., Syoji, K.,Komanduri, R. (2001). On the ductile machining of silicon for micro electro-mechanical systems (MEMS), opto-electronic and optical applications, *Materials Science and Engineering: A*, **297**, 230-234.

Yan, Y. D., Sun, T., Liang, Y. C.,Dong, S. (2007). Investigation on AFM-based micro/nano-CNC machining system, *International Journal of Machine Tools & Manufacture*, **47**, 1651-1659.

Yan, Y., Xue, B., Hu, Z.,Zhao, X. (2016). AFM tip characterization by using FFT filtered images of step structures, *Ultramicroscopy*, **160**, 155-162.

Ye, Y., Biswas, R., Morris, J., Bastawros, A.,Chandra, A. (2003). Molecular dynamics simulation of nanoscale machining of copper, *Nanotechnology*, **14**, 390.

Ye, Y., Lu, Z.,Nieh, T. (2017). Dislocation nucleation during nanoindentation in a body-centered cubic TiZrHfNb high-entropy alloy, *Scripta Materialia*, **130**, 64-68.

Zhang, J., Cui, T., Ge, C., Sui, Y.,Yang, H. (2016). Review of micro/nano machining by utilizing elliptical vibration cutting, *International Journal of Machine Tools and Manufacture*, **106**, 109-126.

Zhang, J.-l., Zaefferer, S.,Raabe, D. (2015). A study on the geometry of dislocation patterns in the surrounding of nanoindents in a TWIP steel using electron channeling contrast imaging and discrete dislocation dynamics simulations, *Materials Science and Engineering: A*, **636**, 231-242.

Zhang, L.,Tanaka, H. (1997). Towards a deeper understanding of wear and friction on the atomic scale—a molecular dynamics analysis, *Wear*, **211**, 44-53.

Zhang, L.,Tanaka, H. (1998). Atomic scale deformation in silicon monocrystals induced by two-body and three-body contact sliding, *Tribology International*, **31**, 425-433.

Zhang, L.-C.,Tanaka, H. (1999). On the mechanics and physics in the nano-indentation of silicon monocrystals, *JSME International Journal Series A Solid Mechanics and Material Engineering*, **42**, 546-559.

Zhao, Q. L., Sun, T., Liang, Y. C., Dong, S.,Chen, M. J. (2001). 'Atomic force microscope using a diamond tip: a tool for micro/nano-machining on single crystal silicon surface.' in N. C. Tien and Q. A. Huang (eds.), Micromachining and Microfabrication Process Technology and Devices.

Zheng, Z.,Yu, J. (2007). Using the Dugdale approximation to match a specific interaction in the adhesive contact of elastic objects, *Journal of colloid and interface science*, **310**, 27-34.

Zhong, Q., Inniss, D., Kjoller, K.,Elings, V. (1993). Fractured polymer/silica fiber surface studied by tapping mode atomic force microscopy, *Surface Science Letters*, **290**, L688-L692.

Zhu, B., Zhao, H., Zhao, D., Zhang, P., Yang, Y., Han, L.,Kui, H. (2016). Effects of vibration frequency on vibration-assisted nano-scratch process of mono-crystalline copper via molecular dynamics simulation, *AIP Advances*, **6**, 035015.

Zhu, T., Li, J., Samanta, A., Leach, A.,Gall, K. (2008). Temperature and strain-rate dependence of surface dislocation nucleation, *Physical Review Letters*, **100**, 025502.

Zhu, T., Li, J., Van Vliet, K. J., Ogata, S., Yip, S.,Suresh, S. (2004). Predictive modeling of nanoindentation-induced homogeneous dislocation nucleation in copper, *Journal of the Mechanics and Physics of Solids*, **52**, 691-724.

Zhu, T.,Li, J. (2010). Ultra-strength materials, *Progress in Materials Science*, **55**, 710-757.

Ziegenhain, G., Hartmaier, A.,Urbassek, H. M. (2009). Pair vs many-body potentials: Influence on elastic and plastic behavior in nanoindentation of fcc metals, *Journal of the Mechanics and Physics of Solids*, **57**, 1514-1526.

Appendix A

Basic notions of dislocation motion and plasticity

In this appendix, dislocations which their nucleation, motion, coalescence, and annihilation are used to explain deformation at all dimensional scales, and especially the nanoscale.

The dislocation theory was independently proposed by Orowan, Polanyi and Taylor in 1934 to describe linear faults in crystals. Meanwhile, most of the energy dissipated when a metal is plastically deformed is heat while the remaining approximately 5% is stored internally. The majority of the 5% mentioned is strain energy linked to dislocations.

Dislocations can be found as either edge dislocations, screw dislocations, or a mix of the two mentioned. In nature, the vast majority of dislocations exist as a mix but in rare cases pure edge or screw dislocations can be found.

Motion of dislocations that results in plastic deformation is known as a slip. The plane which the dislocation line passes through is known as the slip plane. In addition, a plastic deformation resembles results from the movement of dislocations as a reaction to an applied shear stress is the slip plane.

In regions adjacent to the dislocation, atoms on one side of the dislocation are squeezed together in a compression strain area while on the other side the atoms are pulled away creating a tension strain area between the atoms. Hence, creating shearing, compressive, and tensile lattice strains in the area surrounding the dislocation.

When different dislocations are near in such way that they affect each other, the forces (i.e., tension, compression, and shear) impact the reaction between the near dislocations. Strengthening mechanisms for metals depend highly on the mentioned strain field and their respective related forces.

Extra dislocations originate from:

- Already existing dislocations that multiply
- Grain Boundaries
- Internal or external (surface) defects including scratches and nicks, which act as stress concentration locations.

As for the theoretical shear strength of materials, Figure A1.1 below shows atoms arranged in two layers. Figure A1.1 (a) shows the two layers aligned perfectly with no influence of loading whereas Figure A1.1 (b) shows how applying a shear stress displaces one layer a distance x from the other.

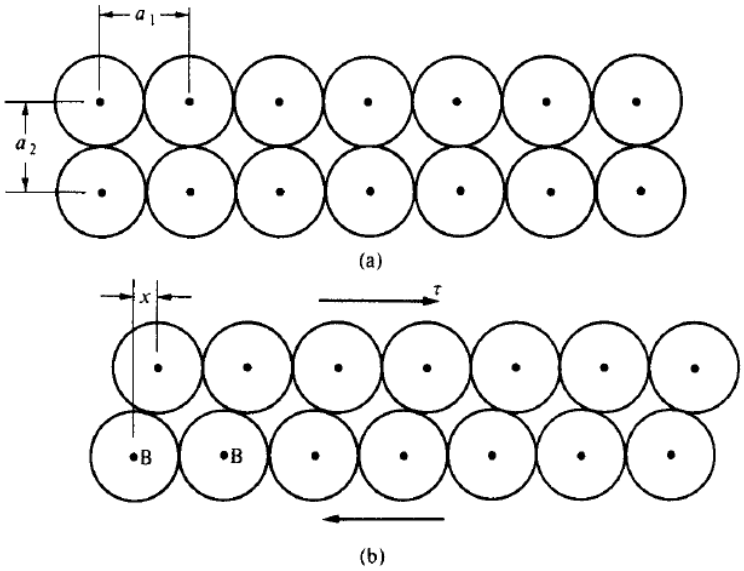

Figure A1.1 Slippage of one layer of atoms: (a) before (b) after slippage (Shaw 2005)

It can be assumed that the resistance stress τ changes linearly with displacement x. Studying Figure A1.1 (see., Shaw 2005), two locations can be extracted (values of x) where the resistance stress (τ) is zero: (i) when $x = a_1$ in which case the atoms are perfectly aligned (ii) $x = a_1/2$ where atoms are displaced but equally attracted to the two adjacent B atoms resulting in a zero-resistance stress as well. On the other hand, the maximum resistive shear stress then must be at $x = a_1/4$ and continuing with the linear relationship assumption between τ and x gives:

$$\frac{\tau}{\tau_0} = \frac{x}{\frac{a_1}{4}} \tag{A1.1}$$

But the shear strain γ can be represented as $\gamma = x/a_2$ resulting in:

$$\tau_0 = \frac{G}{4}\frac{a_1}{a_2\gamma} \cong \frac{G}{4} \tag{A1.2}$$

The approximation was done using Hooke's law since $a_1 \cong a_2$.

Figure A1.2 below highlights an edge dislocation where the number of atoms above the slip plane is higher than the one below causing an attraction force from the above layer atoms towards the ones neighbouring them in the bottom one and at the same time avoiding separation from atoms within the same layer.

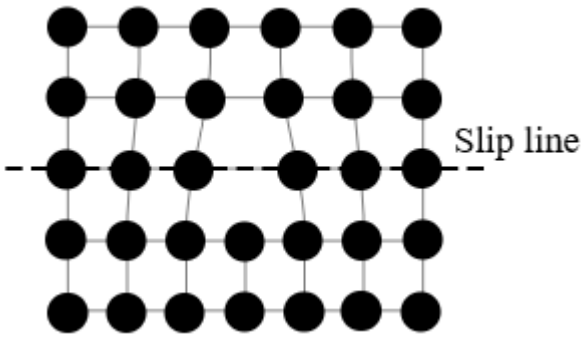

Figure A1.2 Edge dislocation demonstrating the slip plane

The motion of a dislocation within a crystal includes a displacement of a single atom spacing a_1. Observing Figure A1.2, if dislocations exist in all planes of atoms in the a_2 then the motion of a dislocation represents a single local shear strain equal to a_1/a_2. In practice, dislocations within planes are dispersed by relatively large distances and to be able to notice a plastic strain a big number of dislocations on the active slip plane are needed.

No material in the real world is 100% perfect and must have imperfections with spacing of 1μm approximately corresponding to the maximum spacing for a given shear plane. These imperfections cause stress concentration in their vicinity. An example of such imperfections would be microcracks as Figure A1.3 shows.

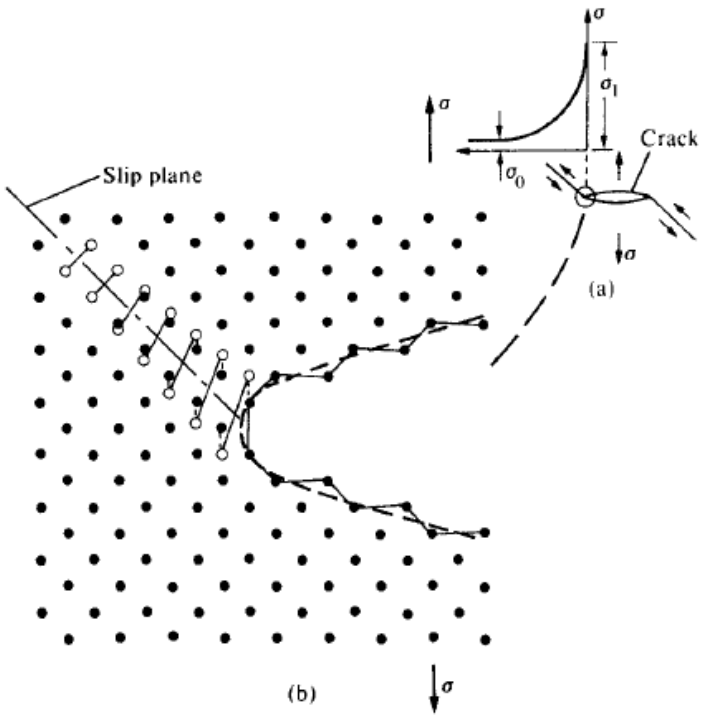

Figure A1.3 (a) stress concentration at a crack (b) displacement of ions at a crack's tip showing the effect after stress

Figure A1.3 (a) shows how stress values increase above the homogenous value σ_0 when approaching the crack tip. Meanwhile, Figure A1.3 (b) shows atoms along a 45° slip line, where the solid dots show how the unstressed state of atoms while the open ones show the state of the atoms after loading. The open dots highlight how the crystal looks after a dislocation moving across the crystal. Whenever a dislocation is nucleated and is moving within the crystal under tensile stress, the crack (similar to the one in Figure A1.1 (b)) will continue to grow until a threshold is reached.

Heat has the ability to remove flow stress caused by the plastic strain by increasing the amplitude of vibrations in the atoms to a degree where it is able to shake the dislocation from the structure. This, however, is usually followed by a rearrangement of crystal boundaries and a reduction in grain size.

Although dislocations are too small for any sort of conventional photography to capture, techniques such as transmission electron microscopy (TEM) of thin

films can be used to investigate the formation and motion of dislocations (see., Berghezan and Fourdeux 1959).

To understand how crystals plastically deform, a single crystal deforming under tensile loading can be taken as an example. A monocrystal would start to deform under tension via a slip on a well-defined parallel plane. Then, parts of the crystal start to slide away from each other resulting in a continuously changing geometry.

Slip planes are the crystallographic planes where slips constantly happen. Whereas the directions of the slips that are consistent with the slip planes are referred to as slip directions. A slip system is the combination of a slip plane and its slip direction. In addition, a miller index is a notation used to express a slip system where FCC metals for example slip on $\langle\bar{1}10\rangle\{111\}$ where this slip direction coincides with the slip plane.

Critical resolved shear stress (CRSS) is the shear stress component necessary to initiate slip and is resolved in the direction of the slip. This concept is used to provide proof at the end of this chapter, hence is explained here first.

The resolved shear stress (RSS) is the component of the shear resolved along a slip plane (tension or compression), that is not parallel nor perpendicular to the stress axis (see., Bragg and Nye(1947).

The more shear stress applied the more slipping occurs due to the overcoming of resistance of dislocation motion once a critical value is reached. The applied stress needed for plastic deformation is known as the tensile yield stress which can be related to the shear stress acting on the slip direction (Boas and Schmid 1935):

$$\tau_{RSS} = \frac{Fcos\lambda}{A/cos\varphi} = \frac{F}{A}cos\lambda cos\varphi = \sigma_{app}cos\lambda cos\varphi \qquad \text{(A1.3)}$$

And,

$$\tau_{CRSS} = \sigma_y m_{max} \qquad \text{(A1.4)}$$

where;

- σ_{app} is the applied stress

- φ is the angle separating the normal of the slip plane and the force applied
- λ is the angle separating the slip direction and the direction of the force applied
- $cos\lambda cos\varphi$ is the Schmid Factor (m)
- σ_y is the yield stress

Schmid's Law suggests that τ_R for a specific material with certain dislocation density is a constant known as critical resolved shear stress τ_C. And according to Gottstein (2013), Schmid factor applies to mainly to single crystals of FCC metals. Li (2007) used a modified version of the above equation for further analysis discussed at the end of this chapter.